UNIVERSITÉ
LAVAL

Optimization of a Fully-Passive Flapping-Airfoil Turbine

Mémoire

Jean-Christophe Veilleux

Maîtrise en génie mécanique
Maître ès sciences (M.Sc.)

Québec, Canada

Résumé

Ce mémoire concerne l'étude aéroélastique des oscillations auto-soutenues en pilonnement-tangage d'une aile portante montée sur des supports élastiques et exposée à un écoulement. De telles oscillations pourraient être utilisées afin de développer un nouveau type de turbine hydrocinétique relativement simple d'un point de vue mécanique. Ceci est possible car les oscillations qui résultent de l'interaction fluide-structure entre l'écoulement, l'aile et ses supports élastiques sont entretenues par un transfert d'énergie de l'écoulement vers la structure.

Dans cette étude numérique, le logiciel *OpenFOAM-2.1.x* est utilisé afin de résoudre le problème aéroélastique. À l'aide de simulations instationnaires en deux dimensions d'un écoulement visqueux à nombre de Reynolds de 500 000, ce type de turbine est optimisé et amplement étudié afin de développer une meilleure compréhension de la physique en jeu.

Suite à une optimisation de la turbine à l'aide d'une méthode de type gradients, des efficacités relativement élevées ont été obtenues. En effet, le cas optimal qui est présenté dans cette étude a une efficacité qui est de l'ordre de 34%. Cela correspond à une efficacité relativement élevée lorsqu'elle est comparée à l'efficacité d'une turbine hydrolienne cinématiquement contrainte qui est de l'ordre de 43%. Il faut noter que la version pleinement passive est mécaniquement beaucoup plus simple que la version cinématiquement contrainte. Un tel avantage mécanique peut, en soi, justifier pleinement une efficacité légèrement plus faible. De plus, la solution optimisée proposée dans ce mémoire n'est certainement pas unique et ne correspond pas au seul extremum du vaste espace paramétrique. En fait, d'autres solutions efficaces sont présentées dans ce mémoire et une optimisation complète autour de ces solutions demeure toujours à être effectuée. Dans tous les cas, ces résultats démontrent le grand potentiel d'utiliser des ailes oscillantes pleinement passives en guise d'hydroliennes efficaces.

D'un point de vue physique, ce mémoire met en valeur que le phénomène d'oscillations de cycle limite auquel l'aile est sujette est le résultat d'un flottement de décrochage. Cela est ainsi en raison de la forte interaction entre l'aile et les tourbillons largués pendant le grand décrochage dynamique. En fait, c'est spécifiquement cette interaction entre l'aile et les vortex qui donne lieu au mouvement de tangage. De plus, deux mécanismes responsables des bonnes performances de la turbine ont été mis en valeur. Ces mécanismes sont la synchronisation adéquate entre les deux degrés de liberté, ainsi que le mouvement non sinusoïdal en tangage.

Abstract

This master's thesis deals with an aeroelastic problem that consists into self-sustained, pitch-heave oscillations of an elastically-mounted airfoil. Such oscillations of an airfoil could be used in order to develop a novel fully-passive flow harvester that is relatively simple from a mechanical point of view. Indeed, the motion of an airfoil that is elastically mounted emerges as a result of the fluid-structure interaction between the flow, the airfoil and its elastic supports, and is sustained through a transfer of energy from the flow to the structure.

In this numerical study, the *OpenFOAM-2.1.x* CFD toolbox is used for solving the aeroelastic problem. Through unsteady two-dimensional viscous simulations at a Reynolds number of 500,000, such a fully-passive turbine is optimized and extensively investigated to develop a better comprehension of the physics at play.

Following a gradient-like optimization of the turbine, relatively high efficiencies have been obtained. Indeed, the optimal case found in this numerical study has a two-dimensional efficiency in the range of 34%. This is fairly high when compared to the two-dimensional efficiency of a kinematically-constrained turbine, which is in the range of 43%. Further, the fully-passive version of the turbine is far less mechanically complex than its kinematically-constrained counterpart. Alone, such a mechanical advantage could justify the slightly lower efficiency of the fully-passive turbine. Nevertheless, the optimized solution suggested within this thesis is certainly not the only local extrema of the vast parametric space pertaining to the aeroelastic device. Other efficient cases have been found, and complete optimizations about these solutions still need to be achieved. Overall, the results demonstrate the great potential of using fully-passive, flapping airfoils as efficient hydrokinetic turbines.

From a more physical perspective, this thesis highlights the fact that the airfoil is undergoing limit-cycle oscillations as a result of stall flutter. This is because the interaction between the airfoil and the vortices shed during the dynamic stall events is large. In fact, it is specifically this interaction that mostly accounts for the pitching motion of the airfoil. Further, two fundamental mechanisms have been found to be very beneficial for enhancing the performances of the turbine. These mechanisms are the adequate synchronization between both degrees-of-freedom, and the nonsinusoidal shape of the pitching motion.

Contents

List of Tables

List of Figures

Nomenclature

List of symbols

A^* = normalized amplitude of motion of the oscillating cylinder
C_A = potential added mass coefficient
$C_{\mathcal{D}}$ = instantaneous coefficient of aerodynamic drag
$C_{\mathcal{L}}$ = instantaneous coefficient of aerodynamic lift
C_{Mea} = instantaneous coefficient of aerodynamic moment about the elastic axis
C_P = instantaneous coefficient of power normalized by the chord length, $\frac{P}{\frac{1}{2}\rho U_\infty^3 c}$
$C_P{}^*$ = instantaneous coefficient of power normalized by twice the amplitude of motion, $\frac{P}{\frac{1}{2}\rho U_\infty^3 2y_0}$
$C_{P,tr}$ = instantaneous coefficient of power transfered between the pitch and the heave
C_{Py} = instantaneous coefficient of aerodynamic power in heave
$C_{Py,damp}$ = instantaneous coefficient of power available to the electrical generator
$C_{P\theta}$ = instantaneous coefficient of aerodynamic power in pitch
$C_{P\theta,damp}$ = instantaneous coefficient of power available to the pitch damper
C_Y = instantaneous coefficient of lift on the oscillating cylinder
D = diameter of the oscillating cylinder
D_h = heave damping coefficient
D_θ = pitch damping coefficient
E_0 = voltage of the electrical generator
F = instantaneous lift on the oscillating cylinder
F_{nc} = non-conservative forces
I = electrical current from the generator
I_θ = moment of inertia about the elastic axis
K = proportionality constant for the equivalent damping from the electrical generator
$\mathcal{L}$ = instantaneous aerodynamic lift
M_{ea} = instantaneous aerodynamic moment about the elastic axis
M_{nc} = non-conservative moments
P = instantaneous aerodynamic power
P_y = instantaneous aerodynamic power in heave
P_θ = instantaneous aerodynamic power in pitch

Re = Reynolds number based on the chord length, $U_\infty \, c \, / \, \nu$

S = static imbalance, $m_p x_\theta$

T = period of oscillation

T_E = total kinetic energy

T_g = required torque to drive the electrical generator

T_h = kinetic energy of the heaving components

T_p = kinetic energy of the pitching components

U_{cr} = critical flutter velocity

U_E = total potential energy

U_∞ = freestream velocity

Z = number of conductors in the armature of the electrical generator

b = wing span

c = chord length or damping coefficient of the oscillating cylinder

d = flow window

e = distance between the aerodynamic center and the elastic axis

f = frequency of oscillation

f^* = reduced frequency of oscillation, fc/U_∞

f_N = natural frequency of the oscillating cylinder

$f_{N,h}$ = decoupled natural frequency in heave

$f_{N,p}$ = decoupled natural frequency in pitch

h_s = thickness of the solid structure

k = spring stiffness of the oscillating cylinder

k_h = heave stiffness coefficient

k_θ = pitch stiffness coefficient

m = mass of the oscillating cylinder

m_h = mass of all moving components of the aeroelastic device

m_p = mass of all pitching components of the aeroelastic device

n = electrical generator's armature angular velocity in rotations per minute

p = pressure

q = dynamic pressure, $\frac{1}{2}\rho U_\infty^2$

q_{cr} = critical dynamic pressure

q_{div} = divergence dynamic pressure

q_i = i^{th} generalized coordinate

$\mathbf{r}$ = instantaneous displacement of a point on the airfoil's chord line

t = time

$\overline{u'v'}$ = Reynolds stresses

x_c = chordwise distance between any station on the chord line and the elastic axis

x_{cm} = chordwise position of the center of mass

x_{ea} = chordwise position of the elastic axis

x_θ = distance between the pivot and the center of mass
y = instantaneous vertical position of the pivot
y_0 = amplitude of motion in heave
y^+ = distance in wall coordinates
$\dot{y}$ = instantaneous heaving velocity
$\dot{y}_i$ = initial heaving velocity
$\ddot{y}$ = instantaneous heaving acceleration
x_{le} = chordwise position of the leading edge
x_{te} = chordwise position of the trailing edge
α = effective angle of attack
γ = angular frequency of oscillation, $2\pi f$
Δ = filter width of the SGS model
Δt = timestep
Δt^* = non-dimensional convective timestep, $\Delta t U_\infty / c$
η = energy harvesting efficiency
θ = instantaneous pitch angle
θ_0 = amplitude of motion in pitch
θ_i = initial angle in pitch
$\dot{\theta}$ = instantaneous angular velocity in pitch
$\dot{\theta}_i$ = initial angular velocity in pitch
$\ddot{\theta}$ = instantaneous angular acceleration in pitch
Λ = mass-damping parameter
μ_{max} = largest eigenvalue of the discrete operator in the structural solver discretization
ν = kinematic viscosity of the fluid
ν_t/ν = turbulent viscosity ratio
ξ = damping ratio of the oscillating cylinder
ξ_h = damping ratio in heave
ξ_θ = damping ratio in pitch
ρ_f = density of the fluid
ρ_s = density of the solid
ϕ = phase lag
ϕ_p = flux per pole of the electrical generator
ψ_h = fraction of dry friction in heave
ψ_θ = fraction of dry friction in pitch
ω = vorticity vector

List of superscripts

$'$ = fluctuating value of a variable
— = average value of a variable
* = non-dimensional variable

List of abbreviations

CFD = Computational Fluid Dynamic
DNS = Direct Numerical Simulation
FSI = Fluid-Structure Interaction
GUI = Graphical User Interface
ILES = Implicit Large Eddy Simulation
LCO = Limit-Cycle Oscillations
LES = Large Eddy Simulation
LHS = Left Hand Side
LMFN = Laboratoire de Mécanique des Fluides Numérique
LSB = Laminar Separation Bubble
RHS = Right Hand Side
RMC = Royal Military College
RMS = Root Mean Square
RPAS = Reverse Passive-Airfoil Solver
SGS = Sub-Grid Scales
URANS = Unsteady Reynolds-Averaged Navier-Stokes
VIV = Vortex Induced Vibrations
2D = Two-dimensional
3D = Three-dimensional

Remerciements

Pour débuter, je souhaite exprimer ma plus profonde gratitude à l'égard de mon directeur de recherche, le professeur Guy Dumas. Son encadrement hors pair, sa grande expérience dans le domaine de la mécanique des fluides, sa motivation ainsi que sa passion sont des éléments qui ont nécessairement contribué au succès de mes études de deuxième cycle. Tous ces ingrédients réunis font également de lui un directeur de recherche exceptionnel.

Je souhaite aussi remercier tous mes collègues du *Laboratoire de Mécanique des Fluides Numérique* (LMFN). Vous avez fait du LMFN un milieu où l'entraide et la coopération sont des valeurs prépondérantes, ce qui contribue au succès de tous. Cet esprit collaboratif donne également lieu à un climat de travail exceptionnel. Je tiens plus particulièrement à remercier Simon Lapointe, qui a su m'initier brillamment à la CFD dès mon arrivée au laboratoire dans le cadre de mon projet de fin d'études. La transmission de ses connaissances relativement au logiciel *OpenFOAM* a représenté un atout considérable tout au long de mes travaux. De plus, je tiens à remercier Mathieu Olivier pour son aide dans le domaine de l'interaction fluide-structure. Bien qu'occupé par sa jeune famille, il a pris le temps nécessaire afin de m'aider et je lui en suis très reconnaissant. Je dois également souligner la grande contribution de Thomas Kinsey par son support et son expertise dont il sait nous faire bénéficier.

Je souhaite également remercier le *Conseil de Recherche en Sciences Naturelles et en Génie du Canada* (CRSNG) pour l'octroi d'une bourse de maîtrise en recherche. Par cet appui financier, le CRSNG m'a permis de me dévouer pleinement à mes études et à ma recherche afin d'en assurer le succès. De plus, je tiens à remercier l'Université Laval et ses généreux donateurs pour l'appui financier reçu par l'entremise de la bourse Marthe-et-Robert-Ménard.

Sur une note plus personnelle, je tiens à souligner l'appui inconditionnel de mes parents tout au long de mes études de deuxième cycle. Sans eux, cette grande aventure n'aurait simplement pas été possible et je leur en serai toujours reconnaissant.

Enfin, je ne peux passer sous silence la grande contribution de ma conjointe, Audrey. Son appui constant a été une source de motivation pour moi. De plus, elle a su trouver les bons mots afin de m'encourager dans les périodes plus exigeantes et plus difficiles.

Introduction

Context

The fluid-structure interaction of an airfoil with its surrounding fluid is of great interest in the design process of several devices and structures. In the field of aeroelasticity, much effort has been directed towards a better understanding of flutter phenomena combined with the development of effective predictive techniques. Flutter is the result of a positive net exchange of energy from the fluid to the structure due to the negative aerodynamic damping that may arise. Sometimes, one is not interested in having an accurate prediction of the total energy transfered to the solid body, and only seeks an efficient way to determine whether the structure is stable or not. Various analytical tools have been developed for this specific task, and they have proven to be very successful at it. In other circumstances, an accurate prediction of this energy transfer is critical in order to avoid high-amplitude vibrations of a system, a situation that could cause structural fatigue or failure. In such cases, the solution is to keep the relative transfer of energy from the fluid to the structure as low as possible when compared to the damping capacity of the apparatus. Conversely, structures undergoing flutter, such as airfoils, could be conceived as devices to harvest energy from an incoming fluid, thus transforming the flapping airfoil into some sort of novel turbine. Unlike the previous case, one would want the positive flux of energy from the fluid to the structure to be maximized, and, at the same time, make sure the machine could resist to these high-amplitude, flow-induced oscillations over long terms.

Following the pioneering work of McKinney and DeLaurier (1980) in the field of flapping-wing turbines, significant research on the subject has been performed by several groups in the last decade with a general goal of optimizing the concept. The increasing amount of publications on this matter is indicative of the rapidly growing interest towards the concept, which is justified by several advantages over the more conventional flow harvesters (see Xiao and Zhu (2014)). To state only a few of them, these bio-inspired turbines are not subject to the high centrifugal stresses associated to the rotating blades found in most turbines. This makes the oscillating-foils devices structurally robust. Further, the oscillating foils sweep a rectangular flow window, which can be relatively wide and shallow. This is particularly interesting for the purpose of harvesting rivers, especially those that are not very deep.

The promising potential of flapping foils as wind or hydrokinetic turbines has been confirmed both numerically (see Kinsey and Dumas (2006, 2008, 2012a,b,c, 2014)) and experimentally (see Kinsey et al. (2011)) by the *Laboratoire de Mécanique des Fluides Numérique* (LMFN) at Laval University over the past decade. Several other groups also confirmed its potential, and the reader may refer to a recent review paper by Young et al. (2014) for an overview of the various concepts suggested and studied. Another recent review paper by Xiao and Zhu (2014) draws a clear portrait of the current state-of-the art, and the main findings of several studies are gathered within this publication. In several of the concepts suggested, the rigid wing is mounted on a clever mechanical system in which the cyclic shape of the motion and the relation (phase lag) between the pitching, which is the angular motion, and the heaving, which is the translational motion, were enforced in such a way as to significantly increase the efficiency of the turbine, and the total energy it harvests from the flow (see Kinsey et al. (2011)). Among these systems, some involved a well-designed mechanical coupling between both motions, and this reduced the device to a single degree-of-freedom mechanism. Whether it has one or two degrees-of-freedom, optimization of the energy harvester has typically been achieved through a direct implicit or explicit control on the shape, frequency and phase lag of the airfoil's motions in pitch and in heave. Energy harvesting efficiencies as high as 43% have been reported by Kinsey and Dumas (2014). Nevertheless, the mechanical components required to achieve this implicit or explicit control may add some mechanical complexity to the device, and this, in turns, may impair its mechanical efficiency, which should not be confused with the energy harvesting efficiency. A concept not making use of such a mechanical coupling could therefore be greatly beneficial.

Recently, some research groups reported promising results concerning a simplified, semi-passive version of the flapping-foil flow harvester. In these semi-passive systems, the pitching motion of the foil is prescribed while the heave results naturally through the interaction of the foil with the flow and the supporting mechanism (see Shimizu et al. (2008); Zhu et al. (2009) and Zhu and Peng (2009)). Energy harvesting efficiencies as high as 25% have been reported following numerical studies, thus confirming the interesting potential of this simplified mechanism. An experimental study has also been conducted on such a semi-passive device in a water tunnel, and efficiencies around 24% have been reported by Huxham et al. (2012).

According to Zhu et al. (2009) and to Kinsey and Dumas (2008), flapping-airfoil devices essentially harvest the flow through the heaving motion. This means that the pitching motion produces or incurs only modest input or output of energy in the mean, which suggests the concept of a further simplified, fully-passive system (see Zhu (2011)). This idea that the pitching motion could be fully autonomous in an energetic sense has been experimentally (see Poirel et al. (2008)) and numerically (see Lapointe and Dumas (2011)) validated by observing self-sustained, pitching-only motion of a wing at transitional Reynolds numbers.

In a simplified fully-passive system, both the heaving and the pitching motions are entirely determined through the fluid-structure interaction between the foil, the flow and the elastic supports. Large-amplitude, self-sustained oscillations have been experimentally observed for such a system (see Dimitriadis and Li (2009); Mendes et al. (2011); Poirel and Mendes (2011) and Razak et al. (2011)). The relatively new idea of using a fully-passive system to harvest energy from a flow offers significant mechanical advantages over the preceding mechanisms at the cost of having no direct control over the motion of the foil. For a foil mounted on a rotational spring and a linear damper undergoing large-amplitude, cyclic oscillations, Peng and Zhu (2009) reported energy harvesting efficiencies up to 20%. Although the 2D numerical study was conducted at fairly low Reynolds number (Re = 1,000), it revealed the potential of this new kind of turbine, and further optimization of this passive system is probably at reach. However, as mentioned by the authors of the aforementioned paper, the response of the airfoil to the flow excitation might be significantly different for high Reynolds numbers that are more representative of real turbine applications, and this remains to be investigated.

The optimization of the fully-passive, flapping airfoil must be achieved by adjusting parameters of the apparatus having only an indirect effect on the motion of the foil, thus implying that a thorough understanding of the physical mechanisms through which each parameter influences the motion is critical. Note here that for the purpose of turbine applications, only cases for which limit-cycle oscillations (LCO) emerge are of interest. For such cases, the wing oscillates in a nonchaotic way with a single frequency for both motions (pitching and heaving), and the amplitudes of motion are relatively constant. This well-behaved motion of the airfoil, as explained later, is possible due to the nonlinearity of the aerodynamic forces, which is associated to the periodic dynamic stalling of the streamlined solid body (see Dowell et al. (2005)).

Before moving on to the objectives of this work, the reader should note that there remains some confusion in the literature on what a fully-passive, flapping-airfoil turbine really is. This is because some research groups consider that a device is fully-passive as soon as the motion is induced by the flow. Nevertheless, this is not strictly correct. This is because some devices make use of a mechanical linkage between both degrees-of-freedom, thus imposing some constraints on the motion of the foils. However, actuators are not necessarily used in such cases, which means that the oscillations are entirely flow-induced. Indeed, categorizing such devices as being fully-passive would certainly be misleading. In this work, the adjective *fully-passive* is exclusively reserved for devices where no actuators are present, and no mechanical linkage or coupling between both degrees-of-freedom are used. The reader should refer to Kinsey and Dumas (2014) for a clarification on the terminology to be adopted.

Objectives and structure

In this context of using a fully-passive, flapping airfoil as a wind or hydrokinetic turbine, Lapointe (2012), a former student from the author's group, initiated a numerical study dealing with transitional flows. The current master's thesis is a continuation of this interesting work, and the specific objectives are :

- To introduce some theoretical concepts pertaining to the field of aeroelasticity.
- To formally introduce the aeroelastic problem along with its modeling.
- To introduce the fluid-structure interaction (FSI) solver used for the task of predicting the LCO of an elastically-mounted, rigid airfoil at high Reynolds numbers ($\mathrm{Re} = 500{,}000$).
- To optimize the fully-passive, flapping-airfoil turbine through a vast numerical campaign, and suggest an optimal and realistic case that appears well-suited for the purpose of efficiently harvesting energy from a flow.
- To perform a sensitivity study of the device in order to determine the effect of each key parameter on the performances of the turbine at harvesting a flow, and to gain physical insight into the mechanisms at play.

In order to fulfill these objectives, the master's thesis is organized as follows. Chapter 1 includes a presentation of a non-passive, kinematically-constrained, flapping-airfoil turbine which has been developed and studied at the LMFN. Because the main underlying objective of this study is to simplify this device by getting rid of the mechanical linkage between both degrees-of-freedom, it is important to introduce this apparatus. Further, a fully-passive, flapping airfoil experimentally studied at the Royal Military College (RMC) is presented. The results from this experiment conducted in the transitional range of Reynolds numbers will reveal to be very useful for the task of validating the numerical solver of this study. Then, a discussion on classical flutter, stall flutter and limit-cycle oscillations is presented. There are several types of flutter, and a single structure may be subject to one or many of them. The physical processes involved depend on the type of flutter encountered, and, as a result, the means of affecting the level of energy transfered from the fluid to the structure may vary significantly. In addition, some flutter phenomena may lead to a well-behaved motion of fairly constant amplitude known as limit-cycle oscillations (LCO). This type of motion, and the physical characteristics associated to it, are also discussed.

Chapter 2 deals with the methodology used to solve the aeroelastic problem. Before introducing the computational methodology, the aeroelastic problem of the elastically-mounted airfoil is formally introduced and discussed. Then, the fluid-structure interaction (FSI) solver that has been implemented within the open-source CFD toolbox *OpenFOAM-2.1.x* is described, with some emphasis on the methodology used for coupling the structural and the fluid solvers. This reveals to be significant as there are inherent limitations pertaining to all types of fluid-structure coupling schemes, and this can limit the use of a specific solver.

Chapter 3 focuses on the validation of the FSI solver presented in Chapter 2. The first section aims at assessing the independence of the results from the numerics, as much as assessing its ability at accurately predicting the motion of a solid body which is elastically supported in a freestream flow. This is where the experiment from the RMC, which is discussed in Chapter 1, becomes relevant. These results allow a validation of the FSI solver, but they are also used to validate the choice of a specific turbulence model in the last section. To end, the vortex induced vibrations (VIV) of a round cylinder oscillating transversally to a flow are considered. This is a well-known benchmark case that is well documented in the literature (see Bearman (2011); Dimitriadis and Li (2009); Durgin et al. (1980); Leontini et al. (2006); Morissette (2009); Williamson and Govardhan (2004) and Yang et al. (2008)), thus making it well-suited for validating the current solver.

Chapter 4 is really at the heart of this thesis as it deals with the optimization of the fully-passive, flapping-airfoil turbine. The first part of this chapter is used to introduce a tool developed by the author in order to facilitate and speed-up the optimization process. Next, a more general presentation of the methodology used to optimize the device is presented. The results of the optimization process are then presented extensively, analyzed, and discussed. Further, a sensitivity study that has been carried about an optimal case is presented in order to assess the physical influence of each structural parameter of the apparatus, followed by a presentation of an oscillating-foil device where no structural springs are present.

Then, Chapter 5 discusses the feasibility of the concept. The effect of dry friction is considered, and the modeling of the generator is discussed. Next, the optimized case found in Chapter 4 is dimensionally scaled for an experiment in both air and water. This is to determine how easy or how difficult it would be to pursue the research on this device through experimental work, as this could be seriously considered following this study. The chapter ends with a brief opening on other numerical results that should be further investigated in the very near future.

To end, a conclusion that summarizes the main findings of this thesis is presented. Also, a discussion on the recommended steps to be achieved following this numerical study is presented. This is an opening on the remaining work, and it is provided as a guideline for those who would like to carry-on with the interesting research on fully-passive, flapping-airfoil turbines.

Chapter 1

Preliminary concepts

The purpose of this first chapter is essentially to review some literature of interest concerned with subjects that are key to the work presented in this master's thesis. In the first section, the extensive work performed at the *Laboratoire de Mécanique des Fluides Numérique* (LMFN) located at Laval University on a kinematically-constrained (i.e., non-passive), flapping-airfoil turbine is introduced. This brief review specifically focuses on a description of the device, along with pertinent numerical results concerning its efficiency at harvesting kinetic energy from a flow. The second section deals with the experimental work conducted at the Royal Military College (RMC) located in Kingston, Ontario, on a fully-passive, flapping-airfoil device. Although the objective of the work performed there was to develop a better comprehension of the physical mechanisms involved in the low-amplitude, self-sustained motion of an airfoil, some results have also been published concerning the large-amplitude motion of the elastically-mounted airfoil. These results prove to be very useful for the current study as the experiment has been performed with a device very similar to the one treated in this master's thesis. Last but not least, a section introduces the main theoretical concepts of flutter. To achieve this, the section is divided in three subsections where each one corresponds to a specific physical mechanism more or less involved in the aeroelastic problem of this thesis. They are respectively classical flutter, stall flutter and limit-cycle oscillations (LCO).

1.1 Kinematically-constrained turbine

A kinematically-constrained, flapping-airfoil turbine may consist of one or multiple tandem-mounted foils oscillating with a constrained motion in both pitch and heave. Notwithstanding this fact, the current review section is only concerned with the single-foil version of the device studied at the *Laboratoire de Mécanique des Fluides Numérique* (LMFN). For such an apparatus, the shape of both motions is constrained to be sinusoidal, and the phase lag between both degrees-of-freedom, namely pitch and heave, is enforced through a clever mechanical linkage. As a result of this coupling between both motions, the device, in fact, only has one degree-of-freedom. This turns out to be an efficient way to maximize the energy harvesting efficiency (η). As previously mentioned in the introduction of this thesis, the LMFN at Laval University has been conducting extensive numerical (see Kinsey and Dumas (2006, 2008, 2012a, 2014)) and experimental (see Kinsey et al. (2011)) research on this matter, and relatively high energy harvesting efficiencies (η) in the range of 43% have been reported.

Contrary to this kinematically-constrained device, the fully-passive, flapping-airfoil concepts of turbine, such as the one considered in this master's thesis, would certainly not make use of a mechanical linkage between both degrees-of-freedom. It is therefore impossible to *directly* enforce an efficient kinematics. If this was doable, the same efficient kinematics as the one used with the kinematically-constrained device could be used, and the problem would already be solved. Instead, this efficient kinematics must emerge by itself through the interaction of the foil with the flow and its elastic supports. Nevertheless, it appears conceivable to *indirectly* control the kinematics of the device through its numerous structural parameters to be introduced, and the ultimate objective would certainly be to achieve the same efficiencies as those obtained with the kinematically-constrained device. In these circumstances, the resulting fully-passive turbine would be significantly less complex, in a mechanical sense, and would still be as energetically efficient. Since the performances of the kinematically-constrained turbine are the ideal aiming point of the optimized, fully-passive turbine, it appears relevant, not to say inevitable, to acquaint the reader with the work performed at the LMFN on a kinematically-constrained device, along with some numerical results regarding its efficiency at harvesting energy from a flow.

To begin with, an extensive two-dimensional (2D) Unsteady Reynolds-Averaged Navier-Stokes (URANS) study has been performed by Kinsey and Dumas (2014) at a Reynolds number of 500,000. In this numerical study, the constrained motion of a rigid, symmetrical NACA 0015 airfoil is sinusoidal in both pitch and heave, and a phase lag (ϕ) of 90 ° between pitching and heaving is used. The pitching ($\theta(t)$) and the heaving ($y(t)$) motions can therefore be mathematically represented as:

$$\theta(t) \;=\; \theta_0 \sin(\gamma t) \;, \tag{1.1}$$

$$y(t) \;=\; y_0 \sin(\gamma t + \phi) \;, \tag{1.2}$$

where θ_0 and y_0 are the prescribed pitching and heaving amplitudes, and γ is the prescribed angular frequency of oscillation ($2\pi f$). With such a motion (see Figure 1.1), whenever the airfoil reaches an extrema in heave, the geometric angle θ is null. Further, the airfoil of chord length c is oscillating about a pivot (i.e., pitching axis) located one third of a chord length ($c/3$) behind its leading edge. A parametric study of such a device has been performed by varying the reduced frequency of oscillation ($f^* = fc/U_\infty$) and the amplitudes of motion (θ_0 and y_0). Following this fairly large numerical campaign, a mapping of efficiency (Figure 1.2) has been

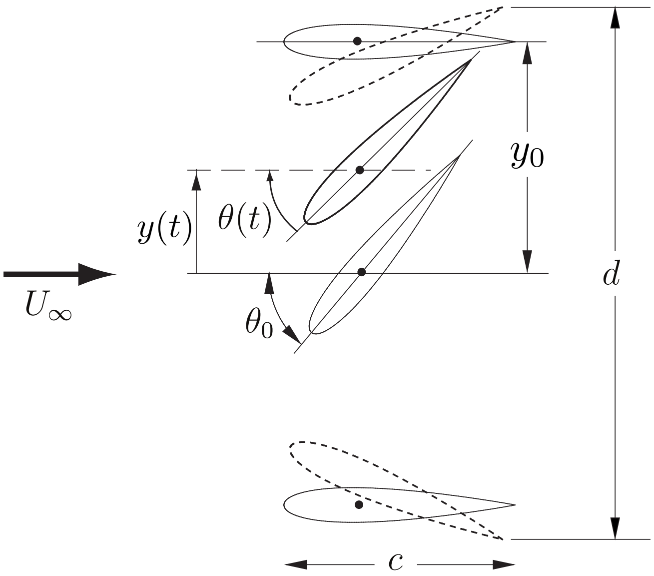

Figure 1.1: Schematic of the kinematically-constrained turbine's motion with key variables used to characterize this motion. Adapted from Kinsey et al. (2011).

produced for both the energy harvesting efficiency (η) and the cycle-averaged power coefficient ($\overline{C}_P{}^*$). Before going any further, these two parameters used to quantify the performances of the device shall be defined. First, the energy harvesting efficiency:

$$\eta = \frac{1}{T}\int_0^T \frac{P}{\frac{1}{2}\rho U_\infty^3 bd}\, dt \ , \tag{1.3}$$

where P is the instantaneous power harvested from the flow, d is the overall vertical displacement of the airfoil, T is the period of oscillation ($T = 1/f$), and b is the span of the airfoil. By considering Figure 1.1, one can convince oneself that the maximum displacement of the airfoil (d), also known as the flow window, is not necessarily equal to twice the heaving amplitude ($2y_0$). Indeed, the heaving amplitude (y_0) corresponds to the vertical displacement of the pivot (i.e., pitching axis), while the flow window (d) per unit span corresponds to the difference between the highest and the lowest heights reached by any point on the foil. Further, the instantaneous power harvested from the flow can be decomposed into the sum of a heaving and a pitching contribution:

$$P = \underbrace{\mathcal{L}\dot{y}}_{\text{heaving}} + \underbrace{M_{ea}\dot{\theta}}_{\text{pitching}} \ , \tag{1.4}$$

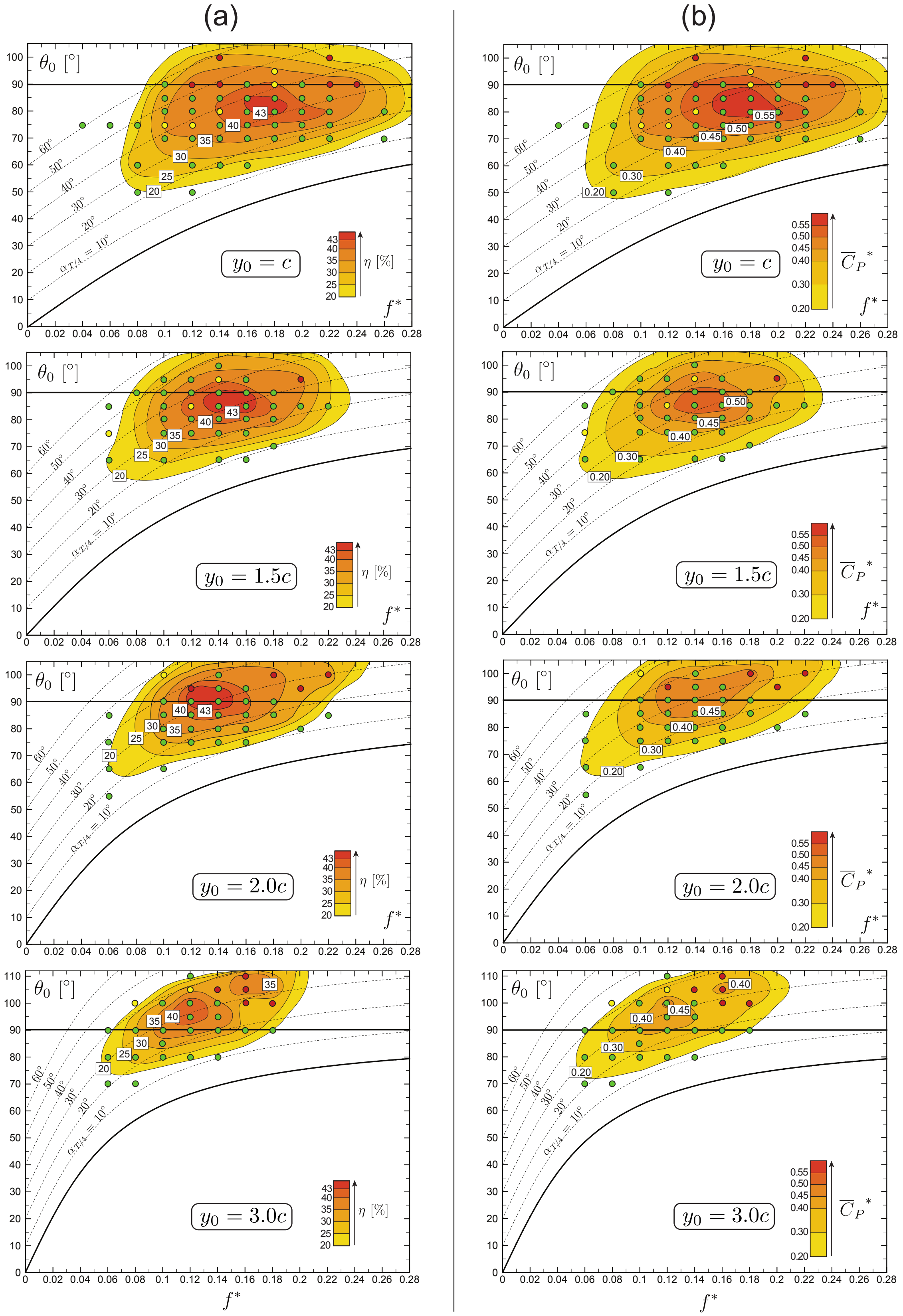

Figure 1.2: Mapping of the energy harvesting efficiency η (a), and the cycle-averaged power coefficient $\overline{C}_P^*$ (b) of the kinematically-constrained, flapping-airfoil turbine for various amplitudes of motion in pitch (θ_0) and in heave (y_0), and for various reduced frequencies (f^*). Values predicted through 2D URANS simulations. Adapted from Kinsey and Dumas (2014).

where $\mathcal{L}$ is the lift (i.e., vertical force), M_{ea} is the moment about the pitching axis, $\dot{y}$ is the heaving velocity, and $\dot{\theta}$ is the pitching rate. However, the contribution from the pitching motion is found to be essentially null in the mean with the extraction of energy being mainly done through the heaving motion (see Kinsey and Dumas (2008)). Physically, the efficiency η corresponds to the cycle-averaged power harvested by the turbine over the total power available through the flow window. This is an aerodynamic efficiency that does not account for the possible mechanical losses, and there exists a well-known theoretical limit to this efficiency. It is known as the Betz's limit, and that takes a value of 59.3% for a single-foil device. This theoretical limit has been obtained through the inviscid analysis of an actuator disk positioned in a stream tube, and it has first been presented by Betz and Prandtl (1919).

Second, the cycle-averaged power coefficient $\overline{C}_P{}^*$ is defined as:

$$\overline{C}_P{}^* = \frac{1}{T}\int_0^T \frac{P}{\frac{1}{2}\,\rho\,U_\infty^3\,2\,y_0 b}\,dt\ . \tag{1.5}$$

This time, the cycle-averaged power harvested from the flow is normalized with the power available in a flow window of height equal to twice the vertical displacement of the pitching axis ($2y_0$). It is also possible to define another cycle-averaged power coefficient $\overline{C}_P$ which allows an even easier, more direct comparison between cases showing different heaving amplitudes. It is defined as:

$$\overline{C}_P = \frac{1}{T}\int_0^T \frac{P}{\frac{1}{2}\,\rho\,U_\infty^3\,bc}\,dt\ . \tag{1.6}$$

Computed this way, $\overline{C}_P$ is a measure of the cycle-averaged power harvested from the flow normalized with the power available through a flow window of height equal to one chord length. As a result, all cases sharing the same chord length are normalized with the same unique value of power, independently of their amplitude of motion. This makes the comparison of cases exhibiting different amplitudes of motion very straightforward. It is worth mentioning that η and $\overline{C}_P$ turn out to be useful metrics used throughout this master's thesis, and the reader should make sure to fully understand their physical meaning.

Returning to the results of Kinsey and Dumas (2014) shown in Figure 1.2, the reader may observe that a measure of $\overline{C}_P$ is not readily available. In fact, it can be obtained by simply multiplying the value of $\overline{C}_P{}^*$ by $2y_0/c$. Figure 1.2 reveals that a maximum energy harvesting efficiency (η) of approximately 43% has been predicted through 2D simulations. Such a high efficiency, when compared to the Betz's limit of 59.3%, has been predicted for an airfoil flapping at a reduced frequency (f^*) of 0.18 with a pitching amplitude (θ_0) of 80° and with a normalized heaving amplitude (y_0/c) of 1. The corresponding value of $\overline{C}_P{}^*$ is slightly over 0.55, which translates into $\overline{C}_P = 1.13$. These 2D numerical results are considered to be representative of the optimal performances of the kinematically-constrained, flapping-airfoil turbine throughout the current thesis, and they will later be used to compare and qualify the predicted performances of the fully-passive, flapping-airfoil turbine.

Numerical three-dimensional (3D) URANS simulations have also been performed at the LMFN (see Kinsey and Dumas (2012a)), along with an experimental study (see Kinsey et al. (2011)) of the kinematically-constrained turbine. The 2D, 3D and experimental results have been compared altogether by Kinsey and Dumas (2012a), and they are here reproduced in Figure 1.3. Although the 3D simulations have predicted a lower efficiency (maximum η of 33%) compared to what has been predicted through 2D simulations (maximum η of 43%), both trends agree fairly well. This provides a strong, valuable argument in favor of conducting a 2D numerical study of the flapping-airfoil turbine. This, of course, turns out to be far less computationally demanding than its 3D counterpart. Indeed, the results suggest that a 2D numerical study can first be performed, followed by only a few 3D computationally demanding simulations to refine the numerical predictions. For this reason, the same strategy is to be used in the current study. Lastly, it is observed that 3D simulations agree very well with the experimentally measured efficiencies not only in the trends, but also in numerical values (maximum η of 30%). This provides great confidence in the numerical methodology used at the LMFN. Also, due to the great similarities between the problem previously considered at the LMFN and the current aeroelastic problem, it provides assurance that this methodology can safely be applied in the current study.

Partial conclusion

To summarize, the kinematically-constrained device has proven to be a relatively efficient way of harvesting energy from an incoming flow with energy harvesting efficiencies ranging from 30% to 43%. Such efficiencies are considerably high when compared to the Betz's limit of 59.3%. Some complexity still resides in the presence of a mechanical linkage between both degrees-of-freedom. The mechanical components required to constrain the motion could increase the production cost and the maintenance cost of the device, and it could impair its mechanical efficiency. For these reasons, a fully-passive, flapping-airfoil turbine, even if it had an energy harvesting efficiency slightly lower than what has been obtained with the kinematically-constrained device, would most probably have significant mechanical and financial advantages over the non-passive system. Further, the 2D and 3D URANS modeling used at the LMFN for the extensive numerical study proved to be adequate for the task of predicting the aerodynamic forces on an foil oscillating in a freestream flow.

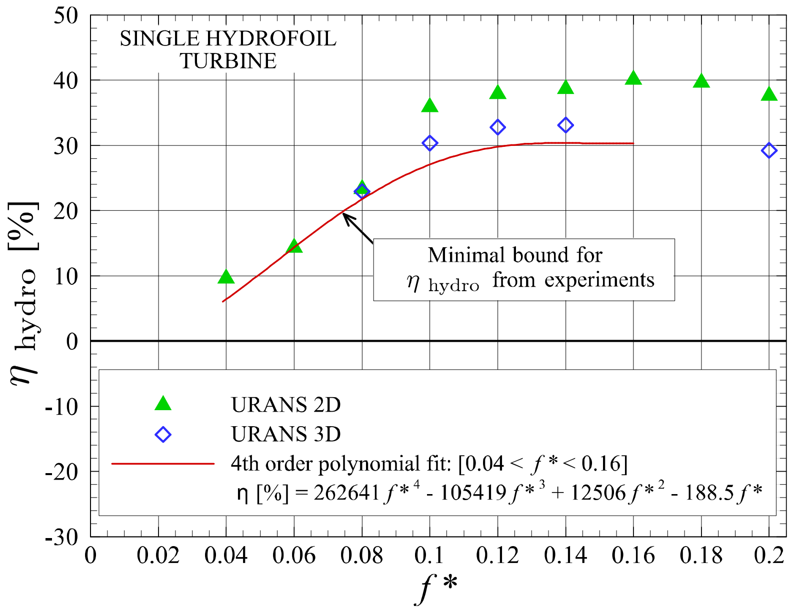

Figure 1.3: Comparison of the energy harvesting efficiencies η predicted through 2D and 3D URANS simulations, along with the experimentally measured efficiency. Reproduced from Kinsey and Dumas (2012a) with permission.

1.2 Fully-passive device - experimental

A research group at the Royal Military College (RMC) located in Kingston, Ontario, conducted an experimental study on an airfoil that was elastically-mounted in both pitch and heave as depicted in Figure 1.4. The study was conducted in a closed-circuit wind tunnel in the transitional range of Reynolds number (Re = [50,000 to 120,000]) (see Mendes et al. (2011) and Poirel and Mendes (2011)). Although this remains far from the range of Reynolds numbers representative of a turbine application, these results turn out to be very useful for the purpose of validating the fluid-structure interaction (FSI) solver which has yet to be introduced. It should be mentioned that both low-amplitude and high-amplitude oscillations of the airfoil have been observed in this experiment. However, the research conducted at the RMC did not focus on a turbine application of the flapping foil, nor on the large-amplitude oscillations that were observed. The study was rather concerned with the small-amplitude oscillations caused by a laminar separation bubble (LSB), and aimed at investigating the physics at play. Because it was not a consideration in the experiment, no energy harvesting efficiencies or power coefficients are available in the literature for this specific setup. Nonetheless, the main features of the motion (i.e., the amplitudes of motion in pitch and in heave and the frequency of oscillation) are available (see Mendes et al. (2011) and Poirel and Mendes (2011)), and this constitutes enough information to validate the FSI numerical solver. The reader may also refer to Chapter 4 of this document for an overview of the efficiencies associated to the large-amplitude, aeroelastic oscillations of the RMC experiment. Indeed, it has

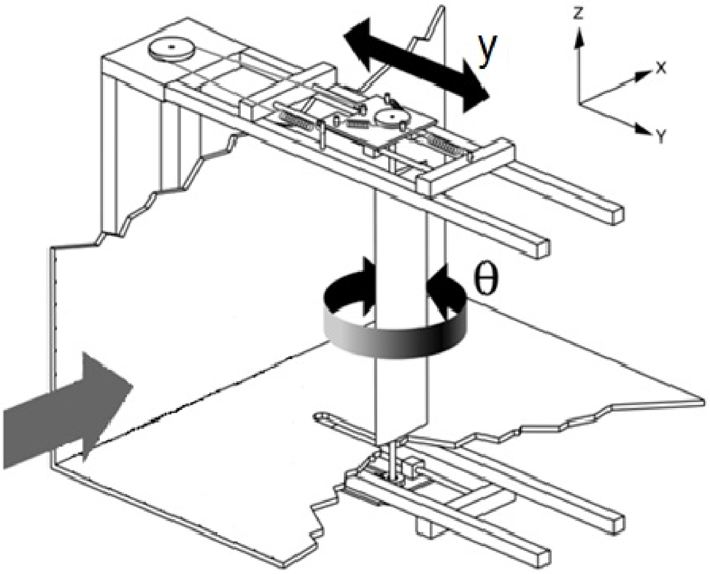

Figure 1.4: Schematic of the symmetrical, rigid, elastically-mounted airfoil used in the wind-tunnel experiment of the Royal Military College (RMC) in the transitional range of Reynolds numbers. Reproduced from Poirel et al. (2006).

been possible to use the FSI solver of the current master's thesis to predict the corresponding efficiencies. All that deserves to be mentioned for now is that the predicted efficiencies of the experimental device appear to be very modest ($\eta \approx 5\%$), and they do not compete at all with the high efficiencies achieved with the kinematically-constrained turbine ($\eta = 43\%$).

As mentioned earlier, the experiment has been conducted with the setup shown in Figure 1.4. Figure 1.5 is a simplified schematic of the elastically-mounted airfoil with symbolic representation of the key structural parameters. In the experiment, the elastically-mounted airfoil is free to pitch around the z-axis and heave along the y-axis. The motion is not possible in any other directions, nor about any other axis. The two degree-of-freedom system consists of a symmetrical, rigid NACA 0012 airfoil mounted on a pivot, referred to as the elastic axis, about which the pitching motion (θ) is possible. Further, the pivot is mounted on a sliding mechanism, thus allowing the heaving motion (y). There is absolutely no mechanical linkage between the pitching and the heaving motions: instantaneous aerodynamics as well as inertial effects are the only possible couplings. As a matter of fact, this apparatus falls into the category of fully-passive, oscillating wings, just as much as the aeroelastic problem considered in this master's thesis. This reveals to be one of the main reasons why the RMC experiment constitutes an adequate case for validating purposes. The various structural parameters involved in the experiment are the following:

- c, the chord length of the airfoil;
- k_h, the heave spring stiffness coefficient;
- k_θ, the pitch spring stiffness coefficient;
- D_h, the heave structural damping coefficient;
- D_θ, the pitch structural damping coefficient;
- I_θ, the moment of inertia about the elastic axis;
- x_{ea}, the distance between the leading edge and the elastic axis;
- x_θ, the distance between the center of mass of the pitching components and the elastic axis (positive when the center of mass is behind the elastic axis);
- m_p, the mass of all components involved in the pitching motion;
- m_h, the mass of all components involved in the heaving motion.

At first, the fact that two masses (m_p and m_h) are required to characterize the device might be striking and counterintuitive. One can convince oneself that such a discretization of the masses is indeed accurate by considering Figure 1.4. Clearly, the mass of the sliding mechanism is not involved with the pitching of the airfoil. Further, in most cases one combines the parameters x_θ and m_p to form what is known, in the field of aeroelasticity, as the static imbalance: $S = m_p x_\theta$. The rationale of this simplification shall become clear when the equations of motion of the fully-passive, oscillating airfoil will be worked out in Chapter 2.

Throughout the experimental study, several parameters have been held constant. Those are summarized in Table 1.1. The only structural parameter not held constant was the heave

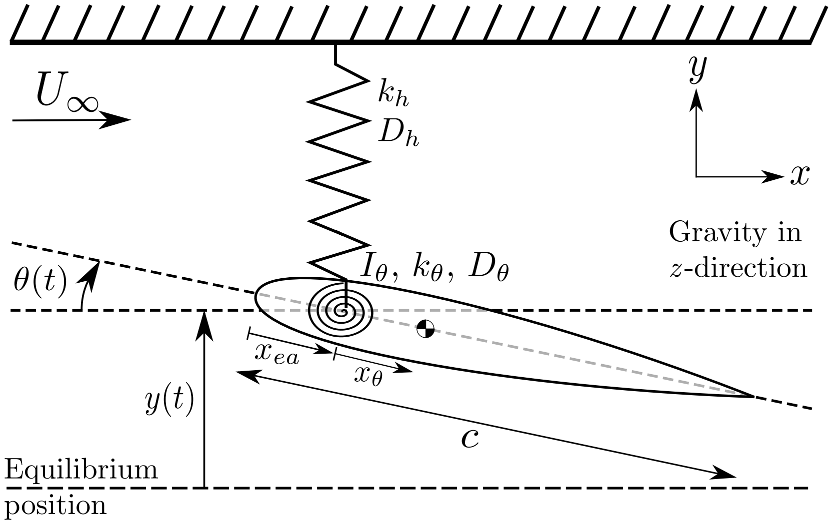

Figure 1.5: Simplified schematic of the symmetrical, rigid, elastically-mounted airfoil of the RMC wind tunnel experiment with symbolic representation of key parameters (not showing the sliding mechanism). Adapted from Lapointe and Dumas (2012).

Table 1.1: Constant parameters in the experiment of the fully-passive, elastically-mounted airfoil conducted at the Royal Military College (RMC) (see Mendes et al. (2011); Poirel (2012); Poirel et al. (2008) and Poirel and Mendes (2011)).

Parameter	Value
c	0.156 m
x_{ea}	0.186 c
x_θ	0.095 c
I_θ	0.00135 kg·m^2
k_θ	0.3 N·m/rad
D_θ	0.002 N·m·s/rad
m_h	2.5 kg
S	0.0114 kg· m

spring stiffness coefficient (k_h), which has been varied to take values of 800 N/m and 1484 N/m. Further, the only flow parameter that varied was the freestream velocity (U_∞), thus also changing the Reynolds number. The amplitudes of motion and the frequency recorded for the cases where large-amplitude oscillations have been observed are reported in Figure 1.6. It is an interesting fact that a single frequency is reported while the device has two degrees-of-freedom. This is because the heaving and the pitching frequencies coalesce together, giving rise to a single frequency for the entire system. As it can be observed, the amplitude of motion in pitch reaches values over 60°, and the amplitude of motion in heave reaches values over 0.4 chord length. For these reasons, the motion is qualified as being of large amplitude. Typically, small-amplitude oscillations are of only a few degrees in pitch, and only a few percent of the chord length in heave. Unfortunately, experimental values for the heaving amplitude are not available for the low heave stiffness case ($k_h = 800\ N/m$).

Table 1.1 does not provide any value for the heave structural damping coefficient (D_h). Instead, Figure 1.7 displays the heave damping ratio (ξ_h) as a function of the normalized heaving amplitude (y_0/c). The raw data of a few free decay tests of the elastically-mounted wing have been obtained from the RMC through a private communication (Poirel (2012)). A calculation of the instantaneous damping ratio has been performed by the author of this thesis using the logarithmic decrement method (see Thorby (2008)). Clearly, the damping ratio is not constant, thus indicating the presence of some nonlinearities in the structural damping of the device. According to Poirel and Mendes (2011), this is believed to be imputable to some misalignments of two sliding rods involved in the heaving motion. The linear representation of the pitch structural damping coefficient (D_θ), as it is pointed out by Poirel et al. (2008), is also questionable. Indeed, the dissipation of energy is primarily due to dry friction and spring compression. The nonlinear character of the damping will later reveal to be significant

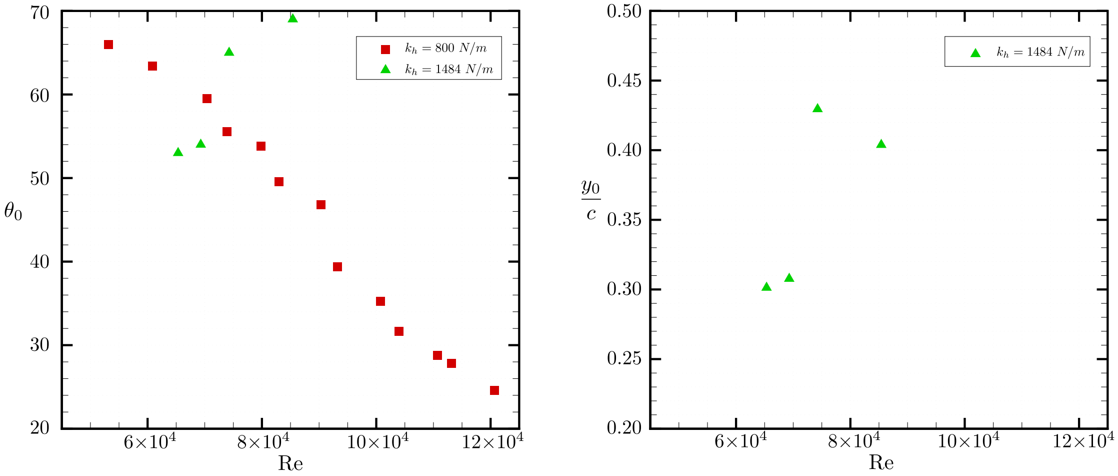

(a) Pitching amplitude.

(b) Normalized heaving amplitude.

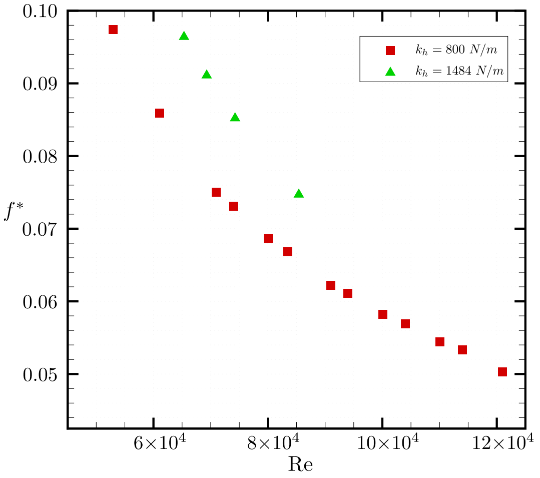

(c) Reduced frequency.

Figure 1.6: Amplitudes of motion (θ_0 and y_0/c) and reduced frequency (f^*) as a function of the Reynolds number (Re) for the fully-passive, elastically-mounted, oscillating airfoil experiment of the Royal Military College (see Mendes et al. (2011); Poirel (2012) and Poirel and Mendes (2011)). The Reynolds number has been varied by changing the freestream velocity (U_∞).

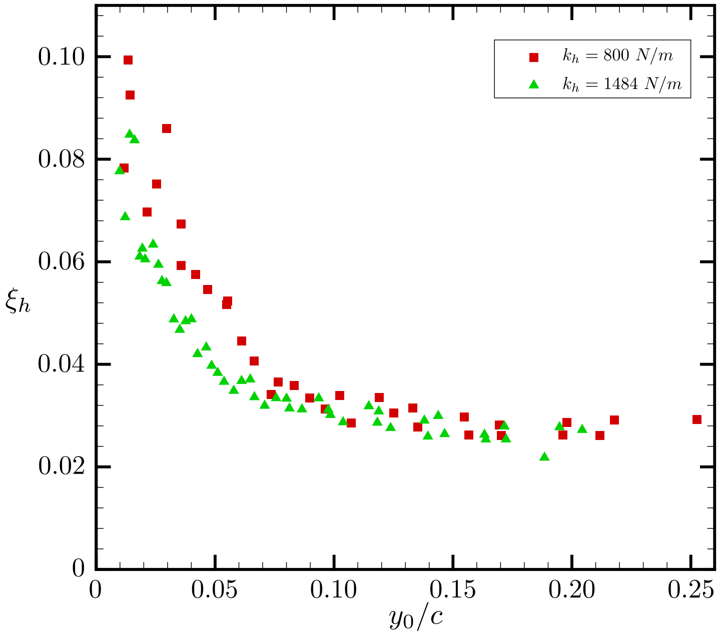

Figure 1.7: Heave damping ratio (ξ_h) of the elastically-mounted, oscillating airfoil used at the Royal Military College (RMC) as a function of the normalized, instantaneous amplitude of motion in heave (y_0/c). Raw data obtained from a private communication (Poirel (2012)). The damping ratios have been calculated with the logarithmic decrement method (see Thorby (2008)).

when the validation of the current FSI solver will be assessed. Even if some uncertainties remain concerning the structural damping of the device, these experimental results are still very useful for validating the numerical predictions obtained through CFD.

Partial conclusion

To summarize this section, the setup used to conduct the experimental study of an elastically-mounted airfoil has been introduced. The experiment of the RMC certainly did not focus on a turbine application of the device, but enough data is available in the literature as to make this experiment very useful for validating the FSI solver of this thesis due to the profound similarities between the aeroelastic problems considered. Nevertheless, some experimental uncertainties remain on the values and on the modeling of some parameters from the experiment. This will be revisited later in this thesis.

1.3 Physics of flutter

Several physical phenomena are of interest in the field of dynamic aeroelasticity. This section does not aim at providing a complete picture of all types of instabilities, but, instead, aims at introducing classical flutter, stall flutter and limit-cycle oscillations (LCO). These aeroelastic phenomena reveal to be significant for the fully-passive, flapping-airfoil turbine problem, and this is the reason why they are here introduced. The reader is referred to Dowell et al. (2005) and Fung (2008) for a complete, comprehensive discussion on flutter. Unless otherwise indicated, these two texts constitute the main references for this section.

1.3.1 Classical flutter

Classical flutter[1] is a type of dynamic instability to which some structures are prone. When this is the case, the amplitude of motion may drastically grow following an external perturbation of some kind. In the case of a streamlined body, such as a wing, this external perturbation could be any symmetry-breaking mechanism: turbulence, atmospheric wind gust, deflection of a control surface, etc. The loss of stability is explained with the concept of negative aerodynamic damping. As the freestream velocity (U_∞) of the flow to which the airfoil is exposed increases, the aerodynamic damping first increases. In other words, the motion induced by an external perturbation is damped (i.e., the kinetic and the potential energy is transfered from the structure to the flow). Further increasing the freestream velocity (U_∞) may result in a rapid decrease of the aerodynamic damping. At the critical flutter velocity (U_{cr}), the aerodynamic damping becomes null, and any further increase of the freestream velocity (U_∞) leads to a negative aerodynamic damping. As a result, when this critical velocity is passed and the airfoil is disturbed from its equilibrium position through a perturbation of any amplitude, the aerodynamic forces are such that the motion is not damped. Instead, the opposite happens, and the flow provides energy to the structure, resulting in some possibly violent, exponentially-growing oscillations. Structural failure is very often the outcome to such an event, which strongly suggests that the typical objective of an aeroelastic study is to avoid such detrimental instabilities.

The use of the term *classical flutter* is normally restricted to an oscillatory instability observed in a potential flow (this assumes the flow to be irrotational and thus inviscid). This implies that nonlinearities are absent from the flow (i.e., neither separations nor shocks are present) or, at least, are not involved in the physical mechanisms through which the instability occurs. Although one-degree-of-freedom, classical flutter has been observed, the linear dynamic instability is generally the result of a well-defined coupling between the various degrees-of-freedom of the structure, with the phase shift between motions being a key parameter.

---

[1] In the literature, classical flutter is often simply referred to as flutter.

In order to understand better classical flutter, it is very useful to consider a simplified aeroelastic problem. For this purpose, a steady flow aerodynamic model along with a typical section model are used. The typical section consists of a rigid, streamlined body mounted on a spring in heave, and on a torsional spring in pitch. This setup is identical to that of Figure 1.5, except that no structural damping is present, and the streamlined body may be of a different shape. The equations of the linear, steady flow aerodynamic modeling are:

$$\mathcal{L} = qbc\frac{\partial C_{\mathcal{L}}}{\partial \theta}\theta \ , \tag{1.7}$$

$$M_{ea} = e\mathcal{L} \ . \tag{1.8}$$

The nomenclature used here is consistent with the previously introduced symbols. The lift slope ($\partial C_{\mathcal{L}}/\partial\theta$) of the airfoil is often assumed to be 2π rad^{-1} according to the thin airfoil theory. Further, e is the distance between the aerodynamic center and the elastic axis (positive when the aerodynamic center is aft of the elastic axis), and q is the dynamic pressure ($\frac{1}{2}\rho U_{\infty}^2$) associated to the undisturbed incoming flow. Assuming an angular motion of small amplitude ($\theta \ll 1$), the linearized equations of motion are:

$$m_h\ddot{y} + S\ddot{\theta} + k_h y + qbc\frac{\partial C_{\mathcal{L}}}{\partial\theta}\theta = 0 \ , \tag{1.9}$$

$$I_\theta\ddot{\theta} + S\ddot{y} + k_\theta\theta - e\left(qbc\frac{\partial C_{\mathcal{L}}}{\partial\theta}\theta\right) = 0 \ . \tag{1.10}$$

The objective here is to investigate the stability of the system, and thus to understand better the fundamentals of classical flutter. The stability analysis can be achieved by assuming solutions of the following form:

$$y = \overline{y}e^{pt} \ , \tag{1.11}$$

$$\theta = \overline{\theta}e^{pt} \ . \tag{1.12}$$

The mathematical problem turns out to be one of finding the values of p, which can indeed be complex. If the real part of p is positive, the amplitude of motion grows exponentially with time, and the device is said to be unstable (i.e., flutter occurs). In order to find the values of p, the problem may be conveniently rearranged in matrix form:

$$\begin{bmatrix} m_h p^2 + k_h & Sp^2 + qbc\frac{\partial C_{\mathcal{L}}}{\partial\theta} \\ Sp^2 & I_\theta p^2 + k_\theta - e\left(qbc\frac{\partial C_{\mathcal{L}}}{\partial\theta}\right) \end{bmatrix} \begin{bmatrix} \overline{y}e^{pt} \\ \overline{\theta}e^{pt} \end{bmatrix} = \begin{bmatrix} 0 \\ 0 \end{bmatrix} \tag{1.13}$$

Nontrivial solutions exist only and only if the determinant of the coefficient matrix is null. This condition leads to the following equation:

$$Ap^4 \ + \ Bp^2 \ + \ C \ = \ 0 \ , \tag{1.14}$$

where

$$A \ \equiv \ m_h I_\theta \ - \ S^2 \ , \tag{1.15}$$

$$B \ \equiv \ m_h \left[k_\theta \ - \ e \left(qbc \frac{\partial C_{\mathcal{L}}}{\partial \theta} \right) \right] \ + \ k_h I_\theta \ - \ S \left(qbc \frac{\partial C_{\mathcal{L}}}{\partial \theta} \right) \ , \tag{1.16}$$

$$C \ \equiv \ k_h \left[k_\theta \ - \ e \left(qbc \frac{\partial C_{\mathcal{L}}}{\partial \theta} \right) \right] \ . \tag{1.17}$$

Solving for p yields:

$$p \ = \ \sqrt{\frac{-B \ \pm \ \left[B^2 \ - \ 4AC \right]^{1/2}}{2A}} \ . \tag{1.18}$$

For any mass distribution, A must be positive in order to be representative of a physical reality. Further, C is positive when the dynamic pressure q is less than its physical divergence value:

$$q_{div} \ = \ \frac{k_\theta}{ebc \frac{\partial C_{\mathcal{L}}}{\partial \theta}} \ . \tag{1.19}$$

The phenomenon of divergence is a *static* instability which happens when the torsional restoring moment is not sufficiently large to counteract the aerodynamic moment exerted by the flow on the structure. This is mathematically expressed as:

$$k_\theta \ - \ e \left(q_{div} bc \frac{\partial C_{\mathcal{L}}}{\partial \theta} \right) \ = \ 0 \ . \tag{1.20}$$

When such a situation occurs, the initial response of the body is not to undergo an oscillatory motion. Instead it strictly diverges from its equilibrium position. For this reason, divergence is sometimes referred to as a form of flutter with null frequency. Structural failure is generally the outcome to such an instability. More details on this matter can be found in Dowell et al. (2005).

Coming back to the current analysis of classical flutter, C must therefore remain positive: the dynamic pressure must be such that the solid did not reach divergence *yet*. As a result, only four cases have to be considered in order to analyze the stability of the typical section:

$$\begin{array}{ll}\textbf{I} & B > 0 \text{ and } B^2 - 4AC > 0 \\ \textbf{II} & B > 0 \text{ and } B^2 - 4AC < 0 \\ \textbf{III} & B < 0 \text{ and } B^2 - 4AC > 0 \\ \textbf{IV} & B < 0 \text{ and } B^2 - 4AC < 0 \end{array}$$

In the first case (**I**), the values of p are purely imaginary, a situation associated to a neutrally stable system. For the second case (**II**), at least one solution of p has a positive real part. This indicates that the solid body is dynamically unstable, and flutter may occur following an external disturbance. As a result, ($B^2 - 4AC = 0$) provides what is known as the flutter boundary.

A deeper analysis of this criterion reveals that the static imbalance (S) must be positive or null for flutter to occur. Conceptually, this indicates that the center of gravity of the solid body must either be positioned behind the elastic axis or coincide with the elastic axis for the structure to be dynamically unstable. Further, as S increases, the dynamic pressure (q_{cr}) at which flutter first appears decreases. In other words, as the center of gravity of the solid is moved farther behind the elastic axis, the critical flutter velocity (U_{cr}) is reduced. This is a very interesting property of flutter indicating that the mass distribution of a solid body plays a key role from an aeroelastic point of view. Very often, structures which are prone to flutter are mass balanced as a way to avoid the dynamic instability within the typical operational range of the device. To achieve this, the center of gravity is moved as close as required to the leading edge[2]. For the third (**III**) and fourth (**IV**) cases, the condition ($B < 0$) is only encountered for relatively high values of the dynamic pressure (q). In practice, the flutter boundary ($B^2 - 4AC = 0$) is crossed before the value of B becomes negative. Therefore, the two last cases are not relevant as they do not bring new information concerning the onset of flutter.

The second case (**II**) can further be analyzed, and it can provide more information concerning the onset of flutter. If the elastic axis coincides with the center of mass ($x_\theta = 0$), the onset of flutter can be predicted solely by considering the relative position (e) of the aerodynamic center in comparison to the position of the elastic axis, and the ratio of the decoupled natural frequency in heave $\left(\omega_h = \sqrt{k_h/m_h}\right)$ over the decoupled natural frequency in pitch $\left(\omega_\theta = \sqrt{k_\theta/I_\theta}\right)$. Flutter will *not occur* if the following conditions are met:

- the aerodynamic center is ahead of the elastic axis ($e > 0$) and $\omega_h/\omega_\theta > 1$;
- the aerodynamic center is behind the elastic axis ($e < 0$) and $\omega_h/\omega_\theta < 1$.

Lastly, if the elastic axis is very close to the center of gravity, but they do not necessarily coincide, a simplification is possible and it is observed that flutter will *not occur* for small

---

[2] Such a structure is said to be mass balanced.

ratios of ω_h/ω_θ if $(-e - x_\theta) > 0$. Conversely, if ω_h/ω_θ is large, flutter will not occur if $(e - x_\theta) > 0$.

From this linear stability analysis, it appears that the mass distribution is not the only significant parameter to determine if an airfoil is linearly dynamically stable or not. Indeed, the relative positions of the elastic axis, of the aerodynamic center, and of the center of mass are of great influence. Further, the ratio of the natural frequencies is very significant, and this will be made clear in the following paragraphs. Following this linear stability analysis, the theoretical influence of several structural parameters has been highlighted, thus providing some knowledge on how to control the onset of flutter via an adequate design of the aeroelastic device.

In order to refine the previous analysis and learn more information from a physical point of view, a quasi-steady or an unsteady potential theory can be used in lieu of a steady theory for the aerodynamic modeling[3]. When this is done, the analysis becomes more convoluted, and numerical, iterative solutions are generally used. The explanation to this increased level of difficulty resides in the complexity of the chosen potential aerodynamic modeling. However, the values for p are found using the same idea as before: one establishes the system of equation in matrix form and seeks a solution by setting the determinant of the matrix of coefficients equal to zero.

Figure 1.8 shows a typical plot of the real (Re) and the imaginary (Im) components of the complex frequency p as a function of the freestream velocity (U_∞). Each root of p corresponds to a different mode (i.e., degree-of-freedom), and the imaginary component of p is, in fact, the frequency of the mode, while the negative of the real component of p represents the aerodynamic damping associated to the mode. As it may be observed in the gray area labeled **FLUTTER**, flutter occurs when one of the modes reaches a negative value for the aerodynamic damping. It is also clear that the frequency of oscillation of both modes tend to merge as the critical flutter velocity is approached. For this reason, this type of flutter is often referred to as coalescence flutter or merging flutter. Recalling the results from Poirel *et al.* introduced previously, this explains why the two-degree-of-freedom aeroelastic device only had a single frequency of oscillation. Indeed, it has been found that this specific device was prone to classical flutter (see Poirel and Mendes (2011)).

There are several other subtypes of flutter that could fit into the family of classical flutter, with some of them having a single degree-of-freedom. In all cases, flutter occurs when the aerodynamic damping of a mode becomes large and negative, and a complete description of all the possible mechanisms through which this might happen is out of the scope of this text. Generally speaking, coalescence flutter is the most common type of dynamic instability encountered on wings. Following this physical introduction, the following items briefly summarize what has been mentioned:

---

[3] The reader may refer to Kinsey (2011) for a concise summary of these aerodynamic models.

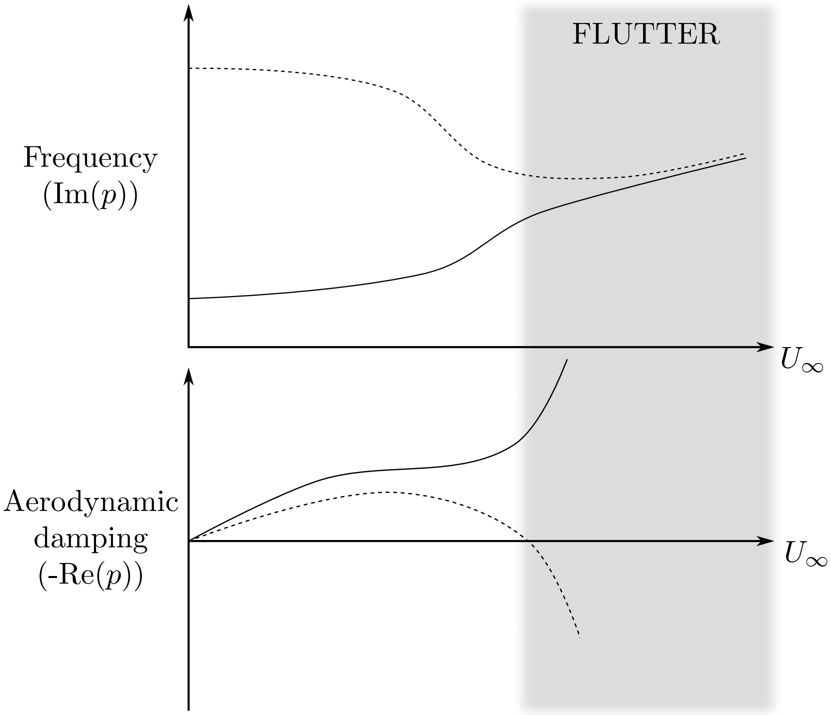

Figure 1.8: Typical frequency (imaginary (Im) component of p) and aerodynamic damping (opposite of the real (Re) component of p) as a function of the freestream velocity (U_∞). The solid and the dashed curves correspond to the first and the second modes of a two-degree-of-freedom flapping-airfoil system.

- The static imbalance (S) is a critical parameter. If the center of gravity is ahead of the elastic axis, no flutter is predicted through a linear stability analysis.
- The ratio of natural frequencies (ω_h/ω_θ) has a large impact on the onset of flutter. As previously described, a merging of the modal frequencies is inherent to coalescence flutter. If the ratio of natural frequencies is close to one, this merging of frequencies happens faster, and flutter occurs at a lower critical velocity.
- Increasing the torsional stiffness (k_θ) generally prevents coalescence flutter from occurring.
- Increasing the structural damping (D_θ and D_h) helps preventing or delaying the onset of flutter, and this is not only true for coalescence flutter. This holds true for various types of dynamic instabilities.

1.3.2 Stall flutter

Stall flutter, as explicitly revealed by its name, involves separations of the flow from the streamlined body undergoing flutter. These separations of the flow may either be complete or partial, and, unlike classical flutter, stall flutter may reveal not to be catastrophic. In fact, due to the presence of aerodynamic nonlinearities, the outcome is very often a cyclic motion of limited amplitude (see Arena et al. (2013); Dimitriadis and Li (2009) and Razak et al. (2011)). This phenomenon is known as limit-cycle oscillations (LCO), and this will be the subject of the next subsection. Even if the amplitude of motion usually stabilizes itself before structural failure occurs, the large-amplitude, cyclic motion may sometimes result in a significant impairment of the service life of the device due to fatigue (see Arena et al. (2013)). For this reason, it is generally better to avoid stall flutter over the complete operational range of a device, or, at least, to drastically limit the amplitude of motion resulting from it.

The physical mechanisms involved in stall flutter greatly differ from those observed in classical flutter. This time, the transfer of energy from the flow to the structure is not the result of an elastic or an aerodynamic coupling between the degrees-of-freedom involved, and the phase lag between the motions is not a parameter of importance. It must be understood that some level of coupling between the various degrees-of-freedom, along with a lag between the motions, may be present and alter the dynamics, but they are not essential features of stall flutter. In fact, stall flutter is possible as a result of the nonlinear behavior of the aerodynamic forces on the body, and these nonlinearities are the result of separations occurring in the flow (see Arena et al. (2013); Dimitriadis and Li (2009) and Razak et al. (2011)).

It is well known that separations occur when an airfoil is undergoing a large-amplitude, periodic motion in a freestream flow. When this happens, there is a time lag in the aerodynamic forces and moments exerted by the flow on the body, along with a hysteresis in the aerodynamic forces. These two phenomena combined, in turns, may give rise to a negative aerodynamic damping, thus implying that the flow is doing some work on the structure. As a result of this positive transfer of energy from the flow to the airfoil, flutter may occur if the structural damping is insufficient.

The occurrence of stall flutter is very often dependent upon the amplitude of the initial external perturbation, especially if the airfoil is linearly dynamically stable. This is in contrast with classical flutter, where an infinitesimal perturbation is enough to induce flutter. For stall flutter, if the initial external perturbation is large enough, the dynamic instability may even be observed at flow velocities well below the critical flutter velocity as predicted through a linear theory (see Arena et al. (2013)), such as the one presented in the previous subsection. Further, stall flutter implies that separation occurs on a cyclic basis. Indeed, separation must be followed by a reattachment of the flow to the airfoil (see Dimitriadis and Li (2009); McCroskey (1981) and Razak et al. (2011)). In cases where the flow is always separated, such as on a bluff body, the structure is said to be galloping[4] whenever flutter occurs (see Dimitriadis and Li (2009) and Razak et al. (2011)).

---

[4] Galloping is a phenomenon very similar to stall flutter, except that there is no reattachment of the flow on the body. The reader is referred to Dowell et al. (2005) and Fung (2008) for more details.

Dynamic stall, the mechanism that accounts for the instability, is the abrupt loss of lift and/or pitching moment observed as a result of a flow separation over an airfoil undergoing motions of large amplitude (see Dimitriadis and Li (2009) and Razak et al. (2011)), and it is well documented in the literature. This unsteady, nonlinear aerodynamic phenomenon may be further subdivided based on the level of flow separation (see McCroskey (1981, 1982)): light stall and deep stall. The airfoil is said to be undergoing deep dynamic stall when the main feature of the flow is the shedding of a large vortex at the leading edge. In such situation, the viscous layer can be as thick as the airfoil's chord length. For deep dynamic stall to occur, a motion that induces angles of attack much larger than the angle of attack needed to reach static stall is required. This large vortex traveling close to the airfoil, at an approximate velocity of $U_\infty/2$, can generate boosted lift and aerodynamic moments that are far in excess from their static counterparts. Conversely, light dynamic stall is more similar to static stall. Trailing-edge separation is encountered, and the thickness of the viscous layer is of the order of the airfoil's thickness. The lift and the moments remain closer to the typical values observed during static stall. Typically, light dynamic stall is observed when the maximum angle of attack is only a few degrees greater than the angle of attack at static stall. It must be mentioned that stall flutter may occur under both types of dynamic stall.

As previously mentioned, negative aerodynamic damping arises as a result of the phase lag between the motion and the aerodynamic forces, combined with a hysteresis in the aerodynamic forces. The large hysteresis, shown with the gray area in Figure 1.9 and the phase lag are associated to the cyclic detachment and reattachment of the flow involved in dynamic stall. This is because the physics of the flow around the airfoil is considerably different as it approaches dynamic stall, than it is when the airfoil is recovering from the stalling event. In the light dynamic stall regime, the lag and the hysteresis are moderate, which implies a potential for some negative aerodynamic damping. For the deep dynamic stall regime, there is a very large hysteresis, which may lead to a considerably more negative aerodynamic damping, thus implying a larger potential for stall flutter.

Returning to deep dynamic stall, the effect of the shed vortex is particularly evident when considering the behavior of the pitching moment, which exhibits an abrupt and strong change of amplitude. The solid curve of Figure 1.9 shows the typical behavior of the lift coefficient ($C_\mathcal{L}$) and the aerodynamic moment coefficient (C_M) as the angle of attack (α) is varied, while the dashed curve shows the trends for static angles. Large differences between the static and the dynamic trends, along with a hysteresis for both $C_\mathcal{L}$ and C_M (gray areas), are observed. The dots identified with numbers correspond to the typical qualitative sequence of events described in Table 1.2. As it may be seen, the shedding of the vortex plays a crucial role in the aerodynamics. In fact, stall flutter is sometimes seen as the result of a coupling between the structure and the flow achieved through vortex shedding. This is because the low pressure in the core of the shed eddy has the potential of generating fairly large forces on the surface of the airfoil as it travels downstream.

Table 1.2: Typical qualitative sequence of events during the deep dynamic stall of an airfoil. The points are related to those shown in Figure 1.9. Inspired from McCroskey (1981).

.

Point	Main flow feature	Forces and moments
1	Thin and attached boundary layer	Linear regime
2	Flow reversal within the boundary layer	Linear and maximum static lift exceeded
3	Vortex shed and moves over the airfoil	Pitching moment diverges and lift due to the vortex is present
4	Vortex continues downstream at approximately $U_\infty/2$	Maximum lift and moment followed by a rapid decay
5	Secondary vortex forms	Secondary peaks on both lift and moment
6	Reattachment of the flow	Return to linear regime

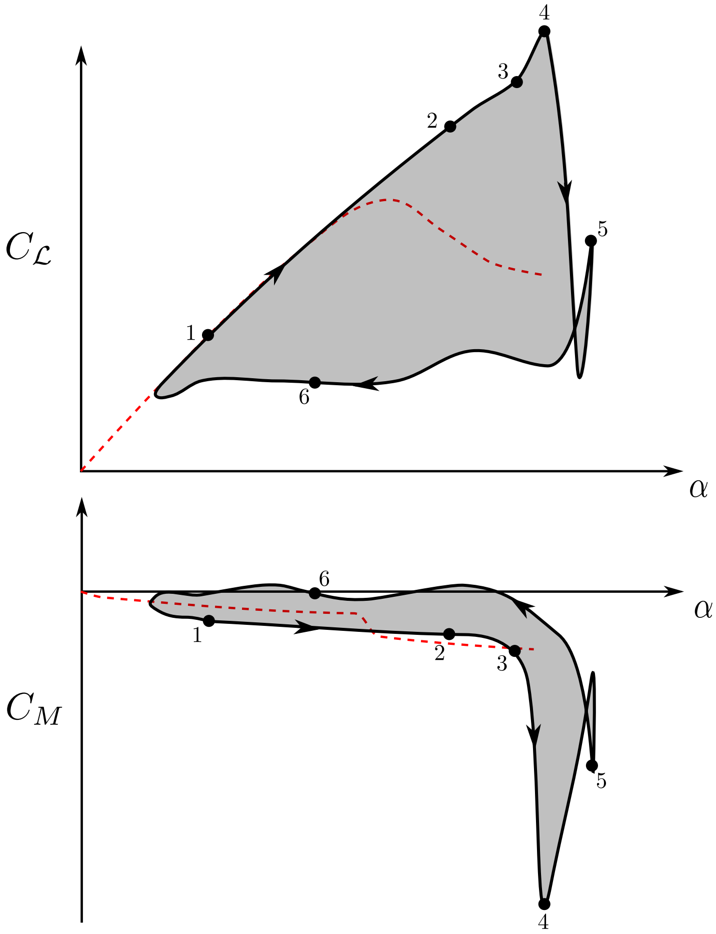

Figure 1.9: Typical lift coefficient ($C_\mathcal{L}$) and aerodynamic moment coefficient (C_M) for a static airfoil (dashed red line) and for an airfoil undergoing deep dynamic stall (solid line). The points with numbers are related to those described in Table 1.2. Inspired from McCroskey (1981).

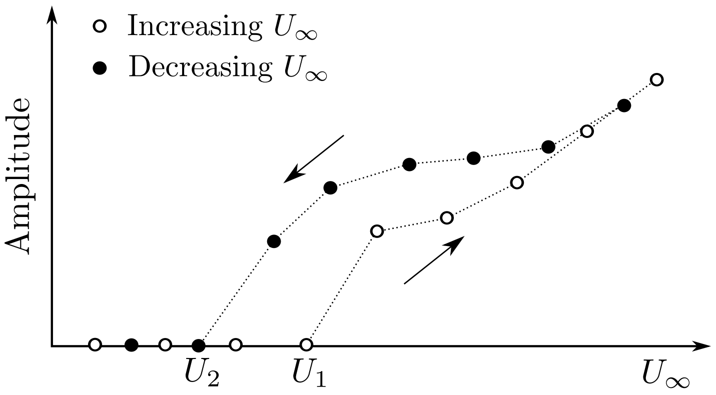

Figure 1.10: Typical hysteretic response of a structure undergoing stall flutter as the freestream velocity (U_∞) is increased (unfilled dots) and decreased (filled dots).

Another typical nonlinear behavior of stall flutter is the hysteresis in the response of the airfoil (not to be confused with the hysteresis of the aerodynamic forces previously discussed). A qualitative example is provided in Figure 1.10. When a critical parameter is varied, here the freestream velocity (U_∞), a sudden appearance of flutter with a brutal jump to large amplitudes of motion is observed at a critical velocity, say U_1. Then, if the velocity is reduced, flutter may persist down to a value U_2, that is well below U_1. The amplitude of motion at a specific velocity may even differ depending on the fact that the velocity is being increased or it is being decreased. Memory effects are therefore inherent to the stall flutter phenomenon.

Recalling that a potential aerodynamic theory has been used in the discussion on classical flutter, one could seek a similar method in order to study stall flutter. In light of all the nonlinear characteristics involved within stall flutter, this appears to be unrealistic. Indeed, potential theories do not aim at predicting the aerodynamic forces exerted on a body when separations are encountered, and, as a result, they fail at predicting stall flutter (see Razak et al. (2011)). To illustrate this statement, stall flutter has been observed at flow velocities well below the critical flutter velocity (U_{cr}) predicted with the linear theories (see Arena et al. (2013)). In order to study the stability of an airfoil when confronted to periodic stalling, semi-empirical stall models have to be used, such as the well-known Leishman-Beddoes (see Leishman and Beddoes (1989)) and the ONERA (see Tran and Petot (1981)) models. As pointed out by Larsen et al. (2007), the objective of these models is essentially to capture the main characteristics of the aerodynamics in a fast and efficient way. That being said, this may prove to be sufficient to conduct the stability analysis of a device, or to roughly estimate the amount of energy harvested from a flow when the motion of the airfoil is enforced, such as in the work of Bryant et al. (2013). However, it may fail at predicting accurately the motion of a fully-passive device. Indeed, in the fully-passive case, the motion depends upon the aerodynamics, and the aerodynamics depends upon the motion. This interdependence may lead to an inevitable amplification of the discrepancies inherent to such a model, the behavior of which is dependent upon an adequate calibration that is case dependent.

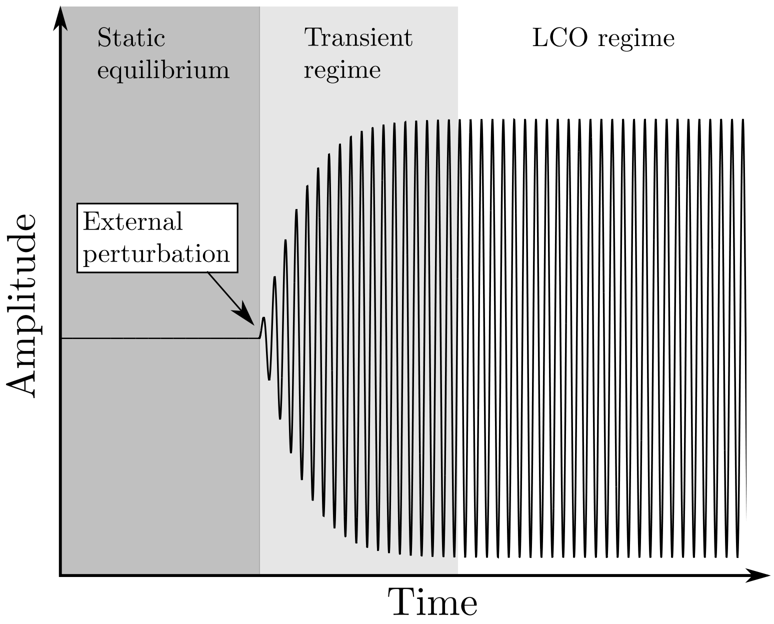

Figure 1.11: Typical qualitative response over time of a dynamically unstable structure that involves nonlinearities leading to limit-cycle oscillations (LCO) of constant amplitude.

1.3.3 Limit-cycle oscillations

Limit-cycle oscillations (LCO) are self-excited, cyclic oscillations of limited and fairly constant amplitude (see Dimitriadis and Li (2009)). For this type of motion, which could easily be characterized as being well-behaved, the amplitude of motion happens to be limited by some nonlinearities present in the dynamics of the system (see Arena et al. (2013)). The typical qualitative response of a dynamically unstable structure that involves nonlinearities leading to LCO is shown in Figure 1.11. Although the representation may suggest that only one degree-of-freedom is involved, LCO may in fact consist in the simultaneous excitation of several modes. In the first stage shown in Figure 1.11, the structure is in static equilibrium and free from any significant motion other than vibrations of very small amplitude (not shown). Then, following an external perturbation that can take the form of any symmetry breaking mechanism, the structure becomes unstable and is subject to an oscillatory motion of growing amplitude throughout the transient regime. As the amplitude grows, the effect of the nonlinearities becomes greater[5]. This turns out to limit the growth of the amplitude of motion until the instability finally saturates, and a permanent LCO regime of constant amplitude is reached.

As previously discussed, the nonlinearities involved in LCO may be due to stall flutter. In this specific case, they are caused by large separations of the flow from the airfoil. However, LCO may emerge from several other sources of nonlinearities. Indeed, the nonlinear behavior introduced by large shocks in a flow or by structural (e.g., freeplay in control surfaces),

---

[5] For example, flow separations may appear.

material (e.g., large deformations) or inertial (e.g., concentrated masses) nonlinearities may be sufficient to limit the exponential growth of a fluttering airfoil's amplitude of motion (see Arena et al. (2013); Dowell et al. (2005) and Razak et al. (2011)). Also, as pointed out by Dowell et al. (2005), LCO is not the only possible outcome to flutter when nonlinearities are involved. Other types of response, such as beating and period doubling[6], may sometimes occur. These behaviors are not discussed further in this text. In fact, due to its well-behaved character, LCO is the only attractive outcome for a fully-passive, flapping-airfoil turbine application.

As pointed out in the previous subsection concerned with stall flutter, a linear stability analysis does not permit to predict the onset of stall flutter due to its nonlinear behavior. As it might be expected, the same is true for most types of LCO. In fact, a linear analysis generally predicts fairly well the frequency of oscillation, but it fails at predicting the onset of the instability or its terminal amplitude of motion. Since one involved in such work generally seeks a flutter boundary in order to avoid the instability, this type of study is not worth the trouble. Instead, some semi-empirical or empirical models can be developed to help study a specific type of system. Nowadays, computational fluid dynamics (CFD) is also used to study LCO. From CFD and experimental work, the general trend of the LCO's amplitude is generally to increase as the flow velocity (U_∞) increases, and hysteretic responses, such as the one depicted on Figure 1.10, are very often observed.

Partial conclusion

The three physical phenomena described in this section will prove to be useful throughout the current master's thesis. Classical flutter has been introduced at first. This type of dynamic instability can be predicted using a fairly simplistic linear, potential aerodynamic theory. All that is needed is to solve an eigenvalue problem. The objective of such a stability analysis is mainly to determine when the aerodynamic damping becomes negative for at least one mode, which indicates the onset of flutter. Indeed, when dealing with classical flutter, the destructive nature of the instability often makes it useless to predict the amplitude of motion. Several key parameters affect the location of the flutter boundary, such as the distribution of mass, the location of the elastic axis, the location of the aerodynamic center and the natural frequencies. Next, stall flutter has been presented. This type of dynamic instability differs greatly from classical flutter in the physical mechanisms involved. During classical flutter, the negative aerodynamic damping arises from the elastic and/or aerodynamic coupling between the modes. For stall flutter, the negative aerodynamic damping is due to the hysteresis in the aerodynamic forces and the phase lag between the motion and the forces. These two phenomena are the result of the highly unsteady flow and the dynamic stall encountered. Very often, the instability saturates through the nonlinearities involved in the massive separations

---

[6] Period doubling is a type of bifurcation (see Broer and Takens (2010)).

present. This limits the growth of the amplitudes of motion, thus leading to a well-behaved, cyclic motion called limit-cycle oscillations (LCO). Although stall flutter often results in LCO, this type of response may also be due to other physical mechanisms. In this study, for the purpose of optimizing the fully-passive, flapping-airfoil turbine, LCO are the only outcome of interest due to its fairly constant amplitude of motion.

Chapter 2

Modeling of the problem and computational methodology

This chapter deals with the modeling and the computational methodology used in order to solve the aeroelastic problem of the elastically-mounted, flapping-airfoil turbine. The first section addresses the modeling of the aeroelastic problem. The main objective is to formally introduce and develop the equations of motion of the aeroelastic device. An interpretation of the various terms involved within the equations is also offered. Because the problem will later be solved in its non-dimensional form, its non-dimensional formulation is also presented in this section. As the reader goes through, he is invited to consider the immense dimension of the parametric space associated to the aeroelastic device, and the richness of the physical mechanisms involved. In the second section of this chapter, the numerical methodology implemented within the *OpenFOAM* CFD toolbox and used to solve both the equations of the flow and the equations of motion of the airfoil is introduced. This section surely does not aim at drawing a complete picture of the very vast domain of CFD and the numerical methodologies typically used to solve the equations involved. Instead, the main objective is essentially to acquaint the reader with the particular choices that have been made for the task of solving the equations of the two-dimensional problem here considered, and also to provide a warrant for these choices whenever needed. The last section of this chapter copes with the fluid-structure interaction (FSI) coupling scheme. One can have accurate flow and solid solvers, but they must somehow be linked in order to predict fully and accurately the flow field and the airfoil's motion. An overview of the most commonly used coupling schemes is presented, followed by a description of the specific scheme used in this work. Further, some inherent, well-known limitations associated to the chosen coupling scheme are discussed.

2.1 Aeroelastic modeling

In the aeroelastic problem of interest in this master's thesis, the rigid, elastically-mounted airfoil is free to pitch around the z-axis and heave along the y-axis. This is clearly illustrated in Figure 2.1. The motion is not possible in any other direction, nor about any other axis. As schematically shown, the two-degree-of-freedom system consists of a rigid airfoil which is mounted on a pivot about which the pitching motion (θ) is possible. Further, the pivot is mounted on a sliding mechanism, thus allowing the heaving motion (y). It is to be noted that the sliding mechanism is not schematically shown in Figure 2.1, but the reader may refer to the previously introduced Figure 1.4 for one particular example of such mechanisms.

Figure 2.1 also schematically depicts several key parameters of interest in the formulation of the aeroelastic problem. However, not all parameters are explicitly displayed in the figure for clarity. As previously suggested, the motion of the airfoil which is elastically-supported in a freestream flow and undergoing LCO may be indirectly controlled through an adequate, well-studied choice of all structural parameters. This is exactly what has to be achieved in the current study for the task of optimizing the fully-passive, flapping airfoil as a wind or hydrokinetic turbine. For clarity and convenience, all variables involved in the current aeroelastic problem are here enumerated and commented:

- U_∞, freestream velocity : velocity of the undisturbed flow upstream of the airfoil;
- airfoil's profile : the airfoil's profile is assumed rigid at all time;
- c, airfoil's chord length: distance between the leading edge and the trailing edge;

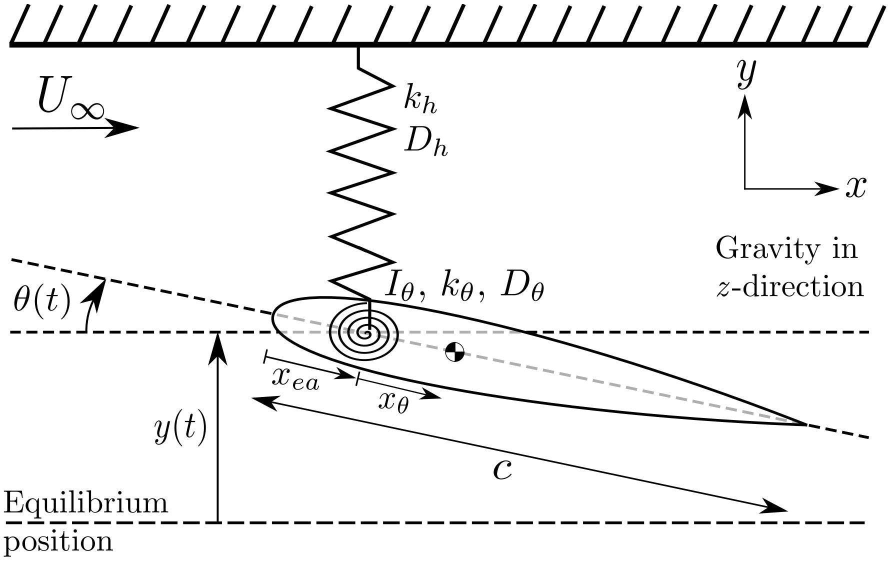

Figure 2.1: Simplified schematic of the symmetrical, rigid, elastically-mounted airfoil with symbolic representation of key parameters (not showing the sliding mechanism). Refer to the text for a description of all parameters. Adapted from Lapointe and Dumas (2012).

- m_p, pitching mass : mass of all components involved in the pitching motion;
- m_h, heaving mass : mass of all components involved in the heaving motion (including the pitching mass so that $m_h \geq m_p$);
- I_θ, moment of inertia : airfoil's moment of inertia about the elastic axis (i.e., pitching axis);
- x_{ea}, location of the elastic axis : distance between the elastic axis and the leading edge of the airfoil;
- x_θ, location of the center of mass : distance between the elastic axis and the center of mass (positive when the elastic axis is ahead of the center of mass);
- k_h, heave stiffness coefficient : linear stiffness coefficient used to account for the restoring force of the linear spring;
- k_θ, pitch stiffness coefficient : linear stiffness coefficient used to account for the restoring moment of the torsional spring;
- D_h, heave damping coefficient : linear damping coefficient used to account for the dissipation of energy associated to the energy extraction mechanism connected to the oscillating airfoil (i.e., the electrical generator);
- D_θ, pitch damping coefficient : linear damping coefficient used to account for the dissipation of energy associated to structural damping in pitch [1];
- $\mathcal{L}$, aerodynamic lift: lift force generated by the flow field on the airfoil (upward positive);
- M_{ea}, aerodynamic moment: moment generated by the flow field on the airfoil (clockwise positive);
- y, heave position: vertical position of the elastic axis (upward positive), where the superscript $(\cdot)$ denotes its time derivatives;
- θ, pitch angle: angular position of the airfoil i.e., geometric angle between the chord line and the freestream flow (clockwise positive), where the superscript $(\cdot)$ denotes its time derivatives [2].

Figure 2.1 also introduces the main system of coordinates used throughout the study. It is defined such that it corresponds to a right-hand system with the x-axis rightward positive, and the y-axis upward positive. Further, gravity is assumed in the z-direction, which obviously excludes it from the dynamics of the airfoil.

It is worth pointing out now that the heaving mass (m_h) and the pitching mass (m_p) of such a system do not need to be equal, and this must be taken into account within the equations

---

[1] The reader should understand that viscous damping, which is obviously involved in the dynamics of the airfoil, is encompassed within the lift force and the moment calculated within the flow solver. Therefore, no additionnal term is required within the equations of motion to account for its contribution.

[2] The reader should note that θ is *not* equal to the airfoil's angle of attack (α). Indeed, the angle of attack must account for the heaving velocity of the airfoil, thus changing the effective velocity of the flow. A better formulation would be: $\alpha = \theta - \arctan(\dot{y}/U_\infty)$.

of motion. One can convince oneself by considering the previously introduced Figure 1.4, which is the perfect example of an aeroelastic device where the mass of the sliding mechanism is *not* involved in the pitching motion of the airfoil. At all time, the heaving mass of the system must remain greater or equal to the pitching mass. Indeed, some components may be involved solely in the heaving motion, but a mechanism where some components are only involved in the pitching motion is hardly conceivable. Last, it has been pointed out within the previous enumeration of the flow and the structural parameters that the effect of the electrical generator connected to the device is here modeled as a viscous damper with a purely linear behavior. Such a hypothesis is certainly not new, and more details will be provided on this in Chapter 5. Nevertheless, the reader might appreciate to be informed now that an electrical generator[3] may indeed be designed such that it has a linear behavior. Therefore, making such a hypothesis is not far fetched at all.

With this general picture of the fully-passive, flapping-airfoil turbine, the equations of motion can be derived in a fairly straightforward way by making use of the Lagrange's equation (see Dowell et al. (2005)). A more traditional Newtonian derivation would be equally valid, and, of course, the same system of equations would be obtained[4]. However, using a Newtonian-type derivation is more work intensive in the current case.

The general trend of the Lagrange-type derivation can be divided into three relatively simple steps. First, equations for the potential energy (U_E) and the kinetic energy (T_E) of the system are found:

$$U_E = U_E\left(\dot{q}_i, q_i, t\right) \ , \tag{2.1}$$

$$T_E = T_E\left(\dot{q}_i, q_i, t\right) \ , \tag{2.2}$$

where q_i is the i^{th} generalized coordinate of the system, t is the time and the superscript $(\dot{\cdot})$ denotes differentiation with respect to time. As a second step, the i^{th} equation of motion can be written as:

$$-\frac{d}{dt}\left[\frac{\partial\left(T_E - U_E\right)}{\partial \dot{q}_i}\right] + \frac{\partial\left(T_E - U_E\right)}{\partial q_i} + F_{nc} = 0 \ , \tag{2.3}$$

where F_{nc} stands for all the nonconservative contributions. The third and last step is to find an expression for these nonconservative contributions, which often turns out to be relatively simple. As the reader can surely appreciate, this approach is very systematic. It can now be successfully applied to the aeroelastic device at the heart of this study, but some details

---

[3] The term electrical generator here refers to the motor/generator itself connected to the oscillating airfoil, as much as to the electronics used to control and regulate the generator.

[4] In fact, the author carried out a Newtonian-type derivation of the equations of motion and obtained, without great surprise, the same equations as those which will be obtained in this section.

related to the system of coordinates used in the following derivation should first be clearly introduced. As shown in Figure 2.2, the *generalized* coordinates (i.e., q_1 and q_2) are y and θ, together corresponding to both degrees-of-freedom of the oscillating airfoil. Further, x_c is the chordwise distance between any station on the chord line and the elastic axis. Last, $\mathbf{i}$ and $\mathbf{j}$ are the unit cartesian vectors forming an orthonormal system of coordinates. For convenience, $\mathbf{j}$ is chosen such that it is parallel to the heaving motion of the airfoil. With these formal definitions, the displacement of any point located on the chord line of the airfoil may be mathematically represented with a vector $\mathbf{r}$. The geometric construction representing this entity is presented in Figure 2.2, and $\mathbf{r}$ can be defined as:

$$\mathbf{r} \;=\; u\mathbf{i} \;+\; v\mathbf{j} \;, \tag{2.4}$$

where

$$u \;=\; x_c \left(\cos\theta - 1\right) \;, \tag{2.5}$$

$$v \;=\; y \;-\; x_c \sin\theta \;. \tag{2.6}$$

Three more very useful definitions can be made before working out the equations. If the linear density of the structure (ρ_s) is multiplied by powers of x_c and integrated along the chord line, one obtains:

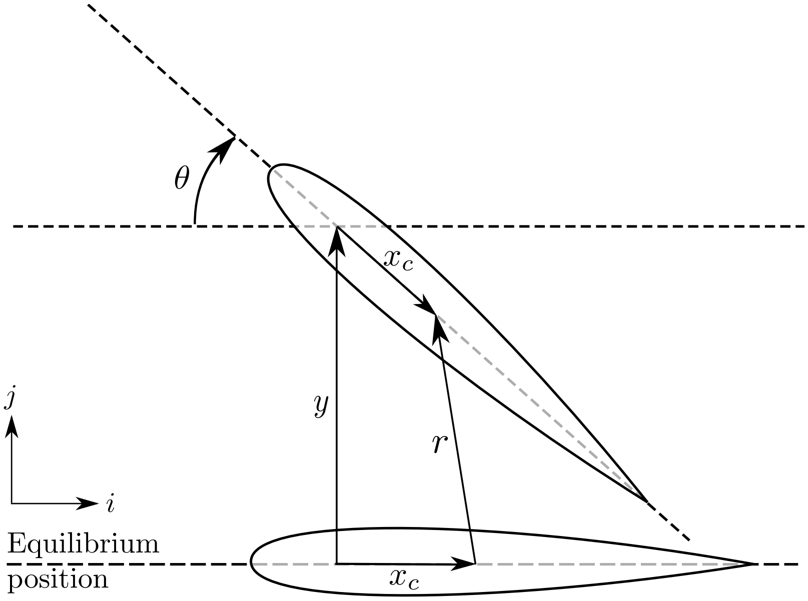

Figure 2.2: Complete system of coordinates used for the derivation of the general equations of motion of the fully-passive, flapping-airfoil turbine.

$$m_p \;=\; \int \rho_s \, dx_c \;, \tag{2.7}$$

$$m_p x_\theta \;=\; \int \rho_s x_c \, dx_c \;, \tag{2.8}$$

$$I_\theta \;=\; \int \rho_s x_c^2 \, dx_c \;. \tag{2.9}$$

With these, the kinetic energy of the components involved in both the pitching and the heaving motions (T_p) can be found. Some simplistic mathematical manipulations are here skipped:

$$\begin{aligned} T_p \;&=\; \frac{1}{2} \int \left[\left(\frac{du}{dt} \right)^2 \;+\; \left(\frac{dv}{dt} \right)^2 \right] \rho_s \, dx_c \;, \\ &=\; \frac{1}{2} \left(m_p \dot{y}^2 \;-\; 2\, m_p x_\theta \, \dot{y} \, \dot{\theta} \cos\theta \;+\; I_\theta \dot{\theta}^2 \right) \;. \end{aligned} \tag{2.10}$$

The kinetic energy associated to the components involved *only* in the heaving motion (T_h) must also be considered:

$$T_h \;=\; \frac{1}{2} \left(m_h - m_p \right) \dot{y}^2 \;, \tag{2.11}$$

thus yielding the following expression for the total kinetic energy:

$$T_E \;=\; \frac{1}{2} m_h \dot{y}^2 \;-\; m_p x_\theta \, \dot{y} \, \dot{\theta} \cos\theta \;+\; \frac{1}{2} I_\theta \dot{\theta}^2 \;. \tag{2.12}$$

The potential energy is more readily found because only the elastic supports contribute to its value:

$$U_E \;=\; \frac{1}{2} k_h y^2 \;+\; \frac{1}{2} k_\theta \theta^2 \;. \tag{2.13}$$

Using the Lagrange's equation, the equation for the heaving motion can be obtained:

$$-\frac{d}{dt} \left(\frac{\partial (T_E - U_E)}{\partial \dot{y}} \right) \;+\; \frac{\partial (T_E - U_E)}{\partial y} \;+\; F_{nc} \;=\; 0 \;. \tag{2.14}$$

Injecting Eqs. 2.12 and 2.13 for the kinetic and the potential energy into Eq. 2.14, the following is obtained after simplification:

$$- m_h \ddot{y} \;+\; m_p x_\theta \, \ddot{\theta} \cos\theta \;-\; m_p x_\theta \, \dot{\theta}^2 \sin\theta \;-\; k_h y \;+\; F_{nc} \;=\; 0 \; . \tag{2.15}$$

The nonconservative forces involved in this degree-of-freedom are the lift ($\mathcal{L}$) and the damping force ($D_h \dot{y}$). After isolating the lift on the left-hand side (LHS), this yields:

$$\boxed{\mathcal{L} \;=\; \underbrace{m_h \ddot{y}}_{\substack{\text{inertial}\\ \text{term}}} \;+\; \underbrace{S\left(\dot{\theta}^2 \sin\theta - \ddot{\theta}\cos\theta\right)}_{\substack{\text{inertial coupling}\\ \text{term}}} \;+\; \underbrace{k_h y \;+\; D_h \dot{y}}_{\substack{\text{structural}\\ \text{terms}}} \; .} \tag{2.16}$$

To obtain the previous equation, the sign associated to each nonconservative force has been chosen according to the physics at play. Indeed, a positive lift ($\mathcal{L}$) must result in a positive acceleration ($\ddot{y}$), and the damping force ($D_h \dot{y}$) must always be opposed to the heaving motion ($\dot{y}$). As a last simplification, the previously introduced static imbalance ($S = m_p x_\theta$) has been used to reinforce the idea that $m_p x_\theta$ forms a single structural parameter [5].

The same derivation can now be done for the equation of motion related to the pitching motion:

$$-\frac{d}{dt}\left(\frac{\partial(T_E - U_E)}{\partial \dot{\theta}}\right) \;+\; \frac{\partial(T_E - U_E)}{\partial \theta} \;+\; M_{nc} \;=\; 0 \; , \tag{2.17}$$

where the nonconservative forces (F_{nc}) have been replaced with the nonconservative moments (M_{nc}). Using Eqs. 2.12 and 2.13 again, this yields after simplification:

$$m_p x_\theta \, \ddot{y} \cos\theta \;-\; I_\theta \ddot{\theta} \;-\; k_\theta \theta \;+\; M_{nc} \;=\; 0 \; . \tag{2.18}$$

The nonconservative contributions to this last equation are the aerodynamic moment about the elastic axis (M_{ea}) and the damping moment ($D_\theta \dot{\theta}$). Again, the signs are easily determined: a positive aerodynamic moment must yield a positive angular acceleration ($\ddot{\theta}$), and the damping moment must be opposed to the angular motion ($\dot{\theta}$). The final result can therefore be written as:

$$\boxed{M_{ea} \;=\; \underbrace{I_\theta \ddot{\theta}}_{\substack{\text{inertial}\\ \text{term}}} \;-\; \underbrace{S \ddot{y} \cos\theta}_{\substack{\text{inertial coupling}\\ \text{term}}} \;+\; \underbrace{D_\theta \dot{\theta} \;+\; k_\theta \theta}_{\substack{\text{structural}\\ \text{terms}}} \; .} \tag{2.19}$$

---

[5] The origin of the name static imbalance is simple and very meaningful. If gravity was such that it played a role in the dynamics of the airfoil, a nonzero value of S, which implies that the center of mass does not coincide with the elastic axis, would yield a nonzero value of θ at static equilibrium. Because gravity is not involved in the current problem, the static equilibrium is not affected by S. However, the typical terminology used in aeroelasticity is here retained.

Equations 2.16 and 2.19 constitute the two equations of motion of the fully-passive, flapping-airfoil turbine modeled in this study. In each of these equations, there is an aerodynamic force or moment with an inertial term, an inertial coupling term and two structural terms. The inertial coupling term explicitly couples the equations of motion when $S \neq 0$. It can be seen that no inertial coupling term is present when the elastic axis coincides with the center of mass of the pitching components ($S = 0$). To illustrate the effect of this inertial coupling, one can think of holding a small beam in his hands. If the beam is held at a location which does not coincide with its center of mass, moving the beam up and down (heaving motion) will necessarily induce some angular motion of the beam. However, if the beam is supported at its center of mass, a heaving motion will not engender any angular motion.

There is another form of coupling between the equations of motion. Contrary to the inertial coupling, the aerodynamic coupling is *always* present, whatever the choice of the structural parameters. Indeed, $\mathcal{L}$ and M_{ea} are always greatly linked together, and this implicitly[6] couples both equations of motion. As it may be observed, no other form of coupling is possible between the equations of motion, and this is in agreement with the modeled device: there is no mechanical linkage between the degrees-of-freedom to control the phase lag between the motions, and there is no way to control explicitly the shape of any of the two motions. The equations of motion are indeed those of a fully-passive, flapping airfoil.

Within the structural terms, the assumed linear behavior of the structural restoring forces and moments, along with the damping forces and moments, is necessarily a simplification over the physical reality. It is worth pointing out that even with this simplification of the equations of motion, together they contain a total of seven structural parameters. Each one of these parameters can be individually varied, thus providing several ways to indirectly control the dynamics of the airfoil. The reader may appreciate the vast parametric space of the aeroelastic device, and, as a result, the richness of the physics embodied within the problem modeled. If nonlinearities were introduced within the model, this would add further dimensions to an already immense parametric space, and this would certainly make the optimization of the device much more challenging at different levels.

For convenience and later use, both equations of motion can be written in their non-dimensional form. The following reference values are used:

- Length: $L_{ref} = c$;
- Velocity: $V_{ref} = U_{\infty}$;
- Time: $T_{ref} = c/U_{\infty}$;

---

[6] This coupling is characterized as implicit because its presence is not obvious when looking at the equations of motion. Conversely, the inertial coupling is explicit because it is obvious at first glance.

- Pressure: $p_{ref} = \rho_f U_\infty^2$;
- Aerodynamic lift: $\mathcal{L}_{ref} = \frac{1}{2}\rho_f U_\infty^2 bc$;
- Aerodynamic moment: $M_{ref} = \frac{1}{2}\rho U_\infty^2 bc^2$.

The details of the non-dimensionalization process, which may be found in Kundu et al. (2012), are left behind and only the results are presented. The superscript $(^*)$ is here used to identify a non-dimensional parameter. The equations of motion then become:

$$C_{\mathcal{L}} \;=\; m_h^* \, \ddot{y}^* \;+\; S^* \left(\dot{\theta}^2 \sin\theta - \ddot{\theta}\cos\theta\right) \;+\; D_h^* \, \dot{y}^* \;+\; k_h^* \, y^* \;, \tag{2.20}$$

$$C_M \;=\; I_\theta^* \, \ddot{\theta} \;-\; S^* \ddot{y}^* \cos\theta \;+\; D_\theta^* \, \dot{\theta} \;+\; k_\theta^* \, \theta \;, \tag{2.21}$$

with the following definitions for the non-dimensional parameters:

$$C_{\mathcal{L}} = \frac{\mathcal{L}}{\frac{1}{2}\rho U_\infty^2 bc} \;, \quad C_M = \frac{M_{ea}}{\frac{1}{2}\rho U_\infty^2 bc^2} \;, \quad I_\theta^* = \frac{I_\theta}{\rho bc^4} \;, \quad k_\theta^* = \frac{k_\theta}{\rho U_\infty^2 bc^2} \;, \quad D_\theta^* = \frac{D_\theta}{\rho U_\infty bc^3} \;,$$

$$k_h^* = \frac{k_h}{\rho U_\infty^2 b} \;, \qquad D_h^* = \frac{D_h}{\rho U_\infty bc} \;, \qquad m_h^* = \frac{m_h}{\rho bc^2} \;, \quad S^* = \frac{S}{\rho bc^3} \;, \qquad y^* = \frac{y}{c} \;.$$

As one might expect, this choice of non-dimensional parameters is not unique but their number is. The reader may find a concise overview of some other possible choices in the master's thesis of Metivier (2012). To this, one must add the Reynolds number (Re) which comes from the fluid equations (Navier-Stokes) in incompressible form.

2.1.1 Equation for the cycle-averaged power

It is possible to find an equation for the cycle-averaged power of such a device. As one might expect, if the airfoil has reached a permanent regime of motion, the inputs of power are exactly balanced by all outputs. Writing such an equation will prove to be helpful at understanding better the fully-passive turbine. As a first step towards that equation for the cycle-averaged power, an equation for the instantaneous power can be found by simply multiplying all terms of the equation in heave by the heaving velocity, and all terms of the equation in pitch by the pitching rate. Once this is done, all terms can be summed (the $(^*)$ notation is dropped to avoid overloading the equations):

$$\begin{aligned} C_{\mathcal{L}}\dot{y} \;+\; C_M\dot{\theta} \;=\; & m_h \, \ddot{y}\dot{y} \;+\; S\left(\dot{\theta}^2 \sin\theta \, \dot{y} - \ddot{\theta}\cos\theta\dot{y}\right) \;+\; D_h \, \dot{y}^2 \;+\; k_h \, y\dot{y} \\ & +\; I_\theta \, \ddot{\theta}\dot{\theta} \;-\; S\ddot{y}\cos\theta\dot{\theta} \;+\; D_\theta \, \dot{\theta}^2 \;+\; k_\theta \, \theta\dot{\theta} \;. \end{aligned} \tag{2.22}$$

Over a complete cycle of oscillation, the contribution of some terms is expected to be zero. In order to demonstrate that some terms do not contribute to the cycle-averaged equation of power, the following very general cyclic motion is assumed:

$$\theta \;=\; \sum_{n=1}^{\infty} \Big(a_n \cos\left(2\pi n f t\right) \;+\; b_n \sin\left(2\pi n f t\right) \Big) \;\;, \tag{2.23}$$

$$y \;=\; \sum_{n=1}^{\infty} \Big(c_n \cos\left(2\pi n f t\right) \;+\; d_n \sin\left(2\pi n f t\right) \Big) \;\;. \tag{2.24}$$

Because the aerodynamic forces and the aerodynamic moments remain unknown, the terms on the LHS of Eq. 2.22 cannot be treated. Nevertheless, they are obviously expected to have a cycle-averaged contribution. In fact, they will have a positive contribution whenever negative aerodynamic damping is present. This is obviously the case here since LCO are assumed. All terms on the right-hand-side (RHS) can now be treated, and the interested reader may find the formal proof in Appendix B. Only the final equation for the cycle-averaged power is shown here, which is:

$$\frac{1}{T}\int_0^T \Big(C_{\mathcal{L}}\dot{y} \;+\; C_M\dot{\theta} \Big)\, dt \;=\; \frac{1}{T}\int_0^T \Big(D_h\dot{y}^2 \;+\; D_\theta\dot{\theta}^2 \Big)\, dt \;. \tag{2.25}$$

With this in hand, it is clear that over one complete cycle in the mean, only the aerodynamics can provide some energy to the airfoil, while both damping coefficients provide the energy sinks. At each cycle where the airfoil is in a permanent regime, this equality must be satisfied. Because it will be useful, later, to quantify the contribution of each term involved into this equation for the cycle-averaged power, some coefficients of power can be defined. They are complementary to the coefficient of power $\overline{C}_P$ previously defined in Chapter 1, which will also prove to be useful later. These new coefficients are:

$$\overline{C}_{Py} \;=\; \frac{1}{T}\int_0^T \frac{\mathcal{L}\dot{y}}{\frac{1}{2}\,\rho\, U_\infty^3\, bc}\, dt \;, \tag{2.26}$$

$$\overline{C}_{P\theta} \;=\; \frac{1}{T}\int_0^T \frac{M_{ea}\dot{\theta}}{\frac{1}{2}\,\rho\, U_\infty^3\, bc}\, dt \;, \tag{2.27}$$

$$\overline{C}_{Py,damp} = \frac{1}{T}\int_0^T \frac{D_h\dot{y}^2}{\frac{1}{2}\,\rho\,U_\infty^3\,bc}\,dt\ , \tag{2.28}$$

$$\overline{C}_{P\theta,damp} = \frac{1}{T}\int_0^T \frac{D_\theta\dot{\theta}^2}{\frac{1}{2}\,\rho\,U_\infty^3\,bc}\,dt\ . \tag{2.29}$$

One should note that by using these definitions, the following cycle-averaged equation holds true, which is simply another way of writing Eq. 2.25:

$$\overline{C}_P = \overline{C}_{Py} + \overline{C}_{P\theta} = \overline{C}_{Py,damp} + \overline{C}_{P\theta,damp}\ . \tag{2.30}$$

Further analysis, which is included in Appendix B, also reveals that:

$$\frac{1}{T}\int_0^T S\left(\dot{\theta}^2\dot{y}\,\sin\theta - \ddot{\theta}\,\dot{y}\cos\theta\right) = \frac{1}{T}\int_0^T S\,\ddot{y}\,\dot{\theta}\cos\theta dt\ . \tag{2.31}$$

This equation states two very important findings. First, and this is already known from Eq. 2.25, the inertial coupling term does not contribute, over one complete cycle, at providing or incurring some power to or from the airfoil. However, the cycle-averaged power calculated for the inertial coupling term coming from the equation of motion in heave (LHS of Eq. 2.31) exactly balances the contribution of the inertial coupling term coming from the equation of motion in pitch (RHS of Eq. 2.31). Second, the only way to guarantee that the LHS and the RHS of Eq. 2.31 are equal to zero is by setting $S = 0$. This indicates that the inertial coupling terms provide a way to transfer energy from one degree-of-freedom to the other. However, it is not possible to predict in what direction this will happen as this remains case dependent. In order to quantify this internal transfer of power between the pitching motion and the heaving motion, the following coefficient of power is to be used:

$$\overline{C}_{P,tr} = \frac{1}{T}\int_0^T \frac{S\left(\dot{\theta}^2\dot{y}\,\sin\theta - \ddot{\theta}\,\dot{y}\cos\theta\right)}{\frac{1}{2}\,\rho\,U_\infty^3\,bc}\,dt = \frac{1}{T}\int_0^T \frac{S\,\ddot{y}\,\dot{\theta}\cos\theta}{\frac{1}{2}\,\rho\,U_\infty^3\,bc}\ , \tag{2.32}$$

With all the previous definitions, the following can also be written for convenience:

$$\overline{C}_{P,tr} = \overline{C}_{Py,damp} - \overline{C}_{Py} = \overline{C}_{P\theta} - \overline{C}_{P\theta,damp}\ . \tag{2.33}$$

Again, these definitions will prove to be very useful later in this master's thesis in order to qualify and quantify the contribution of each degree-of-freedom to the harvested power, and, also, to the power dissipated through the dampers connected to the device. This will greatly help at developing better understanding of how the fully-passive, flapping-airfoil works.

2.2 Fluid-structure solver

The fully-passive, flapping-airfoil problem is solved using *OpenFOAM-2.1.x*, a finite-volume, open-source CFD toolbox[7]. Other than being costless, this open-source software is making use of the object-oriented paradigm and is written with the C++ language which offers the great advantage of allowing the user to implement its own applications through high-level programming. For a complete description of the numerical methods readily available within the CFD toolbox, the reader is referred to the *OpenFOAM-2.1.x* official documentation (see OpenCFD (2012a,b)). The reader is also referred to the book of Ferziger and Perić (2002), which deals with the numerical methods used for CFD in general. Otherwise said, this last reference is not specific to *OpenFOAM* or any CFD code. Instead, it offers a comprehensive discussion about CFD in general with some emphasis on the numerical methods used to solve the equations of the flow.

2.2.1 Equations of the flow

The equations of the flow, including the equations presented within the subsection on the modeling of turbulence, are written using the indicial notation. With this notation, implicit summation, or Einstein summation, is assumed whenever an index is repeated twice within a monomial. The governing equations of the incompressible, viscous flow with constant and uniform properties are the continuity and the Navier-Stokes equations, which are respectively:

$$\frac{\partial u_i}{\partial x_i} = 0 \, , \tag{2.34}$$

$$\frac{\partial u_i}{\partial t} + u_j \frac{\partial u_i}{\partial x_j} = -\frac{1}{\rho_f}\frac{\partial p}{\partial x_i} + \nu \frac{\partial^2 u_i}{\partial x_j^2} \, , \tag{2.35}$$

where u_i are the velocity components, p is the pressure, x_i are the cartesian coordinates, ρ_f is the density of the fluid and ν is the kinematic viscosity of the fluid. In order to solve for the flow field, the momentum equations (Eq. 2.35) are used to determine the magnitude of each velocity component of the flow. As a result, this leaves the continuity equation (Eq. 2.34) to calculate the last unknown, which is the pressure. However, the continuity equation

---

[7] The complete code of the current FSI solver implemented within the *OpenFOAM-2.1.x* CFD toolbox is available at the LMFN upon request.

does not contain any pressure term. One possible solution to this *apparent* issue is to take the divergence of the momentum equation, and to use the continuity equation to simplify the result. This yields an elliptical Poisson equation for the pressure:

$$\frac{\partial^2 p}{\partial x_i^2} \;=\; -\rho_f \frac{\partial}{\partial x_i}\left(u_j \frac{\partial u_i}{\partial x_j}\right) \;. \tag{2.36}$$

The pressure and momentum equations may be solved in two different ways: either simultaneously (a coupled approach) or sequentially (a segregated approach). Within the *OpenFOAM-2.1.x* CFD toolbox, only the segregated approach is readily available, and this is the method used for this study. In this method, the momentum equation is first solved using an approximation of the pressure field throughout the fluid domain. Following this, the pressure field is corrected and updated. Through an iterative procedure, this routine may be repeated as many times as required in order to converge the solution up to a specified level of tolerance.

More than a single scheme have been designed to achieve this coupling of the pressure and the velocity. The most famous schemes are SIMPLE (Semi-Implicit Method for Pressure Linked Equations) and PISO (Pressure Implicit with Splitting Operator). In the current study, the PISO algorithm has been chosen. In fact, both PISO and SIMPLE schemes have been tested, and the PISO algorithm has demonstrated a superior efficiency for the present application. Indeed, PISO has shown to require less computational time over SIMPLE in order to converge the solution up to the exact same level of tolerance. The PISO algorithm is summarized in Figure 2.3. As it can be seen, the main characteristic of this coupling scheme is certainly the presence of not one, but two corrections on the pressure field. Another characteristic not shown on this figure is the fact that no under-relaxation is required. This last property partly explains the reduced computational cost of PISO over SIMPLE.

2.2.2 Turbulence modeling

In the current numerical study, the Reynolds number ($\mathrm{Re} = U_\infty c/\nu$) is set to a value of 500,000 unless otherwise noted. That being said, directly solving all scales of motion, including the turbulent ones, is strictly out of reach. Indeed, direct numerical simulations (DNS) are not conceivable for flows at such high Reynolds numbers with today's computational and memory resources. This is such because DNS calculations require that the spatial and temporal resolutions be fine enough to capture the smallest length and time scales of turbulent motions (i.e., the Kolmogorov scales). This results in very fine grid spacings and very fine time steps, especially for calculations at moderate to high Reynolds numbers. In fact, the full spectrum of turbulence is resolved when a DNS calculation is performed, and the result is certainly the most accurate that one could expect to obtain through CFD. As a rule of thumb, the cost of a DNS calculation goes approximately with Re_L^3 (see Ferziger and Perić (2002)), where Re_L is a Reynolds number based on the magnitude of the velocity fluctuations and on the integral

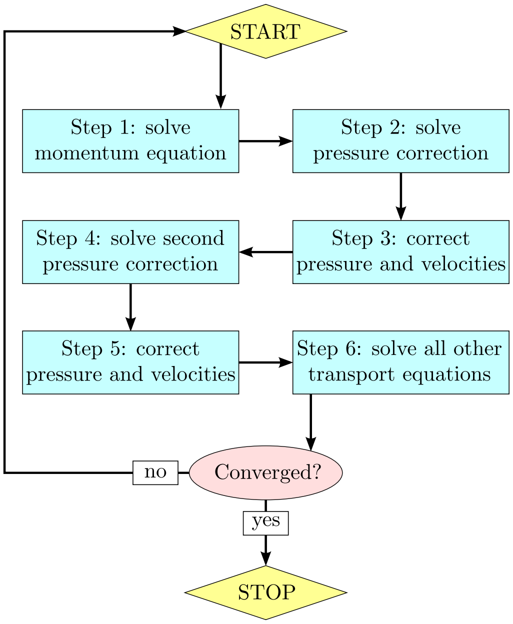

Figure 2.3: Representation of the PISO segregated algorithm for pressure-velocity coupling within a computational time step of the FSI solver.

length scale. This result indicates that this type of calculation rapidly becomes prohibitive as the Reynolds number grows. Nowadays, this type of calculation is only at reach for some canonical flows at relatively low Reynolds numbers.

An alternative to DNS calculations is the large eddy simulation (LES) approach. The philosophy behind LES is essentially to resolve the motions at the larger scales (i.e., the scales above a certain filter width Δ), and to model the effect of the motions at the smaller scales (i.e., the scales below the same filter width Δ). As a result, a part of the turbulence spectrum is resolved, while the rest of it is being modeled. The filter width Δ is somewhat dependent upon the grid resolution. In fact, its size is always greater or equal to the grid spacing. As a direct result of this, the modeled scales are often referred to as the sub-grid scales (SGS), and they are taken into account through a SGS model. Further, in order to resolve a fair portion of the turbulence spectrum, the resolution of the grid must be fine enough to permit relatively small values of the filter width Δ. Although this type of numerical simulations is less computationally demanding than DNS, the strict requirements on the temporal and on the spatial resolutions still make it very computationally demanding for flows at moderate to high Reynolds numbers. Therefore, LES is rarely used for engineering purposes nowadays.

The Unsteady Reynolds-Averaged Navier-Stokes (URANS) approach is another well-known methodology. Its ability to predict all types of flow fields for all Reynolds numbers at a relatively low cost compared to DNS and LES simulations makes it very useful for engineering purposes. The philosophy is here to decompose all variables into the sum of an averaged value ($\overline{\phi}(x_i, t)$) and a fluctuating value about that average ($\phi'(x_i, t)$):

$$\phi(x_i,t) \ = \ \overline{\phi}(x_i,t) \ + \ \phi'(x_i,t) \ , \tag{2.37}$$

where the averaged value, for an unsteady flow, is calculated by ensemble averaging:

$$\overline{\phi}(x_i,t) \ = \ \lim_{n\to\infty} \frac{1}{N}\sum_{n=1}^{N} \phi_n(x_i,t) \ , \tag{2.38}$$

with N being the number of members contained within the ensemble. With this concept, the process of Reynolds averaging can be performed on the Navier-Stokes and on the continuity equations (Eqs. 2.34 and 2.35), a process that yields the famous URANS equations:

$$\frac{\partial \overline{u}_i}{\partial x_i} \ = \ 0 \ , \tag{2.39}$$

$$\frac{\partial \overline{u}_i}{\partial t} \ + \ \frac{\partial}{\partial x_j}\left(\overline{u}_i\overline{u}_j + \overline{u'_i u'_j}\right) \ = \ -\frac{1}{\rho}\frac{\partial \overline{p}}{\partial x_i} \ + \ \frac{\partial \overline{\tau}_{ij}}{\partial x_j} \ , \tag{2.40}$$

where

$$\overline{\tau}_{ij} \ = \ \nu\left(\frac{\partial \overline{u}_i}{\partial x_j} \ + \ \frac{\partial \overline{u}_j}{\partial x_i}\right) \ . \tag{2.41}$$

In the URANS equations, the presence of the Reynolds stresses ($\overline{u'_i u'_j}$) means that the system of equations is not closed anymore. Closure requires some form of approximation where the Reynolds stresses are calculated in terms of the averaged flow quantities (i.e., the system is closed, in part, by reducing the number of unknowns). This is exactly the task of the several turbulence models that have been developed and validated in the past. In this study, the Spalart-Allmaras, one-equation turbulence model originally presented by Spalart and Allmaras (1994) is used, except that no trip term is present. This corresponds to what is known as the fully-turbulent mode of the Spalart-Allmaras model. As demonstrated by Rumsey and Spalart (2008), this turbulence model intends to be used for fully-turbulent, high Reynolds number flows, and should never be used to predict the laminar to turbulent transition. This is one main reason why the fully-turbulent mode is preferred by most users of this model.

In the Spalart-Allmaras turbulence model, as much as for several other models, the effect of turbulence is taken into account through the eddy-viscosity concept[8]. Indeed, the mixing effect of turbulence is here modeled as an increase of the fluid's molecular viscosity. With this concept, the Spalart-Allmaras turbulence model calculates the Reynolds stresses as:

---

[8] The Spalart-Allmaras turbulence model does not make use of the *original* eddy-viscosity concept. See Appendix A for more details.

$$-\overline{u_i' u_j'} \;=\; \nu_t \left(\frac{\partial \overline{u}_i}{\partial x_j} \;+\; \frac{\partial \overline{u}_j}{\partial x_i} \right) \;, \tag{2.42}$$

where ν_t is the turbulent kinematic viscosity. Following this modification, there is still one unknown in excess compared to the number of equations available. To solve this issue, a transport equation for ν_t has been developed based on an empirical approach, thus finally closing the system of equations. The interested reader may find the complete mathematical description of the turbulence model in Appendix A.

Previous work at the LMFN on pitch-heave oscillations of an airfoil, such as Julien et al. (2007) and Lapointe and Dumas (2012), validated the use of the Spalart-Allmaras turbulence model for this specific task. The authors came to the conclusion that although this model does not always provide excellent quantitative agreement with experimental data, the qualitative results and the trends are typically fairly good and reliable. As for any URANS model, great care must be taken when massive separations are encountered, and the reader must keep in mind the usual limitations of URANS simulations. It is recalled that this study is primarily concerned with the general trends and engineering predictions of the physical responses. Further, the good agreement between the URANS simulations and the experimental results for the kinematically-constrained device should not be forgotten (see Chapter 1). For these reasons, URANS simulations making use of the Spalart-Allmaras turbulence model appear to be justified in the present study. This will further be validated in Chapter 3.

2.2.3 Dynamic mesh and boundary/initial conditions

In the current implementation, the pitching and heaving airfoil problem is conveniently solved in a non-inertial frame of reference. The translational, heaving motion of the airfoil is thus taken into account via a proper volume, momentum source term effective over the entire calculation domain (100 chords × 100 chords), along with unsteady boundary conditions on the velocity at all inlets. The purpose of these boundary conditions is simply to add a time-varying y-component of velocity on the frontiers of the calculation domain. This component of velocity, in order to account for the heaving velocity of the airfoil, must be equal to the opposite of the heaving velocity ($-\dot{y}$). Conversely, the pitching motion of the airfoil requires moving-body and moving-grid capabilities, all of which are readily available within the *OpenFOAM-2.1.x* CFD toolbox. As shown in Figure 2.4, the central, circular portion of the mesh, which has a radius of 2 chords, is free to rotate about an axis passing through the circle's center. In fact, this rotating mesh is adjusted so that its center coincides with the elastic axis of the airfoil, and the rotation of this dynamic portion of the mesh is simply equal to the airfoil's angular position (θ). At the interface between the static and the dynamic portions of the mesh, an interpolation scheme is required due to the obvious non-conformity of the grids. This is achieved with the native *OpenFOAM* Arbitrary Mesh

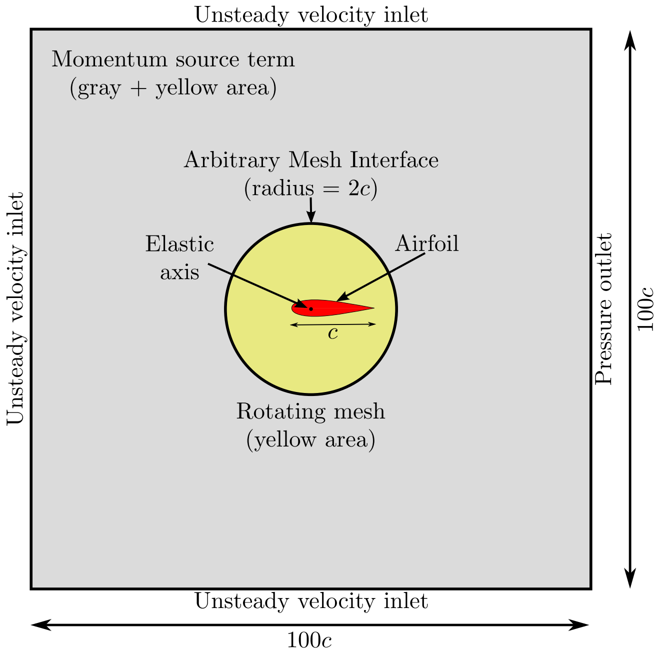

Figure 2.4: Configuration of the computational domain (not shown to scale) with its dimensions, the boundary conditions and the main features for solving the aeroelastic problem in a heaving reference frame.

Interface algorithm (see Farrell and Maddison (2011)).

This idea of solving the problem in the heaving frame of reference and using dynamic meshes for the pitching motion has been validated in the past by Kinsey and Dumas (2008) and Lapointe and Dumas (2011). The accuracy of the method has also been confirmed in the present investigation through the general validation of the solver (see Chapter 3). The main advantage of this technique is surely that it does not make use of remeshing or deforming meshes, which can turn out to be significantly demanding from a computational point of view.

Figure 2.4 also shows the boundary conditions used on the computational domain. The boundary conditions are further described in more details in Table 2.1. It is to be noted that the boundary conditions applied on the airfoil's surface are those required to satisfy the no-slip condition and the impermeability of the surface. Further, the derivative of a given parameter ϕ in a direction perpendicular to a boundary is written as $\partial\phi/\partial n$, and the value of the flow velocity ($\mathbf{u}$) is given in the form of a vector. Last, the numerical value of ν_t/ν given in Table 2.1 at the unsteady velocity inlets will be discussed in Chapter 3.

Concerning the initial conditions of the numerical problem, each simulation is initialized with uniform pressure and velocity fields throughout the domain. The initial value of the pressure field is set to zero, while the value of the velocity field corresponds to the superposition of the freestream velocity (U_∞) along the x-axis, and the opposite of the initial heaving velocity

Table 2.1: Boundary conditions used for solving the aeroelastic problem of a fully-passive, flapping-airfoil turbine in a heaving reference frame using *OpenFOAM-2.1.x*. Refer to Figure 2.4 for the location of each boundary in the calculation domain.

Boundary	Parameter	Type	Value
Unsteady velocity inlet	$\mathbf{u}$	Dirichlet	$\mathbf{u} = (U_\infty, -\dot{y}, 0)$
	p	Neumann	$\dfrac{\partial p}{\partial n} = 0$
	ν_t	Dirichlet	$\nu_t/\nu = 1$
Pressure outlet	$\mathbf{u}$	Neumann	$\dfrac{\partial \mathbf{u}}{\partial n} = 0$
	p	Dirichlet	$p = 0$
	ν_t	Neumann	$\dfrac{\partial \nu_t}{\partial n} = 0$
Airfoil's surface	$\mathbf{u}$	Dirichlet	$\mathbf{u} = (0, 0, 0)$
	p	Neumann	$\dfrac{\partial p}{\partial n} = 0$
	ν_t	Dirichlet	$\nu_t = 0$

$(-\dot{y}_i)$ along the y-axis. A uniform value of the turbulent viscosity field is also used throughout the domain. The prescribed value is the same as the one prescribed at the inlets (see Figure 2.1 and Table 2.1). Last, an initial heaving velocity $(\dot{y}_i)$ and/or an initial pitching rate $(\dot{\theta}_i)$ of the foil can be enforced at the beginning of the calculation. These initial velocities may model an external perturbation with which the airfoil is disturbed from its equilibrium position. Such a perturbation is not always required for the LCO to develop, but it has been found that an adequate choice of these initial velocities can greatly help at shortening the duration of the transient regime, which in turns shortens the total computational time. As a rule of thumb, a heaving initial perturbation $\dot{y}_i = 0.1U_\infty$ combined with the absence of an initial perturbation in pitch is generally an adequate initial setting.

2.2.4 Numerical schemes and solvers

To complete the description of the numerical methodology used to solve the aeroelastic problem, the various numerical schemes and solvers used to solve the equations of the flow should at least be mentioned. The transient terms are discretized using a second-order backward implicit scheme, while the convective terms are treated with a second-order scheme based on a linear upwind interpolation. Finally, the diffusive terms are discretized using a second-order scheme based on a linear interpolation, and an explicit non-orthogonal-limited surface-normal gradient scheme is also used. Furthermore, the linear equations solver is a generalized geometric-algebraic multigrid (GAMG) method for both the pressure and momentum equations, while a smooth solver using Gauss-Seidel method is used for the transport equation of ν_t.

For the task of solving the equations of motion of the airfoil (Eqs. 2.16 and 2.19), the system of two differential equations of degree two is decomposed into a system of four differential equations of degree one. In fact, *OpenFOAM-2.1.x* also demands an equation of degree one for all constants that appear in the equations of motion, but the value of their derivative is, of course, equal to zero. The resulting system of equations is then solved using a 4^{th} order Runge-Kutta method (see Fortin (2001)) readily available within *OpenFOAM-2.1.x*.

2.3 Fluid-structure coupling

Fluid-structure interaction (FSI) is a multiphysics problem that involves some interaction between a fluid and a body submerged within that same fluid. FSI is of great interest in several fields of engineering because vibrating structures or structures undergoing some sort of motion in a flow are frequently encountered. When this is the case, there exists a *two-way* interaction between the fluid and the structure. Indeed, the motion of the structure very often arises from the fluctuating forces generated by the fluid on the structure. In turns, the motion of the structure typically alters the flow pattern close to the structure (see He et al. (2012) and Yang et al. (2008)), which of course affects the forces. The strength of this dual interaction, which is often referred to as the FSI strength, is certainly variable and dependent upon various parameters. Howbeit, some situations where this two-way coupling between the equations of the fluid flow and the equations of the structure becomes large enough not to be negligible are frequently encountered in practice. This is certainly the case of airfoils undergoing LCO as a result of stall flutter such as those considered in the current study. To exemplify concretely this two-way interaction, it should be recalled from Chapter 1 that the flapping airfoil considered in this study is fluttering due to the hysteresis in the aerodynamic forces, thus giving rise to negative aerodynamic damping, while this same hysteresis depends upon the specific motion of the airfoil. Until recently, this type of interaction had primarily been studied experimentally. Nevertheless, experimental work is not always available or practical for various reasons, and numerical methods making use of CFD have been actively developed to fulfill the needs for accurate and inexpensive predictive methods of FSI phenomena.

In the relatively young field of numerical FSI, the aeroelastic problems studied have proven, in several circumstances, to be quite challenging and computationally demanding. The phenomena involved in FSI are often nonlinear and relatively convoluted. Some even believe that FSI is one of the most challenging current topics in the field of CFD (see He et al. (2012)). The challenge does not arise, per se, from the fact that numerical methods do not exist for the task of solving FSI problems. The challenge emerges much more from the fact that *robust* numerical solvers able to solve all FSI problems, regardless of the strength of the dual interaction, turn out to be highly expensive from a computational point of view. Therefore, the goal of recent research has been to actively develop numerical methods proving to be robust at a specific task, and also to make these methods much less computationally demanding.

Numerical approaches dealing with FSI are frequently divided into two main categories: the monolithic approach and the staggered (or partitioned) approach. In the first category, the equations of both the structure and the flow are combined within a single solver, and the whole system is solved iteratively. This methodology, apart from being computationally expensive, often demands a great deal of work in order to implement the solver that combines all equations. When a whole new FSI problem is considered, the equations may change significantly, and this can demand extensive work in order to adapt the monolithic solver. Although this is probably the most robust and accurate method for solving a FSI problem, it is not the most frequently encountered one due to its lack of flexibility and its high cost.

In the second category, one solves the equations of the flow and the equations of the solid in a sequential manner. This methodology offers attractive advantages over the monolithic one. This is because it permits recycling some numerical solvers that have previously been developed, and have already proven their numerical efficiency as much as their accuracy. In other words, implementing a staggered solver is much simpler, and generally requires far less work than what is needed for implementing a monolithic solver. To use the same terminology as the one from Degroote et al. (2008) and Olivier (2014), it is best to think of the fluid solver and the solid solver of the staggered approach as independent black boxes where each one of these black-box solvers may have been *individually* designed without giving thoughts about its interaction with other solvers. Very often, these black boxes are solvers that have been designed in order to be efficient at a specific task which is not necessarily FSI. To make use of these well-designed, specialized solvers within a FSI staggered solver, all that is required is to implement an adequate coupling scheme between them. Because of their great independence, one of the solvers can be changed at any time without altering the behavior or the implementation of the other. These properties make the staggered approach very convenient due to the minimal amount of work required to adapt the numerical solver to a whole new FSI problem. As a result of their great flexibility, it is without great surprise that they are more frequently used than monolithic solvers.

Staggered FSI solvers can be further subdivided according to the strength of the coupling schemes between the fluid and the structural solvers. This should not be confused with the aforementioned physical strength of the two-way interaction between the structure and the flow. Here, the coupling strength is purely a numerical matter, and refers to the robustness of the implemented numerical scheme dealing with the flow of information between the solvers, along with the sequential manner though which each solver is called. In the literature, the staggered solver is often qualified as being coupled explicitly, implicitly, strongly, weakly, etc.

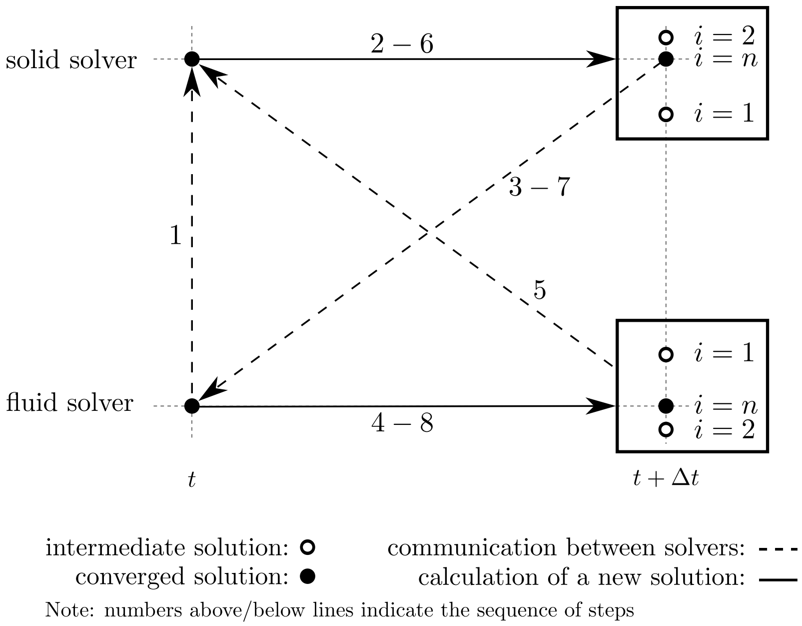

Figure 2.5: A typical implicit coupling scheme between the solid and the fluid solvers in a staggered, fluid-structure interaction CFD solver.

There is a plethora of terms that can be found, with many of them, in fact, referring to the same type of coupling. However, two main subcategories can be distinguished, here referred to as implicit and explicit coupling.

Generally speaking, a strongly or implicitly coupled staggered scheme includes subiterations within each numerical time step. The typical example of such a coupling scheme is shown in Figure 2.5. The numbers above the lines represent the sequence of events within the two initial subiterations. Of course, the subiterations improve the numerical accuracy of the solution. This is what is represented in Figure 2.5 with the solutions at $t+\Delta t$. As the number of iteration increases (i.e., i increases), the intermediate solution of each solver, represented with an unfilled circle, gets closer and closer to the converged solution, represented with a filled circle. The subiterations also have another great advantage: they make the procedure insensitive to the well-known added mass instability, which is discussed later. The implicit coupling is thus more robust and so is called *strong coupling*. However, this type of coupling scheme remains relatively expensive. In fact, if C_{FSI} is the computational cost of the FSI solver, C_F is the cost of the fluid solver and C_S is the cost of the solid solver, one can safely argue, in general, that:

$$C_{FSI} \gg C_F + C_S . \tag{2.43}$$

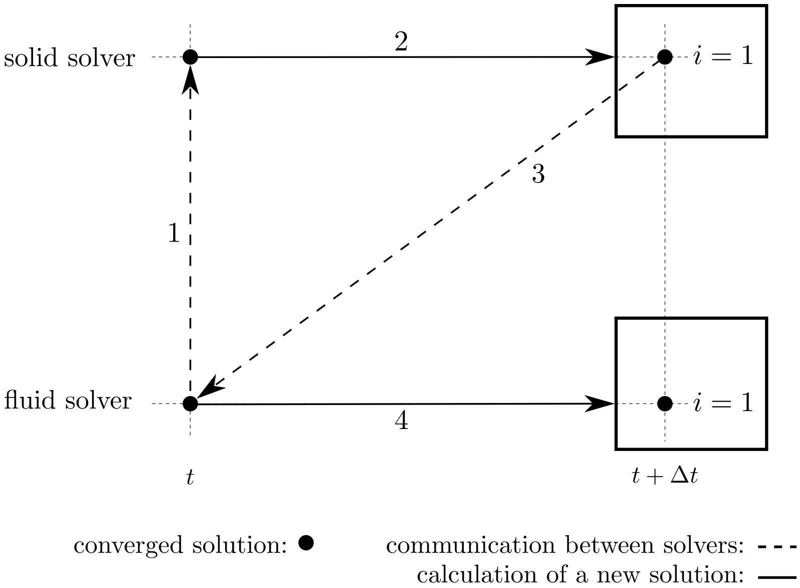

Note: numbers above/below lines indicate the sequence of steps

Figure 2.6: A typical explicit coupling scheme between the solid and the fluid solvers in a staggered, fluid-structure interaction CFD solver.

In the best case, one could replace the *much greater* symbol ($\gg$) of the above relation with a less restrictive *greater* symbol ($>$). One reason for this relatively high cost of computation is the fact that this coupling scheme should include some relaxation. This inevitably makes the convergence of the solution more computationally demanding. Other alternatives to relaxation exist, such as the use of pseudo-compressibility (see Olivier (2014)), but the cost remains fairly high in all cases. Another reason for the increased numerical cost is obvious: each solver is called more than once per time step in most situations. However, this coupling scheme has not been retained in the present study for reasons that shall shortly become clear.

The second subcategory of staggered solvers is the explicitly or weakly coupled one. In this approach, no subiterations are carried out within a numerical time step. A typical example of such coupling scheme is shown in Figure 2.6. Again, the numbers above the lines indicate the sequence of events, and the schematic depicts clearly that a single iteration is performed, thus leading immediately to the next-step solution for each solver (i.e., no intermediate solution is present). The main advantage of such a strategy can be conveniently expressed through the following relation:

$$C_{FSI} \;\approx\; C_F \;+\; C_S \;. \tag{2.44}$$

Indeed, the cost of such a numerical methodology is considerably lower than the cost of an implicit numerical scheme. In the explicit scheme, the coupling itself has a negligible cost, and each solver, fluid and structure, is called only once. The minimal cost of this method turns out to be very appealing, but unfortunately there are some drawbacks associated to it. As a matter of fact, this type of coupling can prove to be unstable under some circumstances due to the well-documented added mass effect[9] (see Causin et al. (2005); Degroote et al. (2008); Förster et al. (2007) and He et al. (2012)). As a result of the staggered character of this scheme, and the absence of subiterations, there is an inherent time lag between the fluid and the structural subsystems. More concretely, this means that when a solver is called, the other one is conceptually at a different solution time. This time lag becomes a numerical stability issue when the CFD solver deals with the equations of an incompressible fluid, and when the strength of the interaction between the fluid and the structure is important. Indeed, when an incompressible fluid is assumed, the elliptical character of the pressure equation becomes problematic[10]. As mentioned previously, the role of the pressure equation is to enforce the incompressibility constraint, and it turns out to be a relatively stiff equation (i.e., it is more reactive to numerical errors). Because it is elliptical in character, any error on the pressure propagates instantaneously through the whole domain and affect the entire pressure field. A very raw but meaningful explanation is to think of the time lag as introducing some sort of holes in the calculation grid, the holes being the locations where there is no fluid and no solid. When the interaction between the solid and the structure is strong, the motion of the solid between each time step is greater, and the size of the holes created in the grid increases. When the CFD solver tries to calculate a new flow field and tries filling the holes, this locally affects greatly the pressure field. However, because of the elliptical character of the pressure equation, perturbations on the pressure field propagate instantaneously throughout the whole calculation domain. This has catastrophic effects on the overall numerical solution, if any is obtained, and it is generally impossible for the solver to recover from such an undesirable situation.

It is well known that the strength of the FSI is particularly important when the density of the fluid (ρ_f) is comparable or greater than the density of the solid (ρ_s). This is so because the forces exerted on the structure are proportional to the fluid's density (ρ_f), while the reaction of the solid is proportional to its own density (ρ_s). As the ratio ρ_s/ρ_f becomes smaller, the structure becomes more and more responsive. This, in turns, amplifies the numerical errors arising from the mismatch in time of both solvers. Generally speaking, the following stability criterion may be obtained through advanced mathematical considerations of simplified aeroelastic problems (see Causin et al. (2005) and Förster et al. (2007)):

---

[9] This instability is called added mass effect in the literature because the effect of the fluid entrained with the moving body can be seen as an increase of the total mass of the structure. The rationale of this becomes more obvious when advanced mathematical studies of the instability are performed, but this is beyond the scope of the present text.

[10] When a compressible fluid is assumed, the instability due to the added mass effect is not present. This is the basis of the artificial compressibility method previously mentioned. More details can be found on this matter in the thesis of Olivier (2014).

$$\frac{\rho_s h_s}{\rho_f \mu_{max}} > \zeta \ , \tag{2.45}$$

where h_s is a characteristic thickness of the structure and μ_{max} is the largest eigenvalue of the discrete operator arising in the structural solver discretization. This last parameter only depends on the geometry of the problem considered. On the other hand, the value of ζ may depend upon the specific numerical schemes used, such as the order of convergence of the numerical schemes, to solve the equations. In general, increasing the order of the numerical schemes increases the value of ζ, which makes the stability criterion more restrictive (i.e., the solver is less robust). As a rule of thumb, and as a first order approximation, this stability criterion may be approximated as:

$$\frac{\rho_s}{\rho_f} > 1 \ . \tag{2.46}$$

That being said, Eq. 2.46 shows that decreasing the ratio ρ_s/ρ_f may lead to a numerical instability. Further, as shown with Eq. 2.45, decreasing the characteristic thickness of the structure is also problematic. This last finding is of no concern in the current work as the thickness of the airfoil is held constant.

The time lag between both solvers being the reason why some numerical instabilities can be encountered, one could reasonably suggest to reduce the size of the time step in order to avoid the numerical instability. However, the effect of such a modification is counter-intuitive, and it turns out to only make things worse. Indeed, when the displacement error of the fluid-structure boundary is divided by a smaller time step, this increases the error on the velocity of that same boundary. Otherwise said, decreasing the time step amplifies the numerical errors already present, thus leading to a divergence of the physical variables from the physical reality. FSI problems making use of a staggered coupling scheme are then subject to a classical upper bound criterion on the time step (i.e., the CFL condition), as much as to a criterion on the minimal value of the time step, which is due to the added mass instability.

With this in hand, the main reason why the staggered, explicit coupling scheme is so successful in the field of aeronautics is not obvious. In fact it is simple. Because the density of the fluid is typically considerably smaller than the structural densities used in this specific discipline, most aeroelastic calculations in aeronautics are not prone to the added mass instability. As a result, using an explicit coupling scheme provides the desired accuracy at a minimal cost when compared to an implicit coupling scheme.

In the current study, the staggered coupling scheme has been chosen due to its lower numerical cost. This, of course, is achieved at the cost of being susceptible to the added mass instability. For fully-passive, flapping-airfoil wind turbines, this is certainly not an issue as a result of the low fluid's density. However, for a hydrokinetic turbine, this numerical stability criterion may restrict the size of the parametric space that can be investigated with the implemented tools. Indeed, hydrokinetic turbines are typically conceived with a lower density ratio than what is found in wind turbines.

The reader who might be interested in having more details on the various coupling schemes used in FSI is referred to a comprehensive text on this matter within the thesis of Olivier (2014). Further, the staggered FSI coupling scheme chosen for the sake of this study will later be validated and characterized more precisely in Chapter 3.

Conclusion

Within this chapter, the aeroelastic modeling of the fully-passive, flapping-airfoil turbine has first been introduced. All parameters involved in the modeling have been presented, followed by the formal derivation of the equations of motion. This has been achieved by making use of the well-known Lagrange's equation. This method is the one typically used in order to obtain the governing equations of motion in the field of aeroelasticity. It has been found that the equations of motion are coupled through the aerodynamics and through an inertial coupling term arising from the voluntary misalignment of the elastic axis and the center of mass of the pitching components. Further, a total of seven structural parameters can be varied to modify the dynamics of the oscillating airfoil. The non-dimensional formulation of the aeroelastic problem has also been introduced, and this formulation will be used throughout the current document for convenience.

Next, the fluid-structure solver has been presented. This includes a presentation of the methodology used to solve the equations of the flow and the equations of the structure. Through this section, the various choices made on the modeling and on the numerical methodology have been briefly discussed.

In the last section, an overview of the various coupling schemes between the fluid and the structural solvers has been presented. Some limitations associated to the scheme used in the current study, namely the staggered explicit scheme, have also been addressed. In fact, a numerical instability known as the added mass effect emerges when a strong interaction between the fluid and the structure is involved, and when an incompressible fluid is considered. This numerical instability is greatly related to the elliptical character of the stiff Poisson equation for the pressure. A validation of the numerical methodology is to be presented in the next chapter, and this coupling scheme will also be further investigated.

Chapter 3

Validation of the FSI solver

This chapter aims at validating the methodology used for the task of solving the aeroelastic problem of the fully-passive, flapping-airfoil turbine. The specific methodology, which has been thoroughly presented within the previous chapter, is here validated into two complementary ways. First, some experimental results for a fully-passive, flapping airfoil investigated at the RMC in Kingston, Ontario, are compared to the present FSI solver's predictions. This experiment has been described in Chapter 1 of this thesis. The idea here is really to put the FSI solver to the test by comparing the numerical predictions with the experimental observations from the RMC. While reading through this section, the reader should remain fully aware that the RMC experiment has been performed in the transitional range of Reynolds number, while the current FSI solver has been specifically developed to be used in a turbulent regime more representative of a turbine application. Nevertheless, such a validation of the numerical predictions, as it will be seen, proves to be very useful, and it helps assessing the validity of the solver.

As a second validation, the well-documented aeroelastic problem of an oscillating cylinder is used. In this FSI problem, the cylinder is undergoing vortex induced vibrations (VIV). Some past numerical results are used for the sake of studying the validity of the numerical predictions obtained with the FSI solver of this thesis. Moreover, the results of a low Reynolds number experiment are used to push the validation a step further. As a final case, the same aeroelastic problem of the cylinder undergoing VIV is used as a way to assess the performances of the present FSI solver when the physical strength of the FSI is increased. The objective here is to characterize the specific behavior of the solver when a moderate to high interaction level is present between the fluid and the structure.

3.1 Flapping airfoil

The main validation of the complete flapping-airfoil model has been carried out through two-dimensional numerical simulations in the transitional range of Reynolds numbers. As pointed out in Chapter 1, a research group from the RMC in Kingston, Ontario, published some results concerning a fully-passive, flapping-airfoil aeroelastic device that is very similar to the one considered in this study (see Mendes et al. (2011) and Poirel and Mendes (2011)). In fact, the apparatus at the heart of the experimental study conducted at the RMC shares the exact same equations of motion as those derived in Chapter 2 of the current study. The only difference between the experimental work and the current study resides in the choice of the flow and the structural parameters. This is so because the objectives of both studies are significantly different, and, as a result, a different region of the parametric space has been investigated. Nevertheless, this indicates that no modification at all of the FSI solver is required in order to numerically replicate the experiment of the RMC.

It should be recalled from Chapter 1 that the experimental work conducted at the RMC has involved Reynolds numbers between 50,000 and 120,000. This is, of course, in contrast with the Reynolds number of 500,000 used in the current numerical study of the fully-passive, flapping-airfoil turbine. Nevertheless, the experimental results remain of great interest for validating the solver. For this reason, the experiment of the RMC has been reproduced with the current FSI solver over this range of transitional Reynolds numbers. The set of structural parameters reported in Table 1.1 has been used throughout this validation, and it is based on the values published for the setup used at the RMC. Further, both the low heave stiffness case ($k_h = 800\ N/m$) and the large heave stiffness case ($k_h = 1484\ N/m$) have been studied numerically, which are the same cases as those of the experiment. As the reader will soon realize, this test case is not only used in order to assess the physical validity of the numerical results. In fact, it is also used to the extent of studying the independence of the numerical results from the temporal and the spatial discretizations, as well as from the convergence criteria, and from the turbulence model.

3.1.1 Baseline numerical values

The baseline numerical parameters presented here are those used for predicting the motion of the airfoil in the transitional range of Reynolds numbers, as well as for the case at Re = 500,000. This means that the same numerics is used for the simulations in the transitional range of Reynolds number of this chapter, and for the simulations at Re = 500,000 of the following chapters. The specific choice of each numerical value will be validated and justified within the following subsections.

In all simulations of this thesis, a time step providing a minimum of 3,000 steps per period of oscillation (T) and a minimum of 200 steps per convective time unit (c/U_∞) is used, unless otherwise noted. To respect these constraints, the choice of a time step can be summarized with the following equation:

$$\Delta t \;=\; \min\left\{\frac{1}{3000\,f}\;,\;\frac{c}{200\,U_\infty}\right\}\;, \tag{3.1}$$

where f is the frequency of oscillation. It is worth mentioning that the specific frequency of oscillation is not always known *a priori*. This means that the requirement on the time step given by Eq. 3.1 should also be verified *a posteriori*, once the predicted motion of the airfoil is obtained. Further, a baseline convergence criterion of 1×10^{-5} is enforced on the pressure residuals, while a criterion of 1×10^{-6} is used for both the momentum and the turbulent quantities.

The 2D computational grid used is shown in Figure 3.1, and it is in agreement with the general description of the computational domain presented in Chapter 2. The grid is built with approximately 65,000 cells with close to 450 points on the airfoil to provide enough near-body resolution, and to capture sufficiently the physics of the flow. The first cell thickness is set in order to respect $y^+ \approx 1$ on the airfoil's surface for all simulations. It must be clear that the mesh used for the simulations in the transitional range of Reynolds numbers is the same for all velocities of the freesteam flow, which means that the first cell thickness has been chosen according to the most restrictive case considered, which is here the one at Re = 120,000. Further, the 2D grid used for the numerical study at Re = 500,000 is very similar to the one here presented. In fact, only the wall-normal resolution has been slightly refined in order to again respect a value of y^+ approximately equal to 1.

Concerning the turbulent viscosity ratio, a value of $\nu_t/\nu = 1$ is used at all inlets of the computational domain. This yields negligible turbulent mixing at a station immediately upstream of the airfoil. Some simulations have been carried out with a ratio of ν_t/ν greater and lower by one and two orders of magnitude (i.e., ratio of ν_t/ν of 0.01, 0.1, 10 and 100), and no significant variations have been observed on the numerical results. This indicates that the airfoil's motion is not sensitive to the chosen value of ν_t/ν at the inlets, as much as from the initial condition within the domain. Furthermore, a value of $\nu_t/\nu = 1$ is consistent with the recommended value for the Spalart-Allmaras turbulence model when used in the fully turbulent mode (see Spalart (2000) and Spalart and Rumsey (2007)).

As mentioned in Chapter 2, all simulations are initialized with a perturbed airfoil unless otherwise noted. This is achieved here by specifying an initial heaving velocity ($\dot{y}_i$). All other initial values are set to zero, namely $y_i = 0$, $\theta_i = 0$ and $\dot{\theta}_i = 0$. The parameter $\dot{y}_i$ is set to approximately 5-10% of U_∞. After trying several initial perturbations, it has been found that such a value of $\dot{y}_i$ typically shortens the duration of the transient regime. The flow and the structural parameters also influence the duration of the transient regime, and care must

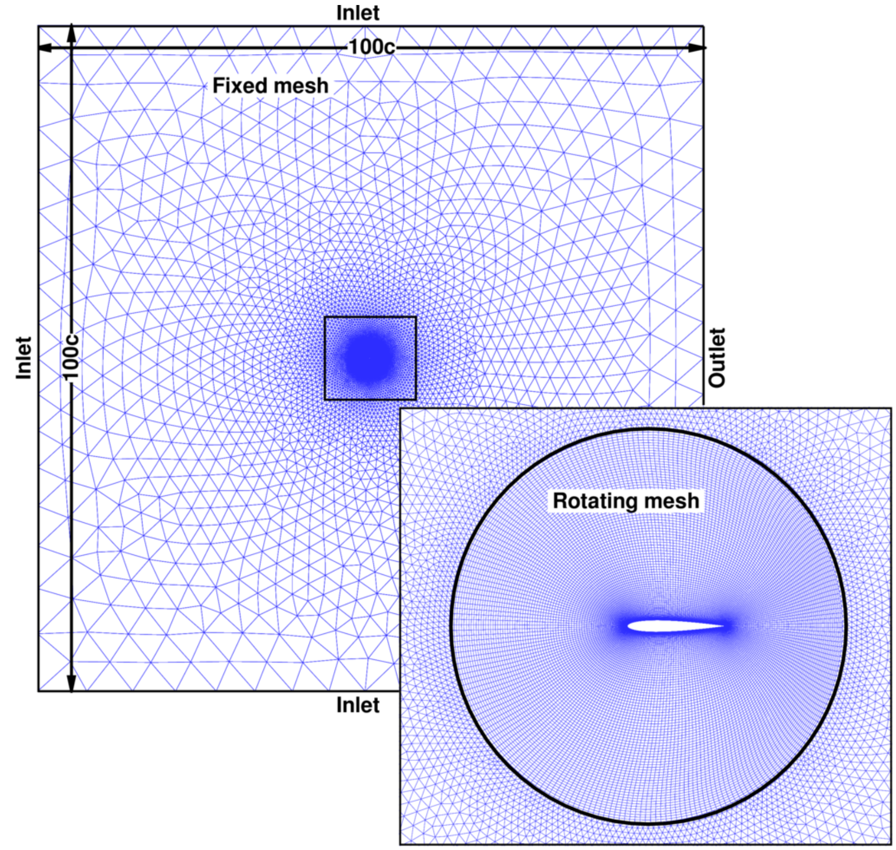

Figure 3.1: Main features of the computational grid used for the numerical simulations in the transitional range of Reynolds numbers, as well as for those at Re = 500,000.

be taken in order to minimize its duration as this directly affects the total time required to achieve a complete simulation. Nevertheless, it has been verified that the terminal LCO regime is not dependent upon the initial perturbation unless an excessively large perturbation is provided. When such an excessively large perturbation is provided, the airfoil simply flips over (i.e., $\theta > 180°$), and this rapidly has disastrous consequences on the numerical solution.

As it has been stated earlier, the one-equation Spalart-Allmaras turbulence model has been used throughout the current research project. However, this chapter contains some laminar [1] computations (i.e., no turbulence model is used), and some computations using the SST k-ω turbulence model from Menter (1994) (see Appendix A for a description of this model). The objective is to assess the independence of the results from the chosen turbulence model. In the simulations using the SST k-ω model, various inlet turbulence intensity have been

---

[1] This type of numerical simulations can be thought of as an under-resolved DNS, or an Implicit LES (ILES) (see Jiang and Lai (2009)). Typically, DNS and LES are used for 3D simulations. However, the same *philosophy* has been used here for 2D simulations: no explicit SGS model is present. Instead, dissipation of the turbulent energy is achieved through numerical dissipation. Generally, ILES requires the use of some very specific numerical schemes where the truncation error is chosen in order to act as a well-adapted SGS model. In the simulations here achieved, the numerical schemes have not been changed or adapted. It must be emphasized that the idea is only to assess the effect of the chosen turbulence model by simply deactivating it.

Table 3.1: Relative effect of the time step with respect to the most refined simulation results on the lift coefficient ($C_{\mathcal{L}}$), the aerodynamic moment coefficient (C_{Mea}) and the drag coefficient ($C_{\mathcal{D}}$), along with its effect on the motion in both pitch (θ) and heave (y).

Time step	$C_{\mathcal{L}}$ (%)	C_{Mea} (%)	$C_{\mathcal{D}}$ (%)	θ (%)	y (%)
Coarse (500 steps/cycle)	2.63	2.20	3.12	0.40	0.18
Baseline (3,000 steps/cycle)	0.42	0.59	0.72	0.16	0.05
Fine (26,000 steps/cycle)	—	—	—	—	—

investigated, and very little change have been observed for an increase or decrease of one order of magnitude of this parameter. A fairly low inlet turbulence intensity of approximately 0.2% has finally been retained for the calculations making use of this turbulence model.

3.1.2 Results' independence

The independence of the numerical results from the time step size has been demonstrated by varying the time step from the baseline criterion used throughout the simulations, which is provided by Eq. 3.1. Table 3.1 shows the effect of varying the time step. The effect is quantified by computing the RMS value over three complete cycles of oscillations for the lift coefficient ($C_{\mathcal{L}}$), the aerodynamic moment coefficient about the elastic axis (C_{Mea}), the drag coefficient ($C_{\mathcal{D}}$), and the motion in both pitch (θ) and heave (y). The relative variations shown are in percents, and they have been computed by taking the most refined case as the reference. The most refined time step provides 26,000 steps per period of oscillation and 2,400 steps per convective time unit. Using the baseline requirement instead of the fine time step did not affect noticeably the results. Variations of less than 0.2% are observed on both motions, and variations of 0.75% or less are observed on the aerodynamic forces and moments. Conversely, a coarser time step providing 500 steps per period and 50 steps per convective time unit has also been investigated, and variations of less than 0.4% are observed on both amplitudes of motion, but the differences are in the range of 2% to 3% for the aerodynamic forces and moments. These results confirm that the baseline requirement provided by Eq. 3.1 is sufficient and adequate.

Concerning the numerical convergence criteria used on the physical quantities, a refinement and a coarsening of one order of magnitude from the baseline values did not significantly affect any of the parameters recorded, which are the same as the ones considered above. The results are shown in Table 3.2, and the effect is again quantified as a relative variation, in percents, from the case using the most refined criteria. The maximum differences on $C_{\mathcal{L}}$, C_{Mea} and $C_{\mathcal{D}}$ have been found to remain below 0.01%, which is certainly a very negligible difference. The same observations hold true for both motions. As a result, it could be justified

Table 3.2: Relative effect of the convergence criteria on the lift coefficient ($C_{\mathcal{L}}$), the aerodynamic moment coefficient (C_{Mea}) and the drag coefficient ($C_{\mathcal{D}}$), along with its effect on the motion in both pitch (θ) and heave (y). Refer to the text for a description of the criteria used.

Mesh	$C_{\mathcal{L}}$ (%)	C_{Mea} (%)	$C_{\mathcal{D}}$ (%)	θ (%)	y (%)
Coarse	0.004	0.004	0.006	0.002	0.002
Baseline	0.000	0.000	0.000	0.000	0.000
Fine	—	—	—	—	—

Table 3.3: Relative effect of the grid resolution on the lift coefficient ($C_{\mathcal{L}}$), the aerodynamic moment coefficient (C_{Mea}) and the drag coefficient ($C_{\mathcal{D}}$), along with its effect on the motion in both pitch (θ) and heave (y).

Mesh	$C_{\mathcal{L}}$ (%)	C_{Mea} (%)	$C_{\mathcal{D}}$ (%)	θ (%)	y (%)
Coarse (30,000 cells)	0.52	1.37	1.62	0.88	0.17
Baseline (65,000 cells)	0.13	0.97	1.38	0.67	0.18
Fine (120,000 cells)	—	—	—	—	—

to use the coarser criteria. However, using the coarser criteria does not provide much gain in computational time. For this reason, it remains safer to use the baseline values throughout the numerical study.

Mesh refinements in the rotating portion of the grid have been considered both in the streamwise and the wall-normal directions. The validation has been achieved with a run on a coarse grid of approximately 30,000 cells with approximately 250 points on the airfoil, and with a run on a refined grid of approximately 120,000 cells with 650 points on the airfoil. The results are shown in Table 3.3, where the same quantities as before are used to quantify the effect of the mesh resolution. Once again, the relative differences, in percents, are calculated using the fine grid as a reference. As shown, the variations on $C_{\mathcal{L}}$, C_{Mea} and $C_{\mathcal{D}}$ are in the range of 1.6% and below for both the coarse and the baseline grid, and the differences on θ and y remain well below 1%. It should be noted that the parameter most influenced by the grid resolution, namely the drag coefficient, is not involved in the equations of motion of the fully-passive, flapping airfoil. Therefore, these results confirm that using the baseline grid is sufficient and adequate for the current task.

At last, because all computations have been performed on multiple processors in parallel, the results of a serial computation have been compared to those of a parallel computation achieved on eight cores. All quantities checked matched nearly perfectly, thus indicating the adequate parallelization of the tools used to solve the current aeroelastic problem.

3.1.3 Comparison with experimental results

Before moving on to the comparison of the CFD results with the experimentally measured values, it must be recalled from Chapter 1 that a numerical value for the heave structural damping coefficient (D_h) has not been provided for the experimental setup of the RMC. Instead, Figure 1.7 displays the experimental heave damping ratio (ξ_h) as a function of the normalized heaving amplitude (y_0/c). However, the current implementation of the FSI solver does not allow to modulate any of the damping coefficients according to the instantaneous dynamics of the airfoil. In order to circumvent this possible issue, a hypothesis has been made concerning the value of the heave damping coefficient: the damping ratio (ξ_h) in heave is considered to be constant and equal to the asymptotic value for a large amplitude of motion in heave. This yields a damping coefficient $D_h = 2\ Ns/m$. This hypothesis will be revisited and discussed *a posteriori* once a prediction of the amplitudes of motion is available.

Using the aforementioned parameters of Table 1.1, several numerical simulations have been performed for the range of freestream velocities (U_∞) investigated in the wind-tunnel experiment of the RMC. In the experiment, the velocity of the flow has been varied between 4.68 m/s, which corresponds to Re = 50,000, and 11.23 m/s, which corresponds to Re = 120,000. However, it should be mentioned that experimental results are not available throughout this complete range of freestream flow velocities for the large heave stiffness case. This is because the amplitude of motion of the flapping airfoil became large enough to fear that it would impair its structural integrity. Nevertheless, this complete range of velocities has been experimentally studied for the low heave stiffness case. As it will be seen, the amplitudes of motion are not as important, and no structural failure was feared.

Large heave stiffness

Experimental and CFD results for the case using a large heave stiffness of $k_h = 1484\ N/m$ are gathered in Figures 3.2 and 3.3, where the reduced frequency ($f^* = fc/U_\infty$), the normalized heaving amplitude (y_0/c) and the pitching amplitude (θ_0) are shown for various Reynolds numbers. The decoupled reduced natural frequencies for both the pitch ($f_{N,p}\, c/U_\infty$) and the heave ($f_{N,h}\, c/U_\infty$) degrees-of-freedom are also plotted, where:

$$f_{N,p} \; = \; \frac{1}{2\pi}\sqrt{\frac{k_\theta}{I_\theta}} \; , \tag{3.2}$$

$$f_{N,h} = \frac{1}{2\pi}\sqrt{\frac{k_h}{m_h}} . \qquad (3.3)$$

As it can be observed in Figure 3.2, a single frequency of oscillation emerges for this two-degree-of-freedom device (i.e., the frequencies in pitch and in heave are the same). The coalescence of the frequencies has already been explained in Chapter 2 within the theoretical discussion on flutter. It can be seen that an excellent match is obtained between the experimentally measured frequencies and the numerically predicted frequencies for the limited range of Reynolds numbers covered by the experiment. For both the experimental and the CFD values, the apparatus oscillates at a frequency nearly identical to the calculated decoupled natural frequency in heave ($f_{N,h}$). This indicates that aerodynamic stiffening in heave is not significant in this specific regime of oscillation. However, the aerodynamic stiffening is significant on the rotational motion of the airfoil. Outside of the experimental range, the predicted frequencies still agree fairly well with the decoupled natural frequency in heave, but there is no way to tell if this is in agreement with the experiment. Further, the values predicted without turbulence modeling, which are labeled as laminar, are almost identical to those predicted using the Spalart-Allmaras URANS model. This is not unexpected at these moderate Reynolds numbers.

Figure 3.3 shows that the experimentally measured amplitudes of motion compare well with those predicted through the FSI solver over the limited experimental range of Reynolds numbers. Nevertheless, as previously mentioned, the experiment on the large heave stiffness case has been stopped at a lower freestream flow velocity due to the rapid growth of the amplitudes of motion. That being said, the predicted values indeed show that both amplitudes of motion keep growing past the maximum wind-tunnel velocity for which experimental values have been published. This appears to be in qualitative agreement with the observations of the RMC.

Concerning the laminar results shown in Figure 3.3, some error bars are shown as a way to quantify the amount of fluctuations within the predicted amplitudes of motion from one cycle to the other[2]. The average amplitude is therefore displayed with error bars extending up to the maximum and the minimum amplitudes recorded. These laminar simulations predict amplitudes that are slightly lower or equal to those predicted with the Spalart-Allmaras turbulence model. It must be noted that the differences between the predictions of both series increase as the Reynolds number grows.

Unfortunately, the experimental uncertainties over the results, as much as the uncertainties over the structural parameters of the device, have not been addressed in the work of the RMC. Nevertheless, the good agreement with the experimentally measured values is a first

---

[2] Indeed, stable LCO are not obtained through laminar simulations. Instead, a modulation of the amplitudes is observed.

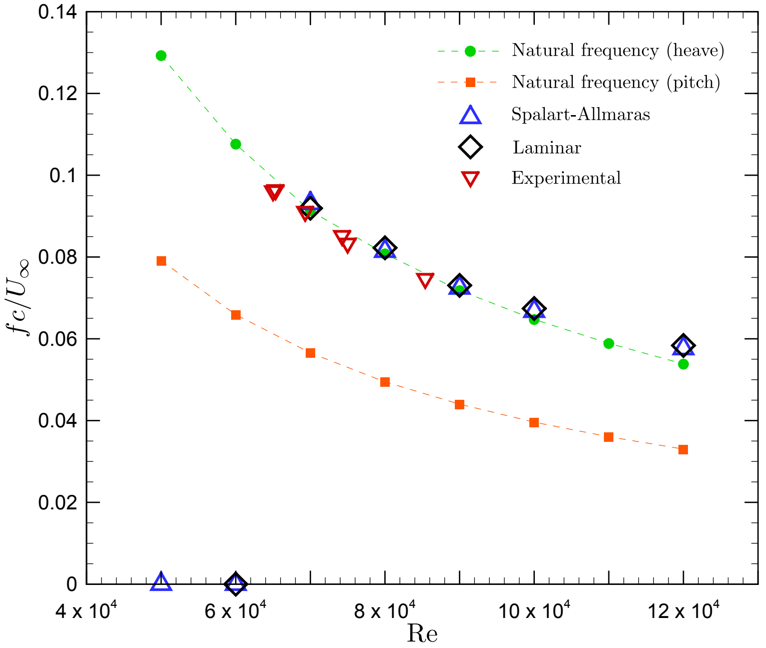

Figure 3.2: Comparison of the numerically predicted reduced frequencies with the experimentally measured reduced frequencies and with the calculated decoupled natural structural frequencies for the large heave stiffness case ($k_h = 1484\ N/m$). Experimental values from Poirel (2012) and Poirel and Mendes (2011).

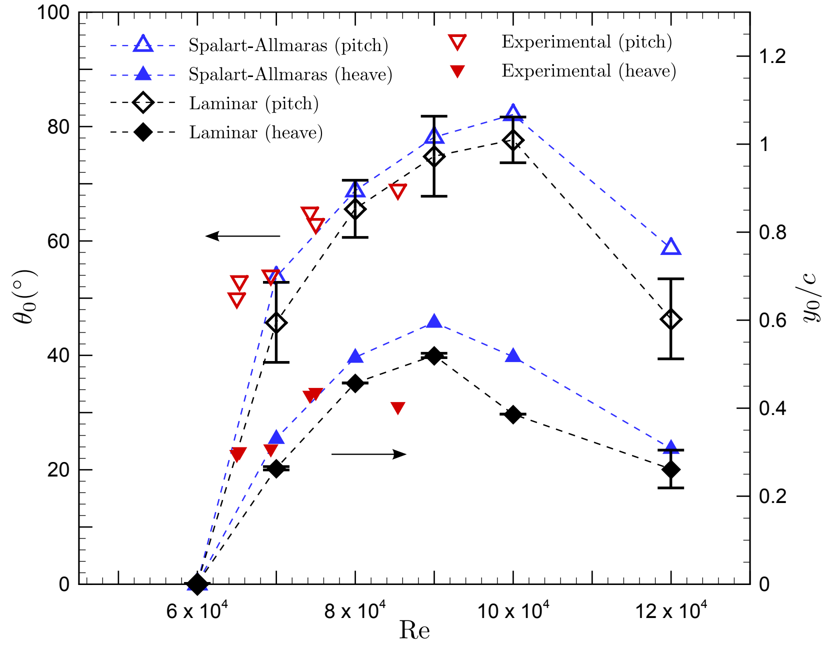

Figure 3.3: Comparison of the numerically predicted amplitudes of motion in both pitch and heave with the experimentally measured amplitudes of motion for the large heave stiffness case ($k_h = 1484\ N/m$). Error bars on the laminar results show the amount of fluctuations within the amplitude of motion from one cycle to the other. Experimental values from Poirel (2012) and Poirel and Mendes (2011).

confirmation of the validity of the FSI solver used in this numerical study. Furthermore, the numerical results obtained with and without the modeling of turbulence are definitely in the same range of values, and the trends are the same.

Low heave stiffness

Several numerical simulations have also been carried out for the low heave stiffness case, where $k_h = 800\ N/m$. The experimentally measured reduced frequency of oscillation, along with the frequency predicted with the FSI solver, are shown in Figure 3.4. Further, the maximum effective angle of attack of the airfoil is shown in Figure 3.5. Unfortunately, the experimental pitching amplitude (θ_0) of the airfoil has not been published. Instead, only the effective angle of attack has been published, and this quantity is classically calculated as follows[3]:

$$\alpha = \theta - \arctan\left(\dot{y}/U_\infty\right) \ . \tag{3.4}$$

Defined as such, the effective angle of attack accounts for the pitching motion, as much as for the heaving velocity ($\dot{y}$) of the airfoil, which changes the magnitude and orientation of the effective freestream flow seen by the airfoil. Because not enough data has been published, it has not been possible to extract the pitching amplitude from the results of the RMC. For this reason, the results obtained with CFD, which are shown if Figure 3.5, also correspond to the effective angle of attack so that a direct comparison among all sets of data is still possible. Another unfortunate circumstance is the lack of published results concerning the amplitude of motion in heave. Although no comparison of this parameter is possible with the experiment, the amplitudes predicted with the FSI solver are shown in Figure 3.6.

As shown in Figure 3.4, the reduced frequencies predicted through CFD compare very well with the experimentally measured reduced frequencies. For the simulations making use of the Spalart-Allmaras turbulence model, the match is excellent in the lower range of Reynolds numbers, and a slight discrepancy appears as the Reynolds number is increased. Concerning the maximum effective angle of attack shown in Figure 3.5, the CFD values predicted with the Spalart-Allmaras turbulence model exhibit a trend that agrees favorably well with the experiment, especially for Reynolds numbers below 80,000. Nonetheless, the CFD values obtained with the Spalart-Allmaras model remain lower than the values measured during the experiment. The same conclusions still hold true concerning the numerical results obtained through simulations making use of the SST k-ω turbulence model. In fact, it is observed that the Spalart-Allmaras turbulence model provides results that are very close to those obtained with the SST k-ω turbulence model. For this reason, it does not appear justified to use the

---

[3] Unfortunately, some uncertainties remain on the method used by the RMC to compute/measure the maximum effective angle of attack.

two-equation SST k-ω turbulence model. Indeed, the one-equation Spalart-Allmaras model turns out to be sufficient and adequate for the current task.

In counterpart, the numerical values predicted with the laminar simulations appear to be more representative of the experimental results for both the reduced frequency and the maximum effective angle of attack, but this is especially true for the predicted frequencies. The fact that a better match is obtained between CFD and the experiment through laminar calculations suggests that the turbulence model struggles at predicting some features of the flow. In fact, this is not a great surprise, and this has been expected before running any CFD simulation: the Spalart-Allmaras turbulence model and the SST k-ω turbulence model have not been developed for applications in the transitional range of Reynolds numbers. As a matter of fact, they both appear to produce too much turbulent viscosity (ν_t), especially in the higher range of the transitional Reynolds numbers investigated in the experiment. This alone could explain why the slight mismatch between the experiment and the CFD increases with the Reynolds number when one of the turbulence models is used.

Contours of the turbulent viscosity ratio (ν_t/ν) in the vicinity of the airfoil's surface are shown in Figure 3.7. As one might observe, the ratio of turbulent viscosity in the attached boundary layer (i.e., on the upper surface) is somewhat larger than expected, especially for Re = 120,000 at which one might suspect a laminar boundary layer in that region. Contours of vorticity are shown in Figure 3.8, and the vorticity field is found to be very different for a laminar simulation than what is obtained with the Spalart-Allmaras turbulence model. The effective body of the airfoil is therefore considerably thinner for the laminar simulations, which affects the forces on the airfoil. The Reynolds number also has a significant effect on the vorticity field, but direct comparison between cases at different Reynolds numbers is more iffy since the dynamics of the airfoil is also significantly modified when the Reynolds number is varied by changing the freestream velocity (U_∞). An alternative to these issues would be to make use of a transitional turbulence model, but this is certainly out of the scope of this study due to the intent of using the FSI solver at Re = 500,000 for studying the fully-passive, flapping-airfoil turbine. The reader should understand that for Re = 500,000, the preceding issues observed with the turbulent modeling are not likely to be a factor.

In order to assess the effect of the aforementioned uncertainty relative to the numerical value of the heave damping coefficient (D_h), a few simulations have been carried out with some variations of this parameter. The effect of these modifications on the reduced frequency and on the maximum effective angle of attack are shown in Figures 3.9 and 3.10. The variations of D_h were such that self-sustained oscillations were still possible (i.e., no extreme values of the damping in heave preventing flutter to occur have been used). As shown in Figure 3.9, these modifications did not prove to have a significant effect on the reduced frequency. Note that the label *strong damping* refers to $D_h = 3.5\ Ns/m$ ($\xi_h = 0.15$), and the label *no damping* obviously refers to $D_h = 0\ Ns/m$ ($\xi_h = 0$). Concerning the baseline value of the damping,

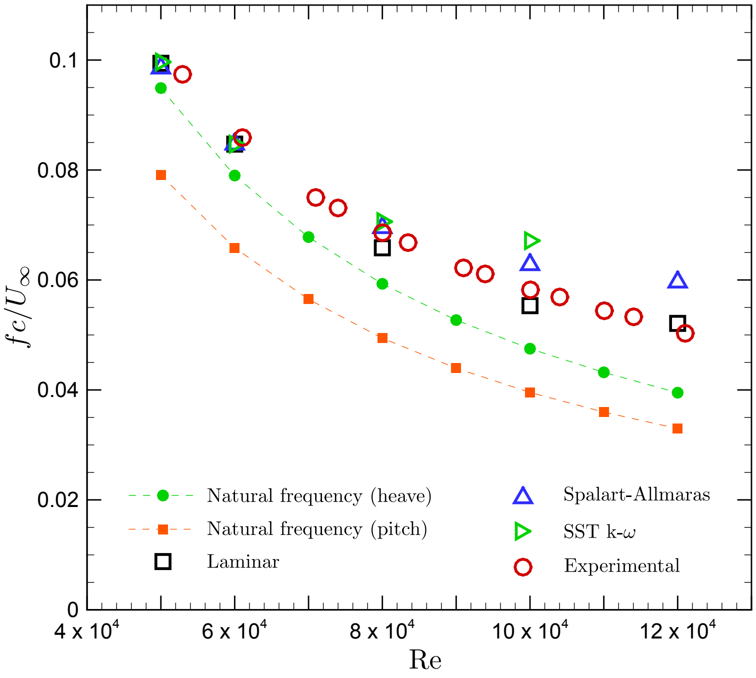

Figure 3.4: Comparison of the numerically predicted reduced frequencies with the experimentally measured reduced frequencies and with the calculated decoupled natural structural frequencies for the low heave stiffness case ($k_h = 800\ N/m$). Experimental values from Mendes et al. (2011).

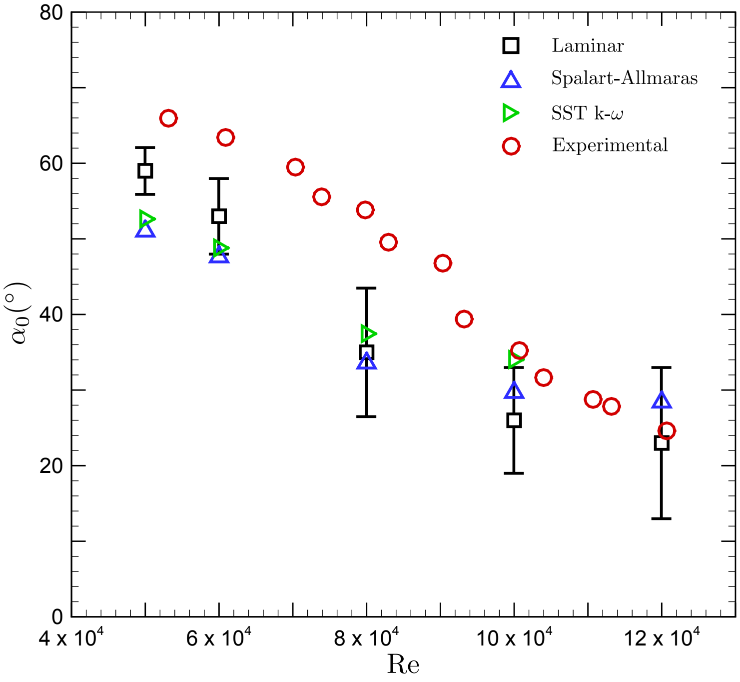

Figure 3.5: Comparison of the numerically predicted maximum effective angle of attack with the experimentally measured maximum effective angle of attack for the low heave stiffness case ($k_h = 800\ N/m$). Error bars on the laminar results show the amount of fluctuations within the amplitude of motion from one cycle to the other. Experimental values from Mendes et al. (2011).

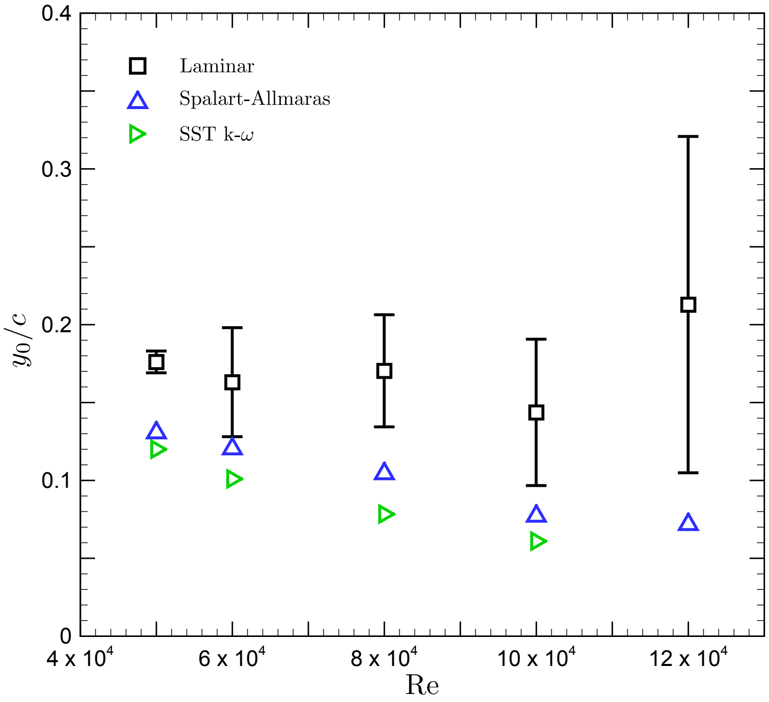

Figure 3.6: Numerically predicted heaving amplitude for the low heave stiffness case ($k_h = 800\ N/m$). No experimental data available. Error bars on the laminar results show the amount of fluctuations within the amplitude of motion from one cycle to the other.

it was previously defined as $D_h = 2\ Ns/m$ ($\xi_h = 0.09$). The maximum effective angle of attack shown in Figure 3.10, does exhibit some significant variations when the damping coefficient in heave is varied, but this alone cannot account fully for the slight mismatch with the experimental values.

One should recall the hypothesis made at the beginning of this section where the damping has been assumed *linear*. However, as clearly mentioned in Chapter 1, the heave damping of the RMC aeroelastic device is definitely not linear. Recalling from Chapter 2 that structural nonlinearities can significantly affect LCO, the linear modeling of the heave damping could likely account for the slight discrepancies observed. Last, the uncertainties on the experimental measurements of the airfoil's motion and of the structural parameters have not been addressed by the research group at the RMC. This could certainly account for another part of the discrepancies. It should be clear that because such an aeroelastic device is passive, even slight modifications of the structural parameters can turn out to have a significant impact on the airfoil's response. This is because of the two-way interaction between the flow and the structure, which can amplify what appears, at first, to be a relatively small difference.

To complete this first validation process, the reader has probably noticed that the experimentally measured reduced frequencies and the reduced frequencies predicted through CFD for

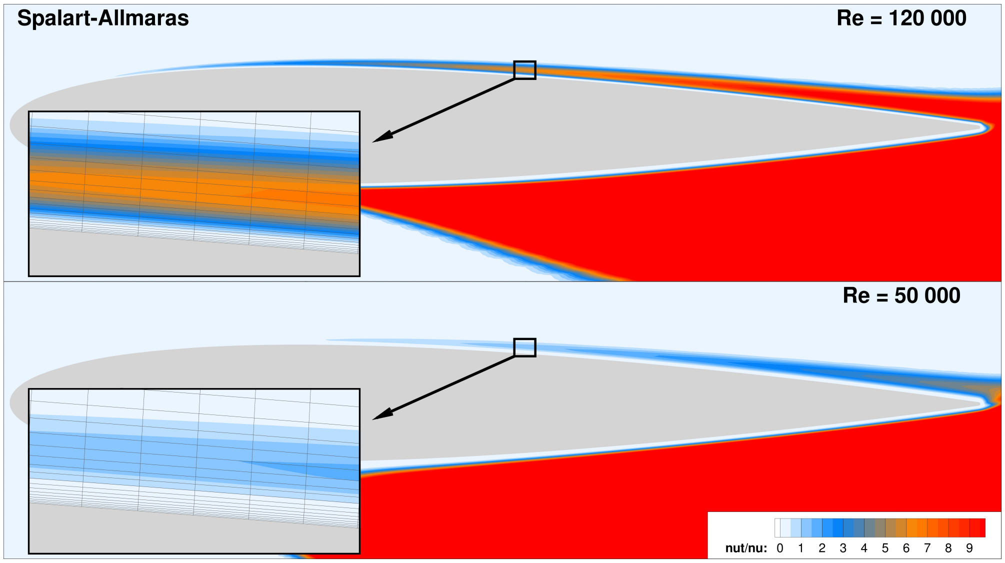

Figure 3.7: Close up view on the instantaneous turbulent viscosity ratio (ν_t/ν) for Re = 120,000 and Re = 50,000 at a similar moment within their cycle of oscillation. This is for the low heave stiffness case ($k_h = 800\ N/m$) simulated with the Spalart-Allmaras model. Note that the values of ν_t/ν extend beyond the max value shown on the color scale.

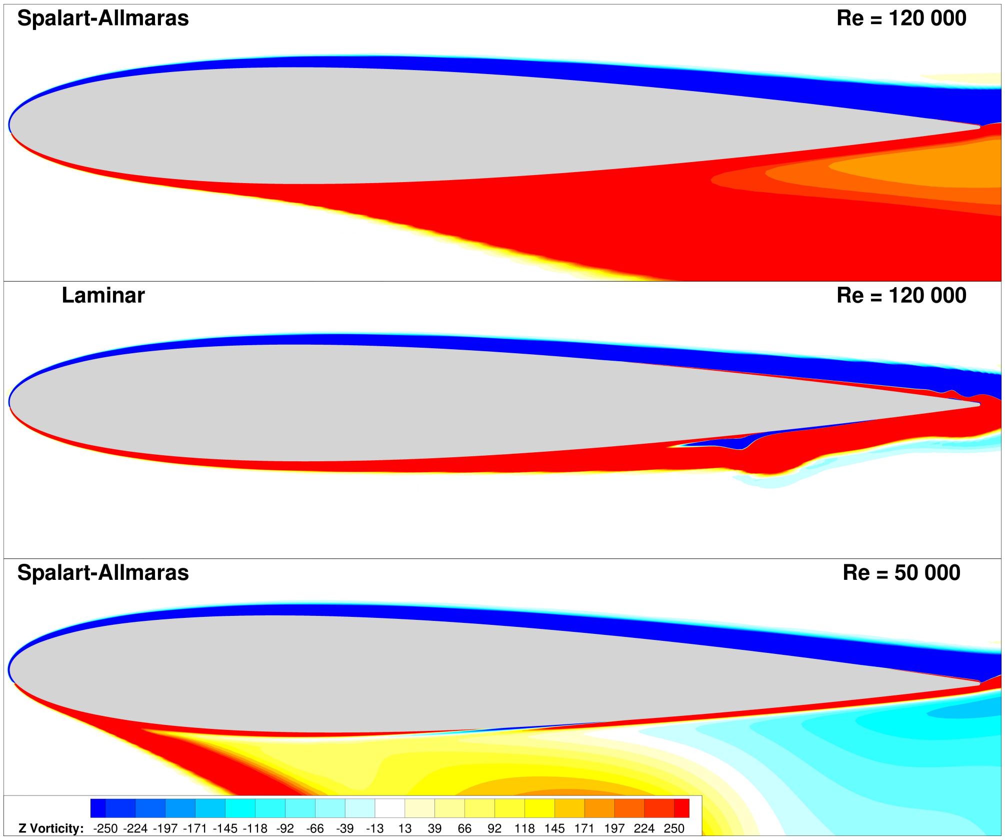

Figure 3.8: Comparison of instantaneous vorticity contours for Re = 120,000 and Re = 50,000 at a similar moment within their cycle of oscillation. This is for the low heave stiffness case ($k_h = 800\ N/m$). Note that the values of the vorticity extend beyond the min/max values shown on the color scale.

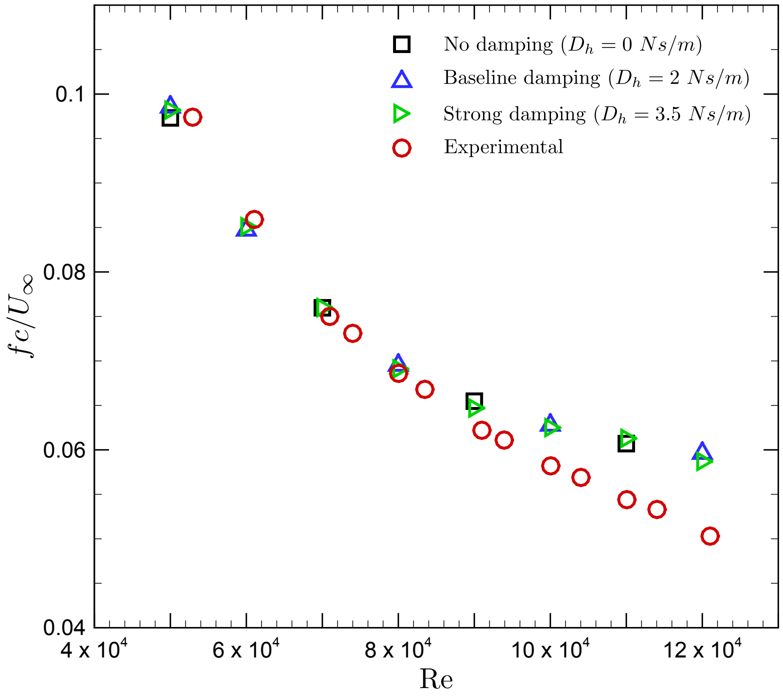

Figure 3.9: Comparison of the numerically predicted reduced frequencies with the experimentally measured reduced frequencies for various heave damping coefficients (D_h) for the low heave stiffness case ($k_h = 800\ N/m$). Experimental values from Mendes et al. (2011).

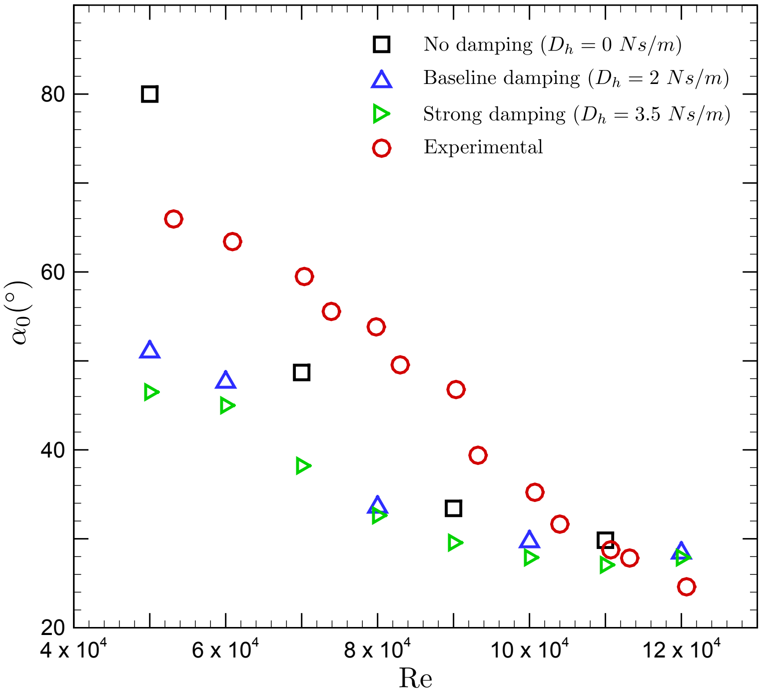

Figure 3.10: Comparison of the numerically predicted maximum effective angle of attack with the experimentally measured effective angle of attack for various heave damping coefficients (D_h) for the low heave stiffness case ($k_h = 800\ N/m$). Experimental values from Mendes et al. (2011).

the low heave stiffness case are not equal to the pitching decoupled natural frequency, nor to the heaving decoupled natural frequency. This is in contrast with the large heave stiffness case, where the reduced frequency is very close to the decoupled natural frequency in heave. For the low heave stiffness case, aerodynamic stiffening is present and active for both the pitch and the heave degrees-of-freedom. This suggests that the aerodynamics is far more dominant here than it is with the large heave stiffness case. The fluctuations of the predicted amplitudes of motion observed with laminar simulations being greater with the low heave stiffness case suggests the same conclusion. This makes sense from a physical point of view as the restoring forces generated by the spring in heave are necessarily greater for the large heave stiffness case, thus leaving less room for the aerodynamics at governing the airfoil's motion. This could partially explain as well why the turbulence model has a more significant effect on the results obtained for the low heave stiffness case.

Summary of the validation using the RMC experiment

To summarize, laminar simulations in the transitional range of Reynolds numbers provide numerical results that are in better agreement with the experimental values when compared to the predictions obtained with the Spalart-Allmaras or the SST $k - \omega$ turbulence model. This is especially true for the low heave stiffness case, where the aerodynamics appears to be more dominant than it is for the large heave stiffness case. This is due to the smaller restoring forces from the spring in heave, thus leaving more room to the aerodynamics for governing the airfoil's motion. These results suggest that the numerical solver could be improved by making use of a transitional turbulence model[4], which would be more appropriate for the transitional flow regime considered in this section. However, this would most likely not be necessary for the simulations at Re = 500,000. A second refinement of the numerical predictions could certainly be achieved by making use of a nonlinear damping model in both pitch and heave. Even if such a refinement would most probably provide a better match with the experimental results from the RMC, this would not be of great interest for the current optimization of the fully-passive, flapping-airfoil turbine. Indeed, including a nonlinear damping model would increase the size of the already immense parametric space by adding more structural parameters. Finally and most importantly, the results obtained in this section provide great confidence in the current FSI solver, and it can certainly be used without risks at higher Reynolds numbers more representative of a wind or hydrokinetic turbine.

---

[4] A transitional turbulence model is not readily available within the *OpenFOAM-2.1.x* CFD toolbox, which explains why simulations making use of such modeling have not been tried. Of course, implementing such a model was an option, but this requires extensive work. Because the FSI solver is intended to be used at Re = 500,000, this idea was quickly rejected.

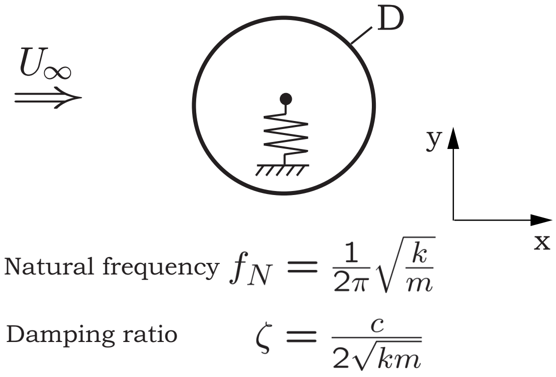

Figure 3.11: Schematic of the elastically-mounted cylinder which is free to oscillate transversally to the freestream flow. Reproduced from Morissette (2009).

3.2 Vortex induced vibrations of a cylinder

3.2.1 Description of the aeroelastic problem

In order to further validate the FSI solver, a relatively simple and well-documented aeroelastic problem is used. It consists of a rigid, two-dimensional cylinder which is elastically mounted in a freestream flow. The cylinder only has one degree-of-freedom: it is free to oscillate transversally to the flow (i.e., along the y-axis). The configuration of the benchmark is schematically depicted in Figure 3.11. As it will be seen, this very simple aeroelastic problem is especially useful for the task of validating the numerical scheme used in order to couple the fluid and the structural solvers (see Chapter 2 for a description of the numerical scheme).

The physical explanation to the self-sustained and self-induced oscillations of the cylinder is relatively simple: they are due to the alternating vortex shedding behind the cylinder. This alternating shedding, which is not a physical mechanism attributed to the motion of the solid (i.e., it is also observed on static cylinders), implies that the flow around the cylinder is not symmetrical and not steady. As a result, the cylinder is exposed to a non-zero fluctuating vertical force (i.e., along the y-axis) that sets the solid structure into motion. Because vortex shedding is the key element here, the phenomenon has been given the name of vortex induced vibrations (VIV). This phenomenon is very well documented in the literature, and the reader may refer to a fairly complete review article by Williamson and Govardhan (2004) for a comprehensive discussion on this matter, and also to obtain a clear picture of the state-of-the-art. This review article also contains an extensive list of published results obtained through both CFD and experimental work. Several studies also enabled the motion of the cylinder along the x-axis (i.e., the cylinder had two degrees-of-freedom), but the current validation is limited to the one-degree-of-freedom case.

Before making use of this simple aeroelastic problem for validating the solver, the equation of motion first has to be introduced. For such an elastically mounted cylinder, the equation of motion is that of a simple spring-mass-damper system:

$$F \;=\; m\ddot{y} \;+\; c\dot{y} \;+\; ky \;, \tag{3.5}$$

where F is the fluctuating vertical force, m is the mass of the cylinder, c is the structural damping coefficient, and k is the spring stiffness coefficient. All these previous parameters are given per unit depth of the cylinder. Further, y, $\dot{y}$ and $\ddot{y}$ are respectively the vertical position, the velocity and the acceleration of the cylinder's center of mass, which is located at the center of the cylinder. As the reader may already have noticed, Eq. 3.5 is very similar to the equation of motion in heave of the fully-passive, flapping airfoil (Eq. 2.16). The only difference is the absence of the inertial coupling term in the case of the oscillating cylinder.

In most published work, the following non-dimensional formulation of the problem is preferred over Eq. 3.5:

$$\frac{2}{\pi m^*}C_y \;=\; \ddot{y}^* \;+\; 2\xi\left(\frac{2\pi}{U^*}\right)\dot{y}^* \;+\; \left(\frac{2\pi}{U^*}\right)y^* \;. \tag{3.6}$$

In this equation, the vertical position (y) is normalized with the cylinder's diameter (D) in the following way:

$$y^* \;=\; \frac{y}{D} \;. \tag{3.7}$$

Further, the non-dimensional mass per unit depth (m^*) simply corresponds to the ratio of the cylinder's density (ρ_s) to the fluid's density (ρ_f):

$$m^* \;=\; \frac{\rho_s}{\rho_f} \;. \tag{3.8}$$

Defined as such, m^* is also a direct measure of the fluid-structure interaction strength. For reasons explained in Chapter 2, decreasing m^* increases the strength of the FSI, and vice-versa. Concerning the non-dimensional velocity of the flow (U^*), it is calculated as:

$$U^* \;=\; \frac{U_\infty}{f_N D} \;, \tag{3.9}$$

where U_∞ is the velocity of the freestream flow, and f_N is the natural frequency of the oscillating cylinder. This frequency is, in turns, calculated as:

$$f_N = \frac{1}{2\pi}\sqrt{\frac{k}{m}} \ . \tag{3.10}$$

Finally, the coefficient of vertical force per unit depth (C_y) is obtained by making use of the dynamic pressure ($\frac{1}{2}\rho_f U_\infty^2$), along with the cylinder's diameter (D):

$$C_y = \frac{F}{\frac{1}{2}\rho_f U_\infty^2 D} \ , \tag{3.11}$$

and the damping ratio is:

$$\xi = \frac{c}{2\sqrt{km}} \ . \tag{3.12}$$

3.2.2 Comparison with results available in the literature

The fact that several two-dimensional experimental and numerical studies have been performed on the one-degree-of-freedom elastically-mounted cylinder within various ranges of flow and structural parameters turns out to be very useful for validating the FSI solver of this study. In fact, some of the previously published CFD results have been obtained for Reynolds number of 200, where the Reynolds number is based on the cylinder's diameter. Obviously, the flow regime is expected to be laminar at such Reynolds number, and this turns out to be very appreciated for the current validation. This is because no modeling of turbulence is required for such a low Reynolds number. As a result, these CFD computations offer the possibility of validating the FSI modeling and the numerical methodology alone: there is no uncertainty associated to the modeling of turbulence. If the validation was achieved at a higher Reynolds numbers where a turbulence model was needed, it would be hard to state if either the turbulence modeling, the FSI or the numerics would account for possible mismatches with the experimental values.

Validation using other CFD studies

In this subsection on VIV, a total of three numerical studies are used for the sake of comparing the results obtained with the FSI solver of this thesis. The first numerical study is from Yang et al. (2008), where the laminar results have been obtained using a strong coupling scheme between the equations of the incompressible flow and the cylinder's equation of motion. The second numerical study is from Leontini et al. (2006), and the results have been obtained through a spectral-element method which was coupled to the harmonical equation of the cylinder. The third and last numerical study used within this section is from Morissette (2009), a former student from the author's research group. His numerical results have been obtained using both an in-house lagrangian vortex method, and the commercial CFD software

Table 3.4: Set of non-dimensional parameters used in the numerical studies of the one-degree-of-freedom elastically-mounted cylinder performed by Yang et al. (2008); Leontini et al. (2006) and Morissette (2009). The same parameters are used for the current validation.

Physical parameter	Symbol	Value
Reynolds number	Re	200
Non-dimensional mass	m^*	10
Damping ratio	ξ	0.01
Non-dimensional velocity	U^*	4.5

Fluent 6.3. As the reader may note, these three numerical studies offer some variability in the methods used to solve the same aeroeslastic problem. Despite this variability, the numerical results of all studies are in very good agreement. This well-documented test case therefore provides an opportunity to validate the current implementation of the FSI solver, which is different from any of the previously mentioned studies.

The set of non-dimensional parameters shared by the three numerical studies is shown in Table 3.4. Recalling notions from Chapter 2, the non-dimensional mass ($m^* = 10$) corresponds to a case where the strength of the FSI is moderate. Using such a value of m^* is surely more challenging for the FSI solver, and this particularly puts the FSI coupling scheme to the test.

As a first test, a simulation has been achieved with the same parameters as those shown in Table 3.4. The calculations on the elastically-mounted cylinder have been performed on a 2D grid that has approximately 55,000 cells. Further, a non-dimensional time step ($\Delta t U_\infty / D$) of 0.005 has been used. The rest of the numerical methodology is exactly the same as the one presented in Chapter 2 (i.e., the same frame of reference, the same convergence criteria, the same boundary conditions, etc.).

The normalized maximum amplitude of motion ($A^*_{max} = A_{max}/D$), the maximum force coefficient ($C_{y,max}$), and the reduced frequency of oscillation ($f^* = f/f_N$) of the past and the current numerical studies are shown in Table 3.5. A very good agreement is observed between the results from all studies, including the current one, and this provides good confidence in the FSI solver of this master's thesis.

To push the validation a step further, it is possible to compare the predicted displacement history of the cylinder, as computed in this study, with the displacement history predicted by Morissette (2009). Indeed, he published the displacement history predicted with both computational methods used within his numerical study, and the comparison is shown in Figure 3.12. An excellent agreement is observed between the three sets of data. Again, this

Table 3.5: Results from the numerical studies of the one-degree-of-freedom elastically-mounted cylinder performed by Yang et al. (2008); Leontini et al. (2006) and Morissette (2009), along with the results of the present study.

Results	A^*_{max}	$C_{y,max}$	f^*
Present	0.50	2.31	0.96
Morissette (2009) (*Fluent*)	0.49	1.90	0.96
Morissette (2009) (vortex method)	0.49	2.22	0.95
Yang et al. (2008)	0.42	2.25	0.95
Leontini et al. (2006)	0.47	2.37	0.95

reinforces the idea that the FSI solver of this thesis is indeed accurate at the task of predicting the motion of a solid structure which is elastically supported in a flow.

Another validation is achieved, this time using only the results of Leontini et al. (2006). To obtain the results of interest here, the same set of non-dimensional parameters as the one shown in Table 3.4 is used, except for one parameter: the non-dimensional velocity of the flow is now $U^* = 5.2$. The other three parameters are unaffected. The quantitative results of Leontini *et al.* and those of the current study are compared in Table 3.6. The same metrics as those considered previously are used in order to qualify the match, and an excellent agreement is again observed. Although the displacement histories of the cylinder are not shown here, they have been qualitatively compared by the author, and a very good agreement is again observed between both numerical studies.

Comparing Tables 3.5 and 3.6, the reader may certainly note that the amplitudes of motion of both VIV cases previously considered are somewhat similar, but the values of $C_{y,max}$ are significantly different. This obviously suggests that there are significant differences between the physics at play in both cases. The objective here is not to discuss these differences between the physical mechanisms involved, but instead to offer a rationale for choosing this second validation case (i.e., the one with $U^* = 5.2$). Indeed, because the aerodynamics is different in both test cases, they are certainly complementary to each other, and the FSI solver is able to accurately capture both of them, thus confirming its versatility.

Validation using an experimental study

To further assess the validity of the FSI solver, the numerical predictions obtained with the solver of this study are compared with the results of an experimental study. Very few experiments on the elastically-mounted cylinder have been achieved in the laminar flow regime. Anagnostopoulos and Bearman (1992) published one of the very few studies available in this

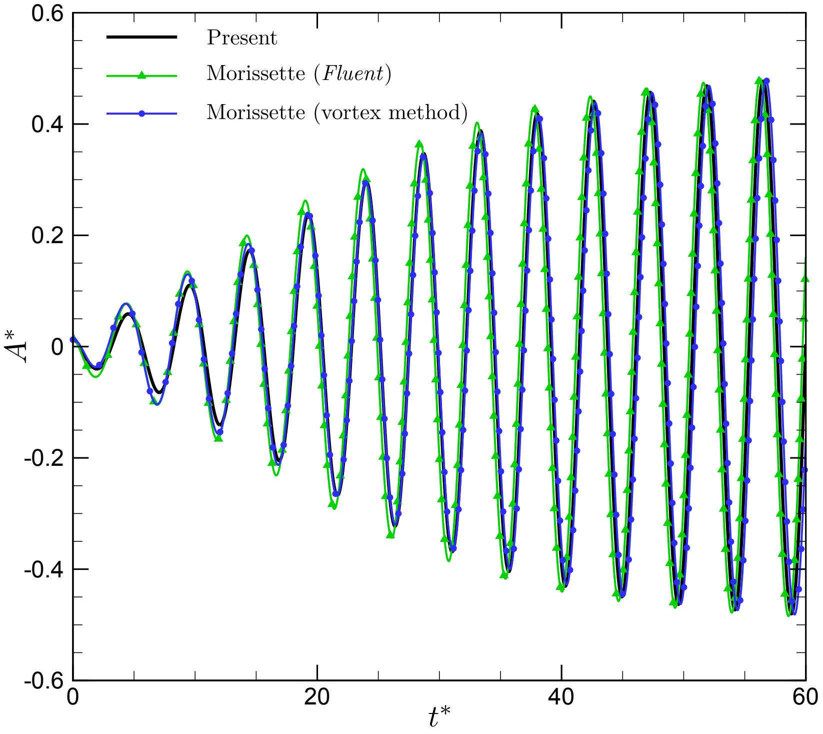

Figure 3.12: Motion history of the elastically-mounted cylinder from Morissette (2009) and from the current study. The simulations have been performed with the parameters shown in Table 3.4.

Table 3.6: Results from the numerical study of the one-degree-of-freedom elastically-mounted cylinder performed by Leontini et al. (2006), along with the results of the present study for $U^* = 5.2$.

Results	A_{max}	C_{ymax}	f^*
Present	0.43	0.20	1.00
Leontini et al. (2006)	0.43	0.25	1.00

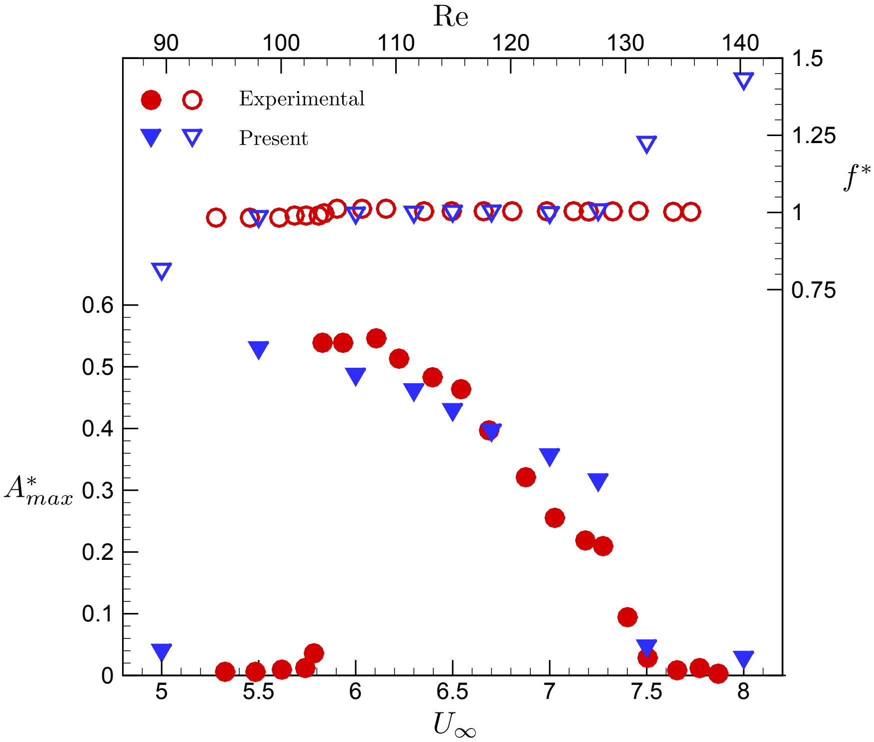

Figure 3.13: Normalized amplitude of motion (A^*_{max}) and reduced frequency of oscillations (f^*) for an elastically-mounted cylinder having a damping ratio (ξ) of 0.0012 and a non-dimensional mass (m^*) of 148.2. Experimental values from Anagnostopoulos and Bearman (1992).

flow regime, and the authors openly stated in their work that one of the main objectives of their study was to develop a useful and well-documented benchmark for validating FSI solvers. In their study, which has been performed in a water-channel, the Reynolds number has been varied between 90 to 150, the damping ratio (ξ) was equal to 0.0012, and the non-dimensional mass (m^*) was equal to 148.2. This value of m^* corresponds to a FSI strength which is somewhat weak. Nevertheless, this test case offers a great validation opportunity, and the physics is again different from the previous cases.

A comparison of the normalized maximum amplitude of motion of the cylinder (A^*_{max}) and the reduced frequency of oscillation (f^*) is shown in Figure 3.13 over the complete range of flow velocities covered within the experiment. A good match is observed between the experiment and the current numerical simulations over most of the velocity range. A slight discrepancy is observed in the vicinity of $U^* = 5.5$. From the experimental data, it is observed that the amplitude of motion quickly drops between $U^* = 5.5$ and $U^* = 6.0$. However, the FSI solver predicts that this happens between $U^* = 5$ and $U^* = 5.5$. Another slight discrepancy is observed, this time concerning the frequency. The results from the experiment show that the cylinder oscillates at a frequency very close to the natural frequency for all velocities of the flow. However, the FSI solver predicts a larger frequency of oscillation for $U^* > 7.5$, and a lower frequency for $U^* = 5$. In fact, further analysis reveals that the frequency of oscillation predicted through CFD in these two regions is very close to the Strouhal number that has been measured in the experimental wake.

These results confirm that the 2D predictions made with the FSI solver are in the same range as the experimentally measured values. Further, the predicted trends are generally in good agreement with the experiment. This again provides a confirmation that the FSI solver of this thesis can be used for the sake of studying the aeroelastic problem of a fully-passive, flapping-airfoil turbine.

3.2.3 Assessment of the FSI scheme's limitations

Williamson and Govardhan (2004) gathered and discussed the results of several studies dealing with the elastically-mounted cylinder. They confirmed that the maximum normalized amplitudes of motion collapse very well when plotted against a mass-damping parameter which is defined as:

$$\Lambda \;=\; (m^* + C_A)\,\xi \;, \tag{3.13}$$

where C_A is the potential added mass coefficient taking a value of 1.0. The authors of this study found that whenever $m^* > 2$ and $\Lambda > 0.006$ simultaneously, the amplitude of motion is fairly constant when Λ remains constant. This offers a great opportunity for the task of validating the robustness and the limitations of the FSI coupling scheme implemented within the FSI solver of the current numerical study. The idea is the following: if Λ remains constant while m^* is reduced, the strength of the fluid-structure interaction increases significantly, but the amplitude of motion is expected to remain constant. As the strength of the FSI increases, the task becomes more and more challenging for the FSI solver, and it can be increased until the coupling scheme becomes numerically unstable. This will allow to investigate the accuracy and the behavior of the solver whenever it is used on the edges of its stability domain.

Using the set of non-dimensional parameters from Table 3.4, except for U^* which is equal to 5.2, the mass-damping parameter (Λ) is found to be equal to 0.11. Fortuitously, this falls into the aforementioned range of validity of the well-verified approximation where a constant mass-damping (Λ) provides a constant amplitude of motion (A^*_{max}). Using these parameters, a few computations have been achieved with the FSI solver of this study, and Table 3.7 summarizes the results for the various runs. The results are presented in decreasing order of m^*, which corresponds to an increasing strength of FSI. As observed, the peak amplitude of motion remains constant for all values of m^*, just as much as the values of $C_{y,max}$ and f^*. However, no result is available for the calculation carried out at $m^* = 2$. This is because the simulation becomes unstable due to a too large interaction between the cylinder and the flow (due to the added mass effect discussed in Chapter 2).

A very interesting observation can be made from these results. Indeed, the values obtained with the FSI solver of this thesis remain accurate even if the strength of the FSI is such that the staggered, explicit coupling scheme is on the edge of its stability domain. Said otherwise, the FSI solver can be considered accurate for whatever strength of the FSI, as long as an instability due to the added mass effect is not encountered. Another interesting point that can be made with the results from Table 3.7 is related to Eq. 2.46. The results of this section tend to confirm that this equation ($\rho_s/\rho_f > 1$) indeed represents a good approximation of the stability criterion associated to the staggered, explicit coupling scheme of this study.

Table 3.7: Results of the computations performed with a constant value of $\Lambda = 0.11$ while the strength of the fluid-structure interaction is increased (i.e., m^* is decreased). The label N/A stands for *not available*, and is used whenever the solver is unable to provide results due to a numerical instability associated to the added mass effect.

m^*	ξ	A^*_{max}	C_{ymax}	f^*
10	0.010	0.43	0.20	1.00
8	0.012	0.43	0.20	0.99
6	0.016	0.43	0.20	1.00
4	0.022	0.43	0.19	0.99
2	0.037	N/A	N/A	N/A

Conclusion

To summarize this chapter, the FSI solver implemented within the *OpenFOAM-2.1.x* CFD toolbox has been thoroughly validated, and the results obtained provide confidence that the numerical predictions are accurate for the current task. To reach this conclusion, the predictions of the FSI solver have been put to the test in various complementary ways.

First, the numerical predictions have been compared with the wind tunnel experiments of the RMC. Overall, a good agreement has been observed between both the experimentally measured values and those predicted with the FSI solver of this study. Nevertheless, some slight mismatches are present, and it is believed that they can essentially be explained by three factors. First, the turbulence model used, namely the Spalart-Allmaras model, has been developed for high Reynolds number applications. The current simulations have been performed in the transitional range of Reynolds numbers, and the turbulence model has some difficulties at predicting accurately some features of the flow. The second factor that could explain the mismatch is certainly the use of a linear damping model. In fact, the damping of the aeroelastic device from the RMC is not linear for both degrees-of-freedom. The last factor is due to the experimental uncertainties on both the structural parameters and the motion of the airfoil, which have not been addressed in the published work from the RMC. Because the device considered here is passive, a slight variation of one structural parameter can change significantly the airfoil's dynamics.

A second validation has been achieved with a simple aeroelastic problem consisting in the VIV of a cylinder. The numerical predictions of the current solver compare very well with the predictions obtained with previous CFD studies. Further, the predicted motion of the cylinder compares favorably well with the data from an experiment. This case has also been used in order to investigate the behavior of the FSI solver whenever it is pushed to its limits and brought very close to being unstable. It has been found that whenever the solver is not subject to the added mass instability, the results remain accurate, whatever the strength of the FSI.

With these very encouraging results in hand, a numerical campaign can safely be started on the fully-passive, flapping-airfoil turbine. This is the subject of the following chapter, where the validated solver is used to optimize the aeroelastic device.

Chapter 4

Optimization of the turbine using 2D simulations

This chapter is really at the heart of this master's thesis as it encompasses the optimization and the main physical study of the fully-passive, flapping-airfoil turbine. The information is organized in the following way. First, a discussion concerning the vast parametric space of the device is presented. Then, an original methodology developed by the author for the task of investigating efficiently the parametric space is introduced. The objective of this *Reverse Passive-Airfoil Solver* presented in the corresponding section is essentially to find an adequate set of structural parameters for the fully-passive, flapping-airfoil turbine in order to begin the optimization process. This in-house solver has indeed permitted to obtain the so-called *initial case* about which an optimization of the efficiency and of the total power harvested from the flow has been achieved. This optimization is the subject of the following section, where the optimization methodology used is thoroughly described, along with the most important results obtained. This optimization has provided a set of structural parameters defining the so-called *optimized case* of the fully-passive, flapping-airfoil turbine.

Following this crucial step, a study of the physical mechanisms involved within both the initial case and the optimized case is presented. The main idea here is to better understand the physical mechanisms involved, and, mainly, to understand how the performances of the device have been optimized. Next, the optimized case is investigated deeper by conducting a sensitivity study about each of the seven structural parameters, as well as about the velocity of the flow. This reveals to be useful for the purpose of understanding the effect of each parameter on the dynamics of the airfoil, and also on its performances. To end, a special and intriguing case of the fully-passive flapping-airfoil turbine is presented: the situation where no spring is present neither in heave nor in pitch. This last section aims at reinforcing our understanding of the physical mechanisms involved, and it clearly highlights the fact that the flapping airfoil is undergoing stall flutter.

4.1 Parametric space and initial case

As previously discussed while working out the equations of motion of the fully-passive, flapping-airfoil turbine (Eqs. 2.16 and 2.19), a total of seven structural parameters are involved within the equations, each of which may be adjusted as a way to indirectly control the dynamics of the airfoil in the current modeling of the device. These seven parameters are:

- S, the static imbalance ($m_p x_\theta$);
- m_h, the heaving mass;
- I_θ, the moment of inertia;
- k_h, the heave stiffness coefficient;
- k_θ, the pitch stiffness coefficient;
- D_h, the heave damping coefficient;
- D_θ, the pitch damping coefficient.

Through astute variations of these structural parameters, the dynamics of the airfoil undergoing LCOs can surely be tuned in order to impact its efficiency and the amount of power harvested from the flow. Of course, a specific modification may either affect negatively or positively the metrics used to characterize the performances of the device in this study. However, through an adequate, well-studied choice of each structural parameter, the efficiency of the device, along with the total power harvested, can be greatly increased. An optimization process is required to specifically achieve this.

Two independent performance metrics need to be optimized. They both have been previously introduced in Chapter 1 of this thesis, and they are the energy harvesting efficiency (η) and the power coefficient ($\overline{C}_P$). As a matter of fact, *both* of these metrics need to be optimized in order to obtain an interesting turbine. This is because a very high value of η combined with small amplitudes of motion would result in a low value of $\overline{C}_P$. In this scenario, the device would be very efficient, but very little power would be harvested from the flow. On the contrary, a fairly low value of η combined with very large amplitudes of motion would result in a moderate to high value of $\overline{C}_P$. However, because of its low efficiency, the device would not be compact at all, and the mechanics could be more complex as a result of the large amplitude of motion in heave.

Having a total of seven adjustable structural parameters implies that there is hope of having enough control on the device in order to optimize both of these metrics, but it also implies that the parametric space of the device is absolutely gigantic. Because a FSI simulation requires approximately two to three days of computation, it is impossible to explore the entire parametric space through complete FSI computations. Instead, choosing astutely among the parametric space the initial case about which the optimization is to be performed turns out

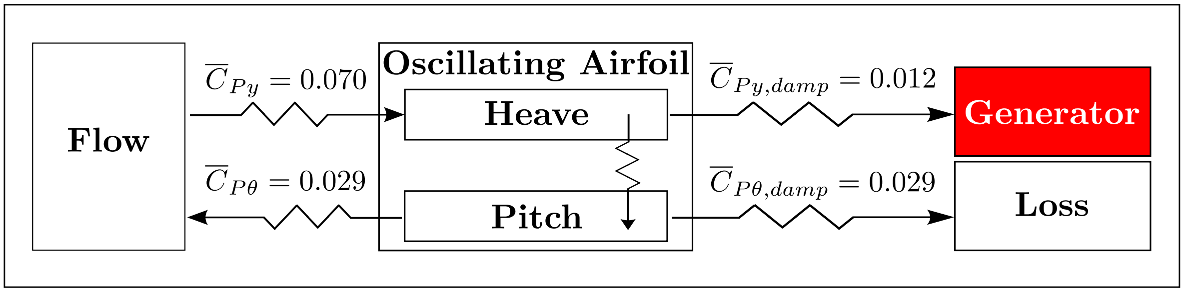

Figure 4.1: Schematic representation of the flow of power through the fully-passive, flapping-airfoil turbine using the structural parameters of the low heave-stiffness case from the RMC experiment at Re = 60,000 (see Figures 3.4 to 3.6).

to be much more judicious. Therefore, it is required to determine a set of seven structural parameters representing this well-chosen initial case. However, there remains a question: what are the properties sought for this well-chosen initial case? Unfortunately, a single answer to this question does not exist. From the author's point of view, this initial setup should be as efficient as possible (i.e., maximize η) in order to minimize the total number of numerical simulations required to complete the optimization process, and this is the main guideline used as a way to find an adequate initial case.

This initial case could certainly be chosen among the parametric space investigated within the experimental study of the research group from the RMC (see Chapter 1 and Chapter 3). Indeed, one possible option would be to use a set of parameters that already gave rise to large-amplitude LCOs in the experiment. Further, these oscillations have already been simulated with the FSI solver in Chapter 3 dealing with the validation of the numerical method. However, it turns out that the efficiencies related to the various cases investigated in this experimental study are very modest ($\eta < 5\%$). A typical example of such performances is here provided in Figure 4.1 for the low heave-stiffness case at Re = 60,000 (see Chapter 3), where η takes a value of only 3.1% and $\overline{C}_P$ takes a value of 0.041. Figure 4.1 introduces the flow of power throughout the turbine using the various coefficients of power previously introduced in Chapter 2. It can be seen that some power is harvested through the heave motion, while the pitching motion achieves some work on the flow in the mean. In fact, very little power is available to the generator as the pitching motion is very costly.

As a matter of fact, such performances are quite far from being optimal when compared to what can be achieved experimentally and numerically with a kinematically-constrained flapping-airfoil turbine (see Kinsey and Dumas (2012a) and Kinsey et al. (2011)). As discussed in Chapter 1, energy harvesting efficiencies as high as 43% have been predicted through two-dimensional simulations for this non-passive device, and efficiencies as high as 30% have been experimentally measured. Therefore, using the experimental work from the RMC for choosing the initial case has rapidly been ruled out.

Another possible option is to make use of the current knowledge about the kinematically-constrained, flapping-airfoil turbine. Indeed, this type of flow harvester has been studied intensively and extensively among the author's group in the past few years, and it would certainly make sense to use what is already known about it as a way to adequately select the initial case. After all, one should recall that optimizing the fully-passive turbine in order to achieve the same efficiencies as those of the kinematically-constrained turbine is the main objective of this thesis. This, again, is a convincing rationale for trying to reproduce as closely as possible the efficient aerodynamics and kinematics of the kinematically-constrained device at the very beginning of the optimization process. For this reason, all flow and structural parameters kept constant within this study have been chosen to match the kinematically-constrained device of the LMFN:

- Re = 500,000;
- The airfoil's profile is a symmetrical NACA 0015;
- $x_{ea} = c/3$.

However, the set of seven structural parameters involved within the equations of motion remains unknown. This is because they have no direct equivalent in the case of the kinematically-constrained turbine. For this reason, a particular methodology had to be developed in order to approximate the initial value of each structural parameter. For this specific task, an in-house Reverse Passive-Airfoil Solver (RPAS) has been developed by the author of this thesis, and this is the subject of the following section.

4.2 Reverse Passive-Airfoil Solver (RPAS)

4.2.1 Implementation of the solver

The Reverse Passive-Airfoil Solver (RPAS) is an in-house application written in C++ for the specific task of finding a set of structural parameters that is well suited for starting the optimization process of the fully-passive, flapping-airfoil turbine. It has been developed by the author of this thesis on the Qt-5.1 cross-platform with the interest of implementing a simple graphical user interface (GUI). In fact, Qt-5.1 offers a very friendly GUI developing environment, and it is relatively easy to get familiar with the process. Essentially, RPAS has been designed to solve the reverse mathematical problem of the fully-passive, flapping-airfoil turbine. To highlight what is meant by *solving the reverse problem*, the following should first be recalled concerning the *conventional* FSI solver (i.e., the solver implemented within *OpenFOAM-2.1.x*). For each run of the conventional solver, the following is achieved:

- A total of seven structural parameters are chosen (input);
- The flow parameters are chosen (input);
- The equations of the flow and the equations of the solid are solved using *OpenFOAM*;
- The results are the kinematics and the aerodynamics (output), thus allowing to calculate the performances of the turbine.

Therefore, the resulting aerodynamics and the resulting kinematics of the LCOs are an *output* of the conventional solver. This is the opposite of what happens with the reverse solver. Indeed, the information obtained as an output of the conventional solver becomes an input when the reverse solver is used. The following summarizes the main idea for solving the reverse problem:

- The airfoil's kinematics and aerodynamics are chosen, tabulated and provided to RPAS (input);
- The possible ranges of values of the structural parameters are chosen (input);
- The solver computes the residuals of the equations of motion over all the possible sets of structural parameters among the allowed range of values, and it records the residuals pertaining to each equation of motion;
- The set of structural parameters that minimizes the residuals of both equations is obtained (output).

To explain in more details, the RPAS software enables the user to specify a range (i.e., minimum and maximum value) and an increment for each structural parameter. Through this, the user specifies which portion of the parametric space is investigated, as much as the resolution used to perform the numerical investigation. The user also provides RPAS with the airfoil's tabulated kinematics ($y^*(t^*)$, $\dot{y}^*(t^*)$, $\ddot{y}^*(t^*)$, $\theta(t^*)$, $\dot{\theta}(t^*)$ and $\ddot{\theta}(t^*)$) along with the corresponding tabulated aerodynamics ($C_{\mathcal{L}}(t^*)$ and $C_M(t^*)$) over one complete cycle of oscillation. Of course, the matching kinematics and aerodynamics may be obtained through experimental data or CFD. With this in hand, the solver iterates over each possible combination of seven structural parameters within the specified parametric space. For each set of parameters, all the variables of the equations of motion (Eqs. 2.20 and 2.21) are known. However, there is a residual to these equations. In other words, the LHS does not exactly match the RHS (i.e., the aerodynamics, the kinematics and the structural parameters do not fully satisfy the equations of motion). The residuals are computed in the following way, where the notation (*) over the non-dimensional parameters is dropped to avoid overloading the equations :

$$R_{\mathcal{L}} \;=\; \frac{m_h\,\ddot{y} \;+\; S\left(\dot{\theta}^2\,\sin\theta - \ddot{\theta}\cos\theta\right) \;+\; D_h\,\dot{y} \;+\; k_h\,y \;-\; C_{\mathcal{L}}}{(C_{\mathcal{L}})_{max}}\;, \tag{4.1}$$

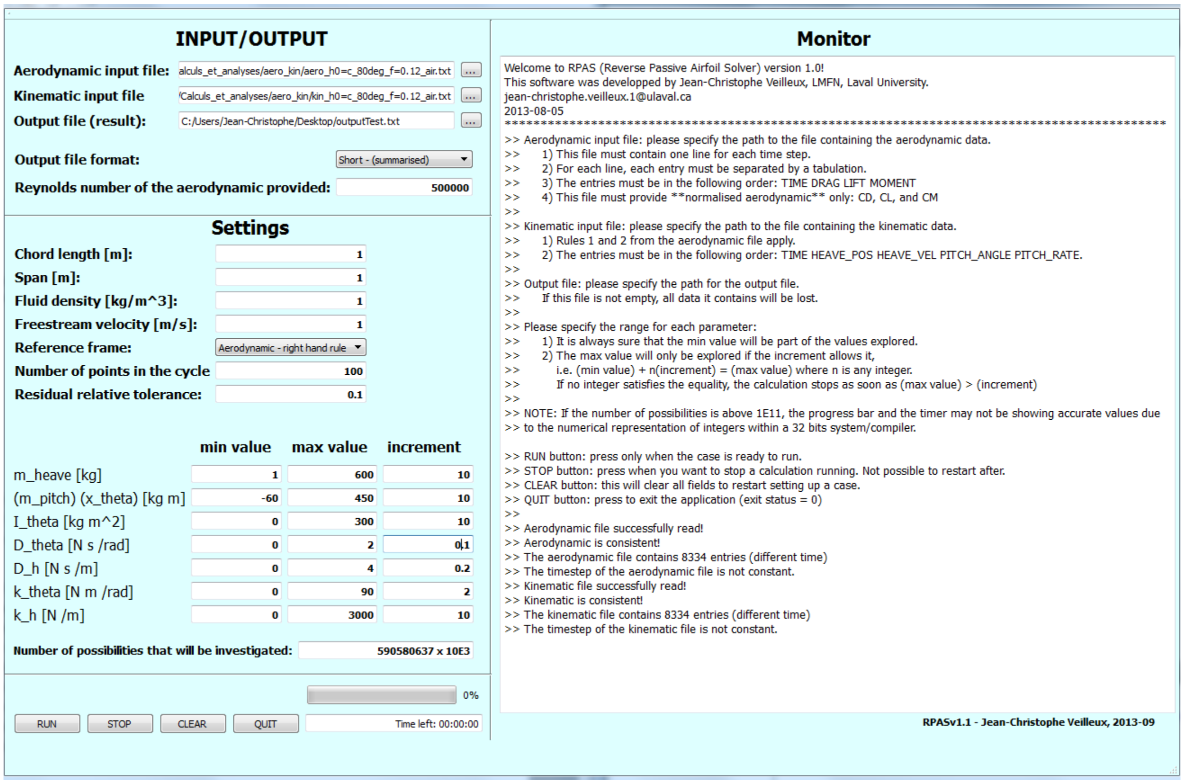

Aerodynamic input file: alculs_et_analyses/aero_kin/aero_h0=c_80deg_f=0.12_air.txt

Kinematic input file /Calculs_et_analyses/aero_kin/kin_h0=c_80deg_f=0.12_air.txt

Output file (result): C:/Users/Jean-Christophe/Desktop/outputTest.txt

Output file format: Short - (summarised)

Reynolds number of the aerodynamic provided: 500000

Chord length [m]: 1

Span [m]: 1

Fluid density [kg/m^3]: 1

Freestream velocity [m/s]: 1

Reference frame: Aerodynamic - right hand rule

Number of points in the cycle 100

Residual relative tolerance: 0.1

	min value	**max value**	**increment**
m_heave [kg]	1	600	10
(m_pitch) (x_theta) [kg m]	-60	450	10
I_theta [kg m^2]	0	300	10
D_theta [N s /rad]	0	2	0.1
D_h [N s /m]	0	4	0.2
k_theta [N m /rad]	0	90	2
k_h [N /m]	0	3000	10

Number of possibilities that will be investigated: 590580637 x 10E3

Time left: 00:00:00

```
Welcome to RPAS (Reverse Passive Airfoil Solver) version 1.0!
This software was developped by Jean-Christophe Veilleux, LMFN, Laval University.
jean-christophe.veilleux.1@ulaval.ca
2013-08-05
****************************************************************************************************
>> Aerodynamic input file: please specify the path to the file containing the aerodynamic data.
>>      1) This file must contain one line for each time step.
>>      2) For each line, each entry must be separated by a tabulation.
>>      3) The entries must be in the following order: TIME DRAG LIFT MOMENT
>>      4) This file must provide **normalised aerodynamic** only: CD, CL, and CM
>>
>> Kinematic input file: please specify the path to the file containing the kinematic data.
>>      1) Rules 1 and 2 from the aerodynamic file apply.
>>      2) The entries must be in the following order: TIME HEAVE_POS HEAVE_VEL PITCH_ANGLE PITCH_RATE.
>>
>> Output file: please specify the path for the output file.
>>      If this file is not empty, all data it contains will be lost.
>>
>> Please specify the range for each parameter:
>>      1) It is always sure that the min value will be part of the values explored.
>>      2) The max value will only be explored if the increment allows it,
>>         i.e. (min value) + n(increment) = (max value) where n is any integer.
>>         If no integer satisfies the equality, the calculation stops as soon as (max value) > (increment)
>>
>> NOTE: If the number of possibilities is above 1E11, the progress bar and the timer may not be showing accurate values due
>> to the numerical representation of integers within a 32 bits system/compiler.

>> RUN button: press only when the case is ready to run.
>> STOP button: press when you want to stop a calculation running. Not possible to restart after.
>> CLEAR button: this will clear all fields to restart setting up a case.
>> QUIT button: press to exit the application (exit status = 0)
>>
>> Aerodynamic file successfully read!
>> Aerodynamic is consistent!
>> The aerodynamic file contains 8334 entries (different time)
>> The timestep of the aerodynamic file is not constant.
>> Kinematic file successfully read!
>> Kinematic is consistent!
>> The kinematic file contains 8334 entries (different time)
>> The timestep of the kinematic file is not constant.
```

RPASv1.1 - Jean-Christophe Veilleux, 2013-09

Figure 4.2: Graphical user interface (GUI) of the Reverse Passive-Airfoil Solver (RPAS).

$$R_M = \frac{I_\theta\,\ddot{\theta} \;-\; S\,\ddot{y}\,\cos\theta \;+\; D_\theta\,\dot{\theta} \;+\; k_\theta\,\theta \;-\; C_M}{(C_M)_{max}}\;. \tag{4.2}$$

The reader should make sure to compare the previously introduced equations of motion (Eqs. 2.20 and 2.21) with the equations for the residuals (Eqs. 4.1 and 4.2) in order to fully understand the methodology used here. The reader will also notice that the residuals are normalized with the maximum lift coefficient ($C_{\mathcal{L}}$) and the maximum aerodynamic moment coefficient (C_M) of a complete cycle of oscillation [1]. For each set of structural parameters, the residuals are computed at various instants throughout the cycle of oscillation. In fact, the user can specify the number of equally-spaced instants of the cycle for which the residuals should be computed. The GUI of RPAS is shown in Figure 4.2 to help better understand the required input, and also to clarify in what form these inputs are provided to the software.

---

[1] This information is readily available from the tabulated aerodynamics.

4.2.2 Investigation of the parametric space

The objective in mind while developing RPAS was to create a user-friendly tool allowing to find a set of seven structural parameters that satisfies as closely as possible the equations of motion of the fully-passive, flapping airfoil over a complete cycle of oscillation. For this reason, all sets of parameters providing relatively low residuals appear suitable at being the initial case of the optimization process to be performed. Again, one should recall that the main idea is to obtain an educated guess of the best initial case minimizing the amount of required simulations to complete the entire optimization process. Obviously, finding a set of parameters that *exactly* matches the equations of motion appears unrealistic, and minimizing the residuals is sufficient. Nevertheless, this numerical method offers great advantages over the complete FSI solver for the task of performing a numerical investigation of the parametric space. As one might expect, computing the residuals over a complete cycle of oscillation for a given set of structural parameters is very quick. In fact, this reverse solver can iterate over approximately 10^4 to 10^5 sets of parameters per hour. In counterparts, this methodology requires some previous knowledge of flapping-airfoil turbines because the aerodynamics and the kinematics must be provided as an input. If the initial guess of the aerodynamics and the kinematics is too off from the physical reality of an airfoil undergoing LCO, even the lowest residuals might, in fact, be very large.

This is where the cleverness of this methodology becomes apparent. The idea is to make use of the well-documented kinematically-constrained, flapping-airfoil turbine in order to provide this genuine guess for the tabulated aerodynamics and kinematics. For this reason, the tabulated kinematics provided as an input to RPAS is that of the kinematically-constrained, flapping-airfoil turbine with an amplitude of motion in pitch (θ_0) of 80°, with an amplitude of motion in heave (y_0^*) of 1 chord length, and with a reduced frequency (f^*) of 0.18. Referring to the mapping of efficiency from the kinematically-constrained turbine shown in Figure 1.2, these metrics correspond to the optimal case (i.e., the case with an efficiency (η) of 43%). Further, the phase between both motions is equal to 90°, which is again the ideal and most efficient value used for the kinematically-constrained turbine. The tabulated kinematics can therefore be summarized with the following equations, where the various variables have been quantified above:

$$\theta(t^*) \;=\; \theta_0 \sin\left(2\pi f^*\, t^*\right) \;, \tag{4.3}$$

$$y^*(t^*) \;=\; y_0^* \sin\left(2\pi f^*\, t^* + \frac{\pi}{2}\right) \;. \tag{4.4}$$

The aerodynamic forces and moments provided as an input to RPAS have been obtained through CFD. *OpenFOAM-2.1.x* has been used for the task of predicting the forces and moments on the NACA 0015 airfoil undergoing the motion described with Eqs. 4.3 and 4.4. The corresponding tabulated aerodynamics has been plotted, and it is shown in Figure 4.3.

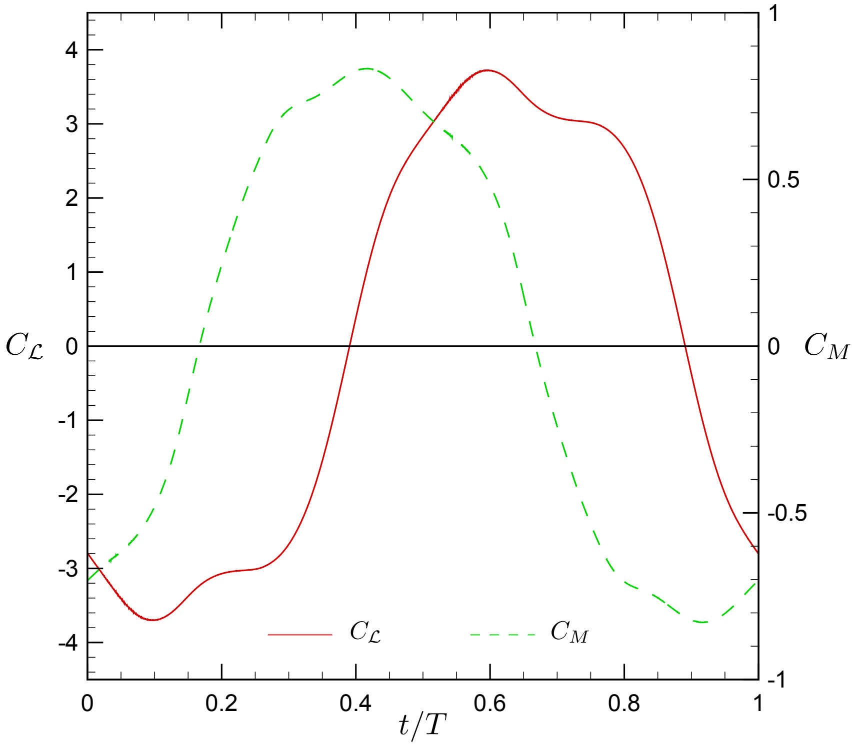

Figure 4.3: Plot of the tabulated aerodynamics provided to the Reverse Passive-Airfoil Solver (RPAS) for a NACA 0015 airfoil oscillating with a reduced frequency (f^*) of 0.18, with a pitching amplitude (θ_0) of 80°, and with a heaving amplitude (y_0^*) of 1 chord length (Re = 500,000).

The drag is not shown on this figure as it is obviously not involved within the equations of motion. Also, the forces and moments shown on this plot have been compared with those of Kinsey from the LMFN (private communication and Kinsey and Dumas (2014)), and they match very closely the forces and moments that have been computed in the past using the commercial CFD code *ANSYS Fluent*.

The last inputs needed by RPAS to perform the residuals scan are the range and increment for each structural parameter. First, a raw and fairly permissive estimation of the realistic range of values pertaining to each parameter has been proposed. This has been done through dimensional considerations of a turbine in both air and water. The resulting permissive range of non-dimensional values, with some emphasis on the word *permissive*, is summarized in Table 4.1. This parametric space has first been investigated with RPAS using a coarse increment between each successive value taken by a given parameter. Following this first swept, some regions of the parametric space where the residuals of both equations proved to be lower have been identified. Within these regions, a second swept making use of a refined increment between successive values has been carried out. The complete process took approximately 45 days of computation on four processors (in serial).

Table 4.1: Range of non-dimensional parameters used for the permissive initial investigation of the parametric space using the Reverse Passive-Airfoil Solver (RPAS).

Parameter	Minimum value	Maximum value
m_h^*	1	600
S^*	-60	450
k_θ^*	0	90
k_h^*	0.004	3000
D_θ^*	0	2
D_h^*	0	4
I_θ^*	0	300

Table 4.2: Set of non-dimensional parameters that minimizes the residuals of both equations of motion within the Reverse Passive-Airfoil Solver.

Parameter	Value	Parameter	Value
m_h^*	2.281	S^*	-0.041
k_θ^*	0	k_h^*	1.654
D_θ^*	0.182	D_h^*	1.393
I_θ^*	0.130		

After a thorough analysis of the results, one particular set of parameters has drawn more attention than the others. Its cycle-averaged residuals on both equations of motion were in the range of 8%, and the maximum residuals within a cycle were in the range of 20%. The numerical value of each non-dimensional parameter pertaining to this set is shown in Table 4.2.

Using this set of parameters, the conventional FSI solver implemented within the *OpenFOAM* CFD toolbox has been used to validate whether or not it constitutes an interesting starting point for the optimization process to follow. To achieve this, a complete FSI simulation has been performed with the parameters given in Table 4.2. The results are presented in Table 4.3, together with the values initially used to run RPAS for comparison. It should be clear to the reader that the values under the column *RPAS* have been provided as *inputs* to the reverse solver, while the values below the column *OpenFOAM* are *outputs* of a complete FSI simulation. In other words, the targeted motion and performances of the kinematically-constrained turbine are represented with the values below the column *RPAS*.

Table 4.3: Frequency, amplitudes of motion and performances predicted with *OpenFOAM* for the case minimizing the residuals of both equations of motion in the Reverse Passive-Airfoil Solver (RPAS). The values provided as inputs to RPAS (optimal kinematically-constrained turbine) are also indicated for comparison.

Parameter	RPAS (input values)	*OpenFOAM* (output values)
f^*	0.180	0.064
θ_0	80°	62°
y_0^*	1.00	0.94
η	0.430	0.123
$\overline{C}_P$	1.17	0.30

It should be noted here that if a set of structural parameters matching exactly the equations of motion had been found (i.e., null residuals at all instants of the cycle), the same kinematics and performances as the kinematically-constrained flapping foil would have been expected for the fully-passive, flapping airfoil. Because such an exact match has not been obtained (and probably does not even exist), the performances and the motion of the fully-passive flapping airfoil do not correspond exactly to the values inputed into RPAS. The results indicate that the predicted amplitude of motion for this set of structural parameters is relatively large in both pitch and heave. Nevertheless, both amplitudes remain slightly below the ideal values provided as an input to RPAS. The frequency of oscillation is also significantly different from that of RPAS. As a matter of fact, the predicted frequency is 2.8 times lower than the frequency associated to RPAS. Last, the metrics quantifying the performances of the fully-passive device, η and $\overline{C}_P$, are 3.5 to 4 times smaller than those of the kinematically-constrained device.

Nevertheless, these results prove that the set of structural parameters described in Table 4.2 allows the existence of large-amplitude LCO. Further, and this is the most important point here, the metrics characterizing the performances of the device are 2 to 4 times greater than those of the RMC experiment. This surely makes this set of parameters very attractive for the task of conducting an optimization of η and $\overline{C}_P$. Further increasing the performances by a factor of 3 would result in a very interesting flow harvester. This set of parameters is therefore chosen as the initial case of the optimization process which will be described in the next section of this chapter. Also, the physics involved in this initial case will later be investigated in more depth when a comparison with the optimal case will be presented.

4.3 Optimization methodology and results

A gradient-like optimization has been performed about the initial case introduced in the previous section of this chapter. This procedure is very systematic and straightforward. Obviously, more refined and elaborate optimization algorithms could have been used for this task, but the simple method presented here proved to be sufficiently efficient. The procedure can be summarized as follows:

1. Individual variations of ± 10% of each structural parameters are prescribed sequentially about the baseline case, and a complete FSI simulation is performed for each. This implies a total of 14 simulations.

2. The values of η and $\overline{C}_P$ are calculated for each one of the 14 simulations.

3. The variations are split into two categories: those which affected positively the performances, and those which affected negatively the performances.

4. A simulation combining together all the individual variations which affected positively the performances is carried out. This set of parameters forms the so-called refined case.

5. The values of η and $\overline{C}_P$ are calculated for the refined case.

6. If η and $\overline{C}_P$ of the refined case are greater than the values of η and $\overline{C}_P$ pertaining to the baseline case, the optimization process is performed one more time (proceed to step **1**) starting with the refined case becoming the new baseline case. If this is not the case, the optimization process is over (proceed to step **7**).

7. The gradient-like optimization is over and a local extrema of η and/or $\overline{C}_P$ has been found.

To make this optimization process as clear as possible, an example is here provided. This example corresponds to the first round of optimization performed about the initial case, here becoming the first baseline case of the previously introduced gradient-like optimization method. As it has been explained, a total of 14 simulations, each showing a single difference from the baseline case, are performed. The results of each one of these simulations is presented in Table 4.4. The column labeled as *Variation* indicates which parameter has been varied, in what direction, and by what amount. For example, the label $m_h^* + 10\%$ indicates that the value of the non-dimensional mass is equal to the baseline value of Table 4.2 increased by 10%. It is to be noted that the initial case features a null rigidity in pitch ($k_\theta^* = 0$). Therefore, the variation is not indicated in percentage for this structural parameter. Further, a lower value has not been investigated as this would make no physical sense.

In light of these results, it is found that the individual variations performed in cases 2, 4, 5, 6, 7, 9, 12 and 13 provide an increase of the turbine's performances. The individual increases of η and $\overline{C}_P$ are not substantial, but the performances are at least changing in the desired direction. The next step is to combine the variations of all these cases providing better

Table 4.4: Effect of varying each structural parameter individually on the motion and on the performances of the flapping airfoil. These numerical values are for the 14 variations performed within the first round of optimization (i.e., the baseline case is the initial case shown in Table 4.2).

Case	Variation	f^*	θ_0^*	y_0^*	η	$\overline{C}_P$
Baseline		0.064	62°	0.94	0.1230	0.3000
1	$m_h^* - 10\%$	0.064	62°	0.93	0.1151	0.2788
2	$m_h^* + 10\%$	0.064	61°	0.94	**0.1291**	**0.3124**
3	$S^* - 10\%$	0.064	62°	0.94	0.1230	0.2985
4	$S^* + 10\%$	0.064	62°	0.94	**0.1241**	**0.3021**
5	$k_\theta^* + 0.0128$	0.075	57°	0.90	**0.1361**	**0.3201**
6	$k_\theta^* + 0.0255$	0.075	56°	0.91	**0.1472**	**0.3201**
7	$k_h^* - 10\%$	0.064	62°	1.01	**0.1293**	**0.3317**
8	$k_h^* + 10\%$	0.064	59°	0.88	0.1168	0.2706
9	$D_\theta^* - 10\%$	0.064	65°	0.96	**0.1280**	**0.3194**
10	$D_\theta^* + 10\%$	0.064	59°	0.92	0.1174	0.2787
11	$D_h^* - 10\%$	0.064	63°	0.99	0.1166	0.2954
12	$D_h^* + 10\%$	0.064	61°	0.90	**0.1297**	**0.3057**
13	$I_\theta^* - 10\%$	0.064	61°	0.93	**0.1282**	**0.3088**
14	$I_\theta^* + 10\%$	0.064	62°	0.95	0.1184	0.2902

performances, and carry out a new simulation. For this task, a simulation is performed using the structural parameters shown in Table 4.5.

The results are encouraging, and the performances are definitely improving. The metrics qualifying the motion of the flapping airfoil, along with those quantifying the performances of the first optimized case, are shown in Table 4.6 and they are labeled *Optimization 1*. A relative increase of approximately 50% of both η and $\overline{C}_P$ compared to the initial case is noticeable, and this is only after a single round of optimization. Therefore, this optimized case described in Table 4.5 becomes the new baseline case, and the same optimization procedures is performed once more. In fact, the procedure is performed four more times before the values of η and $\overline{C}_P$ saturates, suggesting that a local extrema has been reached.

Table 4.5: Set of non-dimensional parameters forming the partially-optimized case resulting from the first round of optimization.

Parameter	Value	Parameter	Value
m_h^*	2.509	S^*	-0.037
k_θ^*	0.026	k_h^*	1.488
D_θ^*	0.164	D_h^*	1.532
I_θ^*	0.117		

The results for each solution emerging from the various rounds of optimization are also shown in Table 4.6. As the reader may notice, the results are absolutely great and very promising. Indeed, after performing the optimization process only five times, which implies a total of only 75 calculations, the efficiency and the total power harvested with the fully-passive, flapping-airfoil turbine have been respectively increased by a factor of 2.7 and 3.5. The amplitude of motion and the frequency of oscillation are now much closer to the values of the kinematically-constrained turbine. Further, the values of η and $\overline{C}_P$ drastically increased with each successive optimization, thus leading to performances not so far behind those of the kinematically-constrained, flapping-airfoil turbine. The set of structural parameters corresponding to this last optimized case, labeled as *Optimization 5*, is described in Table 4.7. These interesting results tend to prove the feasibility and the great potential of using fully-passive, flapping-airfoil turbines as wind or hydrokinetic turbines, just as much as the non-passive, kinematically-constrained device.

Another interesting observation can be made if the optimized case found here is located on the mapping of efficiency shown in Figure 1.2. In fact, for the same amplitude of motion and for the same frequency of oscillation, the efficiency (η) of the kinematically-constrained turbine is around 35%, which is very close to the efficiency of the optimized case. This suggests that this mapping of efficiency could be used as a guideline in order to further increase the performances of the fully-passive turbine.

Within the next sections, a deeper physical analysis of this optimized case is presented. Further, a comparison with the physics of the initial case is also presented in order to better understand the mechanisms through which the performances have been so drastically improved.

Table 4.6: Frequency, amplitude of motion and efficiency predicted with *OpenFOAM* for the initial case and for the subsequent optimized cases.

Case	f^*	θ_0^*	y_0^*	η	$\overline{C}_P$
Initial case	0.064	62°	0.94	0.1230	0.300
Optimization 1	0.080	61°	1.02	0.182	0.474
Optimization 2	0.086	68°	1.11	0.242	0.675
Optimization 3	0.090	75°	1.10	0.319	0.896
Optimization 4	0.096	80°	1.27	0.318	0.929
Optimization 5	0.096	83°	1.26	0.336	1.079

Table 4.7: Set of non-dimensional parameters forming the optimized case resulting from the last round of optimization (optimization 5).

Parameter	Value	Parameter	Value
m_h^*	3.036	S^*	-0.029
k_θ^*	0.031	k_h^*	1.206
D_θ^*	0.119	D_h^*	1.501
I_θ^*	0.095		

4.4 Physics of the initial and the optimized case

The objective of this section is to develop a better understanding of the fundamental differences between the initial and the optimized case in order to highlight what permitted to significantly increase the performances. For this purpose, each of these two cases needs to be investigated with more depth. To achieve this, several key results are thoroughly presented below, and an explanation to the considerably better performances of the optimized case is then formulated.

4.4.1 Initial case

As previously described, the fully-passive, flapping-airfoil turbine making use of the structural parameters forming the initial case oscillates with a reduced frequency (f^*) of 0.064, an amplitude of motion of 62° in pitch (θ_0), and an amplitude of motion of 0.94 chord length in heave (y_0/c). A complementary information to these results and an interesting feature to analyze is the motion history over one complete cycle of oscillation. Note here that the numerical simulations have been computed over enough periods of oscillations so that no distinctive variations are observed from one cycle to the other. For this reason, only the last cycle of oscillation is here considered. This motion history in pitch and in heave is shown in Figure 4.4. The effective angle of attack is calculated as before, specifically:

$$\alpha \;=\; \theta - \arctan\left(\frac{\dot{y}}{U_\infty}\right) \;, \tag{4.5}$$

and it is also shown on this figure. A noticeable feature of the motion is surely that it is not sinusoidal either for the pitching nor the heaving motion. Indeed, it has been found through spectral analysis that the second harmonic is very present within both degree-of-freedom signals, a feature that is clearly visible on the motion history. A second noticeable feature is the lack of symmetry between the upstroke and the downstroke motion of the airfoil[2]. This will be further analyzed when considering the forces and moments experienced by the airfoil. Concerning the effective angle of attack, this quantity will later become useful when analyzing some important features of this case. For the moment, the reader should mostly pay attention to the fact that the peaks of the effective angle of attack and the peaks of the position in heave almost happen at the same moments (i.e., they are in phase).

As previously introduced, the energy harvesting efficiency of the initial case (η) has been found to take a value of 12.3%, while the coefficient of power ($\overline{C}_P$) has been found equal to 0.30. These last two metrics are used to quantify the general aerodynamic performances of the device, but some other metrics reveal to be very useful for the task of understanding in more

---

[2] The upstroke is considered to be the part of the cycle where $\dot{y} > 0$, and the downstroke is the portion of the cycle where $\dot{y} < 0$. Also, the beginning of the downstroke formally represents the beginning of a cycle of oscillation ($t/T = 0$).

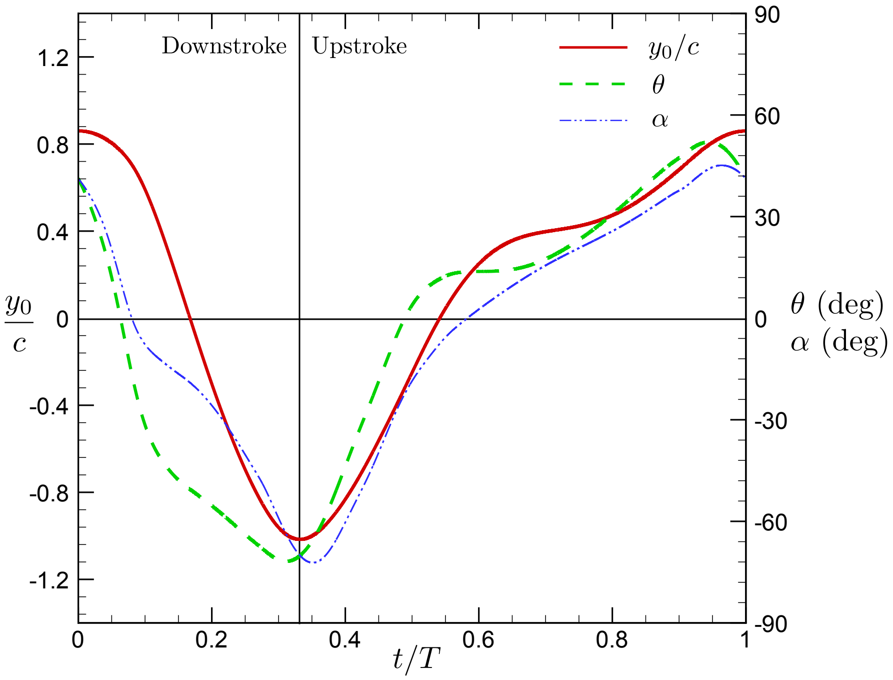

Figure 4.4: Motions history and effective angle of attack of the fully-passive, flapping-airfoil turbine using the structural parameters of the initial case (see Tables 4.2 and 4.3).

details how the turbine operates. More specifically, η corresponds to the total aerodynamic efficiency of the flapping-airfoil turbine: it is a measure of the power transferred to the device over the power available through the flow window of the device. Recalling that the effect of a generator connected to the flapping airfoil is modeled here through a linear damping coefficient in heave (D_h), it is very useful to define another efficiency based on the power dissipated through that linear damper (per unit depth):

$$\eta_{y,damp} = \frac{1}{T} \int_0^T \frac{D_h \dot{y}}{\frac{1}{2}\,\rho\, U_\infty^3\, bd}\, dt \; . \tag{4.6}$$

The interpretation of this last parameter is very analog to that of η, except that it provides a performance metric for the *useful* power only. It corresponds to the ratio of the power available to the generator over the total power available to the turbine. This is a very important metric: a high value of η with a low value of $\eta_{y,damp}$ would imply that most of the power harvested with the device is essentially a loss (i.e., it is dissipated through the pitch damper). The value of $\eta_{y,damp}$ should therefore remain as close as possible to the value of η. However, $\eta_{y,damp}$ can obviously never be greater than η.

Using this new definition, a value of $\eta_{y,damp} = 10.3\%$ has been calculated for the current configuration of the turbine. Remembering the value of η to be 12.3%, this indicates that

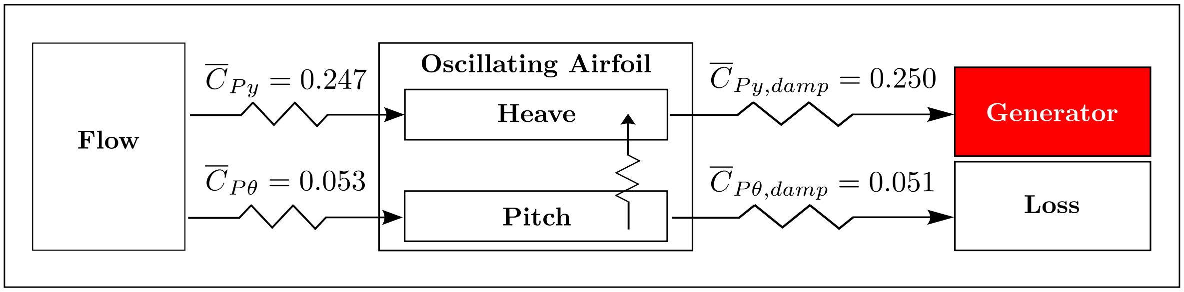

Figure 4.5: Schematic representation of the flow of power through the fully-passive, flapping-airfoil turbine using the structural parameters of the initial case (Table 4.2).

some power is dissipated through the pitch damper, but this represents only a small fraction of the power harvested from the flow. Most of the harvested power is therefore provided to the generator. This observation is further confirmed when considering the various coefficients of power previously introduced in Chapter 2 (Eqs. 2.26 to 2.29), the values of which are shown within the schematic representation of Figure 4.5. As shown, the heaving motion accounts for over 80% of the harvested power. Furthermore, over 80% of the harvested power is provided to the generator[3] [4]. It should also be mentioned that there is a slight internal transfer of energy between both degrees-of-freedom: the pitching motion feeds the heaving motion with some weak power ($\overline{C}_{P,tr} = 0.003$).

The instantaneous coefficients of power can also be analyzed throughout a complete cycle of oscillation in order to obtain a complete picture of the flow harvesting mechanisms. The instantaneous values of C_P, C_{Py}, $C_{P\theta}$ and $C_{Py,damp}$ are plotted in Figure 4.6. Again, the asymmetry between the upstroke and the downstroke of the airfoil is greatly noticeable. It appears that the flow is doing much more work on the airfoil during the downstroke than it does during the upstroke. This is noticeable on the curve of C_P, which exhibits larger values during the downstroke. The same conclusion holds true concerning the generator: it receives more power during the downstroke.

Another noticeable feature is certainly that the airfoil harvests the flow through the heaving motion for most of the cycle, except for two periods of time: approximately $t/T = 0$ to $t/T = 0.07$ and $t/T = 0.33$ to $t/T = 0.47$. These moments correspond to both transitions between the upstroke and the downstroke. During these, the airfoil is in fact doing some work on the flow through its heaving motion. This, of course, is very costly from a performance point of view. Nevertheless, the observed behavior is very different in pitch. Most of the time,

---

[3] It has been verified that $\overline{C}_{Py} + \overline{C}_{P\theta} = \overline{C}_{Py,damp} + \overline{C}_{P\theta,damp}$. However, this condition is not strictly respected on the schematic due to the rounding of numerical values.

[4] It is interesting to mention that verifying if the condition $\overline{C}_{Py} + \overline{C}_{P\theta} = \overline{C}_{Py,damp} + \overline{C}_{P\theta,damp}$ is respected offers a way to determine if the simulation has been carried out for long enough. Indeed, if this condition is not respected, this indicates that the airfoil has not reached its permanent regime yet.

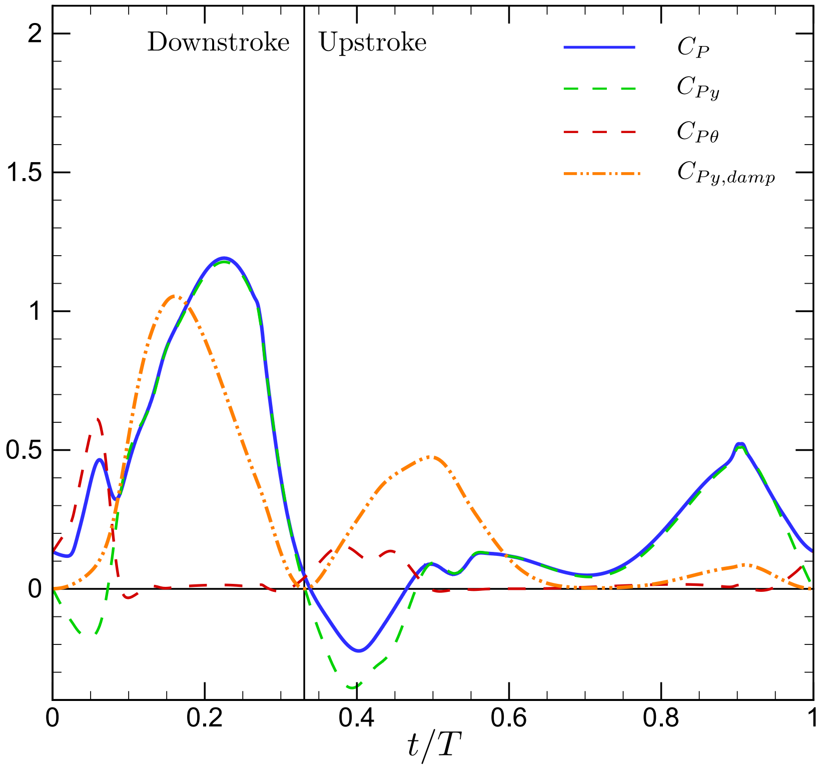

Figure 4.6: Instantaneous coefficients of power for the fully-passive, flapping-airfoil turbine using the structural parameters of the initial case (Table 4.2).

no power is harvested from the flow, nor does the airfoil do some work on the flow. However, during both transitions between the upstroke and the downstroke, some power is harvested from the flow through the pitching motion. In other words, when no power is harvested through the heave, the pitching motion takes over and harvests the flow. As it will soon be highlighted, this is due to the deep dynamic stall of the airfoil. Nonetheless, the contribution of the pitching motion is not always high enough to fully compensate for the work the airfoil is doing on the flow through its heaving motion. This is what happens during the transition between the downstroke to the upstroke ($t/T = 0.33$ to $t/T = 0.47$), thus leading to negative instantaneous values of C_P.

The stalling of the airfoil during its transition from the downstroke to the upstroke ($t/T = 0.33$ to $t/T = 0.47$) can be observed in Figures 4.7 and 4.8 with the frames corresponding to $t = 4T/12$, $t = 5T/12$ and $t = 6T/12$. These figures show the normalized pressure fields and the normalized z-vorticity fields in the vicinity of the airfoil at various equally-spaced moments of the cycle. A large eddy shed from the leading edge of the airfoil is clearly present. Remembering the theoretical notions of Chapter 1, this is a typical characteristic of deep dynamic stall. Whenever a vortex is shed, the low pressure at its core has an influence on the aerodynamic forces experienced by the airfoil. However, the motion of the airfoil during the transition between the downstroke to the upstroke is such that the airfoil's surface does not remain close to the vortex as it is convected downstream. This is particularly clear when the pressure field is examined: the low pressure originating from the eddy is mitigated on the airfoil's surface due to the large distance between the foil and the core. In fact, the motion of the airfoil is such that once the eddy is shed, it starts moving very quickly in the opposite direction due to the effect of the spring in heave, thus taking the airfoil away from the vortex. This certainly restrains the level of interaction between the vortex and the airfoil, thus reducing the work achieved by the vortex on the airfoil.

Although, the vortex does very little work on the airfoil, it does achieve some work on it: because no spring is present in pitch (see Table 4.2), the pitching of the airfoil during the transition from the downstroke to the upstroke is mostly due to this airfoil-vortex interaction. The reader should now return briefly to Figure 4.4 and consider the curve for the effective angle of attack and the curve for the heave position around $t/T = 0.33$ to $t/T = 0.47$. Because the large vortex is approximately shed when the maximum effective angle of attack is reached, it clearly appears that the airfoil is already moving upward when the shedding happens. This can be thought of as being an inadequate synchronization between the heaving motion and the pitching motion [5].

Conversely, during the transition of the airfoil from the upstroke to the downstroke ($t/T = 0$ to $t/T = 0.07$), the large vortex shed at the leading edge remains closer to the airfoil's surface as it is convected downstream. This is observed with the frames corresponding to $t = 11T/12$, $t = 0$ and $t = T/12$ in Figures 4.7 and 4.8. This can also be observed by considering the effective angle of attack and the heave position shown in Figure 4.4. Again, the shedding of the vortex approximately occurs at the extremum value of the effective angle of attack. As this happens, the airfoil continues to move upward for some time, towards the vortex itself, before to start moving in the opposite direction, away from the vortex. The airfoil-vortex interaction is therefore greater than what has been observed during the transition from the downstroke to the upstroke, and this has positive effects overall. Indeed, as the vortex remains closer to the leading edge and moves downstream, the low pressure it causes on the airfoil's surface past the elastic axis leads to a fairly large pitching moment. This, combined with a fairly large pitching rate at the same moment, results in a relatively large power harvested from the flow through the pitching motion. In fact, the harvesting of the flow through the pitching motion is large enough to fully compensate for the work done on the flow through the heaving motion of the airfoil at the same moment, thus leading to an overall positive instantaneous value of C_P during this transition.

---

[5] It is somewhat difficult to talk of an inadequate *phase lag* between both motions. Because of the non-sinusoidal motions, a phase lag would have to be calculated for each of the Fourier modes present in the motions.

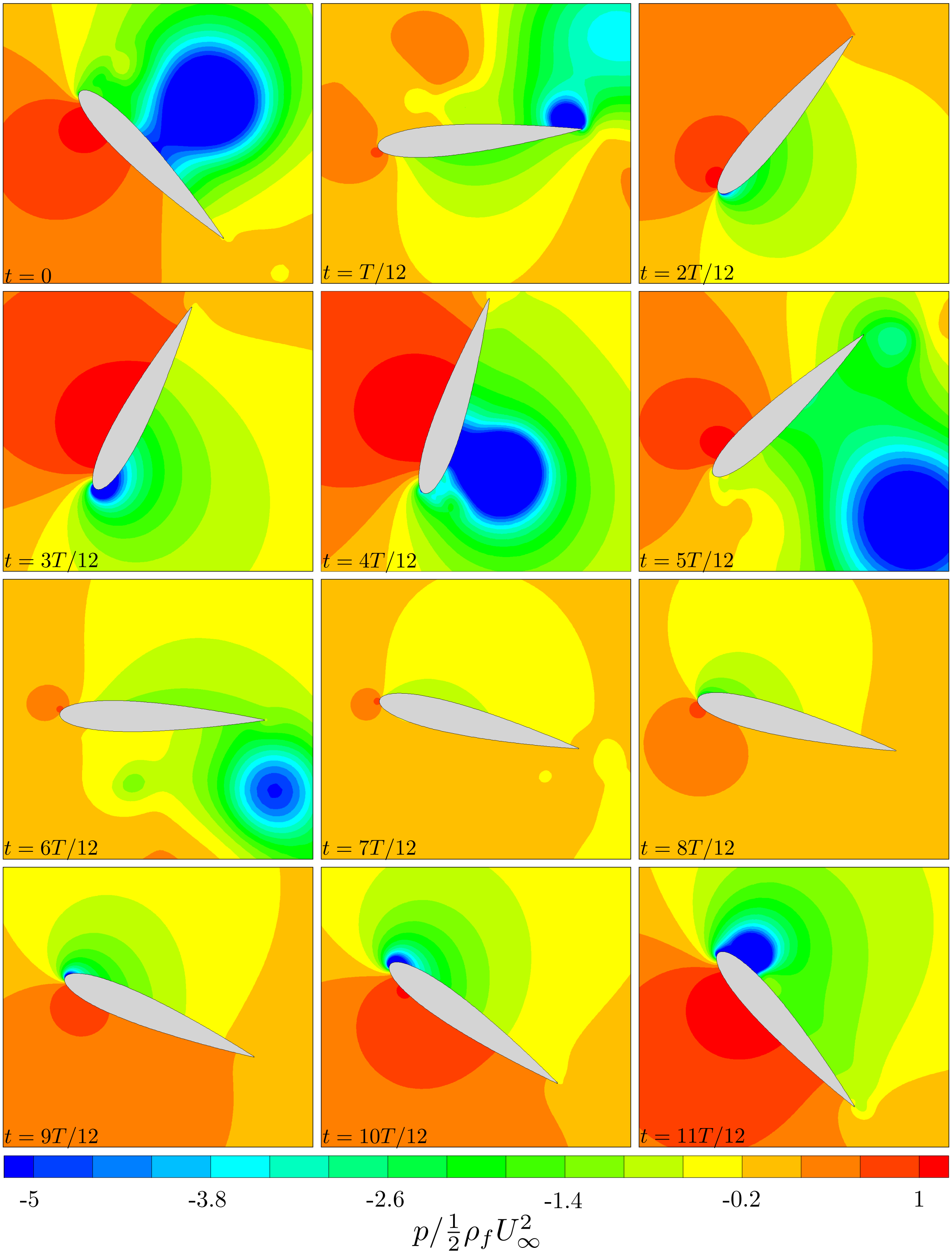

Figure 4.7: Fields of normalized pressure $(p/\frac{1}{2}\rho_f U_\infty^2)$ in the vicinity of the flapping airfoil at various instants throughout one complete period of oscillation (T) for a fully-passive, flapping-airfoil turbine using the structural parameters of the initial case (Table 4.2).

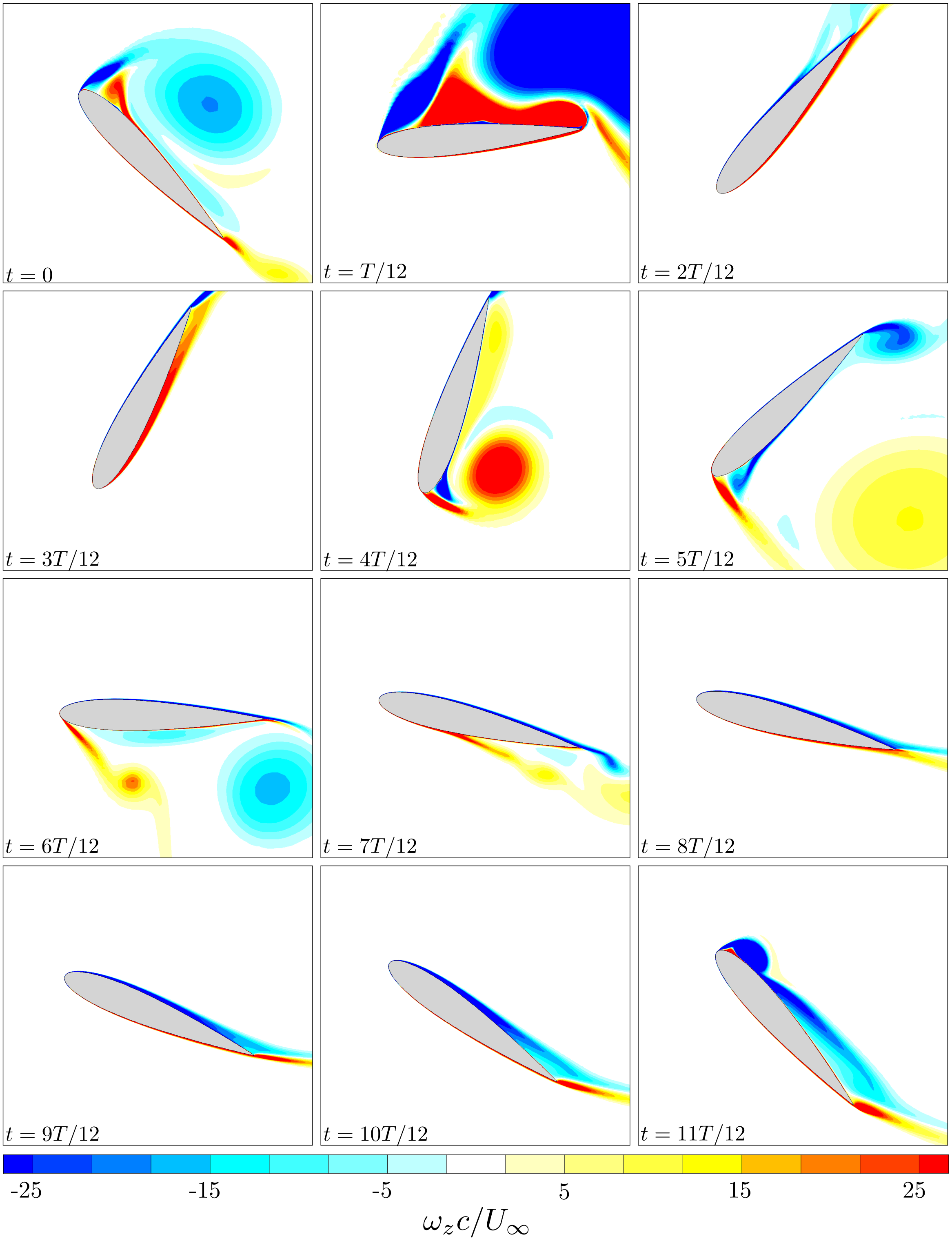

Figure 4.8: Fields of normalized z-vorticity ($\omega_z c/U_\infty$) in the vicinity of the flapping airfoil at various instants throughout one complete period of oscillation (T) for a fully-passive, flapping-airfoil turbine using the structural parameters of the initial case (Table 4.2).

The fact that the airfoil is doing some work on the flow through its heaving motion at both the upstroke and the downstroke extrema is also associated to an inadequate synchronization between the heaving and the pitching motions: as the airfoil reverts direction in heave, the lift is such that it is opposed to the airfoil's motion. This explains why a phase of 90° has been used for the kinematically-constrained device presented in Chapter 1: when the airfoil reaches its maximum and its minimum position in heave, the effective angle of attack is null. This scenario is believed to correspond to the ideal synchronization between both motions. To summarize, in the current case the airfoil changes direction in heave mainly as a result of the structural stiffness in heave. This can be seen on Figure 4.9 which will soon be discussed. In the best case, the reason for the change in the heaving direction should be shared by both the aerodynamics and the heave structural stiffness: the sign of the lift and the sign of the heaving velocity should change at the same moment.

The asymmetry between the upstroke and the downstroke is also very clear when considering the budget of all terms involved within the equations of motion. This is shown in Figures 4.9 and 4.10 where each term has its own curve. The value of each term is computed according to the following equations:

$$C_{\mathcal{L}} \;-\; m_h^*\,\ddot{y}^* \;-\; S^*\left(\dot{\theta}^2\,\sin\theta - \ddot{\theta}\cos\theta\right) \;-\; D_h^*\,\dot{y}^* \;-\; k_h^*\,y^* \;=\; 0\;, \tag{4.7}$$

$$C_M \;-\; I_\theta^*\,\ddot{\theta} \;+\; S^*\ddot{y}^*\cos\theta \;-\; D_\theta^*\,\dot{\theta} \;-\; k_\theta^*\,\theta \;=\; 0\;. \tag{4.8}$$

These are simply the equations of motion where all terms have been switched to the left-hand side. As a result, the summation of all contributions, at any moment of the cycle, is equal to zero.

The effect of deep dynamic stall is visible on both $C_{\mathcal{L}}$ and C_M. As previously mentioned, the effect of the shed vortex is mitigated for $t/T = 0.33$ to $t/T = 0.47$. However, the vortex has a relatively large impact on the aerodynamics in the vicinity of $t/T = 0$ to $t/T = 0.07$, and this is especially clear when considering the aerodynamic moment where a sharp peak is observed. However, it is worth repeating that the pitching of the airfoil at the end of both the upstroke and the downstroke is attributed to the interaction between the vortex and the airfoil, which means that although the interaction is weaker for $t/T = 0.33$ to $t/T = 0.47$, there is obviously one, and it is not negligible. Indeed, it is precisely when the vortex generates a fairly low pressure on the airfoil, close to the trailing edge, thus giving rise to a moderate/strong aerodynamic moment, that the airfoil starts pitching in the opposite direction. This synchronization can be observed if the reader compares the motion history of Figure 4.4 with the history of C_M from Figure 4.10. This highlights the large impact of the vortex shed during the deep dynamic stall event. The fact that the airfoil-vortex interaction is so important indicates that the airfoil is undergoing LCO as a result of stall flutter: it is the periodic stalling of the airfoil

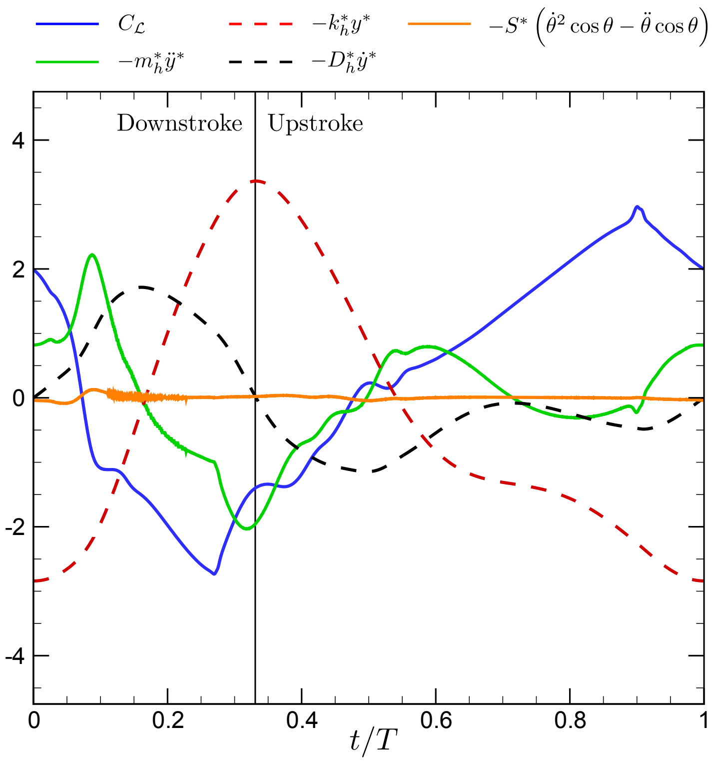

Figure 4.9: Budget of the terms involved within the equation of motion in heave of the fully-passive, flapping-airfoil turbine using the structural parameters of the initial case (Table 4.2).

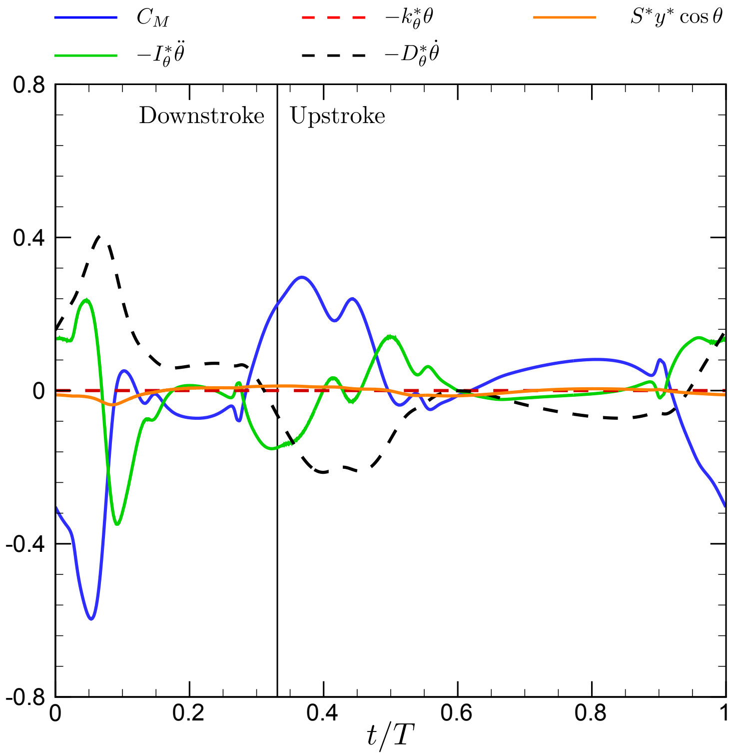

Figure 4.10: Budget of the terms involved within the equation of motion in pitch of the fully-passive, flapping-airfoil turbine using the structural parameters of the initial case (Table 4.2).

that prevents the motion from simply diverging from the equilibrium position, thus leading to the observed cyclic motion.

Another interesting feature observed with Figures 4.9 and 4.10 is certainly that the forces and moments resulting from the inertial coupling are not significant when compared to all the other terms. This is because the static imbalance of the current case is small.

As a last comment on the initial case, one could legitimately ask what mechanism is responsible for the observed asymmetry between the upstroke and the downstroke, some sort of hysteresis behavior. This is a very complex question to answer, and formulating an explanation is not the main focus of this work. The reason why it is so difficult to formulate an answer is certainly a result of this complex two-way interaction between the flow and the aeroelastic structure.

4.4.2 Optimized case

Moving on with the optimized case (see Table 4.7), a reduced frequency (f^*) of 0.096 has been obtained, combined with amplitudes of motions in pitch (θ_0) and in heave (y_0/c) of respectively 83° and 1.26 chord length. The corresponding motion history is shown in Figure 4.11. For the same reasons as before, only one cycle is shown. It is noticeable that the motion in heave is very close to being sinusoidal. Nevertheless, this is not the case for the pitching motion. Indeed, the pitching motion happens in three distinctive phases throughout the cycle. For both the upstroke and the downstroke of the airfoil, there is a phase where the pitching rate is relatively constant and takes a fairly high value. This is referred to as being the "fast pitching regime" (an example of such regime is observed on Figure 4.11 for $t/T = 0.45$ to $t/T = 0.55$). Further, there is another phase where the pitching rate is again relatively constant, but takes a much lower value than previously. This is referred to here as the "slow pitching regime" (an example of such regime is observed on Figure 4.11 for $t/T = 0.60$ to $t/T = 0.85$). Lastly, there is another phase where the pitching rate is not constant. This happens during both transitions between the upstroke and the downstroke. This is referred to as the "transitional pitching regime". This nomenclature will be used later in this subsection. Another feature that can be observed on Figure 4.11 is the great symmetry between the downstroke and the upstroke. This is obviously in contrast with the results of the previously analyzed initial case. As a matter of fact, no distinctive variations are here observed between the downstroke and the upstroke.

For this optimized configuration of the fully-passive, flapping-airfoil turbine, a value of 33.6% has been found for η, and a value of 1.079 has been found for $\overline{C}_P$. The same metrics as those used within the previous subsection can also be used in order to better understand how the turbine is harvesting the flow. It is found that $\eta_{y,damp}$ takes a value of 29.1%, which means that most of the harvested power is again provided to the generator and very little is lost in

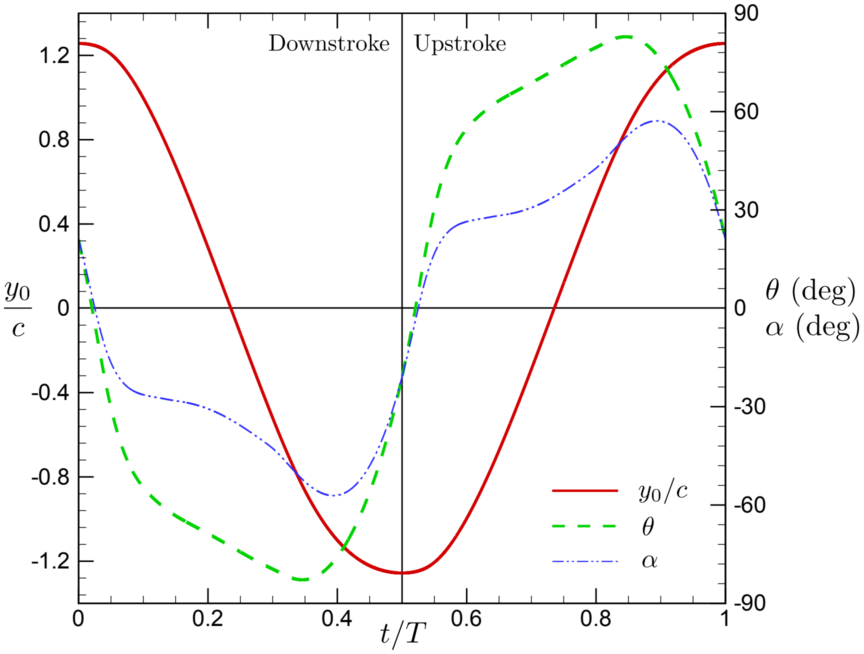

Figure 4.11: Motion history and effective angle of attack of the fully-passive, flapping-airfoil turbine using the structural parameters of the optimized case (see Tables 4.6 and 4.7).

the pitch damper. Again, this is the desired behavior since only the power available to the generator is considered as being useful. The fact that most of the harvested power is indeed useful is further highlighted with a schematic of the coefficients of power characterizing the turbine. This is shown in Figure 4.12. It can be observed that over 85% of the power is harvested through the heaving motion of the turbine. Furthermore, over 85% of the total harvested power is useful and available to the generator. A very small value of $\overline{C}_{P,tr} = 0.009$ has been calculated. Again, this corresponds to what is transferred from the pitch degree-of-freedom to the heave degree-of-freedom. This is the same situation as the one observed for the initial case: the pitch degree-of-freedom feeds very little power to the heave degree-of-freedom, thus providing only slightly more power to the generator than what is harvested through the heave motion. Furthermore, these results demonstrate that the pitching motion can be fully autonomous from an energetic point of view, which has been stated as the expected or ideal behavior within the introduction of this thesis. Indeed, the power dissipated within the pitch damper is fully compensated by the power harvested through the pitch motion.

The instantaneous values of the most important coefficients of power, namely C_P, C_{Py}, $C_{P\theta}$ and $C_{Py,damp}$, have also been computed and plotted throughout a complete cycle of oscillation. This is shown in Figure 4.13. The first noticeable difference from the initial case certainly resides in the far larger values of the power coefficients that are attained with the optimized

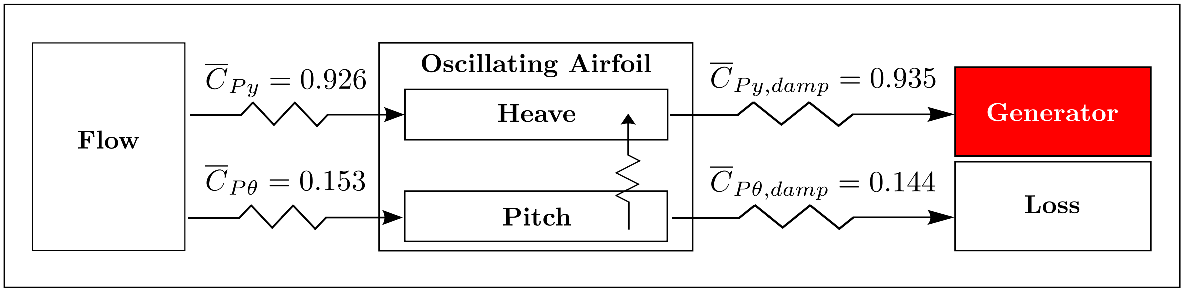

Figure 4.12: Schematic representation of the flow of power through the fully-passive, flapping-airfoil turbine using the structural parameters of the optimized case (Table 4.7).

turbine. This, of course, is in agreement with the fact that more power is harvested with the optimized turbine. Note that the same scales have been used for the plots of the initial case (Figure 4.6) and the optimized case in order to allow an easier comparison of the values and trends. Figure 4.13 also shows the great symmetry previously found between the upstroke and the downstroke.

Further, the curve of C_P indicates that the device harvests the flow at *all* moments throughout its cycle: there is no portion of the cycle where the flapping airfoil is doing some work on the flow (negative C_P). This is in contrast with the initial case, where the airfoil did expend some work on the flow at some moments of the cycle. In addition, the curve of C_P exhibits four distinctive peaks. Two of them are identical and of lower amplitude (peak value of 1.3), and two of them are identical and of larger value (peak value of 2.05). The two peaks with a larger amplitude correspond to the portion of the cycle where the airfoil is approximately in the middle of its downstroke or its upstroke and has a large heaving velocity. The curves of C_P and C_{Py} are very close to each other near these two peaks. During these moments where the airfoil's heaving velocity is great, the pitching motion, in counterpart, does not contribute at harvesting the flow significantly, nor does it achieve some work on the flow. It is therefore the heaving motion that accounts for these peaks of large amplitude.

In contrast, the peaks of lower amplitude happen when the airfoil is transitioning from the downstroke to the upstroke, and vice versa. The peaks are associated to the deep dynamic stall events happening at both extrema of the heaving motion. It can be observed that in the vicinity of $t/T = 0.45$ to $t/T = 0.55$ and $t/T = 0.95$ to $t/T = 0.05$ the curves of C_P and $C_{P\theta}$ are very close to each other, thus indicating that very little or no harvesting of the flow is achieved through the heaving motion. This makes physical sense as the heaving velocity is relatively small during these transitions between the downstroke and the upstroke. It is indeed the pitching motion alone that accounts for these two smaller peaks on the curve of C_P . The effect of the dynamic stall happening at these moments can also be seen in Figures 4.14 and 4.15 where the pressure and the z-vorticity fields are shown in the vicinity of

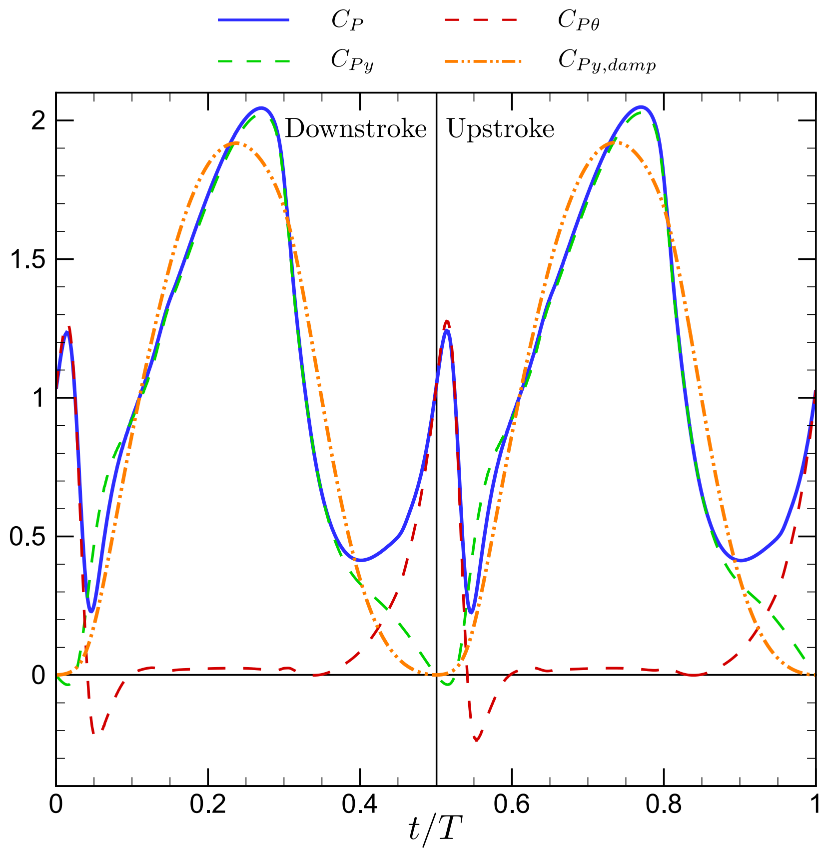

Figure 4.13: Instantaneous coefficients of power for the fully-passive, flapping-airfoil turbine using the structural parameters of the optimized case (Table 4.7).

the airfoil at various moments within a complete cycle of oscillation. The first stalling event, corresponding to the transition between the downstroke to the upstroke, can be visualized with the frames for $4T/12$, $5T/12$ and $6T/12$. The second stalling event, corresponding to the transition between he upstroke to the downstroke, can be observed with the frames for $10T/12$, $11T/12$ and 0.

As it may be observed, the interaction of the shed vortex with the airfoil is very important during the deep dynamic stall events. As the eddy travels downstream, it remains very close to the airfoil's surface, thus generating a relatively intense low pressure on one side of the airfoil. This low pressure on the airfoil's surface is very clear when considering the pressure fields. This is also visible when considering the aerodynamic forces and moments on the airfoil, which are shown in Figures 4.16 and 4.17. These figures show the budget of all terms involved within both equations of motion, just as for Figures 4.9 and 4.10 of the previous subsection. Following the deep dynamic stall event, the value of $C_{\mathcal{L}}$ drops significantly, followed by a partial and momentarily re-augmentation. This re-augmentation of the lift force is due to the low pressure that exists within the core of the vortex. The interaction between the eddy

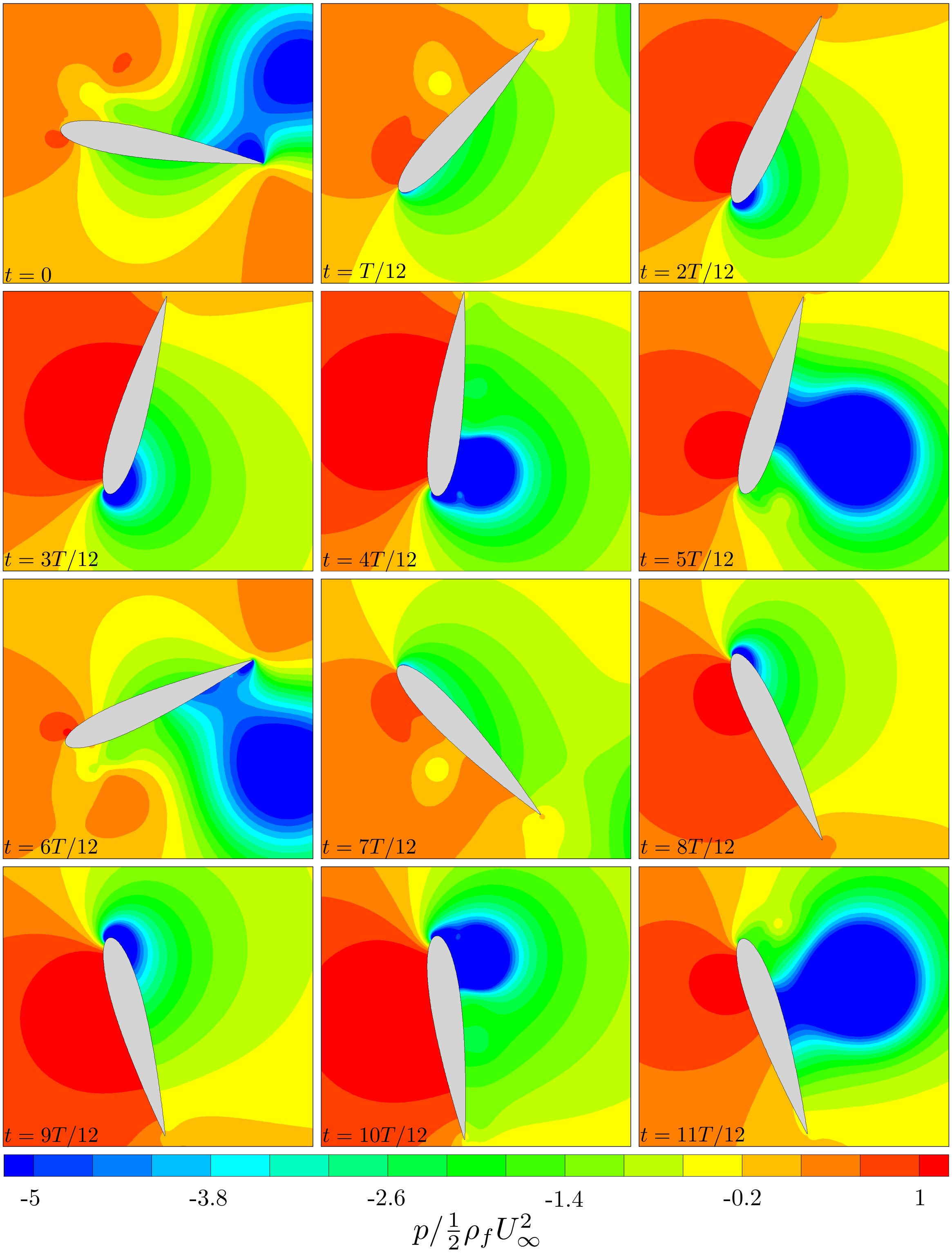

Figure 4.14: Fields of normalized pressure ($p/\frac{1}{2}\rho_f U_\infty^2$) in the vicinity of the flapping airfoil at various instants throughout one complete period of oscillation (T) for the fully-passive, flapping-airfoil turbine using the structural parameters of the optimized case (Table 4.7).

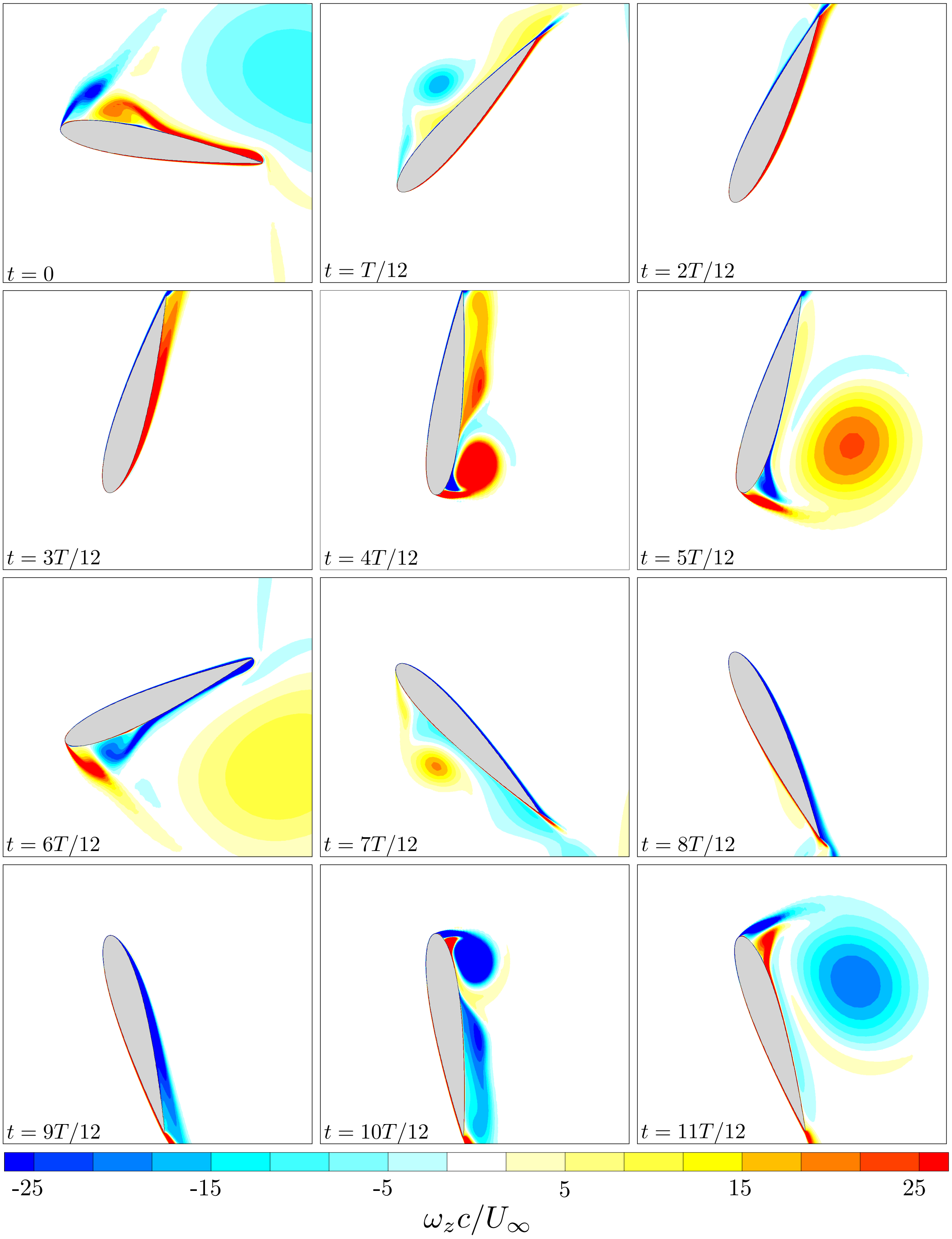

Figure 4.15: Fields of normalized z-vorticity ($\omega_z c/U_\infty$) in the vicinity of the flapping airfoil at various instants throughout one complete period of oscillation (T) for the fully-passive, flapping-airfoil turbine using the structural parameters of the optimized case (Table 4.7).

and the airfoil is also very clear from the curve of C_M. The large peaks are again due to the airfoil-vortex interaction. As the eddy travels downstream, the arm of the forces generated by the eddy on the airfoil increases, and it generates a fairly large aerodynamic moment on the airfoil.

This strong interaction between the airfoil and the vortex is the result of an adequate synchronization between the pitching and the heaving motions, which is very different from what has been observed for the initial case. Indeed, the current motion is such that the vortex remains close the the airfoil's surface for both the upstroke and the downstroke. When the vortex is shed, the airfoil continues to travel towards the vortex, thus keeping it close enough to interact greatly with it. By considering the heave position in time and the effective angle of attack in time, which are shown in Figure 4.11, this becomes obvious. Because the vortex is approximately shed when the airfoil reaches its peak value of the effective angle of attack, it is clear that the airfoil travels for some time towards the vortex after it is shed. This is because the peak values of the effective angle of attack happen significantly before the peak values of the heave position.

This strong interaction with the vortex allows the airfoil to use the low pressure at the core of the eddy to passively pitch the airfoil and to extract more power from the flow. One could have believed that the presence of a spring in pitch is the governing agent of the airfoil's pitching motion, but it turns out that this is clearly not the case. It is obvious from Figure 4.17 that it is the interaction with the vortex that is mainly responsible for the pitching of the airfoil at the extrema of the upstroke and the downstroke. Indeed, the moments generated by the spring are approximately one order of magnitude smaller than the moments associated to the airfoil-vortex interaction. Further, the reader can verify that the large aerodynamic moment corresponds precisely to the moment where the airfoil is in this fast pitching regime previously described. Again, this confirms that stall flutter is definitely the physical mechanism through which the amplitude of motion of the airfoil is limited, thus leading to a periodic motion.

The adequate synchronization between both motions also has another positive effect on the efficiency of the device. Returning to Figure 4.13, it is observed that the heaving motion of the airfoil never actually does work on the flow. In the analysis of the initial case, it had been found that the airfoil was indeed doing some work on the flow at some moments. In the current case, the moment when $\theta = 0°$ is well synchronized with the moment where the airfoil is at its extrema in heave, and this does not permit such a detrimental situation as doing some work on the flow to occur. This is because the effective angle of attack passes through a null value at the same time the heaving velocity passes through a null value. This means that the lift coefficient and the heaving velocity change sign at the same moment, and this does not lead to the detrimental situation where the lift and the heaving velocity are in opposite directions. This adequate synchronization can be appreciated from Figure 4.11.

Returning to the fast and the slow pitching regimes of the airfoil, these turn out to have a

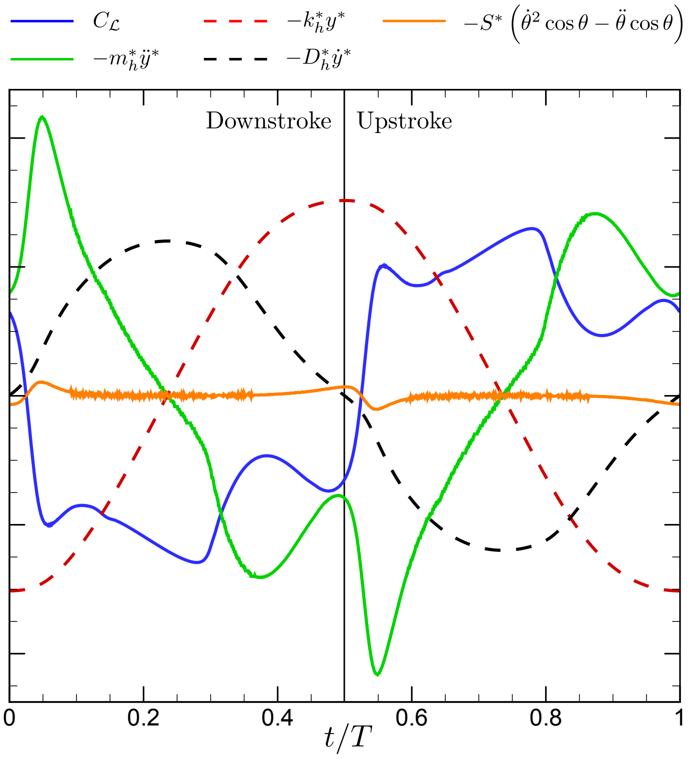

Figure 4.16: Budget of the terms involved within the equation of motion in heave of the fully-passive, flapping-airfoil turbine using the structural parameters of the optimized case (Table 4.7).

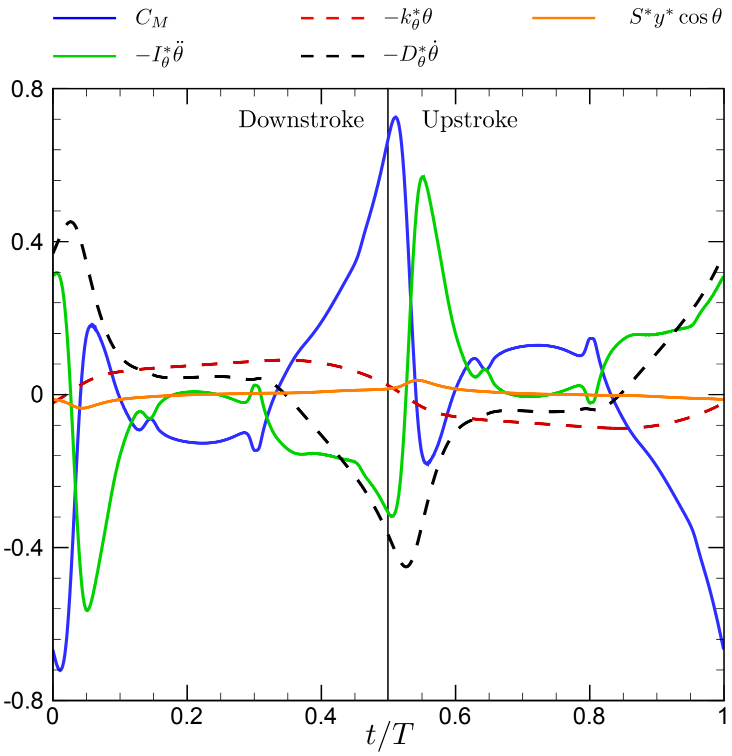

Figure 4.17: Budget of the terms involved within the equation of motion in pitch of the fully-passive, flapping-airfoil turbine using the structural parameters of the optimized case (Table 4.7).

very significant and positive impact on the performances of the turbine. Indeed, the curve of $C_{\mathcal{L}}$, which is shown in Figure 4.16, is very different from that of the initial case shown in Figure 4.9. Because the airfoil exhibits a fast pitching regime right after it has transitioned from the upstroke to the downstroke, or vice versa, the lift coefficient quickly reaches fairly high values, thus maximizing the power harvested through heaving. If the pitching of the airfoil were to happen slowly at the beginning of the upstroke or the downstroke, such as if the pitching was sinusoidal in time, the value of the lift coefficient would remain much lower for a significant portion of the cycle, which would necessarily imply a lower value of the power extracted from the flow. To make this point clear, the idea here is that the fast pitching regime minimizes the impact of the transition from the upstroke to the downstroke, and vice versa. Obviously, the lift force has to take a null value at some point during this transition, but the lift should not remain close to this value for long. The fast pitching regime achieves exactly this task by increasing the lift very quickly.

As a last comment, it is interesting to note that the inertial coupling term shown in Figures 4.14 and 4.15 is again of mitigated importance when compared to all other terms involved within both equations of motion of the fully-passive, flapping-airfoil turbine. This suggests that this coupling term did not play a significant role in the optimization process.

4.4.3 Summary of the physical mechanisms enhancing the turbine's performances

In light of the previous results, two key mechanisms have been identified as being responsible for the significant optimization of the turbine's performances. The first of these mechanisms is the adequate synchronization between both the pitching and the heaving motions, while the second mechanism is the presence of a fast and a slow pitching regime. Both mechanisms are here briefly summarized.

Concerning the first mechanism, namely the adequate synchronization of both degrees-of-freedom, the pitching and the heaving have been observed to be almost in phase for the initial case. This has two detrimental consequences. One is that the airfoil necessarily experiences, momentarily, a lift force which is in opposite direction to the heaving velocity, thus implying that the airfoil is doing some work on the flow (i.e., it returns some power to the flow). The other consequence is that the airfoil does not remain close to the vortex shed at its leading edge during the deep dynamic stall event. Indeed, this vortex plays a key role in the dynamics of the airfoil, and it has the potential of enhancing the power harvested from the flow. The synchronization between both motions is adequate in the case of the optimized turbine. In some sense, this observed adequate synchronization is similar to the prescribed phase lag of 90° between the pitching and the heaving motions of the kinematically-constrained, flapping-airfoil turbine: $\theta = 0^\circ$ when the airfoil is at an extrema in heave ($\dot{y}^* = 0$).

Concerning the second mechanism, the presence of a fast pitching regime followed by a slow pitching regime has been found to be very beneficial. Indeed, this affects the shape of the lift curve. Instead of having a single isolated peak in the lift force, such as for the initial case (Figure 4.9), the value of the lift force remains close to this peak value over a much larger portion of the cycle. This larger lift force is, of course, fully correlated to an increase of the power extracted from the flow. In fact, this fast pitching regime minimizes the effect of the airfoil changing direction when it reaches the extrema of its upstroke or its downstroke. During this transition the airfoil must necessarily pass through a value of $\alpha = 0$, and the lift must therefore pass through a null value. The effect of this fast pitching regime is to pass very quickly over these effective angles of attack associated to small values of the lift force, which are necessarily associated to small values of the instantaneous harvested power.

Lastly, the reader should now be fully convinced that the LCO of the airfoil are the result of stall flutter. The periodic encounter of deep dynamic stall introduces the nonlinearities required in the aerodynamics as a mean of limiting the growth of the airfoil's amplitude of motion. The reader may return to Table 1.2 and Figure 1.9 to find out that the main features of the flow and the trends of the aerodynamic forces and moments described and presented within this section are in excellent agreement with the general picture drawn of deep dynamic stall within Chapter 1.

4.4.4 Theoretical analysis of the airfoil's loss of stability

As discussed in Chapter 1 of this thesis, clever analytical tools have been developed over the years in order to theoretically predict the flutter phenomena. This is generally achieved with the so-called flutter matrix, which is obtained using the equations of motion of the studied device together with an aerodynamic theory (i.e., one of the steady, quasi-steady or unsteady potential theories). Using such a powerful tool for better understanding the current flapping-airfoil turbine would, of course, be attractive. However, it is not possible to study the dynamical loss of stability of the airfoil. This is because in both the initial case and the optimized case, the actual dynamic pressure is well above the divergence value of the system.

Recalling notions of Chapter 1, divergence is a static instability which happens whenever the torsional restoring moment is not large enough to counteract the aerodynamic moment. Said otherwise, the aerodynamic moment grows faster than the restoring moment from the spring. Using the non-dimensional formulation of this thesis, the ratio of the dynamic pressure at divergence (see Eq. 1.19) over the dynamic pressure is:

$$\frac{q_{div}}{q} = \frac{2\,c\,k_\theta^*}{e\left(\dfrac{\partial C_{\mathcal{L}}}{\partial \theta}\right)} \,, \tag{4.9}$$

which is formally equal to 0 for the initial case, and approximately equal to 0.12 for the

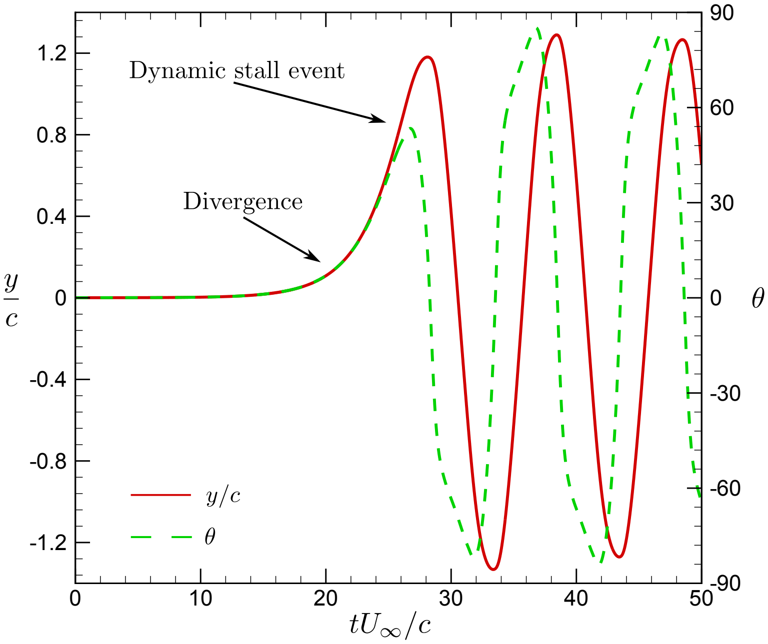

Figure 4.18: Instantaneous position in both pitch (θ) and heave (y/c) following the beginning of a run for the optimized case where no external initial perturbation is applied on the airfoil.

optimized case. This means that the airfoil is statically unstable due to the divergence phenomena. Therefore, as mentioned in Chapter 1, using a linear stability analysis would fail at predicting the onset of classical flutter, as well as the frequency of oscillation.

However, this last result suggests that the LCO of the airfoil are not only self-sustained, but they are also self-induced. Indeed, following any perturbation, as small as it can be, the airfoil starts diverging from its equilibrium position. Once it reaches a large amplitude in both pitch and heave, a deep dynamic stall event occurs, thus limiting the divergence of the airfoil by forcing it to start moving in the opposite direction. This is the process through which the cyclic motion is initiated, and this is clearly illustrated in Figure 4.18 showing the instantaneous position in both pitch (θ) and heave (y/c) following the beginning of a run for the optimized case where no external perturbation is applied on the airfoil.

4.5 Sensitivity study

4.5.1 Sensitivity to the structural parameters

Now that an optimal case has been found, analyzed and well understood from a physical point of view, each one of the seven structural parameter can be varied over a larger range of values. This proves to be very useful in order to study the individual effect of each parameter, and also to determine the sensitivity of the device towards each parameter. The results of the numerous simulations performed for this specific task are presented within Figures 4.19 to 4.24, where each of the seven structural parameters has its own corresponding figure except for I_θ. The reason for that will be given shortly.

For Figures 4.19 to 4.24, each structural parameter has been varied over the following range of non-dimensional values (the values are also indicated in the figures' captions):

- m_h^* : between 2.04 and 6.12; optimized case: $m_h^* = 3.036$;
- S^* : between -0.165 and 0.165; optimized case: $S^* =$ -0.029;
- k_h^* : between 0 and 3; optimized case: $k_h^* = 1.206$;
- k_θ^* : between 0 and 0.056; optimized case: $k_\theta^* = 0.031$;
- D_h^* : between 0 and 3.57; optimized case: $D_h^* = 1.501$;
- D_θ^* : between 0 and 0.68; optimized case: $D_\theta^* = 0.119$;
- I_θ^* : between 0.065 and 0.1302; optimized case: $I_\theta^* = 0.095$.

For each figure, the x-axis corresponds to the relative variation, in percents, of the structural parameter from the baseline case. For all figures, the baseline case is the set of structural parameters forming the optimized case which has already been presented in Table 4.7. Further, the y-axis corresponds to the relative variation of the reduced frequency (f^*), the amplitude of motion in pitch (θ_0), the amplitude of motion in heave (y_0/c), the efficiency (η) and the coefficient of power ($\overline{C}_P$). Again, their variation is expressed as a relative difference, in percents, from the values pertaining to the optimized case, values which have been presented in Table 4.6 (last line of the table). To complete this brief description on the methodology used to present the results, the legend of each figure incorporates the minimum value and the maximum value taken by each parameter within the range over which the structural parameter has been varied.

As previously mentioned, there is no figure showing the effect of varying I_θ. This is because the variations of the recorded parameters over the range of values taken by I_θ throughout the sensitivity study only showed very minor changes: variations of only 2% or less from the baseline values. The author has also tried varying I_θ over a larger range of values, but numerical instabilities have been encountered. Obviously, reducing I_θ is analog to decreasing the mass of the airfoil, and this leads to an instability associated to the added mass effect.

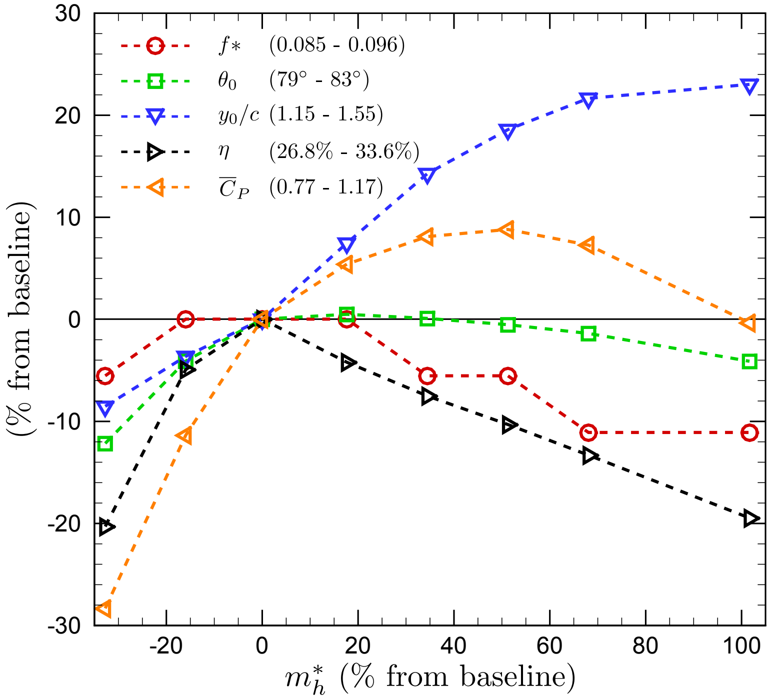

Figure 4.19: Effect of varying m_h^* between values of 2.04 and 6.12 on f^*, θ_0, y_0/c, η and $\overline{C}_P$ (baseline: $m_h^* = 3.036$).

However, no explanation is available at the moment concerning the numerical instability observed while increasing the moment of inertia of the airfoil beyond the range indicated above. This will have to be investigated in the near future. Now that the figures have been introduced, each of the structural parameters can be analyzed.

Heaving mass

Concerning the heaving mass, it has not been possible to reduce m_h^* by more than 40% from its original value. This is because the added mass effect did lead to an expected numerical instability. This is of course a limitation of the current solver, but it only has a minor impact in the current investigation. One noticeable feature of Figure 4.19 is certainly the variation of the reduced frequency. This is because increasing and decreasing the mass both have the same effect on f^*: it is slightly reduced. This is obviously not a surprising finding for the situation where the mass is increased. As a matter of fact, the decoupled natural frequency in heave of the device decreases as the mass in heave is increased. On the other side, the frequency is also decreased as the mass of the device is reduced. This suggests that the aerodynamic plays a significant role concerning the frequency at which the airfoil oscillates. However, the effect of the mass on the reduced frequency is not major, and the observed variations are within ± 10%.

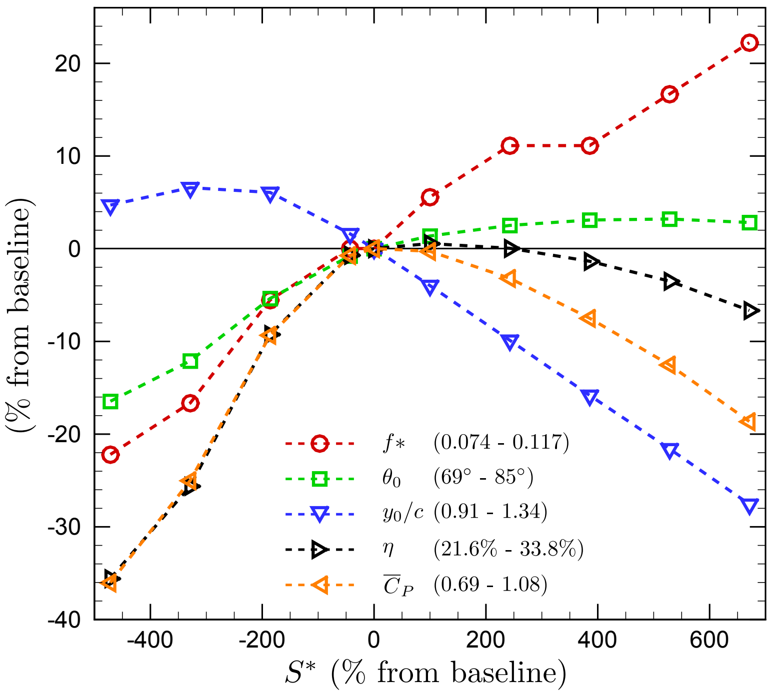

Figure 4.20: Effect of varying S^* between values of -0.165 and 0.165 on f^*, θ_0, y_0/c, η and $\overline{C}_P$ (baseline: S^* = -0.029).

Another finding is that the heaving mass has a significant impact on the heaving amplitude. In fact, increasing/decreasing the mass of the heaving components permits to increase/decrease the amplitude of motion in heave, thus proving to offer a certain degree of control on y_0/c. However, changing the heaving mass leads to a loss in efficiency. Even so, the augmented amplitude of motion can fully compensate for the loss in efficiency when m_h^* is increased, and the device can maintain high values of $\overline{C}_P$. For example, when the mass is increased by 100% from its baseline value, the efficiency is reduced by approximately 20%, but the value of $\overline{C}_P$ is unchanged. This indicates that in order to achieve a certain value of $\overline{C}_P$, one can either choose to conceive an efficient and lighter device having a limited amplitude of motion, or conceive a heavier machine that is less efficient and has a greater amplitude of motion.

Static imbalance

The first feature that is very obvious when considering Figure 4.20 for the variations of the static imbalance is certainly that its largest impact is on the reduced frequency. Indeed, this structural parameter seems to offer a good way of varying the frequency of oscillation of the airfoil. Changing the value of the static imbalance also has some impact on the heaving amplitude of motion, especially if the static imbalance varies towards larger positive values.

Nevertheless, keeping the static imbalance close to zero seems to offer the best performances. In fact, decreasing S^* leads to a relatively rapid decrease of the efficiency, which also quickly drags the value of $\overline{C}_P$ down. Conversely, increasing S^* does not change significantly the efficiency, but the amplitude of motion decreases relatively fast, which again decreases the total power harvested with the turbine.

Recalling the discussion concerning the budget of the terms contained within the equations of motion (Figures 4.9, 4.10, 4.16 and 4.17), it had been found that the coupling terms, which are directly proportional to the static imbalance, remain very small throughout the cycle when they are compared to all other terms involved within the equations. Nevertheless, it appears inadequate to conclude that the effect of such a parameter is unimportant as Figure 4.20 definitely tells the opposite. This is such because the device is passive and all terms, even if it remains relatively small, can lead to differences that are larger than expected. This is a direct consequence of this complex two-way interaction between the flow and the structure, which has the effect of amplifying the impact of a slight variation within the equations of motion.

As a last comment, Figure 4.20 should be interpreted with care: the baseline value of S^* (i.e., the value of the optimized case), is relatively small. Because of that, even small absolute variations of S^* will appear as fairly large relative variations. Although the fully-passive device is sensitive to the static imbalance, this makes it look more sensitive than it is in reality.

Heave stiffness

Figure 4.21 showing the effect of the heave stiffness exhibits some very intriguing features. The first feature, which may appear strange at first, is the fact that reducing the stiffness of the spring in heave by 100% from its baseline value still leads to oscillations of large amplitude, and they are still relatively efficient. It should be stressed that this case corresponds to the situation where there is no spring in heave at all! This situation is intriguing enough to be further investigated, and a complete section of this chapter will be devoted to this matter.

Apart from this interesting finding, the heave stiffness offers a considerable degree of control over the amplitude of motion in heave. However, the efficiency also appears to be significantly dependent upon the heave stiffness. This is because this parameter greatly affects the synchronization between the pitching and the heaving motions, and this has been highlighted as being a key physical mechanism, if not the most important, in order to control the efficiency of the device. Whatsoever, reducing slightly the heave stiffness reduces the efficiency, but the amplitude of motion increases enough to result in an augmentation of the total power harvested from the incoming flow. This makes the fully-passive turbine harvest essentially as much power as the kinematically-constrained turbine.

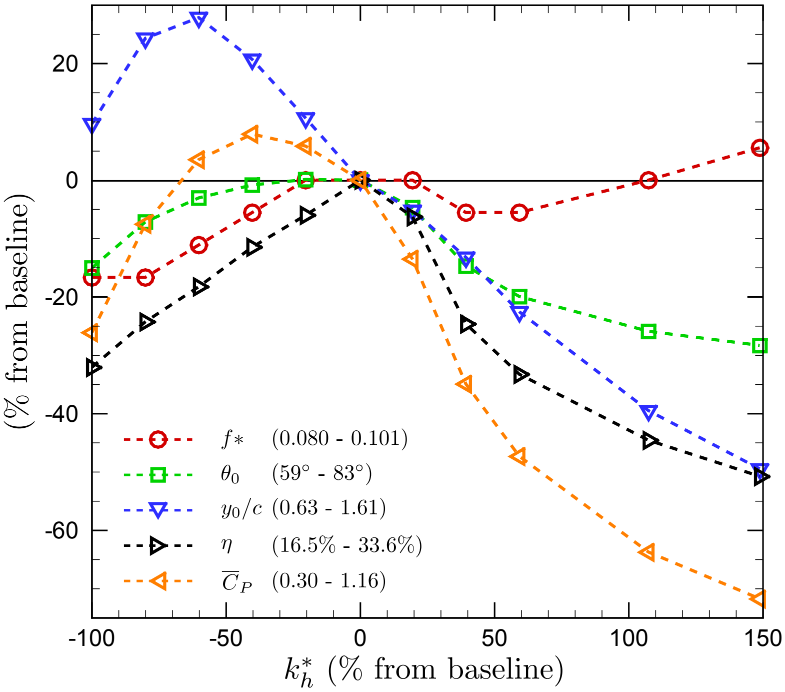

Figure 4.21: Effect of varying k_h^* between values of 0 and 3 on f^*, θ_0, y_0/c, η and $\overline{C}_P$ (baseline: $k_h^* = 1.206$).

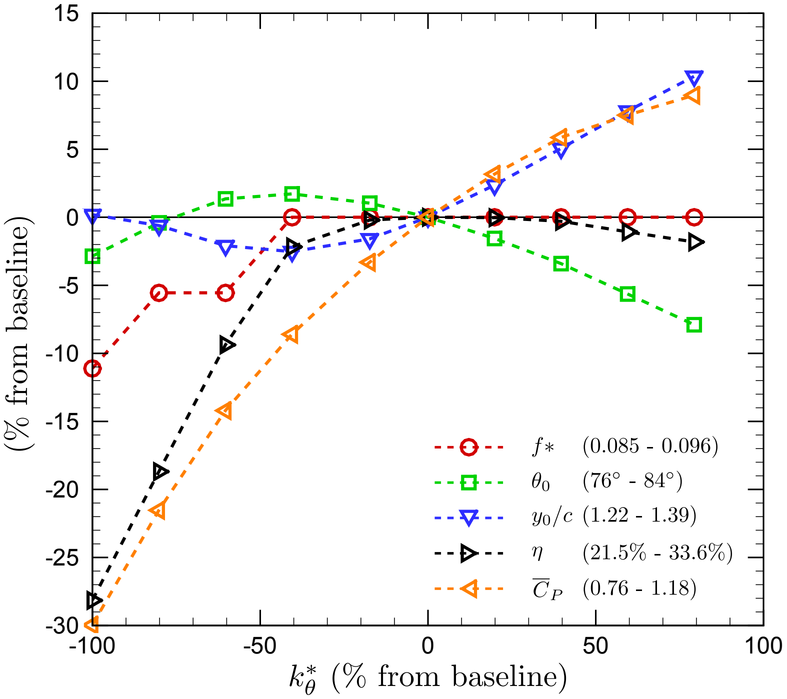

Figure 4.22: Effect of varying k_θ^* between values of 0 and 0.056 on f^*, θ_0, y_0/c, η and $\overline{C}_P$ (baseline: $k_\theta^* = 0.031$).

Pitch stiffness

As shown in Figure 4.22, the stiffness of the spring in pitch does not affect very much the amplitude of motion in pitch. This is in good agreement with the previous discussion on the large importance of the interaction between the airfoil and the vortex shed during the deep dynamic stall event. Indeed, if the pitching motion of the airfoil was governed by the spring in pitch, varying the value of its stiffness would considerably affect the amplitude of motion in pitch. This finding that the spring in pitch is not as significant as the airfoil-vortex interaction has been confirmed with the budget of the terms involved in the equation of motion for the pitch degree-of-freedom (Figures 4.10 and 4.17), where the term resulting from the spring stiffness was found to be approximately one order of magnitude smaller that the aerodynamic moment.

In fact, the fully-passive turbine appears relatively insensitive to variations of ± 50% of k_θ^*. When the stiffness is further reduced, the amplitude of motion quickly drops. This is because although the spring in pitch is not the key element governing the pitching motion, it does play a role on the synchronization between the pitching and the heaving motions, and it is already known that the turbine is quite sensitive with respect to that synchronization. This conclusion becomes clear when the ratio of the decoupled natural frequencies associated to both degrees-of-freedom is calculated:

$$\frac{f_{Nh}}{f_{N\theta}} = \frac{\sqrt{k_h^* \,/\, m_h^*}}{\sqrt{k_\theta^* \,/\, I_\theta^*}} \,. \tag{4.10}$$

The efficiency of the turbine has been found to be maximum when this ratio takes values between 1.0 and 1.1, and this is not only true for the optimized case. Interestingly enough, the efficiency of the turbine seems to be more sensitive to the *relative* choice of k_h^* and k_θ^* than to their individual values. This confirms the importance of having an adequate synchronization between both motions as this is essentially the main feature that is affected when varying the ratio of the decoupled natural frequencies.

Further, simply removing the spring in pitch still gives rise to large amplitude LCO, just as in the case of the heave stiffness. This will later be investigated in more details, but this again indicates that the pitching motion can be fully governed by the interaction between the airfoil and the vortex originating from deep dynamic stall.

Heave damping (generator)

The effect of varying the linear damping coefficient in heave, which accounts for the effect of a generator connected to the turbine, is shown in Figure 4.23. The main impact of this parameter is relatively intuitive: increasing the damping reduces the amplitude of motion,

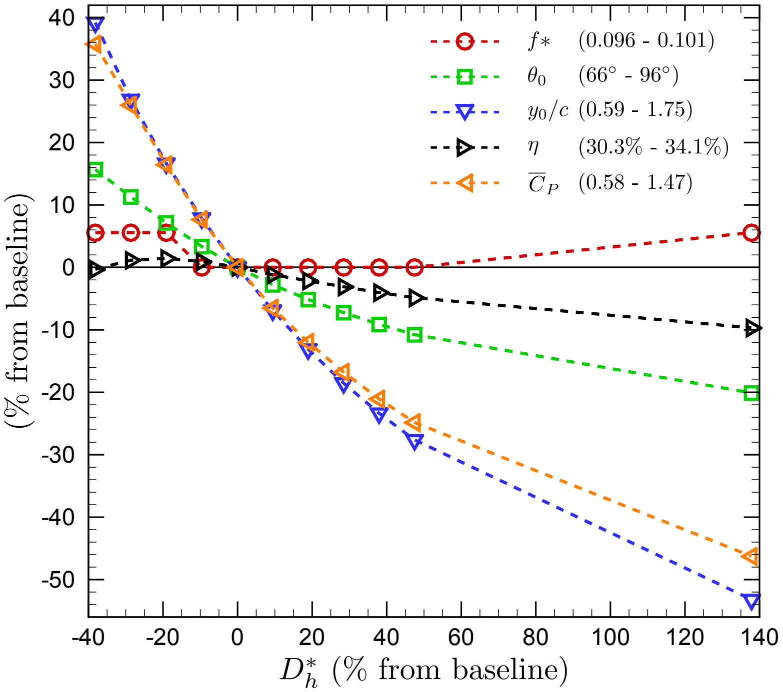

Figure 4.23: Effect of varying D_h^* between values of 0 and 3.57 on f^*, θ_0, y_0/c, η and $\overline{C}_P$ (baseline: $D_h^* = 1.501$).

and vice versa. As a matter of fact, the damping in heave can be used to control the amplitude of motion in heave of the flapping airfoil. Nevertheless, the effect of this parameter on the power harvested from the flow might not reveal to be as intuitive: decreasing the damping coefficient increases the harvested power, just as much as the power available to the generator (this is not shown on the figure, but the power available to the generator is approximately 80% of the harvested power for all cases). This is because the power harvested from the flow is proportional to the square of the heaving velocity. Because decreasing the damping coefficient increases the amplitude of motion as the reduced frequency essentially remains constant, the heaving velocity is increased by such a modification of the damping. This, in turns, accounts for the increase of the total power harvested from the flow.

Reducing the heave damping coefficient further than 40% has also been investigated. However, the motion of the airfoil becomes more chaotic when this is done. The amplitude of motion becomes variable from one cycle to the other, and this is certainly not interesting for a turbine application of the fully-passive, flapping airfoil. Indeed, some damping in heave is required to stabilize the amplitude of motion, but also because it is mandatory to avoid amplitudes so large that the structural integrity of the device could be impaired.

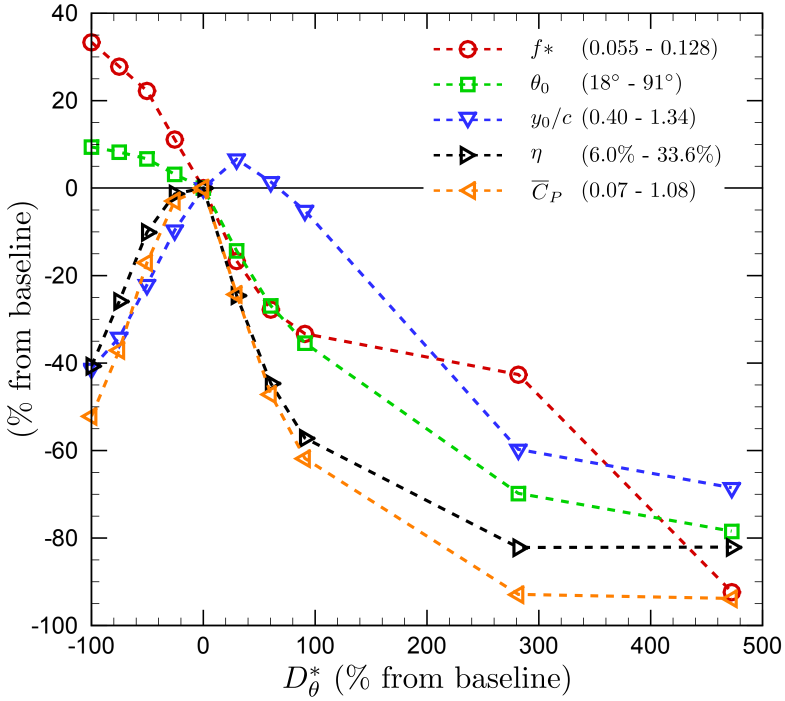

Figure 4.24: Effect of varying D^*_θ between values of 0 and 0.68 on f^*, θ_0, y_0/c, η and $\overline{C}_P$ (baseline: $D^*_\theta = 0.119$).

Concerning the efficiency, it is interesting to note that varying the damping does not affect significantly this performance metric. This is a very interesting finding because the amplitude of motion of the fully-passive, flapping-airfoil turbine could easily be controlled through the damping coefficient of the generator without changing the efficiency of the turbine at harvesting the flow. As a matter of fact, changing the damping of the generator can easily be done (see Chapter 5), thus providing a way of affecting the airfoil's dynamics without changing the device itself, and without changing significantly its efficiency. This means that the heave damping is one of the very few parameters that could be conveniently varied once the fully-passive, flapping airfoil is built and deployed.

Pitch damping

So far, no structural parameter has really provided a good way of affecting the amplitude of motion in pitch. This situation changes with the pitch damping coefficient now offering a certain degree of control over the amplitude of motion in pitch. Its effect is probably as intuitive as it was for the heave damping: increasing the damping reduces the amplitude of motion, and vice versa. However, changing the pitch damping coefficient also affects greatly the amplitude of motion in heave. This is because the heaving motion is greatly dependent upon the amplitude of motion in pitch, which affects the value of the instantaneous lift coefficient. However, the inverse is not true, and this explains why changing the heave damping coefficient did not affect significantly the amplitude of motion in pitch. The reduced frequency is also greatly sensitive to the pitch damping, and it is observed that reducing the value of D_θ^* by 100% (i.e., no damping in pitch) did not lead to non-constant amplitudes of motion. Instead, the simulation without pitch damping showed to be well-behaved, with oscillations of the airfoil that could certainly be used for a turbine application. Nevertheless, this is somewhat conceptual since a device without any damping in pitch is hardly conceivable. The important point here is to realize that the optimal value of the turbine's efficiency, as much as the maximum coefficient of power, is for a case where some damping is present. This is good news as a realistic turbine will include some damping. However, the efficiency and the coefficient of power are greatly dependent upon that specific value of the damping in pitch, thus suggesting that care would be needed, from a mechanical design point of view, in order to respect very carefully the required damping coefficient.

Summary

Following this analysis of the structural parameters, it appears that the parameter having the least impact over the studied range of variations is the moment of inertia of the airfoil. Nevertheless, it should be recalled that some limitations with the FSI solver restricted the range of the possible values taken by this parameters.

For the rest of the structural parameters, none of them proved to be ineffective at changing the airfoil's dynamics or performances. Each parameter offers some degree of control over the performances and/or the dynamics, but each seems to affect more than one of the key parameters recorded during the sensitivity analysis. This testifies of the complex interaction between the structure and the flow. For example, if one wishes to reduce the frequency of the device, one could decide to decrease S^* or increase D_θ^*. This, in turns, will have some impact on the efficiency of the turbine.

The only parameter offering more control than the others is probably the heave damping coefficient, and this is not because the airfoil is more sensitive toward this parameter. This is more because all structural parameters, except for D_h^*, are fixed and chosen when designing the turbine. In the case of D_h^*, this parameter can be varied without changing the turbine itself: it can be adjusted by affecting the *behavior* of the generator connected to the turbine. More details will be provided on this in the next subsection and in the next chapter.

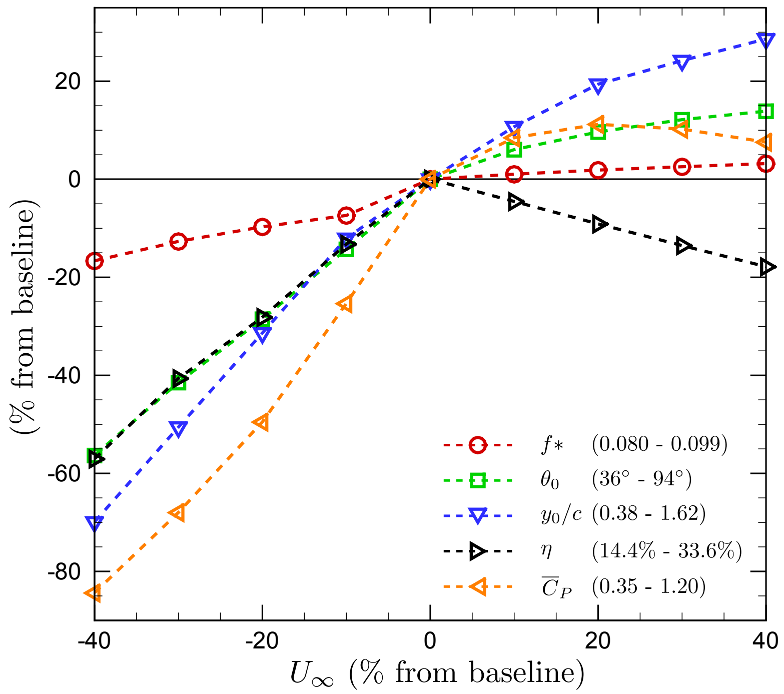

Figure 4.25: Effect of varying U_∞ up to ± 40% from the optimized case on f^*, θ_0, y_0/c, η and $\overline{C}_P$.

4.5.2 Sensitivity to the freestream velocity

A deployed fully-passive, flapping-airfoil turbine would obviously be exposed to a time-varying freestream velocity. The sensitivity of the device towards U_∞ is therefore of great interest. To study this sensitivity, numerical simulations have been performed while varying the freestream velocity of the optimized case up to ± 40%. Because the Reynolds number would vary, in reality, when the velocity of the flow changes, its value has also been varied in the same proportion as U_∞. For example, a reduction of 40% of U_∞ was accompanied by a reduction of 40% of Re.

The effect of such variations is shown in Figure 4.25 where the relative variations of the freestream velocity, in percents, is calculated using the velocity of the baseline case as the reference value. Further, the variations of f^*, θ_0, y_0/c, η and $\overline{C}_P$ are plotted, and the values again correspond to the relative variation from the values of the optimized case previously analyzed. The information is here presented in the same format as it was done in the previous subsection dealing with the sensitivity of the turbine towards the structural parameters.

From Figure 4.25, reducing the velocity of the flow appears to have significantly more impact on the metrics of interest when compared to the situation where the velocity of the flow is increased. The frequency of oscillation appears not to be very sensitive to the velocity of the flow, but all other parameters exhibit a great sensitivity with respect to this parameter. Reducing U_∞ diminishes considerably both amplitudes of motion, the efficiency, and the total power harvested. Of course it had been expected that reducing the velocity would significantly reduce the amplitudes of motion. This is because the aerodynamic forces and moments on the airfoil are proportional to U_∞^2. Therefore, reducing by 40% the velocity of the flow reduces the aerodynamic forces and moments by approximately 65%. Further, a significant reduction of the amplitudes of motion, especially in heave, must necessarily lead to a reduction of $\overline{C}_P$, a fact that is also observed in Figure 4.25. Nevertheless, it had not been possible to anticipate the effect of the velocity on the efficiency, and a significant loss of efficiency is observed as U_∞ decreases. This means that whenever the velocity of the flow is reduced, the device not only extracts power over a reduced flow window, but it extracts less of the total power available within that reduced flow window. As a result, the performances of the turbine are seriously impaired whenever U_∞ diminishes.

Inverse to that, increasing the velocity of the flow has a very different impact on the recorded metrics. Again, the frequency is relatively unchanged, but the relative variation of all other parameters is less significant than it was while reducing the velocity of the flow. This time, the amplitudes of motion are greater, and this makes physical sense as a result of the increased aerodynamic forces and moments on the flapping airfoil. For example, increasing the velocity of 40% almost increases the aerodynamic forces and moments by 100%. The total power harvested from the flow also increases with the flow velocity, which is associated to the enlargement of the harvested flow window. However, the efficiency of the device is reduced by approximately half the relative increase of the flow velocity: increasing U_∞ by 20% engenders a decrease of 10% of the efficiency. This means that the performances of the device are not seriously impaired when U_∞ is increased. This is contrasting with the previous conclusion concerning a reduction of U_∞.

It has already been mentioned that varying the damping coefficient associated to the generator connected to the airfoil would allow to control the amount of power dissipated though the generator. Again, the ways in which this equivalent damping coefficient could be affected by changing the behavior of the generator will be discussed in the next chapter. Nevertheless, it will be seen that D_h could indeed be varied *after* the fully-passive flapping-airfoil turbine is built and deployed. As a direct result, it appears interesting to verify if a modulation of D_h would allow to fully or partially compensate for a reduction or an increase of U_∞. Said otherwise, the idea here is to determine if varying the heave damping coefficient would allow to maintain approximately the same performances as the optimized case, thus making a single fully-passive, flapping-airfoil turbine adapted for a large range of flow velocities.

In the first place, simulations have been performed in order to determine if variations of the heave damping coefficient can compensate for a velocity of the flow that is reduced by 40%. For

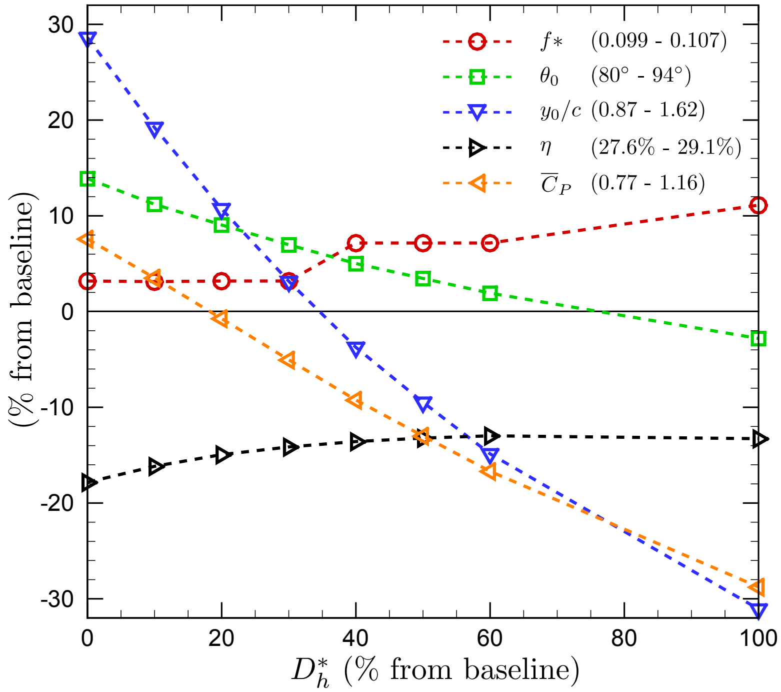

Figure 4.26: Effect of varying D_h^* up to 100% from the optimized case on f^*, θ_0, y_0/c, η and $\overline{C}_P$ for the case where the freestream velocity has been increased of 40%.

this purpose, a few simulations making use of this reduced velocity have been achieved where the heave damping has been reduced up to 60% compared to the optimized case. Reducing the damping coefficient appears to be the most logical choice due to the smaller forces and moments on the airfoil in such circumstances. This means that less power is available for the flapping airfoil, which directly suggests that less power should be dissipated through the generator. That being said, reducing the damping coefficient did not prove to be a successful remedy to the lack of dynamic pressure. In fact, it turns out that it only makes matters worse. The amplitudes of motion remained relatively unchanged with moderate values ($\theta_0 \approx 36°$ and $y_0/c \approx 0.4$), but such modifications of the damping have further reduced the efficiency (η) and the total power harvested from the flow ($\overline{C}_P$).

In the second place, simulations have been performed for the case where the velocity of the flow is increased by 40% relatively to the optimized case. This time, because more power is available to the oscillating airfoil, the heave damping has been increased in order to dissipate more power within the generator. The value of D_h has been increased up to 100% relatively to the baseline value from the optimized case, and the results, which are shown in Figure 4.26, are actually very interesting. Again, the variations of f^*, θ_0, y_0/c, η and $\overline{C}_P$ are plotted, and the values shown, in percents, correspond to the relative variation from the original optimized case (i.e., without any variation of the freestream velocity). With this way of presenting the data, whenever a parameter reaches a value of 0%, this indicates that it is equal to its original value where the velocity of the flow is not increased, nor decreased (i.e., the same value as the optimized case).

The results again suggest that varying D_h does not provide much control over the frequency of oscillation. The situation is somewhat very different concerning the amplitudes of motion. Increasing the heave damping by approximately 60% provides the same amplitude in pitch as the original optimized case, and increasing the heave damping of approximately 30% provides the same amplitude in heave as the original optimized case. This means that it is possible to restrain the growth of both amplitudes of motion through the use of the generator connected to the device. Again, it should be clear that this would not require any modification of the structural components forming the fully-passive turbine.

Concerning the efficiency, increasing the damping in heave does provide a gain. Nevertheless, this gain is not sufficiently high to fully recover from the loss of efficiency attributed to the increase of the flow velocity. At best, the efficiency is approximately 13% below that of the original optimized case ($\eta = 29.1\%$). It should be noted that the resulting efficiency is still high enough to make a fully-passive turbine attractive. Last, the coefficient of power is of course reduced while the heave damping is increased. This is a direct consequence of the reduced flow window when D_h is increased.

In conclusion, exposing the turbine to an increased velocity of the flow appears to be far less detrimental than the inverse. Further, there is a possibility to partially compensate for an increase of U_∞ by making use of the electrical generator connected to the device, which is an interesting finding. These results suggest that if a fully-passive, flapping-airfoil turbine was built by making use of the non-dimensional parameters pertaining to the optimized case, the reference velocity (U_∞) used to scale the structural parameters should correspond to the lower range of velocities encountered at the location where the turbine is to be deployed. To be more precise, if a location where the velocity of the flow is expected to vary between 2 m/s and 3 m/s was chosen to deploy such a turbine, it would be better to scale the components using a reference velocity of 2 m/s[6]. As a result, variations of the velocity of the flow would most often be positive, thus minimizing the impact of such a change on the performances of the turbine.

---

[6] Because we are here working with non-dimensional parameters, there is a need to revert back to the dimensional space whenever a realistic turbine is designed. To achieve this, the definition of the non-dimensional coefficients must be used (see Chapter 2). For this purpose, a velocity of the flow must be chosen, and the dimensional value of some parameter will depend upon that selected value of U_∞. The important point to note here is that all components can be scaled according to any velocity of the flow, and that value of the velocity should be conveniently chosen in order to minimize the occurrence where the velocity of the flow is below its design value.

Table 4.8: Set of non-dimensional parameters forming the case without any spring in heave and in pitch.

Parameter	Value	Parameter	Value
m_h^*	3.036	S^*	-0.029
k_θ^*	0	k_h^*	0
D_θ^*	0.119	D_h^*	1.501
I_θ^*	0.095		

4.6 Case without springs

As previously observed, the fully-passive, flapping airfoil turbine may undergo large-amplitude LCOs when either the spring in heave or the spring in pitch is absent. This finding leads to the idea of simultaneously removing the springs in pitch and in heave. Such a case remains somewhat conceptual as the airfoil does not have a fixed equilibrium position anymore. Nevertheless, this greatly helps at understanding the physics involved, especially concerning the interaction between the airfoil and the vortex associated to the deep dynamic stall events. Indeed, the main idea here is to demonstrate, without doubts, that the vortex is responsible for the cyclic motion of the airfoil.

The non-dimensional structural parameters used for the simulation discussed here are shown in Table 4.8. In fact, this case corresponds to the optimized case previously studied, except that both spring stiffness coefficients have been set to zero. Although there is no restoring force or moment, a well-behaved, cyclic motion is still observed, and the resulting performances of the turbine are very interesting. The frequency of oscillation (f^*) is equal to 0.091, and the amplitudes of motion are 79° in pitch (θ_0) and 1.16 chord length in heave (y_0/c). As there is no spring at all, this frequency of oscillation is purely and undoubtedly the result of aerodynamic forces and moments. Concerning the amplitudes of motion, they are only slightly lower than what has been predicted for the optimized case, and they can obviously still be qualified as being large amplitudes of motion.

The motion history of the turbine is shown in Figure 4.27. Again, the heaving motion is quite sinusoidal, while the pitching motion is characterized by three distinct phases: the fast pitching regime, the slow pitching regime and the transitional pitching regime. In other words, the observed motion is very analog to that of the flapping airfoil making use of the non-dimensional parameters forming the optimized case. The main difference is probably the synchronization between the heaving and the pitching motion, which is somewhat different but expected. As a matter of fact, when the airfoil reaches both of its extrema in heave, θ is

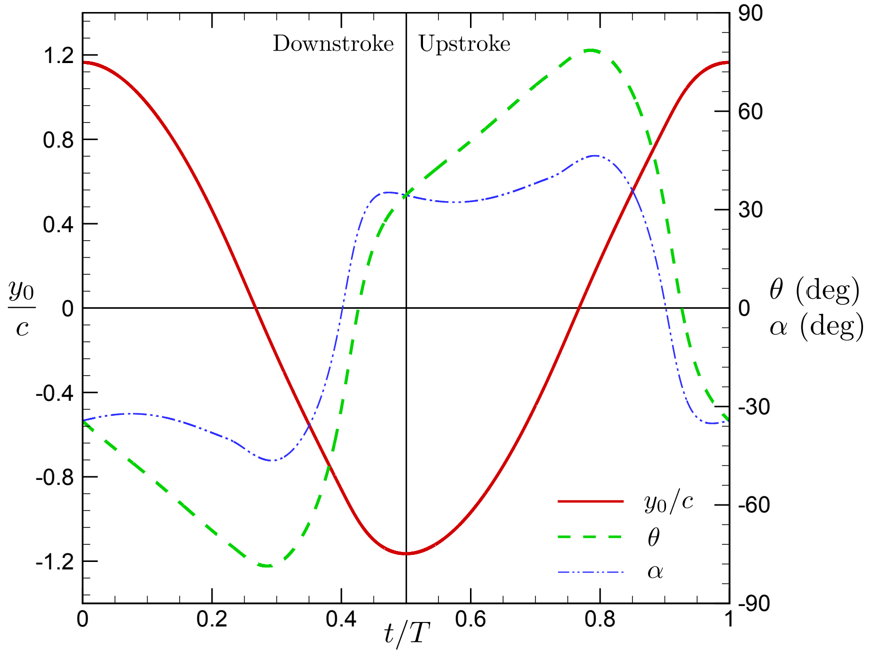

Figure 4.27: Motion history and effective angle of attack of the fully-passive, flapping-airfoil turbine using the structural parameters of the optimized case without any spring in heave and in pitch (Table 4.8).

not equal to 0°. Instead, the airfoil has already past this angle. What this specifically means is that, for example, when the airfoil is switching between its upstroke to its downstroke, when the heaving velocity is null, the angle θ is already negative. Although this may seem surprising at first, this is normal and totally expected. Because no spring is present, the device does not have the capacity of transforming its kinetic energy into potential energy. As a direct result, decelerating the airfoil in order to switch direction in heave essentially has to be done through aerodynamic forces. Indeed, the airfoil must return its kinetic energy to the flow in order to reach a null velocity. To achieve this, the aerodynamic forces must become opposite to the heaving direction *before* the airfoil reaches its extrema in heave. This should not be confused with the initial case where the lift and the heaving velocity were in opposite direction *after* the airfoil had reached its extrema in heave. This finding suggests that one of the main purposes of the spring in heave is to stock the potential energy of the device and reconvert it into kinetic energy at the appropriate moment of the cycle.

This previous observation is confirmed with Figure 4.29 showing various instantaneous coefficients of power. The transition between the upstroke to the downstroke, and vice versa, is accompanied by a fairly large negative peak of C_P. As it can be seen, these large negative peaks are essentially due to the heaving motion. This confirms that decelerating the airfoil in

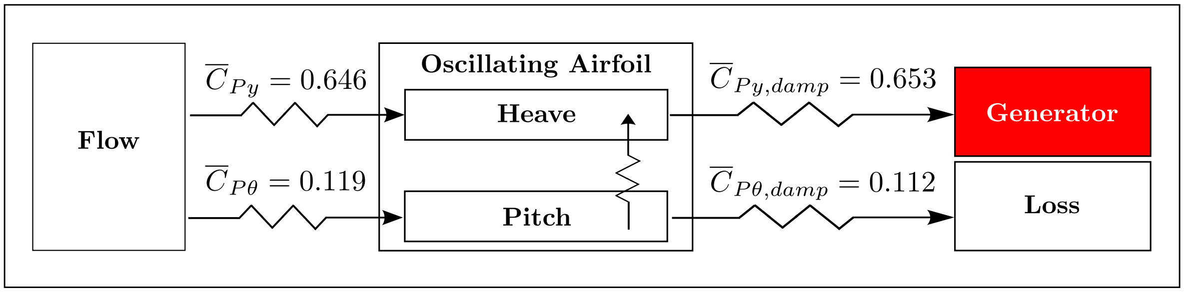

Figure 4.28: Schematic representation of the flow of power through the fully-passive, flapping-airfoil turbine using the structural parameters of the optimized case without any spring in heave and in pitch (Table 4.8).

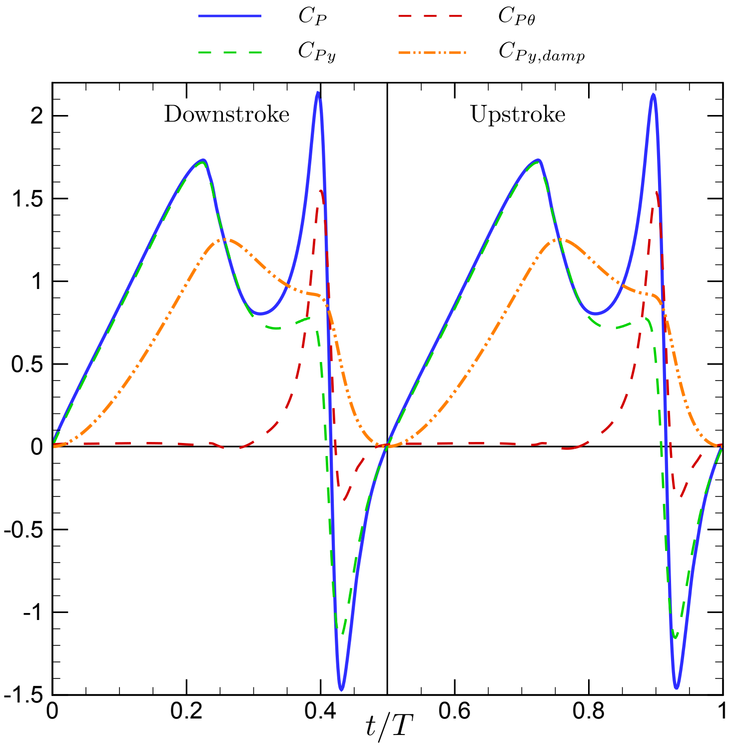

Figure 4.29: Instantaneous coefficients of power for the fully-passive, flapping-airfoil turbine using the structural parameters of the optimized case without any spring in heave and in pitch (Table 4.8).

order to revert its heaving direction is performed by having the airfoil do some work on the flow to reduce its kinetic energy. Although there are large negative peaks of C_P, there are also four positive peaks. Two of them are associated to the pitching motion, and two of them are associated to the heaving motion. Again, the peaks due to the pitching motion are associated with the interaction between the airfoil and the vortex shed during the dynamic stall events. This large vortex is undoubtedly doing the required work on the airfoil to produce the fast pitching regime previously observed. This large airfoil-vortex interaction can be observed on Figures 4.30 and 4.31 where the pressure fields and the z-vorticity fields in the vicinity of the airfoil are shown at several moments throughout a complete cycle of oscillation. The frames $9T/12$, $10T/12$ and $11T/12$ correspond to the dynamic stall event as the airfoil switches from the upstroke to the downstroke, while the frames $3T/12$, $4T/12$ and $5T/12$ correspond to the dynamic stall event when the airfoil switches from its downstroke to its upstroke. This large interaction is again due to the fact that the airfoil travels towards the eddy once it is shed, thus keeping it close to the airfoil's surface.

Although the curve for C_P exhibits large negative peaks, the cycle-averaged value is obviously positive. In fact, a value of $\overline{C}_P = 0.765$ has been calculated, with an efficiency $\eta = 24.3\%$. Figure 4.28 shows the various cycle-averaged coefficients of power. Again, close to 85% of the harvested power has been extracted through the heaving motion, and 85% of the harvested power is available to the electrical generator (i.e., is useful).

Figures 4.32 and 4.33 show the budget of all terms involved within both equations of motion. Necessarily, the terms associated to the heave and the pitch stiffnesses are null at all time. The interaction between the airfoil and the vortex can again be observed through a slight increase of the lift, and also through a large increase of the aerodynamic moment. If Figure 4.27 is compared with Figure 4.32, the reader may note that there are two portions of the cycle where the lift is of opposite sign to the heaving velocity, and this happens before the airfoil reaches its extrema in heave. Figure 4.32 indicates that the inertial term ($m_h^* \ddot{y}^*$) becomes large when there is a change in the sign of the lift force. This is in agreement with the previous assessment that the airfoil is decelerated by returning its kinetic energy to the flow due to the absence of a mean for stoking potential energy within the device itself. As a last comment, the inertial coupling term is found, again, to remain very small compared to the other terms involved within the equations of motion, and this is of course a result of the fairly low static imbalance of this case.

With these results, the reader should now be convinced that the interaction between the vortex and the airfoil is responsible for the limit-cycle oscillations that have been studied in this master's thesis. Alone, the interaction between the airfoil and the vortex can fully account for the pitching motion happening at the extrema of the cycles in heave, thus highlighting that the spring is not playing a key role when one is indeed present.

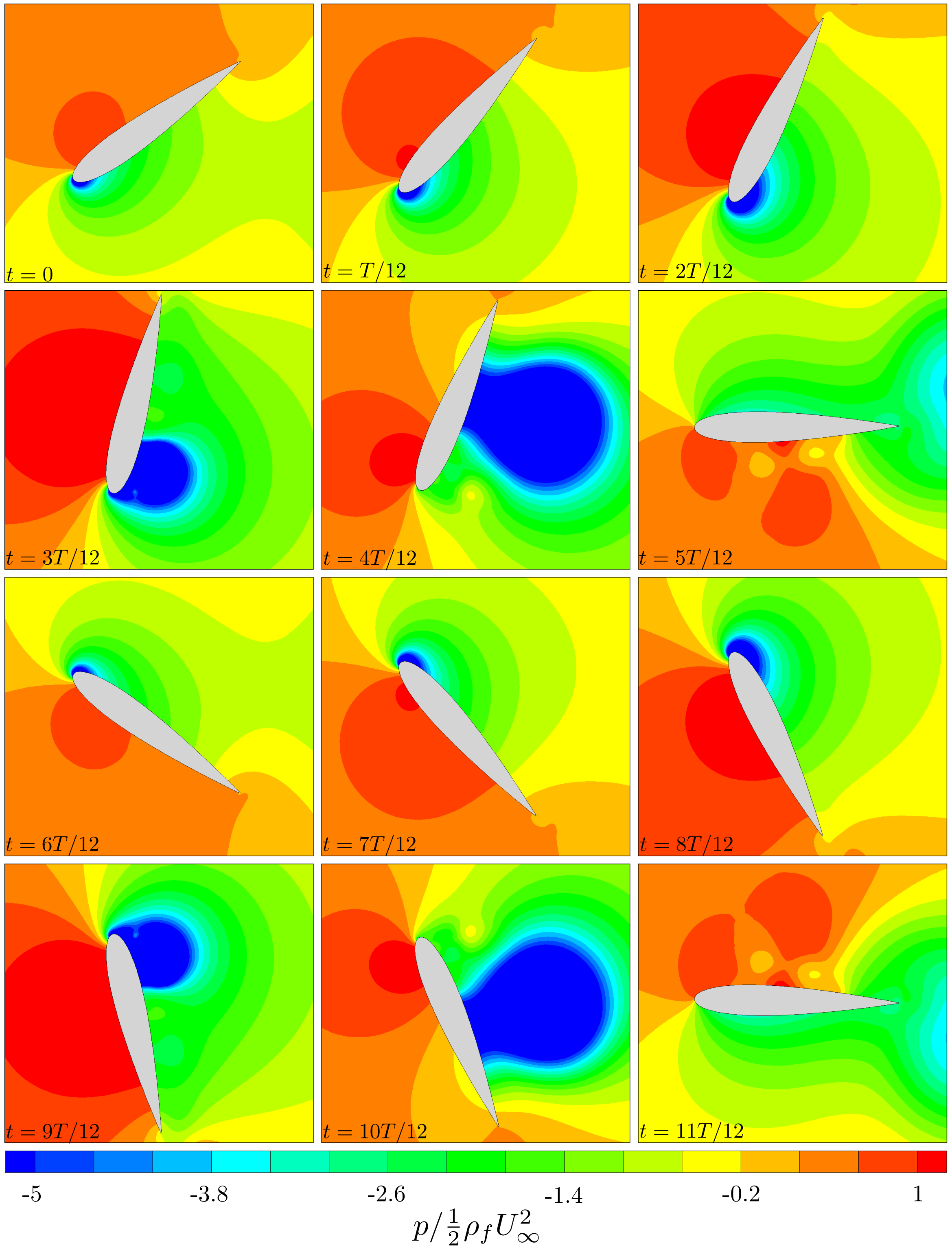

Figure 4.30: Fields of normalized pressure ($p/\frac{1}{2}\rho_f U_\infty^2$) in the vicinity of the flapping airfoil at various instants throughout one complete period of oscillation (T) for the fully-passive, flapping-airfoil turbine using the structural parameters of the optimized case without springs in heave and in pitch (Table 4.8).

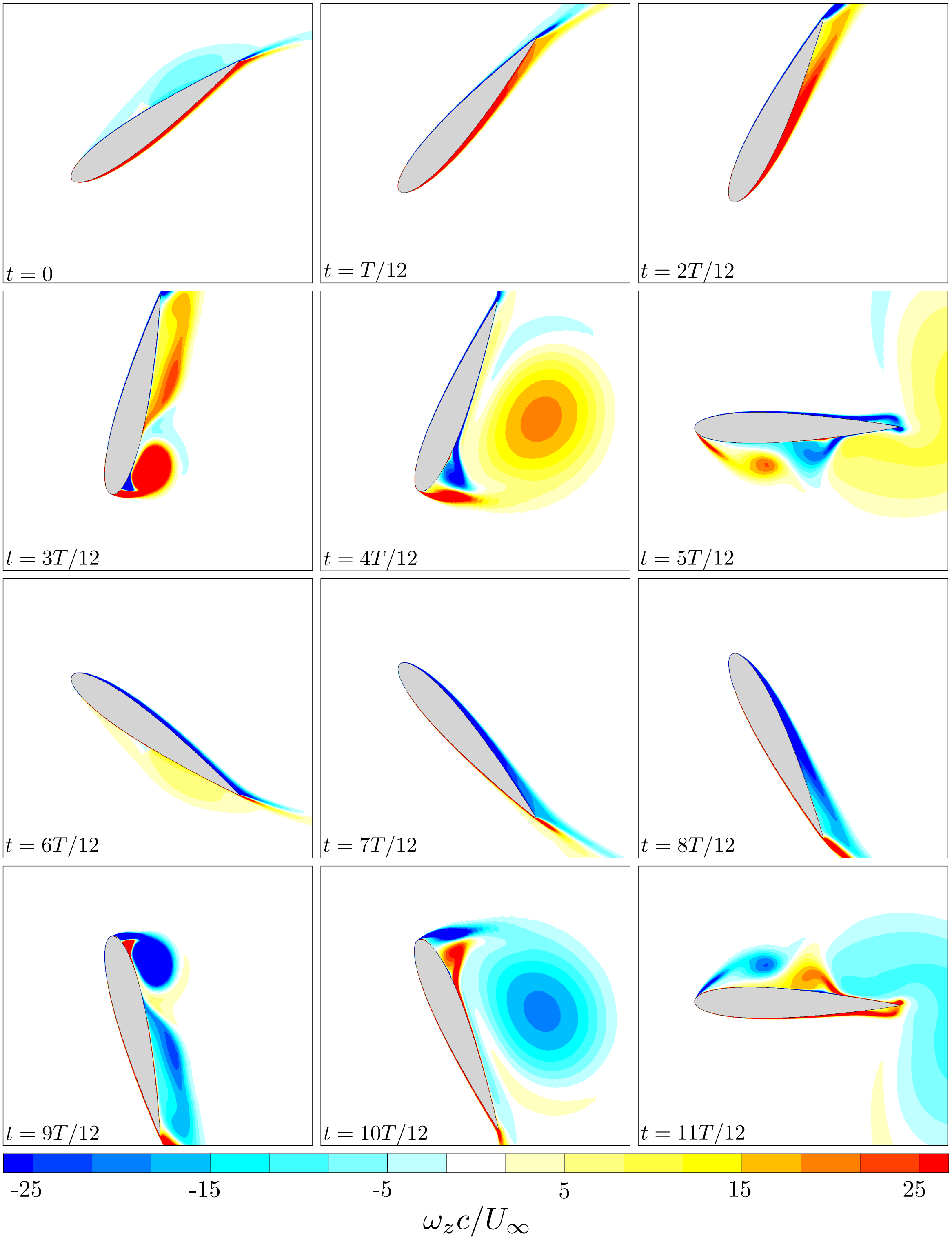

Figure 4.31: Fields of normalized z-vorticity ($\omega_z c/U_\infty$) in the vicinity of the flapping airfoil at various instants throughout one complete period of oscillation (T) for the fully-passive, flapping-airfoil turbine using the structural parameters of the optimized case without springs in heave and in pitch (Table 4.8).

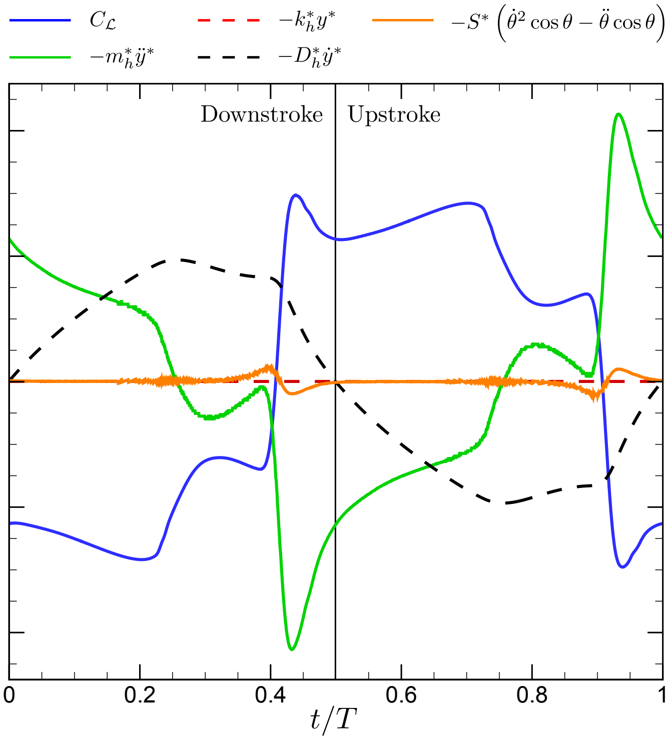

Figure 4.32: Budget of the terms involved within the equation of motion in heave of the fully-passive, flapping-airfoil turbine using the structural parameters of the optimized case without springs in heave and in pitch (Table 4.8).

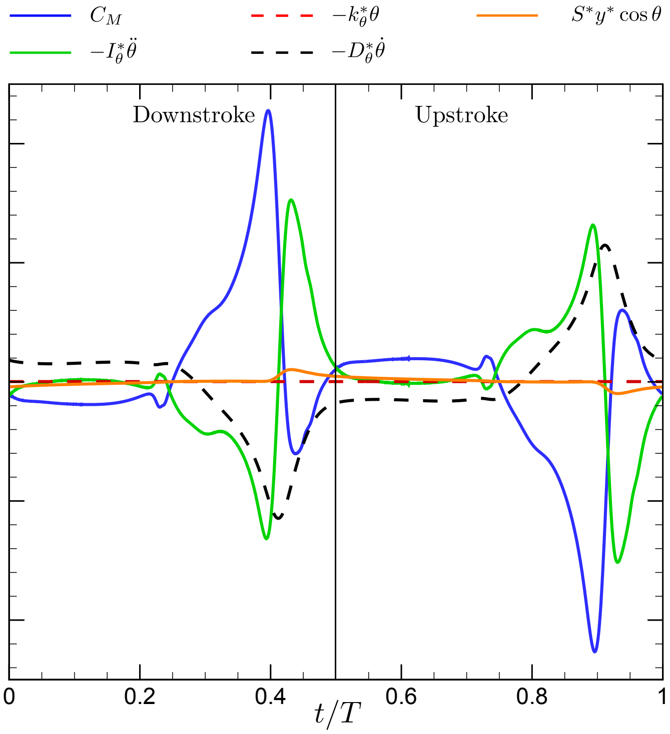

Figure 4.33: Budget of the terms involved within the equation of motion in pitch of the fully-passive, flapping-airfoil turbine using the structural parameters of the optimized case without springs in heave and in pitch (Table 4.8).

The strong interaction between the vortex and the airfoil being highlighted, this suggests that three-dimensional simulations of the fully-passive, flapping-airfoil turbine should be performed. This is to make sure that the effect of the vortex on the airfoil is not overestimated through the current numerical simulations. In fact, in the three-dimensional reality, this vortex would have the possibility to break into smaller structures, and therefore not to remain as coherent as it is forced to be with the current two-dimensional simulations.

Nevertheless, there is a well-known aeroelastic effect that could be of great help on this matter. When a cylinder, circular or not, oscillates in a flow as a result of the fluid-structure interaction, the correlation of the pressure along the span of the structure is significantly increased (see Dowell et al. (2005); Dyrbye and Hansen (1997) and Simiu and Scanlan (1996)). In fact, as the amplitude of motion becomes greater, the correlation length [7] increases significantly. One could believe this is only due to the motion of the cylinder, but this is not the case. Indeed, when the oscillation of the cylinder is forced, there is an increase of the pressure correlation length, but it is far less significant than it is when the motion is emerging from the fluid-structure interaction.

Most of the results available in the literature on this matter are for circular and rectangular cylinders. An example of such results, and also a convincing proof of this effect, can be found in a paper from Ricciardelli (2010). In this paper, it is clearly shown that the correlation length increases very significantly as the amplitude of motion of a rectangular cylinder increases. It is believed that the same aeroelastic effect can be expected for fully-passive, flapping airfoils such as those considered in this thesis. This is because the physics of the flow around an airfoil undergoing motions of large amplitudes is very similar to that of VIV observed on a cylinder where the vortex shedding plays a crucial role.

Conclusion

In this chapter, an original methodology developed by the author in order to find a well-chosen initial guess for conducting an optimization of a fully-passive, flapping-airfoil turbine has first been presented. Using the in-house solver implementing this methodology (RPAS), a set of structural parameters providing large-amplitude LCO of the fully-passive, flapping-airfoil turbine has been obtained. The corresponding efficiency was approximately 12%. Following a gradient-like optimization, the turbine has been effectively optimized, thus providing a new efficiency of approximately 34%. This demonstrates that there is surely some potential at using a fully-passive, flapping airfoil as an efficient wind or hydrokinetic turbine.

Further, the physics of both the initial and the optimized cases has been studied, and it has been found that the airfoil is undergoing stall flutter. Indeed, the structure undergoes deep dynamic stall twice per cycle, and the strong interaction between the airfoil and the vortex

---

[7] The correlation length is a measure of the spanwise distance over which a specific physical parameter can be considered fully correlated.

shed from the leading edge is responsible for the cyclic motion of the airfoil. This idea has been reinforced by studying the physics of a fully-passive, flapping airfoil where no spring is present in both heave and pitch.

The synchronization between the pitching and the heaving motions has also been investigated, and it proved to be a key element in order to obtain an efficient turbine. In fact, this synchronization is crucial for the purpose of efficiently using the low pressure at the core of the shed eddy in order to passively pitch the airfoil. This also enhances the total power harvested from the flow with the turbine.

Furthermore, a sensitivity study of the device towards some structural and flow parameters has been carried out. It has been found that all of these parameters have an effect on the metrics characterizing the turbine, except for the moment of inertia about the pitching axis. The effect of this last parameter remains fairly insignificant. Nevertheless, a key finding is that the heave damping coefficient, which here accounts for the effect of the generator connected to the turbine, enables to partially compensate the effect of increasing the velocity of the flow above the design value. However, reducing the velocity of the flow below the design value is highly detrimental for the turbine's performances, and this suggests that the design of such a passive turbine should be based on the lower range of expected velocities of the flow.

Chapter 5

Feasibility of the concept

The scope of this chapter is to investigate the feasibility of a fully-passive, flapping-airfoil turbine. In the first section, the effect of dry friction on both degrees-of-freedom is investigated. This is because the damping, up to now, has been entirely modeled through a viscous model. With such a modeling, the damping force is proportional to the velocity. However, all real machines have some amount of dry friction where the magnitude of the damping force is relatively constant. In the present case, it is important to investigate the sensitivity of the aeroelastic device towards dry friction to make sure that self-sustained LCOs are still possible when it is included within the aeroelastic model. In the second section of this chapter, the modeling of the electrical generator's effect is discussed and analyzed. As it has been briefly introduced in Chapter 2, the effect of a generator connected to the turbine has been taken into account through a viscous type of damping. This section aims at investigating more deeply this modeling in order to determine if it is fully or only partially representative of the physical reality.

In the third section of this chapter, two actual cases of the optimized fully-passive, flapping-airfoil turbine are considered in real terms (dimensional parameters). One of these physical cases is for a turbine that would be used within a flow of water, while the second is for a turbine that would be used within a flow of air. Obviously, the set of dimensional parameters pertaining to each apparatus is different, and the objective is to determine if an aeroelastic device respecting the set of parameters from the optimized case could indeed be conceived in order to experimentally study the problem of this thesis. Because several structural constraints are present, there is no guarantee that it is possible to satisfy them all simultaneously.

In the last section, which is more of an opening on future work, other interesting sets of non-dimensional parameters that are worth being further investigated are mentioned. Unfortunately, it has not been possible to fully investigate these sets of parameters within this thesis due to time constraints, but these sets of parameters surely constitute an interesting starting point for a person that would be interested into pursuing the research on this aeroelastic problem.

5.1 Dry friction

The model of the fully-passive, flapping-airfoil turbine used up to now has included some damping for both the pitching and the heaving motions. The damping in heave has been used to account for the effect of the generator connected to the device, while the damping in pitch has been used to account for losses. This has been modeled through a viscous type of damping where the force opposed to the movement is linearly dependent upon the velocity of motion. However, real machines obviously include some amount of dry friction where the magnitude of the opposing force is relatively constant (see Meriam and Kraige (2008)), and this section briefly discusses the effect of including such friction within the aeroelastic model. To carry on numerical simulations that include dry friction, it is of course required to modify the equations of motion of the flapping airfoil by adding some extra terms.

Dry friction is here modeled without making any distinction between the kinetic friction and the static friction. This is without consequence because an initial perturbation is provided to the airfoil when a simulation is initiated. Although dry friction can turn out to be relatively complex and dependent upon several parameters, it is here modeled as a force of constant magnitude which is opposed to the airfoil's motion in both pitch and heave. As a result, the modified equations of motion are:

$$C_{\mathcal{L}} \;=\; m_h^*\,\ddot{y}^* \;+\; S^*\left(\dot{\theta}^2\,\sin\theta - \ddot{\theta}\cos\theta\right) \;+\; D_h^*\,\dot{y}^* \;+\; k_h^*\,y^* \;+\; \underbrace{C_h^*\,\mathrm{sgn}(\dot{y})}_{\text{dry friction}}\;, \tag{5.1}$$

$$C_M \;=\; I_\theta^*\,\ddot{\theta} \;-\; S^*\ddot{y}^*\cos\theta \;+\; D_\theta^*\,\dot{\theta} \;+\; k_\theta^*\,\theta \;+\; \underbrace{C_\theta^*\,\mathrm{sgn}(\dot{\theta})}_{\text{dry friction}}\;, \tag{5.2}$$

where sgn() is the sign function defined as:

$$\mathrm{sgn}(\phi) = \begin{cases} 1 & \text{if } \phi \;\geq\; 0 \\ -1 & \text{if } \phi \;<\; 0 \end{cases} \tag{5.3}$$

Further, C_h^* and C_θ^* are respectively the non-dimensional dry friction coefficients in heave and in pitch, and their values are constant throughout the cycle. These coefficients are normalized as:

$$C_h^* \;=\; \frac{C_h}{\frac{1}{2}\rho U_\infty^2 bc}\;, \tag{5.4}$$

$$C_\theta^* \;=\; \frac{C_\theta}{\frac{1}{2}\rho U_\infty^2 bc^2}\;. \tag{5.5}$$

5.1.1 Effect of dry friction on the fully-passive turbine

In order to assess the effect of dry friction, a few simulations have been performed with various values for the dry friction in both pitch and heave. The baseline case about which this study has been performed is again the optimized case of Chapter 4 (Table 4.7), and the values of the dry friction have been chosen according to the maximum cyclic value of the terms $D_h^*\dot{y}^*$ and $D_\theta^*\dot{\theta}^*$. This information is readily available from Figures 4.16 and 4.17, and the maximum cyclic values are respectively 2.40 and 0.45 in heave and in pitch. What this means is that the constant dry friction is represented as a fraction of this maximum viscous type of damping:

$$C_h^* \;=\; \psi_h \,(D_h^*\dot{y}^*)_{\max} \;, \tag{5.6}$$

$$C_\theta^* \;=\; \psi_\theta \left(D_\theta^*\dot{\theta}^*\right)_{\max} \;, \tag{5.7}$$

where ψ_h and ψ_θ can take any positive value, including 0. For the purpose of performing numerical simulations, it would be very useful to determine an upper bound for these dry friction coefficients. Getting such an upper bound remains approximate as a complete design of the machine would be needed to obtain a more precise value. Assuming some of the worst conditions, such as a dry steel-steel contact, a kinematic coefficient of friction of 0.4 can be assumed for the heaving motion (see Meriam and Kraige (2008)). Knowing that the drag coefficient of the oscillating airfoil, which is a measure of the normal forces along the contacting surfaces, is in the vicinity of 2.5 in average throughout the cycle, a value of $C_h^* \approx 1$ (i.e., $\psi_h \approx 0.4$) is obtained. This is really an upper bound, and the real machine would probably have much less dry friction in heave. In fact, it is hardly conceivable to do worse than that, and great care would be taken in order to reduce such dry friction. Finding an upper bound for the pitch degree-of-freedom is not as easy due to the difficulty of obtaining the order of magnitude of the normal forces at the contacting surfaces. For this reason, it is simply assumed that the maximum value of ψ_θ is the same as the maximum value of ψ_h, specifically 0.4.

The effect of varying ψ_h is shown in Figure 5.1, and the results are presented using the same type of figures as in Chapter 4. This means that the effect on each parameter is shown as a relative variation, in percents, from the baseline values of the original optimized case. As it can be observed, the reduced frequency (f^*) and the efficiency (η) are not very sensitive to the amount of dry friction in heave for the values investigated. However, the amplitude of motion in both pitch and heave decreases significantly as ψ_h is increased. As a result, the total amount of power harvested from the flow ($\overline{C}_P$) is very significantly reduced as ψ_h increases due to the smaller flow window that is harvested. There is another effect of dry friction that should be considered. Dry friction is, in fact, an extra energy sink for the aeroelastic device.

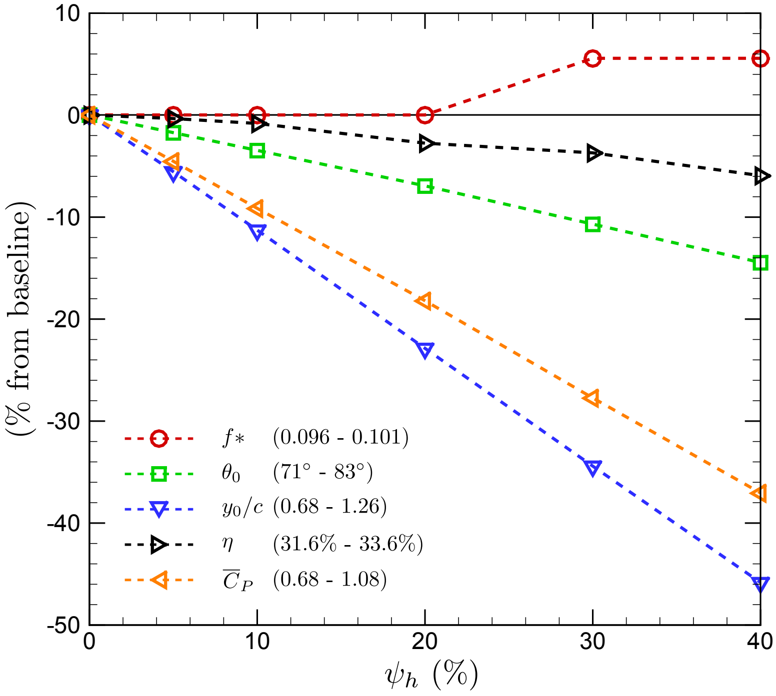

Figure 5.1: Effect of varying the amount of dry friction in heave (ψ_h) between values of 0 and 0.4 on f^*, θ_0, y_0/c, η and $\overline{C}_P$.

Table 5.1: Effect of varying the amount of dry friction in heave (ψ_h) on the coefficient of harvested power ($\overline{C}_P$), on the coefficient of power available to the generator ($\overline{C}_{Py,damp}$), and on the ratio of useful power over the total power harvested ($\overline{C}_{Py,damp}/\overline{C}_P$).

ψ_h (%)	$\overline{C}_P$	$\overline{C}_{Py,damp}$	$\overline{C}_{Py,damp}/\overline{C}_P$ (%)
0	1.08	0.94	87
5	1.03	0.84	82
10	0.98	0.74	76
20	0.88	0.57	65
30	0.78	0.42	54
40	0.68	0.30	44

Said otherwise, it adds a mechanism for dissipating the power harvested from the flow, and this means that less power is dissipated through the heave damper representing the electrical generator. The values of $\overline{C}_P$, $\overline{C}_{Py,damp}$, and $\overline{C}_{Py,damp}/\overline{C}_P$ are shown in Table 5.1. With these results, it is clear that the fraction of harvested power available to the generator is significantly reduced as dry friction increases.

To summarize, dry friction in heave has two main effects. First, the flow window is reduced, thus leaving less available power to the turbine. Second, a smaller fraction of the total power harvested by the turbine is useful, i.e., available to the generator. Nevertheless, a small amount of dry friction, such as $\psi_h = 5\%$ or $\psi = 10\%$, remains fully viable. Indeed, with $\psi = 10\%$, the generator gets approximately 79% of the power it would get without any dry friction. Of course, dry friction should be minimized as much as possible in order not to impair the performances of the fully-passive turbine.

Concerning the effect of dry friction in pitch, the results are shown in Figure 5.2. The first observation is certainly that no LCO are obtained for $\psi_\theta = 40\%$. On Figure 5.2, this is seen with all recorded quantities falling by 100% compared to the baseline case. Further, it is not shown on the figure, but it is an interesting fact that the LCO are now dependent upon the initial perturbation. If the perturbation is such that no deep dynamic stall is encountered, the oscillations are quickly damped and no LCO are obtained. Conversely, if the initial perturbation is large enough as to induce deep dynamic stall, large-amplitude LCO are present. The cases shown in Figure 5.2 are, of course, those for which the initial perturbation was large enough to give rise to LCO. The only exception to that is for ψ_θ where no LCO is observed even when the initial perturbation is large enough to give rise to a deep dynamic stall event.

From Figure 5.2, it is observed that a small amount of dry friction in pitch increases the amplitude of motion in heave. This is believed to be due to the delay of the deep dynamic stall. Because the amplitude of motion in pitch is now slightly lower, the dynamic stall of the airfoil happens when the airfoil is farther away from its equilibrium position in heave. Because the maximum geometric angle θ is smaller, the airfoil must be further decelerated to increase the effective angle of attack enough for stalling to happen. This deceleration is essentially achieved through the spring in heave, and this explains why the airfoil must travel a greater distance in heave. On the contrary, any further increase of ψ_θ beyond 10 % makes the amplitude of motion in heave quickly drop. This time, because of the reduced amplitude of motion in pitch, the lift coefficient does not reach values that are as high, and this reduces the distance over which the oscillating airfoil translates. All the other quantities recorded, namely f^*, θ_0, η and $\overline{C}_P$ seem to be similarly sensitive towards ψ_θ, and they quickly drop as the amount of dry friction increases.

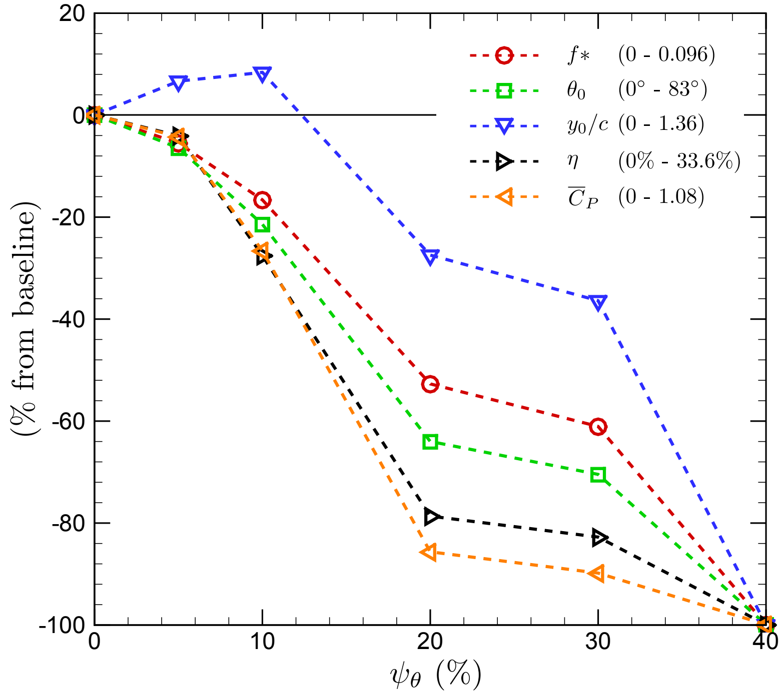

Figure 5.2: Effect of varying the amount of dry friction in pitch (ψ_θ) between values of 0 and 0.4 on f^*, θ_0, y_0/c, η and $\overline{C}_P$.

Table 5.2: Effect of varying the amount of dry friction in pitch (ψ_θ) on the coefficient of harvested power ($\overline{C}_P$), on the coefficient of power available to the generator ($\overline{C}_{Py,damp}$), and on the ratio of useful power over the total power harvested ($\overline{C}_{Py,damp}/\overline{C}_P$).

ψ_θ (%)	$\overline{C}_P$	$\overline{C}_{Py,damp}$	$\overline{C}_{Py,damp}/\overline{C}_P$ (%)
0	1.08	0.94	87
5	1.03	0.91	88
10	0.79	0.70	89
20	0.15	0.13	87
30	0.11	0.09	82
40	0	0	—

Table 5.3: Effect of including dry friction in both pitch (ψ_θ) and heave (ψ_h) on the fully-passive, flapping-airfoil turbine's motion and performances.

ψ_θ (%)	ψ_h(%)	f^*	θ_0	y_0/c	η	$\overline{C}_P$	$\overline{C}_{Py,damp}$	$\overline{C}_{Py,damp}/\overline{C}_P$ (%)
0	0	0.096	82.8°	1.26	33.6	1.08	0.94	87
5	10	0.091	75.0°	1.20	32.2	0.95	0.73	77
10	10	0.080	64.4°	1.23	25.9	0.77	0.59	77

The values of $\overline{C}_P$, $\overline{C}_{Py,damp}$, and $\overline{C}_{Py,damp}/\overline{C}_P$ are shown in Table 5.2. The ratio of useful power over the total harvested power is relatively insensitive to the amount of dry friction in pitch. This means that although an extra sink of energy is included within the model, it essentially only affects the dissipation of energy from the pitch degree-of-freedom, thus leaving the same fraction of useful power to the generator. This is certainly in contrast with the results for the dry friction in heave, where this ratio proved to be very dependent upon ψ_h. Nevertheless, these results suggest that a small amount of dry friction, such as $\psi_\theta = 5\%$ or $\psi_\theta = 10\%$, remains fully viable. Indeed, with $\psi_\theta = 10\%$, the generator gets approximately 74% of the power it would get without any dry friction. Again, dry friction should be minimized as much as possible during the design process to avoid a serious impairment of the turbine's performances.

As a last investigation concerning the effect of dry friction, two simulations have been performed with some dry friction in both degrees-of-freedom simultaneously. Obviously, a real apparatus would include a reasonable amount of dry friction in both degrees-of-freedom, and it should be verified that LCO are still observed when this is the case. Also, it should be verified that the performances of the turbine remain acceptable. The results of these calculations are shown in Table 5.3 along with the baseline case (i.e., the case where no dry friction is included), and they suggest that a small amount of dry friction in both degrees-of-freedom is tolerable as the performances are not unacceptably affected. This is especially true for the case where $\psi_\theta = 5\%$ and $\psi_h = 10\%$. The efficiency of this case, $\eta = 32.2\%$, is almost unchanged compared to the efficiency of the baseline case, $\eta = 33.6\%$. Further, the generator gets approximately 78% of the power it would get without any dry friction, which is not bad at all. Again, the conclusion is certainly that small amounts of dry friction are tolerable, but this surely does not enhance the performances. Nevertheless, large-amplitude LCO are still observed when a reasonable amount of dry friction is included within the model. [1]

---

[1] The reader may take some time to locate the various cases from this section on the mapping of efficiency for the kinematically-constrained turbine shown in Figure 1.2. It is easily found that the values of η are in very good agreement with this mapping of efficiency. Again, this suggests that this mapping, although it has been obtained for a kinematically-constrained turbine, does apply reasonably well for a fully-passive turbine once its kinematics is known.

5.2 Modeling of the generator

This section aims at briefly investigating the current modeling of the electrical generator connected to the device. This modeling of the generator's effect has been done, up to this point, by considering a viscous type of damping. Nowadays, generators have been designed for various applications, and several methods have been developed for controlling the specific way in which generators behave. This section is surely not an extensive review of the theory concerning electrical generators as this falls outside the author's domain of expertise. The reader may find more details within references dedicated to this matter, such as Abad et al. (2011); Tan (2011); Wildi and Sybille (2000) and Wu et al. (2011).

Using basic notions from the field of electrical engineering, a simple analysis of the generator's behavior can be done. This will also prove to be useful for validating the generator's model used in this study. To begin with, the voltage (E_0) induced by a generator through Faraday induction, according to Wildi and Sybille (2000), is given by:

$$E_0 = \frac{Zn\phi_p}{60} \,, \tag{5.8}$$

where Z is the number of conductors in the armature, n is the armature revolution in RPM (rotations per minute) and ϕ_p is the flux per pole of the generator. Further, the required torque to activate the generator (T_g) is given by:

$$T_g = \frac{Z\phi_p I}{2\pi} \,, \tag{5.9}$$

where I is the current produced by the generator. A generator under an electrical load can be represented with the simple equivalent circuit shown in Figure 5.3, where R_0 is the internal resistance of the generator, and R_L is the resistance of the load. With this equivalent circuit, the value of the current can easily be found:

$$I = \frac{E_0}{R_0 + R_L} \,. \tag{5.10}$$

Combining Eqs. 5.8 to 5.10, an expression for the torque is then obtained:

$$T_g = \frac{Z^2\phi_p^2 n}{120\pi\,(R_0 + R_L)} \,. \tag{5.11}$$

Returning to the aeroelastic model of this study, the generator's damping force on the heave motion simply corresponds to the torque required to drive the generator divided by some lever-arm, the value of which depends upon the specific configuration of the apparatus. Further,

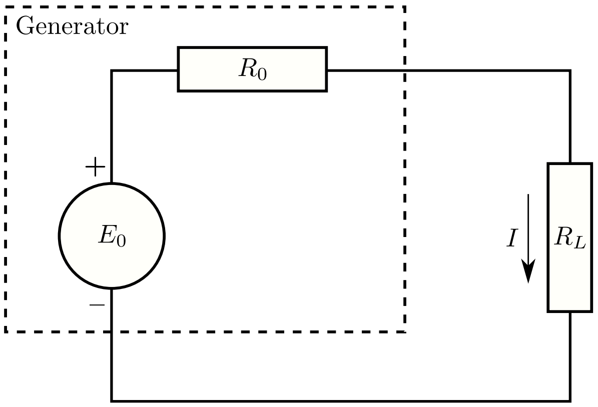

Figure 5.3: Equivalent circuit for an electrical generator under an electrical load.

the angular velocity of the generator's armature (n) is proportional to the heaving velocity ($\dot{y}$). With this, the following can be written:

$$F_{damp} = \frac{KZ^2\phi_p^2\dot{y}}{120\pi\left(R_0 + R_L\right)} , \tag{5.12}$$

where F_{damp} is the damping force and K is a proportionality constant. The interesting point here is to realize that the previous equation can be written in the following form:

$$F_{damp} = D_h\dot{y} , \tag{5.13}$$

where

$$D_h = \frac{KZ^2\phi_p^2}{120\pi\left(R_0 + R_L\right)} . \tag{5.14}$$

This shows that for a constant electrical load and a constant flux within the generator[2], a viscous type of damping indeed models adequately the effect of a generator connected to the fully-passive, flapping-airfoil turbine. This confirms that the simple model used in this thesis is realistic and definitely not far fetched. Further, this demonstrates that the specific value of the damping coefficient can be changed by varying the electrical load, as much as through modulations of the flux ϕ_p.

In fact, several electronic controllers connected to generators achieve a dynamic control of the torque through modulations of the flux[3]. Using such a controller, the equivalent damping coefficient of the generator could not only be modulated depending on the conditions of

---

[2] Such as a generator with permanent magnets.

[3] Such as direct torque control (DTC).

the flow, but it could even be modulated throughout the cycle of oscillation of the flapping airfoil. This would offer the possibility of enforcing other damping laws, thus opening up some new possibilities. Indeed, this could be used for controlling the dynamics of the airfoil. This is because using other damping laws, such as a damping force that is proportional to the square of the heaving velocity for example, could alter significantly the dynamics of the oscillating airfoil, and, as a result, alter its performances at harvesting a flow. This suggests that the electronics connected to the generator probably offers a certain degree of control on the "passive" turbine, and it is surely worth being further investigated in the near future.

5.3 Dimensional cases

Up to now, the aeroelastic problem has been solely considered in its non-dimensional form, and this revealed to be very convenient for the purpose of performing a vast numerical campaign. However, it is also interesting and very important to come back into the dimensional world in order to assess the feasibility of such a device. This is because non-dimensional values do not always speak for themselves, and it is not always easy to determine if a given parameter is physically realistic or not. Therefore, the purpose of this subsection is to propose the dimensional values of the structural parameters that should be used in order to conduct an experimental study of the turbine. With this in mind, two fluids of very different densities are here considered: water and air. In both cases, the non-dimensional parameters used are those of the optimized case which has been extensively described and discussed in Chapter 4.

5.3.1 Dimensional case in air

For the sake of finding a set of dimensional parameters that would be appropriate for an experiment involving a freestream flow of air, the specifications pertaining to an air tunnel located at Laval University could be used. However, the circular shape of the test section does not appear to be adequate for conducting an experiment with a fully-passive, flapping airfoil for several reasons. One of these is certainly that the aspect ratio of the airfoil would need to remain relatively small. This is so because if the airfoil had a too large span, the wing tips could get into contact with the circular walls of the tunnel. An alternative would be to make use of an airfoil having a much smaller chord length, but the Reynolds number would drop significantly. For these reasons, the wind tunnel from the RMC is used here as a reference. Indeed, the rectangular shape of the test section (0.76 m × 1.08 m) appears to be more appropriate for such an experiment, and the span of the airfoil can almost be as large as the vertical extent of the test section. Further, such a study with flapping airfoils has already been conducted within this wind tunnel, and this tunnel can attain flow speeds in the range of 60 m/s.

Table 5.4: Set of dimensional structural parameters for a wind tunnel experiment involving the optimized case of the fully-passive, flapping-airfoil turbine. The following dimensional parameters are proposed: $c = 0.2\ m$, $b = 0.7\ m$, $\rho_f = 1.23\ m/s$, $U_\infty = 60\ m/s$.

Parameter	Value	Parameter	Value
m_h	0.105 kg	S	-0.0002 kg·m
k_θ	3.844 N·m/rad	k_h	3738 N/m
D_θ	0.049 N·m·s/rad	D_h	15.508 N·s/rad
I_θ	0.00013 kg·m^2		

Due to the dimensions of the test section, the chosen span of the wing (b) is set at 0.7 m. Further, because the amplitude of motion of the airfoil can easily reach 1.5 chord length, and because we certainly do not want the airfoil to oscillate too close from the wind tunnel's walls, the chord length (c) is chosen to be 0.2 m. This results in an aspect ratio of 3.5, and a maximum blockage ratio of approximately 17%.

The current numerical study has been performed assuming a Reynolds number of 500,000. However, it would not be possible to attain such a high Reynolds number with the equipment from the RMC. Assuming the maximum flow velocity of 60 m/s, the Reynolds number is approximately 76,000, which is in the transitional range of Reynolds numbers. It then clearly appears that conducting an experiment at Re = 500,000 would require a very large wind tunnel, or a wind tunnel that can provide much higher velocities. Nevertheless, such an experiment in the transitional range of Reynolds numbers would remain very interesting, and it could provide some very relevant informations pertaining to the fully-passive, flapping airfoil. A few numerical simulations have been realized in this range of Reynolds numbers (50,000 to 100,000), and large-amplitude LCO have been predicted with the FSI solver. Further, the predicted efficiencies of the optimized case remained between 25% and 30%, which is not so far from the case at a higher Re = 500,000 (η = 34%).[4]

Using the previously chosen dimensional parameters (i.e., $b = 0.7$ m, $c = 0.2$ m, $U_\infty = 60$ m/s and $\rho_f = 1.23$ kg/m^3) and the dimensionless structural parameters of the optimal case (Table 4.7), the resulting unique set of dimensional parameters shown in Table 5.4 is obtained. Calculating these values is very straightforward using the definitions of the non-dimensional parameters provided in Chapter 2. With this in hand, the mechanical feasibility of a fully-passive, flapping airfoil making use of these parameters can be investigated. It should be understood that the purpose is certainly not to make a complete design of an experimental

---

[4] It should be noted that there is some uncertainty on these values as a transitional turbulence model has not been used for these simulations. Instead, the Spalart-Allmaras turbulence model was used. See Chapter 3 for a brief discussion on this matter.

setup, but instead to verify its feasibility. Further, it should be noted that the flapping airfoil is assumed to be set vertically in the wind tunnel.

Beginning with the stiffness in heave, the best solution would probably be to make use of extension springs. Two sets of these springs would be required: one for $y > 0\ m$ and one for $y < 0\ m$. Because a specific stiffness is required, each set of springs could contain more than one spring in series in order to be as close as possible to the required spring constant. In fact, from an investigation of the products already available on the market, having the adequate stiffness is certainly not the challenge here. Because the maximum deflection of the springs would be in the range of 25 cm, the behavior of the springs has to remain fairly linear up to this extension length, and this appears to be more of a constraint than the stiffness itself. Nevertheless, assembling a set of springs respecting these constraints appears to be possible (see Century Springs (2014)). Several standard extension springs exhibit a linear behavior up to an extension length of approximately 30 cm. Obviously, several combinations of springs are possible, and choosing one over the other could be dictated by other design factors that cannot be considered here.

Concerning the torsional spring, the maximum angular deflection is expected to be in the range of 90°, so that the behavior of the restoring moment should remain fairly linear up to such a deflection. Again, it appears better to use a combination of more than one spring to obtain a stiffness as close as possible to the desired value. Further, several standard torsional springs available on the market meet these requirements (see Century Springs (2014)). This structural component is surely not a constraint from a design point of view.

Concerning the damping coefficients, a complete design of the aeroelastic device would be required to be very specific. This is because there will obviously be some structural damping inherent to the setup, and the damper/generator connected to each degree-of-freedom should be well chosen in order to bring the *total* damping as close as possible to the desired dimensional value of Table 5.4. Nevertheless, the damping ratios are 0.39 in heave (ξ_h) and 1.10 in pitch (ξ_θ). These damping ratios are relatively high when compared to those of the RMC experiment, which are 0.022 in heave (ξ_h) and 0.05 in pitch (ξ_θ). This is great news as this indicates that structural damping inherent to the device would very certainly be low enough to require the use of a damper/generator to increase the total damping. The opposite situation, where very small damping ratios would have been required, could have been a severe constraint on the design of the aeroelastic device, and it could have been harder or impossible to meet such requirements. Indeed, if the structural damping is greater than the total required damping, it would not be possible to add a damper/generator to the device.

Moving to the mass of the airfoil, to its moment of inertia and to its static imbalance, an important point is to verify if it is possible to satisfy the three constraints on m_h, S and I_θ *simultaneously.* To achieve this verification, the airfoil's thickness is here neglected for

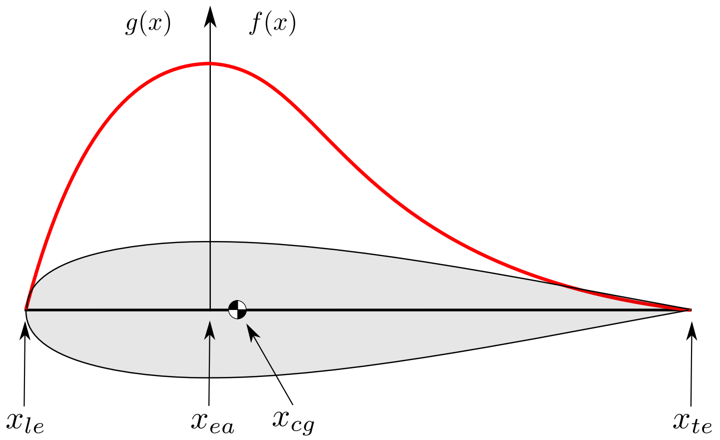

Figure 5.4: Approximate representation of the linear density functions $f(x)$ and $g(x)$ over the airfoil from the leading edge (x_{le}) to the trailing edge (x_{te})

the calculation of I_θ (i.e., the airfoil's mass is assumed to be concentrated on the chord length), which is not too much of a coarse approximation due to the streamlined shape of the airfoil. Further, a linear density function $g(x)$ is assumed ahead of the elastic axis, while a linear density function $f(x)$ is assumed for the part behind the axis. An educated guess of these function's trend over the complete airfoil is presented in Figure 5.4, but the exact shape of these functions representing the distribution of mass along the chord length are here the unknowns of the problem. To find these unknowns, various physical constraints can be mathematically formulated:

$$f(x) \;\geq\; 0 \,\forall\, x \;\in\; [x_{ea},\, x_{te}] \;, \tag{5.15}$$

$$g(x) \;\geq\; 0 \,\forall\, x \;\in\; [x_{le},\, x_{ea}] \;, \tag{5.16}$$

$$g\left(x_{le}\right) \;=\; f\left(x_{te}\right) \;=\; 0 \;, \tag{5.17}$$

$$f(x_{ea}) \;=\; g(x_{ea}) \;, \tag{5.18}$$

$$\left.\frac{d\,f}{d\,x}\right|_{x_{ea}} \;=\; \left.\frac{d\,g}{d\,x}\right|_{x_{ea}} \;, \tag{5.19}$$

$$\int\limits_{x_{le}}^{x_{ea}} g(x)\,dx \;+\; \int\limits_{x_{ea}}^{x_{te}} f(x)\,dx \;=\; m_p \;, \tag{5.20}$$

$$\int_{x_{le}}^{x_{ea}} g(x)x\,dx \;+\; \int_{x_{ea}}^{x_{te}} f(x)x\,dx \;=\; S\;, \tag{5.21}$$

$$\int_{x_{le}}^{x_{ea}} g(x)x^2\,dx \;+\; \int_{x_{ea}}^{x_{te}} f(x)x^2\,dx \;=\; I_\theta\;. \tag{5.22}$$

Equations 5.15 and 5.16 simply state that the linear density functions cannot be negative. Equation 5.17 simply means that the linear density must fall to zero at the leading edge (x_{le}) and at the trailing edge (x_{te}) of the airfoil. Equations 5.18 and 5.19 make sure that the linear density functions match at the elastic axis, and that the transition from one function to the other is smooth. However, note that the specific value of the first order derivative at the elastic axis is not enforced, which means that the maximum linear density is not necessarily encountered on the elastic axis. Equations 5.20 to 5.22 simply correspond to the definitions of the pitching mass, of the static imbalance, and of the moment of inertia about the elastic axis.

It should be noted that it is not possible to obtain an equation for the heaving mass (m_h) without the actual design of the mechanisms. However, in the current case, because the value of m_h is fairly low, it is assumed that the difference between m_p and m_h must remain small if we want m_p to be realistic. For this reason, m_p is here assumed to be equal to m_h, which corresponds to the upper bound value for m_p. Using these equations, the following polynomial forms are assumed for the linear density functions, where the units are kg/m:

$$f(x) \;=\; ax^n \;+\; bx^m \;+\; cx \;+\; d\;, \tag{5.23}$$

$$g(x) \;=\; ex^2 \;+\; hx \;+\; k\;. \tag{5.24}$$

These forms have been chosen based on the shape of the airfoil, which obviously suggests a general trend for the density functions. Again, the general trend of this educated guess is shown in Figure 5.4. Before solving the problem for a, b, c, d, e, h and k, values of n and m must be chosen. Several combinations of n and m have been tried, and the chosen values are those providing a well-behaved linear density function near the trailing edge of the airfoil. For example, simply assuming $n = 3$ and $m = 2$ does give rise to some negative values of the linear density function near the trailing edge. Some other combinations make the value of the mass density function fall too quickly towards zero. One of the possible, well-behaved solution of the problem is:

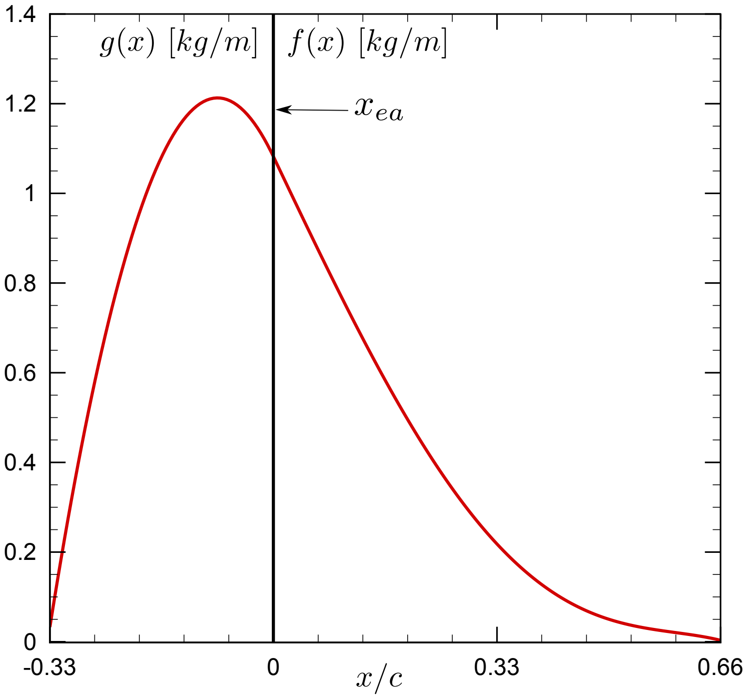

Figure 5.5: Representation of the linear density functions $f(x)$ and $g(x)$ over the airfoil for the dimensional case in air.

$$f(x) \ = \ -14893.133x^5 \ + \ 700.725x^3 \ - \ 15.865x \ + \ 1.082 \ , \tag{5.25}$$

$$g(x) \ = \ -481.426x^2 \ - \ 15.865x \ + \ 1.082 \ , \tag{5.26}$$

and these linear density functions are plotted in Figure 5.5. The very first important observation that should be made is certainly that a solution satisfying all the constraints simultaneously does exist. However, that solution is not unique and the specific shape may be adapted, for example, by varying m and n. Furthermore, the real linear density does not need to be as continuous: internal structural components of the wing, which have a specific dimension, will alter the shape of the linear density.

The reader should make sure to fully understand the physical interpretation of the linear density functions. For example, at the location corresponding to the elastic axis, a value of 1.08 kg/m is obtained. At this same location, the thickness of the airfoil is 0.03 m[5]. This means that if the airfoil's section at this station was extruded of 1 m, thus resulting in a block

---

[5] The elastic axis is located $c/3$ behind the leading edge, which also corresponds to the location of the airfoil's maximum thickness, which is here 15%.

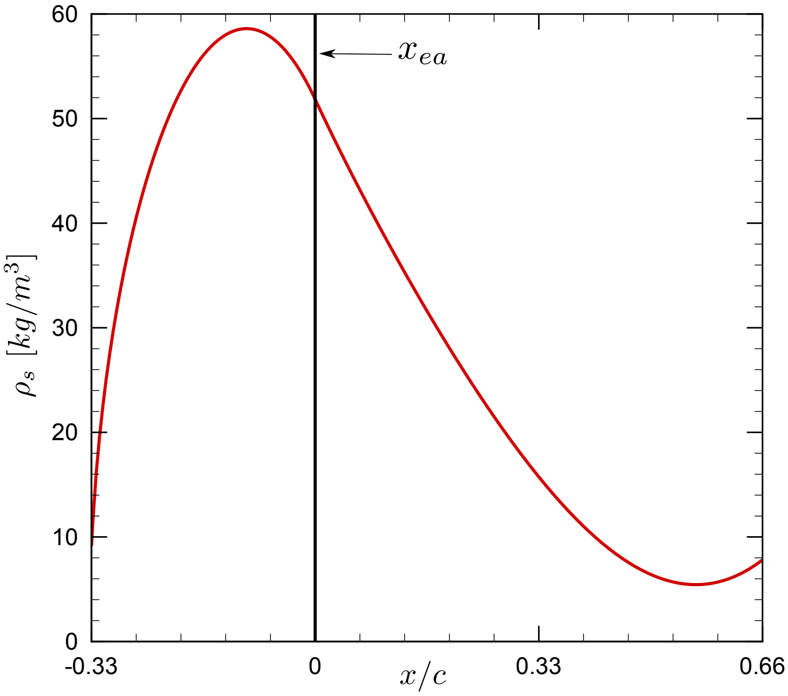

Figure 5.6: Representation of the density distribution (ρ_s) over a NACA0015 airfoil for the dimensional case in air.

of 0.03 m × 0.7 m × 1 m, the mass of that piece of material would be 1.08 kg. If the density of the material was constant and uniform across that section (i.e., a completely filled section), the material used to build this specific section would need to have a density of 51.4 kg/m^3. This material density $\rho_s(x)$ is simply computed as:

$$\rho_s(x) \; = \; \frac{\mu}{e(x)\, b} \; , \tag{5.27}$$

where μ is the function $f(x)$ or $g(x)$ depending on the sign of x, $e(x)$ is the thickness of the airfoil, and b is the span. However, it should be noted that using a completely filled section is not a requirement. In fact, a portion of the airfoil could be hollow, thus making it possible to use a material of greater density to build the airfoil, and, also, providing an efficient way of controlling the material density at each station along the chord length of the airfoil. For example, if the section located at the elastic axis was built with a 1 cm thick shell on both the upper surface and the lower surface, the material used would need to have a density of 77.1 kg/m^3. If the shell was only 0.5 cm thick, this density would increase to 154.2 kg/m^3.

A representation of this density $\rho_s(x)$ is shown in Figure 5.6 for the case of a NACA0015 profile where the density is uniform across each station (i.e., the wing is completely filled).

It can be observed that the maximum is located ahead of the elastic axis, which is a result of the constraint specifying the static imbalance of the airfoil. Knowing that carbon fibers composite materials have a density in the range of 20 kg/m^3, and polystyrene has a density in the range of 10 kg/m^3, it does not seem feasible to make an airfoil that respects this density distribution. Indeed, the required density drops below 10 kg/m^3 close to the leading edge, and because of the very small airfoil's thickness there, it is hard to conceive having a hollow interior surrounded by a thin shell. This matter will be further discussed within the next subsection once the dimensional parameters for the case in water have been introduced.

The frequency of oscillation of such an airfoil also needs to be considered in order to characterize the feasibility of the concept. With a freestream velocity (U_∞) of 60 m/s, a chord length (c) of 0.2 m and a reduced frequency (f^*) of 0.096, a frequency ($f = U_\infty f^*/c$) of approximately 30 Hz is obtained. Such a high frequency of motion is most probably unattainable for the oscillating airfoil described here as it would result in very fast heaving and pitching motions, thus increasing considerably the inertial forces and moments on the turbine. The structural integrity of the flapping airfoil would therefore be compromised. This too high frequency of oscillation could be reduced by using an airfoil having a larger chord length, but this also means that a larger wind tunnel would be needed. Another possibility would be to reduce the frequency by decreasing the freestream velocity, but the Reynolds number would also diminish and move farther away from a value representative of a turbine application.

5.3.2 Dimensional case in water

Concerning the dimensional parameters pertaining to a setup specifically designed to study the fully-passive, flapping-airfoil in a water tunnel, the dimensions of the test section are assumed to be the following: a water depth of 0.5 m, a width of 0.5 m and a length of 2.5 m. Further, the velocity of the flow is assumed to be 1 m/s. These dimensions and this velocity of the flow are representative of the typical water tunnel encountered within academic environments. With such dimensions, the chord length of the airfoil would need to be approximately 0.1 m. Again, this is to make sure the oscillating foil remains at some distance from the walls of the tunnel. Also, it is assumed that the airfoil's vertical extent is equal to the water depth, specifically 0.5 m, thus providing an aspect ratio of 5. The corresponding maximum blockage ratio is 20%, and the Reynolds number is approximately 90,000. With these references (i.e., $b = 0.5$ m, $c = 0.1$ m, $U_\infty = 1$ m/s and $\rho_f = 1000$ kg/m^3), the set of dimensional parameters corresponding to the optimized fully-passive, flapping airfoil is calculated. The values are shown in Table 5.5.

With these values, a resulting frequency ($f = U_\infty f^*/c$) of approximately 1 Hz is obtained. This is in contrast with the frequency of 30 Hz computed for the case in air. Obviously, the lower value of 1 Hz corresponding to an experiment performed in water is more physically plausible, and it would be attained more easily. This is because the inertial forces and moments

Table 5.5: Set of dimensional parameters for a water tunnel experiment involving the optimized case of the fully-passive, flapping-airfoil turbine. The following dimensional parameters have been used: $c = 0.1\ m$, $b = 0.5\ m$, $\rho_f = 1000\ m/s$, $U_\infty = 1\ m/s$.

Parameter	Value	Parameter	Value
m_h	15.180 kg	S	-0.0145 kg·m
k_θ	0.155 N·m/rad	k_h	603 N/m
D_θ	0.060 N·m·s/rad	D_h	75.050 N·s/rad
I_θ	0.0048 kg·m^2		

on the turbine would probably not be large enough to impair the structural integrity of the flapping airfoil or to impose severe mechanical constraints during the design of the turbine.

Again, the stiffness in heave can be best provided by making use of extension springs. Because the chord length of the airfoil is here smaller than in the case of the experiment in air, the extension of the springs will be considerably reduced. This means that the linear behavior of the spring does not need to be maintained up to extensions of 30 cm. Instead, 15 cm would be sufficient, and this means that far more springs already available on the market are suitable for the task. Concerning the torsional spring, the amplitude of the deflection obviously remains unchanged when compared to the case in air. Nevertheless, selecting a particular spring appears to be simplified again by the fact that the required stiffness is smaller than for the previous device in air.

For the damping in both pitch and heave, the same conclusions as for the case in air still hold true. This is because the damping ratios are the same as before, namely 0.39 in heave (ξ_h) and 1.10 in pitch (ξ_θ). Because these damping ratios are fairly high, the inherent structural damping of the device alone should not bring the damping ratios up to these values, which means that a damper and a generator should be added to the device.

The heaving mass of the airfoil is probably the structural parameter that differs the most from the case in air. This is because, it has a value of 15.18 kg for the device in water, while the device in air had a heaving mass of 0.1045 kg. From a design perspective, building a device having a mass of 15.18 kg is probably far less restrictive and much easier to meet that building a device with a mass of 0.1045 kg. The same procedure as before can be applied in order to find the linear density functions. However, this time it is not required to assume $m_p = m_h$. It is even possible to design the wing such that it does not respect the requirement on I_θ and S, and simply add masses that are external to the wing: a form of non-uniform flywheel attached to the shaft. This is of great help as satisfying the three constraints simultaneously does not appear to be possible without external masses. Indeed, if external masses were not used, the density of the required material to build the wing would be far above the density of common metals (i.e., above 30,000 kg/m^3).

One simplistic alternative is to build the wing with some metals without giving thoughts about its mass, its moment of inertia and its static imbalance. This will result in a wing having a total mass in the range of 1 to 3 kg only. Then, a non-uniform flywheel can be added to the shaft, thus bringing the static imbalance and the moment of inertia to the desired values. Last, some masses can be added to the sliding mechanism, thus bringing the total mass of the device to a value of 15.18 kg. A specific solution is not shown here as there are far too many options available. Indeed, the fully-passive, flapping-airfoil in water offers much more flexibility in the design than does the case in air.

The main conclusion of this dimensional study is certainly that investigating the fully-passive, flapping airfoil in a water tunnel experiment is far more plausible than doing the experiment in air. This is because the resulting frequency of motion in air would be too large to be realistic, and the density of the material required for building the wing would be too low. The latest is due to the moderate FSI strength corresponding to the optimized case investigated in this thesis. As a result of this FSI strength, the density of the material used to build the airfoil needs to be approximately in the same range as the fluid's density. This is convenient for the case in water, but this is of course not achievable for the case in air.

As a result of the previous findings, two main statements can be formulated:

- Investigating the fully-passive, flapping-airfoil in a water channel appears to be feasible if one accepts to drop the Reynolds number in the vicinity of 100,000. Furthermore, solutions where the total mass of the turbine (m_h^*) is lower than for the optimized case of this thesis could be considered, and such solutions would remain feasible. However, this implies that the strength of the FSI would increase, and the present numerical solver would have to be modified in order to carry out the simulations (i.e., a strong coupling scheme would be needed).
- The *current* optimized fully-passive, flapping-airfoil device does not appear to be suitable for being experimentally investigated in air. One could of course seek another optimized solution, if any, where m_h^* is larger in order to increase the density of the material used to build the oscillating airfoil, and the solver of this thesis could be used without any modification to carry out the numerical simulations. However, this would only solve a part of the problem as the frequency of oscillation would still be too high to be mechanically possible. The Reynolds number would have to be very significantly lowered in order to obtain a frequency which is at reach for the purpose of investigating the turbine in a wind tunnel.

5.4 Other interesting cases

Because the set of non-dimensional parameters corresponding to the optimized case discussed in Chapter 4 is not suitable for an application in a freestream flow of air, some other interesting cases are here presented. These sets of non-dimensional parameters make use of a higher value of m_h^*, which means that the strength of the fluid-structure interaction is decreased. Therefore, these sets are more appropriate at being used in air.

These sets of parameters have been obtained through RPAS. The same procedure as before has been used (see Chapter 4), except that the prescribed aerodynamics and kinematics make use of a reduced frequency equal to 0.12. A few cases minimizing the residuals, where the average residuals is in the range of 10%, have then been simulated with the FSI solver. The very encouraging results shown in Table 5.6 have been obtained. There still remains the need to perform a complete optimization about these cases to determine if the performances can be further increased. Even without any optimization, the performances are already quite impressive. The amplitudes of motion are large, and the efficiencies are in the range of 25% to 30%. These efficient cases could be an interesting starting point for a person interested into pursuing the research on this aeroelastic problem. Definitely, these results show that there is great potential at obtaining good performances of the flow harvester within other regions of the parametric space. Some of these regions of the parametric space could be more adapted to light fluids than does the optimized case from the previous chapter.

The fact that prescribing a reduced frequency of 0.12 in RPAS provides lower residual than the previous case from Chapter 4, where a frequency of 0.18 had been imposed, is probably not meaningless. The higher performances here obtained, without even performing an optimization, is also in agreement with these lower residuals. One should recall that the residuals of RPAS in Chapter 4 were in the range of 20%.

The low residuals in the range of 10% obtained here can be physically explained. First, it should be mentioned that the optimal reduced frequency of the kinematically-constrained turbine, which is 0.18, does not give rise to massive flow separations. Deep dynamic stall is not encountered at any moment of the upstroke or the downstroke, and this has been easily confirmed by observing the physical fields associated to the aerodynamics imposed within RPAS. However, when a reduced frequency of 0.12 is imposed within RPAS, the corresponding aerodynamics does exhibit some massive separations. In fact, the airfoil encounters deep dynamic stall twice per cycle, just as the optimized fully-passive, flapping-airfoil turbine. Said otherwise, the physics of the flow surrounding a kinematically-constrained airfoil oscillating at a reduced frequency of 0.12 is in better agreement with the physics of the flow around an airfoil undergoing stall flutter. It is not a great surprise to obtain lower residuals when the aerodynamics prescribed within RPAS is in better agreement with the real physics of the flow. These observations, again, are in agreement with the observations of Chapter 4 that confirmed the dominating role of the vortex shedding associated to deep dynamic stall.

Table 5.6: Interesting cases where the fluid-structure interaction is weaker than the optimized case of Chapter 4. These cases have been obtained through RPAS and simulated with the FSI solver, and no optimization has been performed yet.

Parameter	Case 1	Case 2	Case 3	Case 4
m_h^*	5.187	7.628	8.849	12.510
S^*	0.619	0.635	0.619	0.619
k_θ^*	0.061	0.061	0.061	0.061
k_h^*	2.667	4.033	4.748	6.829
D_θ	0.209	0.209	0.209	0.209
D_h	1.337	1.337	1.337	1.337
I_θ	0.286	0.286	0.286	0.286
f^*	0.111	0.111	0.111	0.111
θ_0^*	81°	78°	76°	71°
y_0^*	0.88	0.84	0.83	0.76
η	29.5%	28.9%	28.1%	26.3%
$\overline{C}_P$	0.70	0.66	0.63	0.56

Conclusion

Within this chapter, the feasibility of the optimized fully-passive, flapping-airfoil turbine has been investigated. First, the effect of dry friction in both heave and pitch has been addressed. The main finding, which is not a great surprise, is that dry-friction reduces the performances of the turbine. Nevertheless, small values of dry friction are tolerable since large-amplitude LCO are still possible. This means that care will be needed during the design of a fully-passive turbine in order to minimize the amount of dry friction.

Following this, the modeling of the electrical generator connected to the turbine has been investigated. Through a relatively simple analysis, it has been shown that an electrical generator can indeed behave as a viscous damper, thus confirming the validity of the current model. Further, it has been discussed that the equivalent damping coefficient of the generator can be controlled through electronic controllers by varying the flux and/or the electrical load.

In the following section, the optimized fully-passive turbine has been dimensionally studied. For this purpose, the dimensional structural parameters of a turbine operating in air and a turbine operating in water have been calculated. Through a deeper analysis of these dimensional parameters, it has been found that the optimized fully-passive turbine of this thesis is well adapted for dense fluids, such as water. In order to use a fully-passive turbine within a freestream flow of air, another region of the parametric space where the mass is greater would need to be investigated.

A few cases where this non-dimensional mass is greater have been obtained through RPAS. They were shown within the last section of this chapter, and efficiencies as high as 30% were obtained. It should be recalled that no optimization has been performed on these cases, and the performances can surely be further increased. These four cases are more adapted for a turbine in air, and they are certainly worth being further investigated in the near future.

Conclusion

This master's thesis constitutes a fairly extensive initial investigation of a hydrokinetic turbine making use of the self-sustained, pitch-heave oscillations of an elastically-mounted, symmetrical and rigid airfoil. Such a novel type of flow harvester could prove to be very useful as a result of its relatively simple mechanics when compared to other sorts of hydrokinetic turbines. Further, such a device appears to be well adapted for harvesting a flow of limited depth, thus making it useful for shallow rivers.

The current numerical work is among the first few studies to extensively consider a fully-passive, flapping-airfoil turbine. Also, to the author's knowledge, it is the first time that such a numerical study is achieved at high Reynolds numbers that are representative of a realistic turbine application. Within this concluding chapter, a brief summary of the main results and findings is provided, along with an opening on the future work following this project.

Summary of the results and findings

The first objective of this document was to introduce some theoretical concepts pertaining to the field of aeroelasticity in order to better understand the flutter phenomena to which the oscillating airfoil is exposed. For this reason, classical flutter, stall flutter and limit-cycle oscillations have been discussed. This provided the required knowledge to the reader in order to understand more deeply the aeroelastic problem of the thesis.

The second objective of this thesis was to formally introduce the aeroelastic problem. For this purpose, the aeroelastic device has been thoroughly described, and the equations of motion have been formally derived. Further, the various terms involved within both equations have been discussed and analyzed to provide a better physical understanding of the apparatus. The main findings were certainly that we are dealing with a nonlinear problem, and both equations of motion are greatly coupled. This coupling is achieved through an inertial coupling term, and also through the nonlinear aerodynamics involved. However, it is not possible to prescribe a phase lag between both motions, nor to constrain the shape of the motions. Instead, a total of seven structural parameters are involved within the equations, and all of these parameters can be individually varied as a way to affect and indirectly control the motion of the flapping-airfoil. Through modifications of the airfoil's dynamics, its performances at harvesting a freestream flow can also be modified. Therefore, the device can be optimized through an astute choice of each structural parameter.

The third objective was to introduce the fluid-structure solver used for solving the aeroelastic problem. For this reason, the methodology used and implemented within the *OpenFOAM-2.1.x* CFD toolbox has been thoroughly presented. This methodology has also been validated in various complementary ways. First, the results were shown to be relatively independent from the numerics. Second, an experiment from the Royal Military College has been reproduced with the solver. This experiment deals with an elastically-mounted airfoil oscillating within a flow of air as a result of stall flutter. Although the experiment was conducted in the transitional range of Reynolds numbers and the numerical solver has been designed for high Reynolds numbers, the qualitative and quantitative agreement between the experimental and the numerical data contributed to the proof of the solver's accuracy. A third validation of the solver has been performed with a well-known problem: the vortex induced vibrations of an elastically-mounted cylinder oscillating transversally to a flow. Numerical results from other studies, as well as experimental results, were used to assess the validity and the accuracy of the predictions obtained with the solver of this thesis. Again, the present results were found to be in good agreement with the other numerical studies, as much as with the experimental results.

The fourth objective was to optimize the fully-passive, flapping airfoil as an efficient hydrokinetic turbine, and also to suggest an optimal concept that is realistic. In order to initiate the optimization process with a well-chosen initial case, a clever methodology has been implemented with an in-house application. The objective of the Reverse Passive-Airfoil Solver is to solve the inverse mathematical problem where the kinematics and the aerodynamics are prescribed. The output of such a solver is a set of structural parameters that satisfies as closely as possible the equations of motion. With such a methodology, an initial case having an efficiency in the range of 12% has been obtained. Then, a gradient-like optimization has been achieved about this initial case, thus increasing the efficiency to 34%. Such an efficiency demonstrates that there is obviously great potential at using fully-passive, flapping-airfoils for the purpose of harvesting a flow. It should be recalled that the efficiency of the optimal kinematically-constrained turbine is in the range of 43%. Therefore, an efficiency of 34% is relatively high, especially that the fully-passive turbine is far less complex than the kinematically-constrained one from a mechanical point of view.

The efficient case found with the gradient-like optimization has also been studied more deeply to find out that it is realistic for an application within a flow of water. However, using this optimal set of parameters does not seem to be possible for an application within a flow of air. This is because the resulting frequencies would be too high, and also because the mass of the oscillating wing would need to be very low. It would be very challenging to respect such severe constraints.

The fifth and last objective was to perform a sensitivity study of the device, and also to study the physics involved. The physics has been deeply investigated, and it has been demonstrated that the oscillating airfoil of this study is unstable as a result of a static divergence. Further, the cyclic motion of the airfoil is attributed to stall flutter. During the deep dynamic stall events of the airfoil, a large eddy is shed at the leading edge, and this vortex interacts with the airfoil. It is this interaction with the vortex that provides the aerodynamic moment giving rise to a pitching motion, thus making the airfoil pitch the other way around and revert its heaving direction. The fact that the vortex-airfoil interaction most accounts for the pitching motion has been demonstrated through simulations where no springs were present in both pitch and heave.

Two mechanisms have been highlighted as being responsible for the great performances of the optimized case at harvesting a flow. First, the adequate synchronization between the pitching and the heaving motion is a crucial element. This is because an adequate synchronization will prevent the airfoil from achieving some work on the flow. If the airfoil does some work on the flow at some moments of its cycle, this turns out to be very costly from a performance point of view. Further, an adequate synchronization allows the airfoil to remain closer to the vortex shed during the deep dynamic stall, and this enhances the beneficial airfoil-vortex interaction. The second mechanism is the presence of a fast pitching regime. Because the airfoil must pass through a null effective angle of attack when it reaches an extrema in heave, the lift coefficient must also be momentarily null. Because the airfoil's pitching motion is achieved in three different phases, and because one of these phases has a larger pitching rate, the effective angle of attack does not remain close to zero for too long, and the lift coefficient quickly becomes large again. This minimizes the effect of changing the heaving direction, and the larger lift coefficients resulting from such a motion enhance the harvested power from the flow.

Concerning the sensitivity study, it has been shown that the airfoil is sensitive to all of the structural parameters, except for the moment of inertia. However, because of the complex interaction between both degrees-of-freedom, no parameter has an effect on a single performance metric. Nevertheless, it has been shown that the electrical generator connected to the airfoil could be used to achieve some control over the airfoil's response. This is especially true when the velocity of the flow is increased above the design value. In such a case, the equivalent damping of the generator could be increased in order to maintain high performances, and to avoid amplitudes of motion that are too large. In counterparts, it has not been possible to find an adequate compensation whenever the velocity of the flow is below its design value. This situation proved to be very detrimental for the turbine's performances.

Future work

Following this numerical study, one of the first steps to be performed is certainly to investigate more deeply the various cases shown in Chapter 5 (Table 5.6) where the heaving mass is greater than for the optimized case. An optimization still remains to be performed about these cases, and this could prove to be useful for the sake of finding an optimized case that is well adapted for an application into a flow of air. The performances of these four cases are already relatively high, and there is hope to further increase this efficiency. Using a solver implementing a strong FSI coupling scheme should also be considered in order to investigate other regions of the parametric space that are adapted to an application into a flow of water.

Next, it has not been possible to realize three-dimensional simulations of the fully-passive, flapping-airfoil turbine due to time constraints. It will be important to achieve such simulations in order to refine the numerical predictions. In fact, two main effects will need to be assessed. First, the vortex shed at the leading edge of the airfoil will have the possibility to break down into smaller structures, thus affecting the spanwise correlation of pressure over the airfoil. However, it has been mentioned that structures oscillating as a result of fluid-structure interaction tend to have a relatively strong correlation of pressure along the span, especially when the amplitude of motion is large. For this reason, this effect should not impair the performances of the turbine. The second effect that needs to be investigated is due to the wingtip vortices associated to the finite lateral extent of the wing. Several aspect ratios of the wing will need to be investigated, as much as the effect of using end plates to minimize the effect of the wingtip vortices. This effect might reduce the performances of the turbine, and this needs to be quantify. To end, simulations making use of a more advanced turbulent modeling approach could be used, such as LES or a hybrid method combining URANS and LES, in order to further refine the numerical predictions.

Future studies should also deal with the effect of the location of the elastic axis. Xiao and Zhu (2014) showed that moving the elastic axis can have a significant impact on a passive airfoil. In fact, they suggest that moving the location of the elastic axis is equivalent to changing the phase lag between the heaving and the pitching motions, and the current study showed that this synchronization is a critical parameter in order to optimize the efficiency of the turbine. Another structural parameter that should be investigated is the airfoil's profile. This study made use of a NACA 0015 airfoil, and there is no guarantee that this is optimal.

A following step will be to investigate the behavior of the fully-passive, flapping-airfoil turbine when it is used within a non-uniform flow, such as within a boundary layer. As the fully-passive turbine is relatively a new subject in the literature, there is definitely a lack of information concerning the effect of such a condition of the flow. Further, the effect of perturbations within the flow should be investigated. Indeed, a fully-passive, flapping-airfoil should not be oversensitive to fluctuations of the freestream flow, and this has not been investigated.

Furthermore, experimental work could certainly be achieved on such a fully-passive, flapping-airfoil turbine. Indeed, a recipe has been provided within this thesis in order to design an experimental setup respecting the set of parameters corresponding the the optimized case. Such an experimental work could help at better understanding the physics involved. This could also highlight some special features or some complexities pertaining to such a mechanism, especially concerning the design of the apparatus or its sensitivity. The effect of the self-sustained oscillations on the spanwise correlation of pressure could also be investigated through such an experimental study.

Last but not least, a *semi-passive*, flapping-airfoil turbine could be investigated. Studying the fully-passive turbine surely provided a very good understanding of the physics involved. Nevertheless, a semi-passive turbine where only one degree-of-freedom is prescribed could be studied. In fact, the semi-passive devices that have been studied so far in the literature are aeroelastic apparatus where the pitch is prescribed and the heave results from the fluid-structure interaction. However, a novel system where the heave is prescribed and the pitch results from the fluid-structure interaction could be studied more deeply. Indeed, if a linear motor/generator was connected to the airfoil, it could be used to constrain the heaving motion. Then, the structural parameters of the device could be adjusted in order to obtain an efficient pitching motion. Such a semi-passive turbine where the linear motor/generator is used to control the motion could most probably be more easily optimized than its fully-passive counterpart. Also, the device could probably be efficient over a larger range of flow conditions as a result of the greater control on the dynamics. This is because a linear motor/generator could provide a damping force that is variable throughout the cycle, thus providing much control over the airfoil's motion. Last, the semi-passive device where the heaving motion is constrained has a clear advantage over the semi-passive device where the pitch is constrained. Because the generator must be connected to the heaving motion, constraining the heaving motion means that only one motor/generator is needed. On the contrary, constraining the pitching motion requires a motor for the pitching motion, as much as a generator for the heaving motion.

As a final remark, the author of this document hopes that the reader will show some interest at pursuing the research on the aeroelastic problem here considered. There is still room for the development of novel flow harvesters making use of renewable energies, and the research on oscillating foils as efficient harvesters is only at its beginning. So far, most studies available in the literature have been concerned with a better understanding of the physics. A lot of work remains to be done in order to develop fully-passive or semi-passive, flapping-airfoil turbines, but the encouraging results of this thesis surely demonstrate that it is worth the efforts.

Bibliography

Abad, G., López, J., Rodríguez, M., Marroyo, L., and Iwanski, G. *Doubly Fed Induction Machine: Modeling and Control for Wind Energy Generation.* Wiley, Hoboken, New Jersey, 2011. *Page 150*

Anagnostopoulos, P. and Bearman, P. W. Response characteristics of a vortex-excited cylinder at low reynolds numbers. *Journal of Fluids and Structures*, 6(1):39–50, 1992. *Pages xiii, 79, and 81*

Arena, A., Lacarbonara, W., and Marzocca, P. Nonlinear aeroelastic formulation and post-flutter analysis of flexible high-aspect-ratio wings. *Journal of Aircraft*, 50(6):1748–1764, 2013. *Pages 25, 28, 29, and 30*

Bearman, P. W. Circular cylinder wakes and vortex-induced vibrations. *Journal of Fluids and Structures*, 27(5-6):648–58, 2011. *Page 5*

Betz, A. and Prandtl, L. Schraubenpropeller mit geringstem energieverlust. *Nacht Ges. Wiss. Göttingen Math Phys.*, K1:193–217, 1919. *Page 11*

Broer, H. and Takens, F. *Dynamical Systems and Chaos.* Springer, New York, 2010. *Page 30*

Bryant, M., Gomez, J. C., and Garcia, E. Reduced-order aerodynamic modeling of flapping wing energy harvesting at low reynolds number. *AIAA Journal*, 51(12):2771–2782, 2013. *Page 28*

Causin, P., Gerbeau, J.F., and Nobile, F. Added-mass effect in the design of partitioned algorithms for fluid-structure problems. *Computer Methods in Applied Mechanics and Engineering*, 194:4506–4527, 2005. *Page 55*

Century Springs. Century springs catalog, 2014. URL `http://www.centuryspring.com/pdfs/01-04TOC.pdf`. (visited on 2014/05/30). *Page 154*

Degroote, J., Bruggeman, P., Haelterman, R., and Vierendeels, J. Stability of a coupling technique for partitioned solvers in FSI applications. *Computers and Structures*, 86(23–24): 2224 – 2234, 2008. *Pages 52 and 55*

Dimitriadis, G. and Li, J. Bifurcation behavior of airfoil undergoing stall flutter oscillations in low-speed wind tunnel. *AIAA Journal*, 47(11):2577–2596, 2009. *Pages 3, 5, 25, 26, and 29*

Dowell, E. H., Clark, R., Cox, D., Curtiss, H. C., Edwards, J. W., Hall, K. C., Peters, D. A., Scanlan, R., Simiu, E., Sisto, F., and Strganac, T. W. *A Modern Course in Aeroelasticity*, volume 116 of *Solid Mechanics and Its Applications*. Springer Netherlands, Dordrecht, The Netherlands, 4th edition, 2005. *Pages 3, 19, 21, 25, 30, 36, and 141*

Durgin, W. W., March, P. A., and Lefebvre, P. J. Lower mode response of circular cylinders in cross-flow. *Journal of Fluids Engineering*, 102(2):183–90, 1980. *Page 5*

Dyrbye, C. and Hansen, S.O. *Wind Loads on Structures*. Wiley, West Sussex, England, 1997. *Page 141*

Farrell, P. E. and Maddison, J. R. Conservative interpolation between volume meshes by local Galerkin projection. *Computer Methods in Applied Mechanics and Engineering*, 200(1-4): 89–100, 2011. *Page 49*

Ferziger, J.H. and Perić, M. *Computational Methods for Fluid Dynamics*. Springer, third edition, 2002. *Pages 44 and 45*

Förster, C., Wall, W.A., and Ramm, E. Artificial added mass instabilities in sequential staggered coupling of nonlinear structures and incompressible viscous flows. *Computer Methods in Applied Mechanics and Engineering*, 196(7):1278 – 1293, 2007. *Page 55*

Fortin, A. *Analyse numérique pour ingénieurs*. Presses internationales Polytechnique, second edition, 2001. *Page 51*

Fung, Y.C. *An Introduction to the Theory of Aeroelasticity*. Dover, Mineola, New York, 2008. *Pages 19 and 25*

He, T., Zhou, D., and Bao, Y. Combined interface boundary condition method for fluid-rigid body interaction. *Computer Methods in Applied Mechanics and Engineering*, 223-224: 81–102, 2012. *Pages 51 and 55*

Huxham, G. H., Cochard, S., and Patterson, J. Experimental Parametric Investigation of an Oscillating Hydrofoil Tidal Stream Energy Converter. In *18th Australasian Fluid Mechanics Conference*, Launceston, Australia, 2012. *Page 2*

Jiang, X. and Lai, C.H. *Numerical Techniques for Direct and Large-Eddy Simulations*. Chapman & Hall/CRC Numerical Analysis and Scientific Computing Series. CRC Press, 2009. *Page 62*

Jones, W. P. and Launder, B. E. The calculation of low-reynolds-number phenomena with a two-equation model of turbulence. *International Journal of Heat and Mass Transfer*, 16 (6):1119–30, 1973. *Page 178*

Julien, S., Dumas, G., and Métivier, V. URANS Simulations of High Amplitude Flapping Airfoils. In *15th Annual Conference of the CFD Society of Canada*, Toronto, Canada, May 2007. Paper CFD-2007-1117. *Page 48*

Kinsey, T. *Analysis, Optimization and Demonstration of a New Concept of Hydrokinetic Turbine Based on Oscillating Hydrofoils.* PhD thesis, Université Laval, 2011. *Page 23*

Kinsey, T. and Dumas, G. Parametric study of an oscillating airfoil in power extraction regime. In *24th AIAA Applied Aerodynamic Conference*, San-Francisco, California, 2006. *Pages 2 and 8*

Kinsey, T. and Dumas, G. Parametric Study of an Oscillating Airfoil in a Power-Extraction Regime. *AIAA Journal*, 46(6):1318–1330, 2008. *Pages 2, 8, 11, and 49*

Kinsey, T. and Dumas, G. Optimal Operating Parameters for an Oscillating Foil in Power-Extraction Regime at Reynolds Number 500,000. *AIAA Journal*, 2014. doi: 10.2514/1.J052700. [in press]. *Pages xi, 2, 3, 8, 10, 11, and 94*

Kinsey, T., Dumas, G., Lalande, G., Ruel, J., Mehut, A., Viarouge, P., Lemay, J., and Jean, Y. Prototype testing of a hydrokinetic turbine based on oscillating hydrofoils. *Renewable Energy*, 36(6):1710–1718, 2011. *Pages xi, 2, 8, 9, 12, and 89*

Kinsey, Thomas and Dumas, G. Computational fluid dynamics analysis of a hydrokinetic turbine based on oscillating hydrofoils. *Journal of Fluids Engineering*, 134(2), 2012a. *Pages xi, 2, 8, 12, 13, and 89*

Kinsey, Thomas and Dumas, G. Optimal tandem configuration for oscillating-foils hydrokinetic turbine. *Journal of Fluids Engineering*, 134(3), 2012b. *Page 2*

Kinsey, Thomas and Dumas, G. Three-dimensional effects on an oscillating-foil hydrokinetic turbine. *Journal of Fluids Engineering*, 134(7), 2012c. *Page 2*

Kundu, P.K., Cohen, I.M., and Dowling, D.R. *Fluid Mechanics.* Academic Press, Oxford, England, fifth edition, 2012. *Page 41*

Lapointe, S. Numerical study of self-sustained oscillations in transitional flows. Master's thesis, Université Laval, 2012. *Page 4*

Lapointe, S. and Dumas, G. Improved Numerical Simulations of Self-Sustained Oscillations of a NACA0012 with Transition Modeling. In *41st AIAA Fluid Dynamics Conference*, Honolulu, Hawai, June 2011. Paper AIAA-2011-3528. *Pages 2 and 49*

Lapointe, S. and Dumas, G. Numerical Simulations of Self-Sustained Pitch-Heave Oscillations of a NACA0012 Airfoil. In *CFD Society of Canada*, Canmore, Alberta, May 2012. *Pages xi, xii, 15, 34, and 48*

Larsen, J. W., Nielsen, S. R. K., and Krenk, S. Dynamic stall model for wind turbine airfoils. *Journal of Fluids and Structures*, 23(7):959–982, 2007. *Page 28*

Leishman, J. G. and Beddoes, T. S. A semi-empirical model for dynamic stall. *Journal of the American Helicopter Society*, 34(3):3–17, 1989. *Page 28*

Leontini, J. S., Thompson, M. C., and Hourigan, K. The beginning of branching behaviour of vortex-induced vibration during two-dimensional flow. *Journal of Fluids and Structures*, 22(6–7):857–864, 2006. *Pages ix, 5, 77, 78, 79, and 80*

McCroskey, W. J. The Phenomenon of Dynamic Stall. Technical report, NASA, 1981. *Pages ix, xi, 25, 26, and 27*

McCroskey, W. J. Unsteady Airfoils. *Annual Review of Fluid Mechanics*, 14:285–311, 1982. *Page 26*

McKinney, W. and DeLaurier, J. The Wingmill: An Oscillating-Wing Windmill. *Journal of Energy*, 5(2):109–115, 1980. *Page 1*

Mendes, F., Poirel, D., and Benaissa, A. Experimental Investigation of Self-Sustained Pitch-Heave Aeroelastic Oscillations of a NACA0012 Airfoil at Transitional Reynolds Numbers. In *CASI2011*, Montreal, Canada, January 2011. *Pages ix, xi, xii, xiii, 3, 13, 16, 17, 60, 70, and 73*

Menter, F. R. Zonal Two Equation k-omega Turbulence Models for Aerodynamic Flows. In *11th AIAA Computational Fluid Dynamics Conference*, Orlando, Florida, July 1993. Paper AIAA 93-2906. *Page 180*

Menter, F. R. Two-equation eddy-viscosity turbulence models for engineering applications. *AIAA Journal*, 32(8):1598–1605, 1994. *Pages 62 and 178*

Meriam, J.L. and Kraige, L.G. *Engineering Mechanics: Statics.* Wiley, New York, fifth edition, 2008. *Pages 144 and 145*

Metivier, V. Étude des oscillations auto-excitées d'un profil d'aile NACA 0012 à des nombres de Reynolds transitionnels. Master's thesis, Université Laval, 2012. *Page 41*

Morissette, J.F. Simulations aéroélastiques d'ailes oscillantes multi-segments par méthode vortex. Master's thesis, Université Laval, 2009. *Pages ix, xiii, 5, 75, 77, 78, 79, and 80*

Olivier, M. *A Fluid-Structure Interaction Partitioned Algorithm and Flexible Flapping Wing Propulsion.* PhD thesis, Laval University, 2014. *Pages 52, 54, 55, and 57*

OpenCFD. *OpenFOAM - The Open Source CFD Toolbox - Programmer's Guide.* OpenCFD Ltd., United Kingdom, May 2012a. Version 2.1.1. *Page 44*

OpenCFD. *OpenFOAM - The Open Source CFD Toolbox - User's Guide*. OpenCFD Ltd., United Kingdom, May 2012b. Version 2.1.1. *Page 44*

Peng, Z. and Zhu, Q. Energy harvesting through flow-induced oscillations of a foil. *Physics of Fluids*, 21(12):1–9, 2009. *Page 3*

Poirel, D. private communication, July 2012. *Pages ix, xi, xii, 16, 17, 18, and 67*

Poirel, D. and Mendes, F. Experimental Investigation of Small Amplitude Self-Sustained Pitch-Heave Oscillations of a NACA0012 Airfoil at Transitional Reynolds Numbers. In *50th AIAA Aerospace and Science Meeting*, Nashville, Tennessee, January 2011. *Pages ix, xi, xii, 3, 13, 16, 17, 23, 60, and 67*

Poirel, D., Harris, Y., and Benaissa, A. Aeroelastic dynamics of a NACA 0012 airfoil in the transitional Reynolds number regime. In *2006 Summer Conference of the ASME Pressure Vessels and Piping Division*, Vancouver, Canada, July 2006. Paper PVP2006-ICPVT11-93957. *Pages xi and 14*

Poirel, D., Harris, Y., and Benaissa, A. Self-sustained aeroelastic oscillations of a NACA0012 airfoil at low-to-moderate Reynolds numbers. *Journal of Fluids and Structures*, 24(5): 700–719, 2008. *Pages ix, 2, and 16*

Razak, N. Abdul, Andrianne, T., and Dimitriadis, G. Flutter and stall flutter of a rectangular wing in a wind tunnel. *AIAA Journal*, 49(10):2258–2271, 2011. *Pages 3, 25, 26, 28, and 30*

Ricciardelli, F. Effects of the vibration regime on the spanwise correlation of the aerodynamic forces on a 5:1 rectangular cylinder. *Journal of Wind Engineering and Industrial Aerodynamics*, 98(4-5):215–25, 2010. *Page 141*

Rumsey, C. L. and Spalart, P. R. Turbulence model behavior in low reynolds number regions of aerodynamic flowfields. In *38th AIAA Fluid Dynamics Conference and Exhibit*, Seattle, Washington, June 2008. *Page 47*

Shimizu, E., Isogai, K., and Obayashi, S. Multiobjective design study of a flapping wing power generator. *Journal of Fluids Engineering*, 130(2):1–8, 2008. *Page 2*

Simiu, E. and Scanlan, R.H. *Winds Effects on Structures: Fundamentals and Applications to Design*. Wiley, New York, third edition, 1996. *Page 141*

Spalart, P. R. Trends in turbulence treatments. In *AIAA Fluids 2000 Conference and Exhibit*, Denver, Colorado, June 2000. *Page 61*

Spalart, P. R. and Allmaras, S. R. One-equation turbulence model for aerodynamic flows. *La Recherche Aérospatiale*, (1):5–21, 1994. *Pages 47 and 177*

Spalart, P. R. and Rumsey, C. L. Effective inflow conditions for turbulence models in aerodynamic calculations. *AIAA Journal*, 45(10):2544–2553, 2007. *Page 61*

Tan, Y. K. *Suistainable Energy Harvesting Technologies - Past, Present and Future.* InTech, 2011. doi: 10.5772/945. *Page 150*

Thorby, D. *Structural Dynamics and Vibration in Practice - An Engineering Handbook.* Butterworth-Heinemann, Burlington, Massachusetts, 2008. *Pages xi, 16, and 18*

Tran, C. T. and Petot, D. Semi-empirical model for the dynamic stall of airfoils in view of the application to the calculation of responses of a helicopter blade in forward flight. *Vertica*, 5(1):35–53, 1981. *Page 28*

Wilcox, D.C. *Turbulence Modeling for CFD.* DCW Industries, third edition, 1994. *Page 178*

Wildi, T. and Sybille, G. *Electrotechnique.* Les Presses de l'Université Laval, Québec, Canada, third edition, 2000. *Page 150*

Williamson, C. H. K. and Govardhan, R. Vortex-induced vibrations. *Annual Review of Fluid Mechanics*, 36:413–455, 2004. *Pages 5, 75, and 83*

Wu, B., Lang, Y., Zargari, N., and Kouro, S. *Power Conversion and Control of Wind Energy Systems.* Wiley, Hoboken, New Jersey, 2011. *Page 150*

Xiao, Q. and Zhu, Q. A review on flow energy harvesters based on flapping foils. *Journal of Fluids and Structures*, 46:174–191, 2014. *Pages 1, 2, and 168*

Yang, J., Preidikman, S., and Balaras, E. A strongly coupled, embedded-boundary method for fluid-structure interactions of elastically mounted rigid bodies. *Journal of Fluids and Structures*, 24(2):167–182, 2008. *Pages ix, 5, 51, 77, 78, and 79*

Young, J., Lai, J. C. S., and Platzer, M. F. A review of progress and challenges in flapping foil power generation. *Progress in Aerospace Sciences*, 67, 2014. doi: 10.1016/j.paerosci.2013.11.001. [in press]. *Page 2*

Zhu, Q. Optimal frequency for flow energy harvesting of a flapping foil. *Journal of Fluid Mechanics*, 675:495–517, 2011. *Page 2*

Zhu, Q. and Peng, Z. Mode coupling and flow energy harvesting by a flapping foil. *Physics of Fluids*, 21(3), 2009. *Page 2*

Zhu, Q., Haase, M., and Wu, C. H. Modeling the capacity of a novel flow-energy harvester. *Applied Mathematical Modelling*, 33(5):2207–2217, 2009. *Page 2*

Appendix A

Turbulence modeling

A.1 Spalart-Allmaras RANS model

The Spalart-Allmaras one-equation turbulence model (see Spalart and Allmaras (1994)) makes use of a modified eddy-viscosity concept. Generally speaking, the Boussinesq assumption permits to calculate the Reynolds stresses in the following way, where the indicial notation is used:

$$-\overline{u_i' u_j'} = \nu_t \left(\frac{\partial \overline{u}_i}{\partial x_j} + \frac{\partial \overline{u}_j}{\partial x_i} \right) - \frac{2}{3} k \, \delta_{ij} \; , \tag{A.1}$$

where ν_t is the turbulent kinematic viscosity, and k is the turbulent kinetic energy [1]. However, the Spalart-Allmaras model does not incorporate an equation for k, which means that the term involving the kinetic energy is dropped, thus leaving:

$$-\overline{u_i' u_j'} = \nu_t \left(\frac{\partial \overline{u}_i}{\partial x_j} + \frac{\partial \overline{u}_j}{\partial x_i} \right) \; . \tag{A.2}$$

Now, a transport equation for ν_t is required, and it has been obtained through an empirical approach. In fact, a transport equation for the modified turbulent viscosity ($\tilde{\nu}$) is obtained:

$$\begin{aligned} \overbrace{\frac{\partial \tilde{\nu}}{\partial t}}^{\text{Change rate}} + \overbrace{\overline{u}_j \frac{\partial \tilde{\nu}}{\partial x_j}}^{\text{Convection}} &= \overbrace{c_{b1} \left(1 - f_{t2}\right) \tilde{S} \tilde{\nu}}^{\text{Production}} - \overbrace{\left[c_{w1} f_w - \frac{c_{b1}}{\kappa^2} f_{t2} \left(\frac{\tilde{\nu}}{d} \right)^2 \right]}^{\text{Destruction}} \\ &\quad + \underbrace{\frac{1}{\sigma} \left[\frac{\partial}{\partial x_j} \left(\left(\nu + \tilde{\nu}\right) \frac{\partial \tilde{\nu}}{\partial x_j} \right) + c_{b2} \frac{\partial \tilde{\nu}}{\partial x_i} \frac{\partial \tilde{\nu}}{\partial x_i} \right]}_{\text{Diffusion}} \; , \end{aligned} \tag{A.3}$$

---

[1] The reader can refer to Eqs. 2.37 and 2.38 for a better understanding of the ($'$) notation and the (-) notation.

and the eddy viscosity can be computed as:

$$\nu_t \;=\; \tilde{\nu} f_{v1} \; . \tag{A.4}$$

To complete the model, the following definitions are required:

$$f_{v1} \;=\; \frac{\chi^3}{\chi^3 + c_{v1}^3} \; , \tag{A.5}$$

$$\chi \;=\; \frac{\tilde{\nu}}{\nu} \; , \tag{A.6}$$

$$\tilde{S} \;=\; \Omega \;+\; \frac{\tilde{\nu}}{\kappa^2 d^2} f_{v2} \; , \tag{A.7}$$

$$f_{v2} \;=\; 1 \;-\; \frac{\chi}{1 + \chi f_{v1}} \; , \tag{A.8}$$

$$f_w \;=\; g \left[\frac{1 + c_{w3}^6}{g^6 + c_{w3}^6} \right] \; , \tag{A.9}$$

$$g \;=\; r \;+\; c_{w2} \left(r^6 - r \right) \; , \tag{A.10}$$

$$r \;=\; \min \left[\frac{\tilde{\nu}}{\tilde{S} \kappa^2 d^2}, 10 \right] \; , \tag{A.11}$$

$$c_{w1} \;=\; \frac{c_{b1}}{\kappa^2} \;+\; \frac{1 + c_{b2}}{\sigma} \; , \tag{A.12}$$

where Ω is the vorticity magnitude, and d is the distance to the closest wall. Finally, the following constants are used: $c_{b1} = 0.1355$, $\sigma = 2/3$, $c_{b2} = 0.622$, $\kappa = 0.41$, $c_{w2} = 0.3$, $c_{w3} = 2$, $c_{v1} = 7.1$, and $c_{t4} = 0.5$.

A.2 SST $k - \omega$ RANS model

The SST $k - \omega$ RANS turbulence model from Menter (1994) again makes use of the eddy viscosity concept, but this time the complete equation, specifically Eq. A.1, is used. This model is based on the $k - \omega$ model of Wilcox (1994), and also on the $k - \epsilon$ model of Jones and Launder (1973). In fact, the SST $k - \omega$ model has been developed to take profit of the advantages pertaining to each model. Therefore, it acts as a $k-\omega$ model in the near-wall regions, and as a $k-\epsilon$ model in the free stream regions. This is because the $k-\omega$ model has proven to perform well in regions where separated flows and adverse pressure gradients are encountered. In counterpart, the $k-\epsilon$ model has proven to perform well where the flow is attached and well-behaved. The SST $k-\omega$ model has two transport equations, one for k and one for ω:

$$\overbrace{\frac{\partial k}{\partial t}}^{\text{Change rate}} + \overbrace{\overline{u}_j \frac{\partial k}{\partial x_j}}^{\text{Convection}} = \overbrace{\tilde{P}_k}^{\text{Production}} - \overbrace{\beta^* k\omega}^{\text{Destruction}} + \overbrace{\frac{\partial}{\partial x_j}\left(\left(\nu + \sigma_k \nu_t\right) \frac{\partial k}{\partial x_j} \right)}^{\text{Diffusion}} , \tag{A.13}$$

$$\begin{aligned} \overbrace{\frac{\partial \omega}{\partial t}}^{\text{Change rate}} + \overbrace{\overline{u}_j \frac{\partial \omega}{\partial x_j}}^{\text{Convection}} = \overbrace{\alpha S^2}^{\text{Production}} - \overbrace{\beta \omega^2}^{\text{Destruction}} &+ \overbrace{\frac{\partial}{\partial x_j}\left(\left(\nu + \sigma_\omega \nu_t\right) \frac{\partial \omega}{\partial x_j} \right)}^{\text{Diffusion}} \\ &+ \underbrace{2\left(1 - F_1\right) \sigma_{\omega 2} \frac{1}{\omega} \frac{\partial k}{\partial x_j} \frac{\partial \omega}{\partial x_j}}_{\text{Cross diffusion}} . \end{aligned} \tag{A.14}$$

The turbulent kinematic viscosity is then calculated as:

$$\nu_t = \frac{a_1 k}{\max\left(a_1 \omega,\ S F_2\right)} , \tag{A.15}$$

where

$$S = \sqrt{2 S_{ij} S_{ij}} , \tag{A.16}$$

$$S_{ij} = \frac{1}{2}\left(\frac{\partial \overline{u}_i}{\partial x_j} + \frac{\partial \overline{u}_j}{\partial x_i} \right) . \tag{A.17}$$

Further, F_1 and F_2 are the blending functions to switch between $k-\omega$ and $k-\epsilon$:

$$F_1 = \tanh\left[\left(\min\left\{ \max\left\{ \frac{\sqrt{k}}{\beta^* \omega y}, \frac{500\nu}{y^2 \omega} \right\}, \frac{4\rho\sigma_{\omega 2} k}{CD_{k\omega} y^2} \right\} \right)^4 \right] , \tag{A.18}$$

$$F_2 = \tanh\left[\left(\max\left\{ \frac{2\sqrt{k}}{\beta^* \omega y}, \frac{500\nu}{y^2 \omega} \right\} \right)^2 \right] . \tag{A.19}$$

Next, $CD_{k\omega}$ is defined in the following way to avoid issues associate to divisions by zero:

$$CD_{k\omega} = \max\left\{2\rho\sigma_{\omega 2}\frac{1}{\omega}\frac{\partial k}{\partial x_j}\frac{\partial \omega}{\partial x_j},\ 10^{-10}\right\} . \tag{A.20}$$

Very often, and this is the case in *OpenFOAM-2.1.x*, a limiter is applied on $\tilde{P}_k$ to avoid an artificial production of turbulence within stagnation regions as suggested by Menter (1993). With such a modification:

$$P_k = \nu_t \frac{\partial \overline{u}_i}{\partial x_j}\left(\frac{\partial \overline{u}_i}{\partial x_j} + \frac{\partial \overline{u}_j}{\partial x_i}\right) , \tag{A.21}$$

$$\tilde{P}_k = \min\left\{P_k,\ 20\beta^* \rho\omega k\right\} . \tag{A.22}$$

To end, the constants of the model are calculated through a blending of the constants pertaining to the $k-\omega$ model and to the $k-\epsilon$ model with the following equation:

$$\alpha = \alpha_1 F_1 + \alpha_2 \left(1 - F_1\right) . \tag{A.23}$$

The constants from the $k-\omega$ model are $\beta^* = 0.09$, $\alpha_1 = 5/9$, $\beta_1 = 3/40$, $\sigma_{k1} = 0.5$ and $\sigma_{\omega_1} = 0.5$, while the constants from the $k-\epsilon$ model are $\beta^* = 0.09$, $\alpha_2 = 0.44$, $\beta_2 = 0.0828$, $\sigma_{k1} = 1$ and $\sigma_{\omega 2} = 0.856$.

Appendix B

Equation for the cycle-averaged power

The equation for the instantaneous power has been introduced in Chapter 2. It was found to be:

$$\begin{aligned} C_{\mathcal{L}}\dot{y} \ + C_M\dot{\theta} \ = \ m_h\,\ddot{y}\dot{y} \ + \ S\left(\dot{\theta}^2\dot{y}\,\sin\theta - \ddot{\theta}\dot{y}\cos\theta\right) \ + \ D_h\,\dot{y}^2 \ + \ k_h\,y\dot{y} \\ + \ I_\theta\,\ddot{\theta}\dot{\theta} \ - \ S\ddot{y}\cos\theta\dot{\theta} \ + \ D_\theta\,\dot{\theta}^2 \ + \ k_\theta\,\theta\dot{\theta}\ . \end{aligned} \tag{B.1}$$

In order to find the cycle-averaged equation for the power, each term must be averaged over one complete cycle of oscillation. To achieve this, a very general periodic motion is assumed:

$$\theta \ = \ \sum_{n=1}^{\infty} \overbrace{\Big(a_n\cos\left(2\pi n f t\right) \ + \ b_n\sin\left(2\pi n f t\right)\Big)}^{\theta_n}\ , \tag{B.2}$$

$$y \ = \ \sum_{n=1}^{\infty} \overbrace{\Big(c_n\cos\left(2\pi n f t\right) \ + \ d_n\sin\left(2\pi n f t\right)\Big)}^{y_n}\ , \tag{B.3}$$

where the argument of each summation can be defined as θ_n and y_n. With these definitions, the cycle-averaged contribution of each term can be found, except for those involving the aerodynamic forces and moments. This is because the aerodynamics remains unknown. Starting with the inertial term for the heaving motion ($m_h\,\ddot{y}\dot{y}$), one can write:

$$\frac{1}{T}\int_0^T m_h\ddot{y}\,\dot{y}\,dt \;=\; \frac{m_h}{T}\sum_{n=1}^{\infty}\int_0^T\Big(-\,\omega_n^3 c_n^2\cos(\omega_n t)\sin(\omega_n t)\;-\;\omega_n^3 c_n d_n\cos^2(\omega_n t) \\ +\,\omega_n^3 c_n d_n\sin^2(\omega_n t)\;-\;\omega_n^3 d_n^2\sin(\omega_n t)\cos(\omega_n t)\Big)\,dt\;, \tag{B.4}$$

where $\omega_n = 2\pi n f$. Using a table of integration or a software such as *Maple*, the integral of the previous equation formally gives zero, independently of the values taken by ω_n, c_n and d_n. Therefore:

$$\frac{1}{T}\int_0^T m_h\ddot{y}\,\dot{y}\,dt \;=\; 0\;, \tag{B.5}$$

and the inertial term from the equation of motion in heave does not contribute to the cycle-averaged power. If the same operation is achieved with the inertial term in pitch ($I_\theta\ddot{\theta}\dot{\theta}$), the same equation is obtained except that the coefficients c_n and d_n are respectively replaced by a_n and b_n. The conclusion is therefore the same, and none of the inertial terms contribute to the equation for the cycle-averaged power.

Now, let's move to the damping term in heave ($D_h\dot{y}^2$). Using the same methodology as before:

$$\frac{1}{T}\int_0^T D_h\dot{y}^2\,dt \;=\; \frac{D_h}{T}\sum_{n=1}^{\infty}\int_0^T\Big(\omega_n^2 c_n^2\sin^2(\omega_n t)\;+\,\omega_n^2 d_n^2\cos^2(\omega_n t) \\ -\,2\omega_n^2 c_n d_n\sin(\omega_n t)\cos(\omega_n t)\Big)\;. \tag{B.6}$$

This time, the result of the integral does not fall to zero, and the following result is obtained:

$$\frac{1}{T}\int_0^T D_h\dot{y}^2\,dt \;=\; \frac{D_h}{T}\sum_{n=1}^{\infty}\left(2\pi^2 f n^2\left(d_n^2+c_n^2\right)\right)\;\neq\;0. \tag{B.7}$$

Again, the same conclusion holds true for the damping term involved within the equation for the pitching motion, except that c_n and d_n are respectively replaced with a_n and b_n, and D_h is replaced with D_θ. Concerning the term associated to the restoring force of the spring in heave, the following is obtained:

$$\frac{1}{T}\int_0^T k_h y\,\dot{y}\,dt \;=\; \frac{k_h}{T}\sum_{n=1}^{\infty}\int_0^T \Big(-\;\omega_n c_n^2\cos(\omega_n t)\sin(\omega_n t)\;+\;\omega_n c_n d_n\cos^2(\omega_n t) \\ -\;\omega_n c_n d_n\sin^2(\omega_n t)\;+\;\omega_n d_n^2\sin(\omega_n t)\cos(\omega_n t)\Big)\,dt\;. \tag{B.8}$$

Solving this equation, the result is found to be formally zero:

$$\frac{1}{T}\int_0^T k_h y\,\dot{y}\,dt \;=\; 0\;, \tag{B.9}$$

which is also the solution when the development is done for the cycle-averaged power associated to the restoring moment from the spring in pitch. That being said, the springs do not contribute to the cycle-averaged equation of power. Last but not least, the inertial coupling terms need to be treated. These terms require a special treatment as a result of the sines and cosines that are present. Indeed, because of the cyclic motion assumed, this will lead to terms of the type: $\cos(\cos(\omega_n t))$. To circumvent this issue, the sines and cosines are expressed as Taylor series:

$$\frac{1}{T}\int_0^T S\left(\dot{\theta}^2\sin\theta\dot{y}-\ddot{\theta}\cos\theta\dot{y}\right)\,dt \;=\; \frac{S}{T}\sum_{n=1}^{\infty}\int_0^T \Bigg(\dot{\theta}_n^2\dot{y}_n\sum_{p=0}^{\infty}\frac{(-1)^p}{(2p+1)!}\theta_n^{2p+1)} \\ -\;\ddot{\theta}_n\dot{y}_n\sum_{m=0}^{\infty}\frac{(-1)^m}{(2m)!}\theta_n^{2m}\Bigg)\,dt\;, \tag{B.10}$$

$$-\frac{1}{T}\int_0^T S\left(\ddot{y}\dot{\theta}\cos\theta\right)\,dt \;=\; -\frac{S}{T}\sum_{n=1}^{\infty}\int_0^T \left(\ddot{y}_n\dot{\theta}_n\sum_{q=0}^{\infty}\frac{(-1)^q}{(2q)!}\theta_n^{2q}\right)\,dt\;. \tag{B.11}$$

All terms involved within the previous two equations have not been fully developed here as this would certainly lead to large mathematical expressions. Nevertheless, a symbolic calculation software, such as *Maple*, can be used to verify that Eqs. B.10 and B.11 are not equal to zero unless S is null. This can be verified by using a finite number of terms within the Taylor series, and by successively increasing the number of terms. Furthermore, by using the same strategy it is possible to show that the summation of Eqs. B.10 and B.11 falls to zero as the number of terms is increased. This indicates that the inertial coupling terms do not contribute, overall, to the cycle-averaged equation of power for the fully-passive, flapping-airfoil turbine. Nevertheless, the inertial coupling permits a transfer of energy between both degrees-of-freedom. To summarize, the cycle-averaged equation of power is:

$$\frac{1}{T}\int_{0}^{T}\left(C_{\mathcal{L}}\dot{y} \;+\; C_M\dot{\theta}\right)dt \;=\; \frac{1}{T}\int_{0}^{T}\left(D_h\dot{y}^2 \;+\; D_\theta\dot{\theta}^2\right)dt\ . \tag{B.12}$$